University of Alberta

Magnetotelluric constraints on the role of fluids
in convergent plate boundaries

by

Dennis Rippe

A thesis submitted to the Faculty of Graduate Studies and Research
in partial fulfillment of the requirements for the degree of

Doctor of Philosophy

in

Geophysics

Department of Physics

Fall 2012

Edmonton, Alberta

Abstract

Convergent plate boundaries have played an important role in the growth and assembly of the modern continents. To obtain a better understanding of the tectonic processes in these boundaries, it is necessary to constrain the rheology of the crust and upper mantle in these regions. Magnetotelluric studies measure electrical resistivities and provide an excellent tool to determine the fluid content and thermal structure. These are key parameters in determining the rheology. Magnetotelluric studies were used to investigate two types of convergent plate boundaries: (i) the Cascadia subduction zone as an example for active subduction of an oceanic plate beneath a continent and (ii) the Indian-Eurasian collision as an example for a modern continent-continent collision.

Geodynamic models requiring vigorous convection of a low viscosity mantle have been successful in explaining high mantle temperatures in the backarc of the Cascadia subduction zone. Geochemical calculations indicate that high temperatures and water content can significantly reduce mantle viscosity. Long-period magnetotelluric data of the Cascadia subduction zone are used to determine the electrical resistivity structure and to constrain the backarc mantle rheology, specifically in terms of the amount of fluids. Non-uniqueness in the interpretation is reduced by using constraints from seismic tomography and geochemical calculations. At shallow mantle depths, water contents of 500-1000 ppm and melt fractions of 0.5-2.5% are required, which can reduce mantle viscosity and allow for vigorous mantle convection.

In the India-Eurasia continental collision, models invoking flow in a weak lower crustal layer have been successful in explaining a number of geological and geophysical observations associated with the evolution of the Tibetan plateau. Geophysical observations indicate that the weak lower crustal layer may be the result of partial melting and/or aqueous fluids. Laboratory studies predict an order reduction in strength for melt fractions of 5-10%. By relating these laboratory studies to magnetotelluric observations it is possible to estimate the flow parameters associated with the channel flow model. Magnetotelluric studies require conductances of up to 20,000 S beneath the Tibetan Plateau, suggesting flow velocities of 0.02-4.5 cm/a. These flow velocities support the idea that channel flow could occur beneath parts of Tibet.

Acknowledgements

First and foremost I would like to thank my supervisor Dr. Martyn Unsworth, not only for giving me the opportunity to pursue this research but also for the insightful guidance and the constant support that I received from him during this process. In addition, I would like to thank my supervisory committee Dr. Claire Currie and Dr. Vadim Kravchinsky for their helpful mentoring. I also wish to extend my thanks to my examining committee Dr. Richard Bailey, Dr. John Waldron and Dr. Jeff Gu for their careful and constructive review of this thesis.

I would like to thank the previous and current members of the University of Alberta MT group, Erşan Türkoğlu, Ted Bertrand, Greg Nieuwenhuis, Andrea Cochrane, Matthew Comeau, Mitch Liddell and Juliane Hübert for all the insightful discussions and their support during my studies.

The INDEPTH MT data were collected by the INDEPTH-MT group, which is a collaboration between the University of Washington, China University of Geosciences, Geological Survey of Canada, Dublin Institute for Advanced Study and the University of Alberta. I would like to thank the members of this group which include Wei Wenbo, Jin Sheng, Tan Handong, Alan Jones, Jessica Spratt, Kurt Solon, Paul Bedrosian, Shenghui Li, Juanjo Ledo, Greg Clarke and John Booker.

I would also like to thank Wolfgang Soyer, Volkan Tuncer, Erşan Türkoğlu, Ted Bertrand and Greg Nieuwenhuis for their field assistance in collecting the MT

data of the Canadian Cordillera. Members of the Lithoprobe projects are thanked for the permission to use their data. In addition, Jean-Phillipe Mercier and Michael Bostock are thanked for the permission to use their seismic tomography model. Finally, Gary Egbert, Randy Mackie, Alan Jones and Gary McNeice are thanked for the use of their software.

This thesis as well as the completion of my studies would not have been possible without the support of my family and friends. I would particularly like to thank my mother and stepfather Gerlinde and Wilfried Dankowski as well as my father and his wife Johann and Marion Rippe. Thank you for all your love and for constantly believing in me.

Last but not least, I would like to thank my wonderful wife Maria. Thank you for your love and your patience, especially during the write-up of this thesis. Thank you! I love you so much.

Table of Contents

List of Tables

List of Figures

List of Abbreviations and Symbols

Abbreviations

1D	One-Dimensional
2D	Two-Dimensional
3D	Three-Dimensional
BNS	Banggong-Nuijang Suture
CB	Coastal Belt
cpx	Clinopyroxine
EHS3D	Eastern Himalayan Syntaxis 3D
EM	Effective Medium
FB	Foreland Belt
FTB	Fold-Thrust Belt
Ga	Billion years
GHS	Greater Himalayan Sequence
GPS	Global Positioning System
gt	Garnet
HS	Hashin-Shtrikman
IB	Insular Belt
IMB	Intermontane Belt
INDEPTH	International Deep Profiling of Tibet and Himalaya
ITS	Indus Tsangpo Suture
JRS	Jinsha River Suture
KF	Kunlun Fault
LHS	Lesser Himalayan Sequence
LIMS	Long-period Intelligent Magnetotelluric System
Ma	Million years
MBT	Main Boundary Thrust
MCT	Main Central Thrust
MHT	Main Himalayan Thrust
Moho	Mohorovičić Discontinuity
MT	Magnetotelluric
NIMS	Narod Intelligent Magnetotelluric System
OB	Omineca Belt
ol	Olivine
opx	Orthopyroxene
P wave	Pressure wave
P_n	Moho refracted wave
ppm	Parts per million
r.m.s.	Root mean square
RMT	Rocky Mountain Trench
RRF	Red River Fault
S wave	Shear wave
SEO3	Standard Electrical Olivine 3 Model

SI	International System of Units (abbreviated from French: Système international d'unités)
spn	Spinel
STD	South Tibetan Detachment
TE	Transverse Electric
TM	Transverse Magnetic
TS	Tethyan Sequence
WCSB	Western Canadian Sedimentary Basin
wt-%	Weight percent
XJF	Xiaojiang Fault

Symbols

$\underline{\boldsymbol{A}}$	Splitting tensor
A_{eff}	Material constant
A'_{eff}	Temperature independent material constant
$A^{\text{T}}_{\text{eff}}$	Material constant at Temperature T
$\boldsymbol{B}$, B	Magnetic flux density
$\underline{\boldsymbol{C}}$	Galvanic distortion matrix
C	Schmucker-Weidelt transfer function
C	Conductance
C	Mass fraction
c	Hydrogen concentration
$C^0_{H_2O}$	Bulk water concentration
$C^{melt}_{H_2O}$	Water concentration in the melt phase
$C^{perid}_{H_2O}$	Water concentration in the residual rock crystal
C_w	Water content
$\boldsymbol{D}$	Electric flux density
$\underline{\boldsymbol{D}}$	Magnetic distortion matrix
D	Hydrogen diffusivity
$\boldsymbol{d}$	Data vector
d	Layer thickness
$D_H^{perid/liq}$	Melt partition coefficient
$\boldsymbol{E}$, E	Electric field intensity
E^*	Activation energy
F	Degree of melting
g	Site gain
$\boldsymbol{H}$	Magnetic field intensity
h	Channel thickness
Δh	Topography variation
H^*	Activation enthalpy
$\underline{\boldsymbol{I}}$	Identity matrix

$\boldsymbol{J}$	Current density
J	Misfit
K	Bulk modulus
k	Boltzmann constant
L	Length scale of topography variation
M	Molar mass
$\boldsymbol{m}$	Model parameter vector
m	Cementation factor
m	Mass
n	Power law exponent
n	Amount of a substance
P	Pressure
p	Electromagnetic skin depth
P_0	Reference pressure at the Earth's surface
$\frac{dp}{dx}$	Horizontal pressure gradient
Q	Activation energy
q	Vertical wave number
q	Hydrogen charge
Q_p, Q_μ	Quality factor
R	Universal gas constant
$\underline{\boldsymbol{S}}$	Shear tensor
$\underline{\boldsymbol{T}}$	Twist tensor
T	Temperature
t	Time
T_0	Reference temperature at the Earth's surface
T_e	Effective elastic thickness
T_m	Moho temperature
u_0	Relative velocity
$\bar{u}$	Mean flow velocity
v_p	P wave velocity
v_s	S wave velocity
V^*	Activation volume
$\underline{\boldsymbol{W}}$	Weighting matrix
W	Molar mass
X	Magnesium number
X	Modal proportion
$\underline{\boldsymbol{Z}}$, Z	Electromagnetic impedance
z	Depth
$[H^+]_{\text{ppm Si}}$	Hydrogen solubility
$\Delta\hat{S}_{perid}^{fusion}$	Molar entropy of fusion
$\Delta S_{perid}^{fusion}$	Entropy of fusion per unit mass

α	Strike angle
α	Inversion smoothing factor
α	Thermal expansion coefficient
$\underline{\beta_\vartheta}$	Rotation matrix for a counter clockwise rotation through angle ϑ
ε_0	Permittivity of free space ($\varepsilon_0 = 8.86 \cdot 10^{-12}$As/Vm)
ε_r	Relative permittivity
$\dot{\varepsilon}$	Strain rate
η	Free charge density
η	Phase-sensitive skew
η	Dynamic viscosity
η_{eff}	Effective viscosity
κ	Swift skew
λ	Volumetric mineral fraction
μ	Shear modulus
μ_0	Permeability of free space ($\mu_0 = 4\pi \cdot 10^{-7}$Vs/Am)
μ_r	Relative magnetic permeability
ρ	Bulk resistivity
ρ	Density
ρ_a	Apparent resistivity
ρ_f	Fluid resistivity
ρ_c, ρ_m	Densities of the crust and mantle
$\boldsymbol{\sigma}$, σ	Electrical conductivity
σ_{eff}	Effective electrical conductivity
τ	Inversion regularization parameter
τ	Shear stress
ϕ	Porosity, Melt fraction
φ	Phase
ω	Angular frequency
χ	Melt fraction
χ^2	Misfit

1 Introduction

The theory of plate tectonics has revolutionized our understanding of the Earth and the processes that have formed the modern continents (Fowler, 2004). The idea that the Earth's surface is composed of rigid plates that move over time has been in existence for many years. Early ideas that the surface was dynamic were based on the apparent fit between the continents that border the Atlantic Ocean, leading to the idea that they were once connected (Snider-Pellegrini, 1858). Alfred Wegener advanced this debate with his theory of continental drift. Based on the distribution of fossils, the location of mountain belts and deposits from past glaciations, he suggested that all the continents had once been grouped into one great land mass near the south pole called Pangaea (Wegener, 1912). After the breakup of Pangaea, which Wegener suggested had occurred ~200 Ma, the resulting continents drifted slowly across the Earth's surface, moving relative to each other to their present location. Wegener attributed the continental drift to the rotation of the Earth, which created a centrifugal force towards the equator that he called the "pole fleeing force". However, this mechanism was quickly rejected, as the polar fleeing force was too weak to explain the movement of the continents. For the following decades, Wegener's theory of continental drift remained a source of major controversy, largely because he could not provide a plausible mechanism to explain the movement of the continents. An alternative mechanism to explain the continental drift was proposed by Arthur Holmes, who considered mantle convection caused by radioactive heating as the driving force for

continental drift (Holmes, 1931). However, Holmes' idea did not receive any attention until the 1960s, when the advent of paleomagnetism led to the discovery of sea floor spreading (Hess, 1962; Vine & Matthews, 1963). Based on this discovery a modified form of Wegener's idea was accepted as the theory of plate tectonics (McKenzie & Parker, 1967; Morgan, 1968; Le Pichon, 1968) and gained wide acceptance in the geological and geophysical community. Unlike Wegener's continental drift theory, which thought of continents ploughing through oceanic rocks, it is based on the movement of rigid continental and oceanic plates over the surface of the Earth.

Today the theory of plate tectonics offers a unifying explanation of many geological and geophysical observations. As continental and oceanic plates are moved across the Earth's surface by convection of the underlying mantle, it is the plate boundaries that are of particular interest for understanding a wide range of deformation processes. Plate boundaries can be divided into three categories: (i) divergent boundaries such as mid-ocean ridges and rift valleys, (ii) conservative boundaries, such as transform faults where plates move past each other and (iii) convergent boundaries, such as continent-continent collisions and subduction zones.

In this thesis, the focus will be on convergent plate boundaries. The first type of convergent boundaries that will be considered is the subduction of an oceanic plate beneath a continental plate due to the higher density of the oceanic crust and lithospheric mantle compared to the continental crust. This type of boundary can

be found along the western margins of the North and South American continents. Subduction has played a major role in the growth of the continents by (a) providing a mechanism to generate intermediate to felsic rocks from ultramafic mantle rocks through arc volcanism, (b) driving continent-continent collisions and (c) causing the accretion of small portions of continental and arc crust (Fowler, 2004). This last process is called terrane accretion and was first recognized in the Southern Canadian Cordillera (Coney et al., 1980), where it has significantly contributed to the growth of the North American continent. Today, terrane accretion occurs along the south central coast of Alaska, where the Yakutat block is being accreted to the North American continent (e.g. Bruhn et al., 2004).

The second type of convergent plate boundaries that will be considered is continent-continent collision, a process which has led to the assembly of the modern continents. Continent-continent collisions begin with the subduction of oceanic plate beneath a continental plate, leading to the closure of an ocean basin to give a suture zone. Subduction continues until the continental plate collides with the continental part of the subducting plate, at which point subduction stops due to the low density of the continental lithosphere compared to the underlying mantle (e.g. Unsworth, 2009). A number of examples of this type of collision are preserved in the geological record. These include the collision of East and West Gondwana during the Neoproterozoic, which formed the East African Orogen (Kröner & Stern, 2005), as well as the collision of Gondwana and Laurasia in the late Paleozoic, which formed the supercontinent Pangaea (Matte, 2001). In order to better understand these ancient continent-continent collisions, it is necessary to

study modern examples of active continent-continent collisions. These include the Indian-Eurasian collision, which has formed the Himalaya and Tibetan Plateau (Royden et al., 2008), the Arabian-Eurasian collision, which has formed the Zagros Mountains and the Anatolian-Iranian Plateau (Mouthereau et al., 2012) and the more evolved African-Eurasian collision, which has led to the orogeny of the European Alps (e.g. Coward & Dietrich, 1989). Deformation in these collision zones extends horizontally over several thousand kilometres and the overall mass balance has been explained by a wide range of tectonic processes. These wide zones of deformation are in contrast to divergent and conservative boundaries, where the deformation zone is generally narrow, typically just a few tens of kilometres (Unsworth, 2009).

Previous geophysical studies have shown that fluids may play an important role in the deformation processes occurring in convergent boundaries. In subduction zones, for example, fluids are transported from the surface into the mantle (Hacker, 2008), where they affect both physical and chemical properties of the rocks (Rüpke et al., 2004). Geodynamic studies on the Cascadia subduction zone located on the west coast of North America require vigorous, small scale convection of a weak, low-viscosity asthenosphere to explain elevated mantle temperatures in the backarc of the subduction zone (Currie et al., 2004a). Geochemical studies suggest that high temperatures and water concentrations can significantly weaken the upper mantle by lowering its viscosity (Dixon et al., 2004). In addition, water can also lower the melting temperature of the mantle,

allowing for dehydration melting of mantle rocks at temperatures above the wet solidus (Hirschmann et al., 2009), in which dehydration of the mantle rocks occurs as water partitions into the melt phase. To determine whether vigorous, small scale convection can occur in the backarc of the Cascadia subduction zone, it is therefore necessary to constrain the mantle rheology. While previous geophysical studies have successfully constrained the temperature of the mantle in this region (Currie et al., 2004a), further observations are required to constrain its hydration state and to determine the effect on mantle viscosity.

Fluids also play an important role in continent-continent collisions. For the Indian-Eurasian collision, for example, localized flow of a fluidized, partially molten lower crust may have significantly contributed to the uplift and outward extension of the Tibetan Plateau (Royden et al., 1997; Clark & Royden, 2000). For this kind of flow to occur, the lower crust must be relatively weak. The strength of the crust is controlled by its composition, temperature and the presence of fluid phases such as melt. Laboratory measurements suggest that melt fractions of 5-10 % reduce the crustal strength by one order of magnitude compared to melt absent conditions (Rosenberg & Handy, 2005). To determine whether the crust in Tibet is susceptible to crustal flow, it is therefore necessary to constrain its rheology (McKenzie & Jackson, 2002).

The focus of this work is on the analysis and interpretation of magnetotelluric data. Magnetotelluric data are a powerful tool for constraining the temperature

and presence of fluid phases, which are key parameters governing the rheology of the crust and upper mantle. As part of the study on the Cascadia subduction zone, long-period magnetotelluric data were collected and processed in 2009. These data provide an extension of an existing magnetotelluric data sat for this region by Soyer & Unsworth (2006). For the study of the Indian-Eurasian collision, magnetotelluric data previously collected as part of the multidisciplinary International Deep Profiling of Tibet and Himalaya (INDEPTH) project will be used. The principles of the magnetotelluric method and its application to imaging crustal and mantle structures will be discussed in chapter 2.

In chapter 3, the Cascadia subduction zone located on the west coast of North America will be discussed as an example of a region of active subduction of oceanic crust beneath a continental plate. Previous broadband magnetotelluric studies of the Cascadia subduction zone have successfully determined the electrical resistivity structure of the crust (Gough, 1986; Ledo & Jones, 2001), but the lack of long-period magnetotelluric data prevented imaging of the upper mantle. In chapter 3, an extension of the first long-period magnetotelluric data set of the Cascadia subduction zone by Soyer & Unsworth (2006) will be presented. The combined data sets have been used to determine the electrical resistivity structure to depths of the asthenospheric upper mantle.

The results of these magnetotelluric observations can be used to determine the rheology of the backarc mantle of the Cascadia subduction zone. A previous analysis by Soyer & Unsworth (2006) showed that the observed electrical

resistivities of the backarc mantle can be explained by the presence of either aqueous fluids or melt, but was not able to distinguish which of these fluids is present in different regions of the mantle. In chapter 4, thermodynamic calculations on the reduction of the mantle solidus temperature in the presence of water will be used to constrain regions of dehydration melting, i.e. melting of hydrated mantle rocks at temperatures above the wet solidus. A key aspect in this analysis is a knowledge of the mantle temperature, which will be calculated from seismic velocity data obtained from seismic tomography (Mercier et al., 2009). This joint interpretation will help to reduce the non-uniqueness associated with the interpretation of the type and quantity of fluids required to explain the electrical resistivities of the backarc mantle.

In chapter 5, the Indian-Eurasian collision will be discussed as an example of an active continent-continent collision. This collision follows subduction that has led to the closure of the Tethyan Ocean around 55 Ma. Magnetotelluric data will be used to determine the electrical resistivity structure beneath the Tibetan Plateau, and to constrain the presence of partial melt at lower crustal depths. By relating the magnetotelluric observations to laboratory studies on partially molten rocks, which indicate reduced strength of the crustal rocks with increasing melt fraction (Rosenberg & Handy, 2005), it is possible to estimate the flow parameters associated with crustal flow in Tibet (Rippe & Unsworth, 2010).

Finally, in chapter 6 a summary of the results and an outlook on future research questions will be presented.

2 Principles of electromagnetic depth sounding

Electromagnetic geophysical methods measure the electrical resistivity of the Earth's crust and mantle, which varies by several order of magnitudes for typical crustal and mantle rocks (Figure 2.1). They are also sensitive to the presence of fluid phases or minor conductive mineral constituents, as these strongly affect the electrical resistivity of the Earth's crust and mantle. Therefore, electrical resistivity is an important parameter in constraining the properties of the Earth's crust and mantle. To measure the electrical resistivity structure of the subsurface, a range of electromagnetic geophysical methods can be used. Controlled source electromagnetic methods measure secondary electromagnetic fields induced by a primary electromagnetic field generated by a dipole transmitter. Their depth of investigation is generally limited to the upper crust, ranging from a few hundred metres for frequency domain methods up to a few tens of kilometres for time-domain methods with powerful dipole transmitters (e.g. Ward, 1983).

To further extend the depth of investigation, the magnetotelluric (MT) method can be used. The magnetotelluric method is a passive, electromagnetic method, whose fundamental theory was independently proposed by Tikhonov (1950) and Cagniard (1953). It utilizes time variations in the Earth's magnetic field to measure the electrical resistivity of the crust and mantle to a depth of several hundred kilometres. For periods less than 1 s, the time variations in the Earth's magnetic field are caused by radio atmospheric signals (sferics) generated by meteorological lightning activity, that propagate through the Earth-Ionosphere

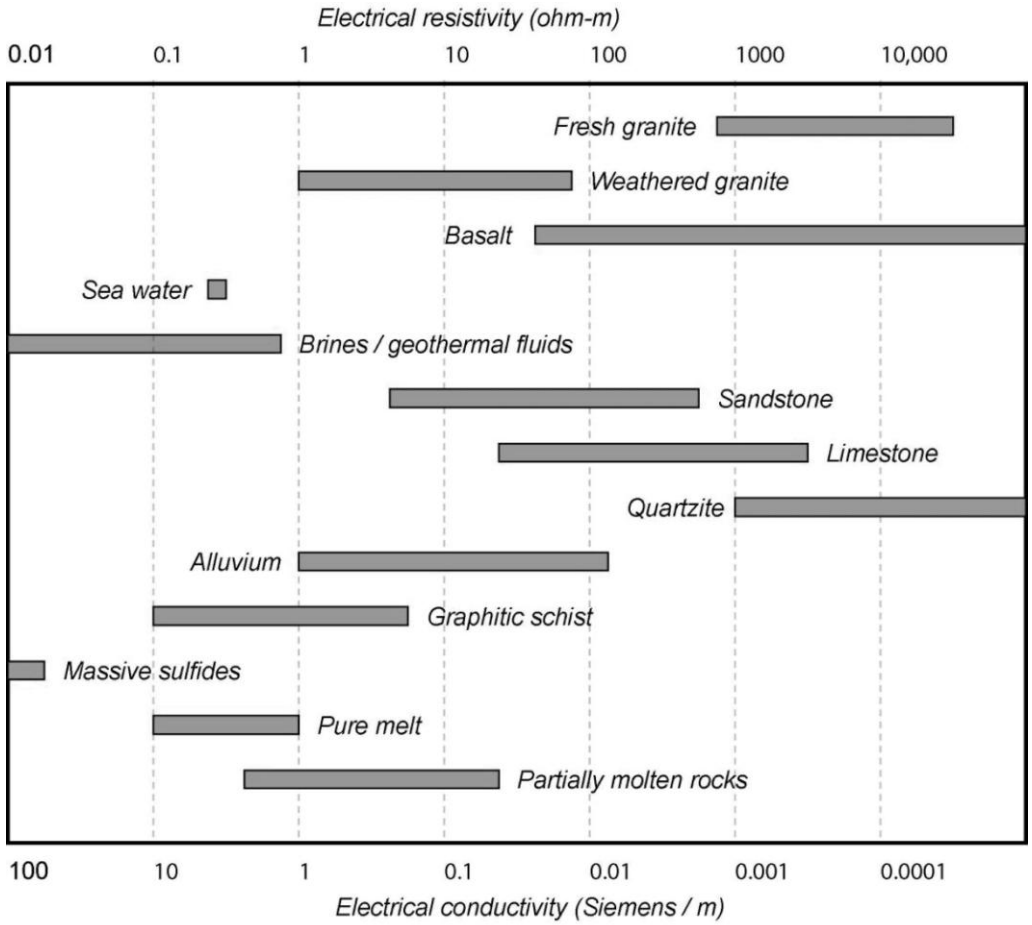

Figure 2.1: Electrical resistivities of some typical crustal and mantle rocks and other Earth materials. (courtesy of Martyn Unsworth, http://www.ualberta.ca/~unsworth/UA-classes/424/424index.html)

waveguide. For periods longer than 1 s, the magnetic field variations are the result of interactions of the solar wind with the Earth's magnetosphere (Simpson & Bahr, 2005).

The remainder of this chapter will discuss how the magnetotelluric method can be used to infer the electrical resistivity structure of the Earth (e.g. Simpson & Bahr, 2005). Starting from Maxwell's equations, the equations governing electromagnetic diffusion in the Earth will be derived. Based on these equations,

the application of the magnetotelluric methods to simple electrical resistivity structures will be described. Finally, the data collection and interpretation techniques of magnetotelluric data will be discussed.

2.1 Electromagnetic induction in the Earth

Maxwell's equations form the foundation of the classical electrodynamics, which describe the electric and magnetic field quantities based on a system of first-order partial differential equations. In the SI system of units they can be written as:

$$\boldsymbol{\nabla} \cdot \boldsymbol{D} = \eta \tag{2.1}$$

$$\boldsymbol{\nabla} \times \boldsymbol{H} = \boldsymbol{J} + \frac{\partial \boldsymbol{D}}{\partial t} \tag{2.2}$$

$$\boldsymbol{\nabla} \times \boldsymbol{E} + \frac{\partial \boldsymbol{B}}{\partial t} = 0 \tag{2.3}$$

$$\boldsymbol{\nabla} \cdot \boldsymbol{B} = 0 \tag{2.4}$$

where $\boldsymbol{E}$ is the electric field intensity, $\boldsymbol{D}$ is the electric flux density, $\boldsymbol{H}$ is the magnetic field intensity, $\boldsymbol{B}$ is the magnetic flux density, $\boldsymbol{J}$ is the current density and η is the free electric charge density. The relation between the electric and magnetic flux densities and the corresponding field intensities is given by the constitutive relations, which for homogeneous, isotropic media with relative permittivity ε_r and magnetic permeability μ_r take the form:

$$\boldsymbol{D} = \varepsilon_0 \varepsilon_r \boldsymbol{E} \tag{2.5}$$

$$\boldsymbol{B} = \mu_0 \mu_r \boldsymbol{H} \tag{2.6}$$

with the permittivity of free space $\varepsilon_0 = 8.86 \cdot 10^{-12}\text{As/Vm}$ and the permeability of free space $\mu_0 = 4\pi \cdot 10^{-7}\text{Vs/Am}$. In addition to these two equations, Ohm's law relates the electric field intensity $\boldsymbol{E}$ to the current density $\boldsymbol{J}$ through the electrical conductivity tensor $\boldsymbol{\sigma}$:

$$\boldsymbol{J} = \boldsymbol{\sigma E} \tag{2.7}$$

Therefore, Maxwell's equations take the following form:

$$\boldsymbol{\nabla} \cdot \boldsymbol{E} = \frac{\eta}{\varepsilon_0 \varepsilon_r} \tag{2.8}$$

$$\boldsymbol{\nabla} \times \boldsymbol{B} = \mu_0 \mu_r \left(\boldsymbol{\sigma E} + \varepsilon_0 \varepsilon_r \frac{\partial \boldsymbol{E}}{\partial t} \right) \tag{2.9}$$

$$\boldsymbol{\nabla} \times \boldsymbol{E} + \frac{\partial \boldsymbol{B}}{\partial t} = 0 \tag{2.10}$$

$$\boldsymbol{\nabla} \cdot \boldsymbol{B} = 0 \tag{2.11}$$

Using the vector identities

$$\boldsymbol{\nabla} \times (\boldsymbol{\nabla} \times \boldsymbol{A}) = \boldsymbol{\nabla}(\boldsymbol{\nabla} \cdot \boldsymbol{A}) - \boldsymbol{\nabla}^2 \boldsymbol{A} \tag{2.12}$$

$$\boldsymbol{\nabla} \times (\lambda \boldsymbol{A}) = \boldsymbol{\nabla}\lambda \times \boldsymbol{A} + \lambda \boldsymbol{\nabla} \times \boldsymbol{A} \tag{2.13}$$

Maxwell's equations can be rearranged as:

$$\boldsymbol{\nabla}^2\boldsymbol{E} = \mu_0\mu_r\left(\boldsymbol{\sigma}\frac{\partial \boldsymbol{E}}{\partial t} + \varepsilon_0\varepsilon_r\frac{\partial^2\boldsymbol{E}}{\partial t^2}\right) - \boldsymbol{\nabla}(\boldsymbol{\nabla}\cdot\boldsymbol{E}) \tag{2.14}$$

$$\boldsymbol{\nabla}^2\boldsymbol{B} = \mu_0\mu_r\left(\boldsymbol{\sigma}\frac{\partial \boldsymbol{B}}{\partial t} + \varepsilon_0\varepsilon_r\frac{\partial^2\boldsymbol{B}}{\partial t^2}\right) - \mu_0\mu_r(\boldsymbol{\nabla\sigma}\times\boldsymbol{E}) \tag{2.15}$$

As $\nabla(\nabla\cdot\boldsymbol{E}) = \frac{1}{\varepsilon_0\varepsilon_r}\nabla\eta$, these two equations can be simplified if a homogeneous conductivity σ and free charge density distribution ($\nabla\eta = 0$) are assumed:

$$\boldsymbol{\nabla}^2\boldsymbol{F} = \mu_0\mu_r\left(\sigma\frac{\partial \boldsymbol{F}}{\partial t} + \varepsilon_0\varepsilon_r\frac{\partial^2\boldsymbol{F}}{\partial t^2}\right) \tag{2.16}$$

In this equation, as well as in all further explanations, $\boldsymbol{F}$ represents the electric field intensity $\boldsymbol{E}$ or the magnetic flux density $\boldsymbol{B}$ depending on the context.

For electromagnetic induction in the Earth, the following simplifying assumptions can be made (e.g. Simpson & Bahr, 2005):

- Spatial variations in the relative dielectric permittivity ε_r and relative magnetic permeability μ_r for different rocks are negligible compared to variations in the electrical conductivity σ. Therefore, the values for $\varepsilon = \varepsilon_0\varepsilon_r$ and $\mu = \mu_0\mu_r$ can be approximated by the values for free space (ε_0 and μ_0).

- For the frequency range used in electromagnetic depth sounding, the displacement current $\varepsilon_0\varepsilon_r\frac{\partial \boldsymbol{E}}{\partial t}$ in equation (2.9) is negligible compared to

the conduction current $\sigma \boldsymbol{E}$. This assumption is known as quasi-static approximation. As a result, no error results from assuming that the dielectric permittivity is the free space value.

Taking these assumptions into account, equation (2.16) takes the form of a Helmholtz equation:

$$\boldsymbol{\nabla}^2 \boldsymbol{F}(\mathrm{x}, \mathrm{y}, \mathrm{z}, \mathrm{t}) = \mu_0 \sigma \frac{\partial \boldsymbol{F}(\mathrm{x}, \mathrm{y}, \mathrm{z}, \mathrm{t})}{\partial t} \tag{2.17}$$

which describes how an electromagnetic wave impinging on the Earth's surface propagates through the Earth by diffusion.

For planar waves with amplitude $\boldsymbol{F_0}$ and harmonic time dependence $e^{i\omega t}$ the Helmholtz equation becomes:

$$\boldsymbol{\nabla}^2 \boldsymbol{F}(\omega) = i\omega\mu_0 \sigma \boldsymbol{F}(\omega) \tag{2.18}$$

This equation can be solved by:

$$\boldsymbol{F}(\omega) = \boldsymbol{F_0} e^{i\omega t - qz} \tag{2.19}$$

with the vertical wave number

$$q(\omega) = \sqrt{i\mu_0 \sigma \omega} = \sqrt{\frac{\mu_0 \sigma \omega}{2}} + i\sqrt{\frac{\mu_0 \sigma \omega}{2}} \tag{2.20}$$

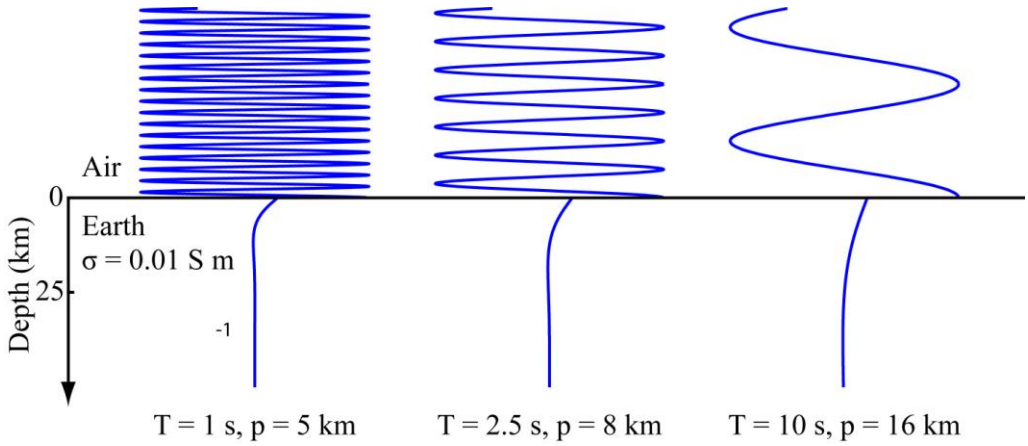

Figure 2.2: Illustration of the skin effect. Long period electromagnetic waves (right) penetrate deeper into the Earth than short period electromagnetic waves (left). The reflected wave is not shown.

The reciprocal of the real part of $q(\omega)$

$$p(\omega) = \frac{1}{\mathrm{Re}(q(\omega))} = \sqrt{\frac{2}{\mu_0 \sigma \omega}} \tag{2.21}$$

is called the electromagnetic skin depth. It defines the depth at which the field intensity $\boldsymbol{F}$ with period $T = \frac{2\pi}{\omega}$ in a homogeneous half space with conductivity σ has decayed to $\frac{1}{e}$ of its original amplitude (Figure 2.2). Furthermore, the reciprocal of $q(\omega)$

$$C(\omega) = \frac{1}{q(\omega)} = \frac{p(\omega)}{2} - i\frac{p(\omega)}{2} \tag{2.22}$$

is called the Schmucker-Weidelt transfer function (Weidelt, 1972; Schmucker, 1973).

2.2 The magnetotelluric method

The magnetotelluric (MT) method is based on the measurement of time-varying, magnetic fields which, as described in the previous section, penetrate the Earth by diffusion. These fields induce electric (telluric) fields in the Earth's interior, which in turn lead to secondary magnetic fields (Tikhonov, 1950; Cagniard, 1953). By measuring variations in the horizontal and vertical components of the magnetic field and the corresponding changes in the horizontal components of the electric field, lateral and vertical conductivity variations can be inferred.

Transfer functions can be determined, which relate the individual components of the electric and magnetic fields. These transfer functions are called impedances and are complex numbers that can be expressed in the form of a frequency dependent impedance tensor $\underline{\boldsymbol{Z}}(\omega)$:

$$\boldsymbol{E}(\omega) = \underline{\boldsymbol{Z}}(\omega) \cdot \boldsymbol{B}(\omega) \tag{2.23}$$

In general, this equation can be written as:

$$\begin{pmatrix} E_x(\omega) \\ E_y(\omega) \end{pmatrix} = \begin{pmatrix} Z_{xx}(\omega) & Z_{xy}(\omega) \\ Z_{yx}(\omega) & Z_{yy}(\omega) \end{pmatrix} \begin{pmatrix} B_x(\omega) \\ B_y(\omega) \end{pmatrix} \tag{2.24}$$

In case of a homogeneous half space it simplifies to:

$$\begin{pmatrix} E_x(\omega) \\ E_y(\omega) \end{pmatrix} = \begin{pmatrix} 0 & Z(\omega) \\ -Z(\omega) & 0 \end{pmatrix} \begin{pmatrix} B_x(\omega) \\ B_y(\omega) \end{pmatrix} \tag{2.25}$$

The impedance $Z(\omega)$ is related to the Schmucker-Weidelt transfer function in equation (2.22) through:

$$Z(\omega) = \frac{E_x(\omega)}{B_y(\omega)} = -\frac{E_y(\omega)}{B_x(\omega)} = i\omega C(\omega) \tag{2.26}$$

Based on the impedance $Z(\omega)$, the following two parameters commonly used in MT can be derived. The apparent resistivity

$$\rho_a(\omega) = \frac{\mu_0}{\omega}|Z(\omega)|^2 \tag{2.27}$$

describes the actual resistivity in case of a homogeneous half space (Cagniard, 1953). If the subsurface is not homogeneous, the apparent resistivity describes the resistivity of an equivalent half space at the frequency used. In addition, the phase difference between the electric and magnetic field components used in the calculation of the impedance $Z(\omega)$ can be calculated as:

$$\varphi(\omega) = \arctan\frac{\mathrm{Im}(Z(\omega))}{\mathrm{Re}(Z(\omega))} \tag{2.28}$$

For the homogeneous half space the phase is 45° for all frequencies.

2.2.1 Magnetotelluric response of a layered Earth

For a layered Earth consisting of N layers (Figure 2.3) the transfer function $C_1(\omega)$ measured at the Earth's surface can be determined recursively. Its calculation is based on Wait's recursion formula (Wait, 1954), which allows the calculation of the transfer function $C_n(\omega)$ at the surface of the n-th layer:

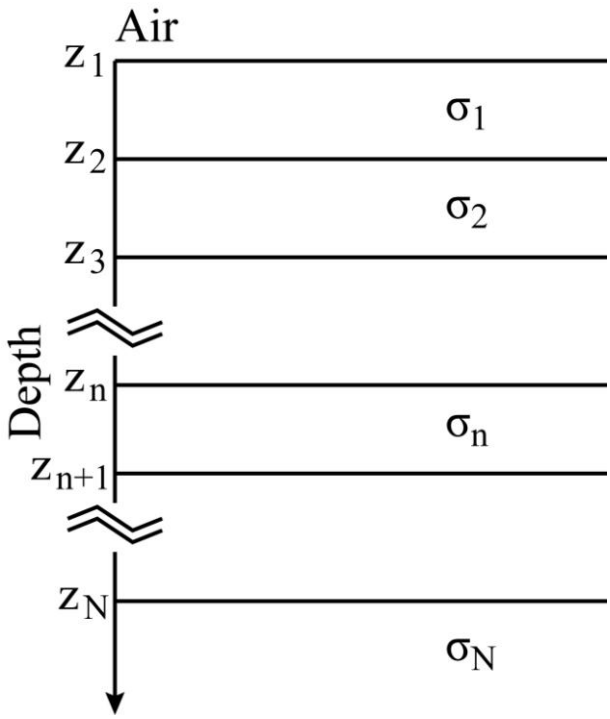

Figure 2.3: Layered Earth consisting of N layers with electrical conductivity σ_n and layer thickness $d_n = z_{n+1} - z_n$. The bottom layer is a homogeneous half space with electrical conductivity σ_N.

$$C_n(\omega) = \frac{1}{q_n} \frac{q_n(\omega)C_{n+1}(\omega) + \tanh(q_n(\omega)d_n)}{1 + q_n(\omega)C_{n+1}(\omega)\tanh\left(q_n(\omega)d_n\right)} \tag{2.29}$$

with $n = 1 \ldots N$. $q_n(\omega) = \sqrt{i\mu_0\sigma_n\omega}$ describes the vertical wave number of the n-th layer with conductivity σ_n and layer thickness d_n.

The final N-th layer is a homogeneous half space, for which according to equation (2.22) the transfer function $C_N(\omega)$ is given by:

$$C_N(\omega) = \frac{1}{q_N(\omega)} \tag{2.30}$$

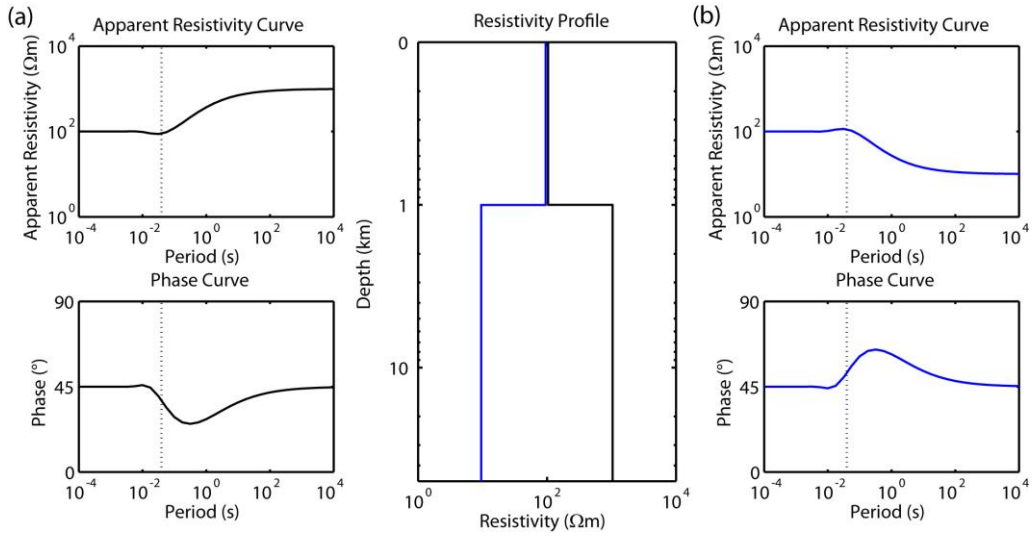

Figure 2.4: Simple two layer models and the corresponding apparent resistivity and phase curves: (a) A resistive half space with a resistivity of 1000 Ωm is overlain by a 1 km thick conductive surface layer with a resistivity of 100 Ωm (black). (b) A conductive half space with a resistivity of 10 Ωm is overlain by a 1 km thick resistive surface layer with a resistivity of 100 Ωm (blue). The dashed line indicates the period that corresponds to the skin depth at which the resistivity change occurs.

The simplest case of a layered Earth is a two layer model consisting of a homogeneous half space overlain by a surface layer. Two distinct scenarios can occur in this model:

- A high resistivity half space is overlain by a low resistivity surface layer. For example, Figure 2.4a shows the apparent resistivity and phase curves calculated from the observed transfer function $C_1(\omega)$ for a 1 km thick conductive layer (100 Ωm) overlying a resistive half space (1000 Ωm). In this case, the apparent resistivity increases from 100 Ωm to 1000 Ωm with increasing period, as longer periods penetrate deeper into the Earth

(equation (2.21)) and begin to image the resistive half space. The corresponding phase is less than 45°.

- A low resistivity half space is overlain by a high resistivity surface layer. For example, Figure 2.4b shows the apparent resistivity and phase curves calculated from the observed transfer function $C_1(\omega)$ for a 1 km thick resistive layer (100 Ωm) overlying a conductive half space (10 Ωm). In this case, the apparent resistivity decreases from 100 Ωm to 10 Ωm with increasing period. The corresponding phase is larger than 45°.

Due to the skin depth effect (equation (2.21)), variations in electrical resistivity at greater depth are imaged at longer periods. As a result, the magnetotelluric method is very effective in determining the depth of a conductive layer. However, it is not very effective in resolving both the electrical resistivity and thickness of the layer, but rather its conductance (i.e. the product of the electrical conductivity, or the reciprocal of the electrical resistivity, and the layer thickness). Figure 2.5 shows the apparent resistivity and phase curves for two conductive layers with different electrical resistivities and thicknesses but with the same conductance (200 S). It can be seen that the apparent resistivity and phase curves are almost identical for both cases, and in the presence of noise in the data it will not be possible to distinguish between them. To overcome this non-uniqueness, additional information from other geophysical methods is required.

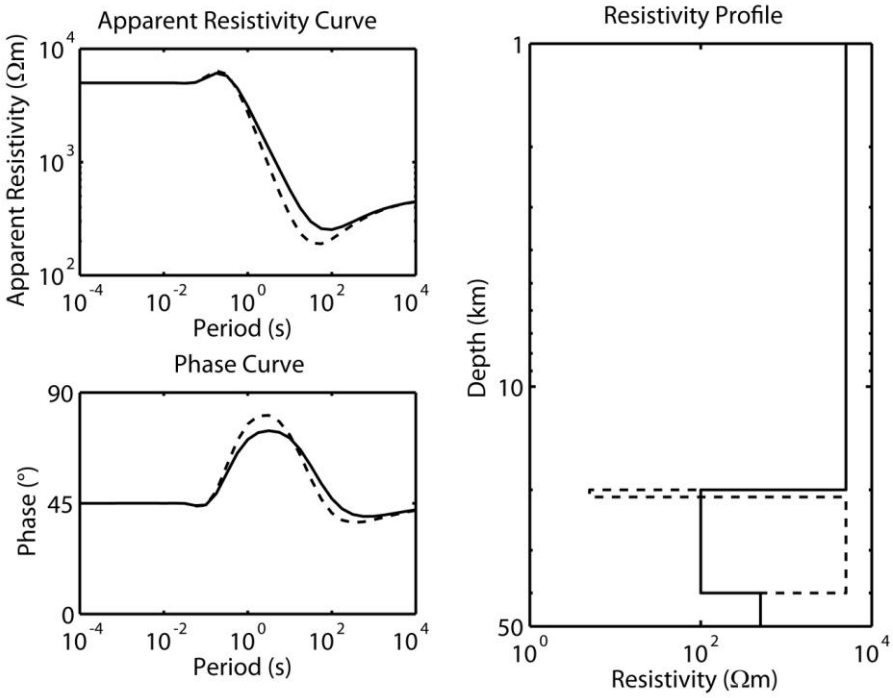

Figure 2.5: Apparent resistivity and phase curves for two models of the continental crust. In the first model the lower continental crust is given by a 20 km thick layer with a resistivity of 100 Ωm (solid line). In the second model a 1 km thick layer with a resistivity of 5 Ωm underlain by a resistive layer with a resistivity of 5000 Ωm is assumed (dashed line). The conductance of the lower crust is 200 S for both models. (redrawn from Jones, 1992)

2.2.2 Two-dimensional Earth resistivity structures

Two-dimensional structures are characterized by both vertical and lateral conductivity variations in one of the horizontal directions. The simplest model is a two-dimensional structure consisting of two quarter spaces with conductivities σ_1 and σ_2 respectively. The following discussion assumes that the two quarter spaces are separated along the x-axis (Figure 2.6), but can be easily extended to any two-dimensional structures.

For two-dimensional conductivity structures equations (2.9) and (2.10) can be separated into two independent polarizations, each of them described by a set of three equations. The ***E***-polarization, also known as transverse electric (TE) mode, describes the case in which the electric currents flow parallel to the strike direction. The corresponding electric field $E_x(\omega)$ only induces magnetic fields perpendicular to strike as well as in the vertical direction (Figure 2.6):

$$\frac{\partial E_x(\omega)}{\partial y} - \frac{\partial B_z(\omega)}{\partial t} = i\omega B_z(\omega) \tag{2.31}$$

$$\frac{\partial E_x(\omega)}{\partial z} - \frac{\partial B_y(\omega)}{\partial t} = i\omega B_y(\omega) \tag{2.32}$$

$$\frac{\partial B_z(\omega)}{\partial y} - \frac{\partial B_y(\omega)}{\partial z} = \mu\sigma E_x(\omega) \tag{2.33}$$

In contrast, the ***B***-polarization, also known as transverse magnetic (TM) mode, describes the case in which the electric currents flow perpendicular to the strike direction. In this case, the magnetic field $B_x(\omega)$ parallel to the strike direction induces electric fields perpendicular to strike as well as in the vertical direction (see Figure 2.6):

$$\frac{\partial B_x(\omega)}{\partial y} = \mu\sigma E_z(\omega) \tag{2.34}$$

$$-\frac{\partial B_x(\omega)}{\partial z} = \mu\sigma E_y(\omega) \tag{2.35}$$

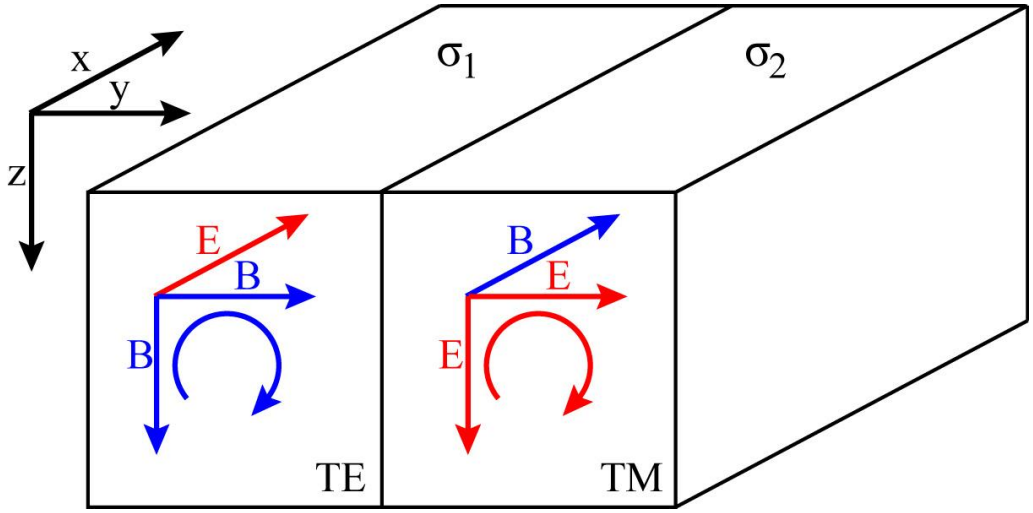

Figure 2.6: Two-dimensional conductivity structure consisting of two quarter spaces with conductivities σ_1 and σ_2 separated along the x-axis. The transverse electric (TE) mode, in which the electric currents flow parallel to the strike direction and the transverse magnetic (TM) mode, in which the electric currents flow perpendicular to the strike direction are illustrated.

$$\frac{\partial E_z(\omega)}{\partial y} - \frac{\partial E_y(\omega)}{\partial z} = i\omega B_x(\omega) \tag{2.36}$$

In the coordinate system aligned with strike direction, only the off-diagonal elements of the impedance tensor $\underline{\boldsymbol{Z}}(\omega)$ are non-zero:

$$\begin{pmatrix} E_x(\omega) \\ E_y(\omega) \end{pmatrix} = \begin{pmatrix} 0 & Z_{xy}(\omega) \\ -Z_{yx}(\omega) & 0 \end{pmatrix} \begin{pmatrix} B_x(\omega) \\ B_y(\omega) \end{pmatrix} \tag{2.37}$$

2.2.3 Determination of strike direction

The strike direction of a two-dimensional structure is generally not coincident with the alignment of the measuring instruments. In this case, the impedance tensor does not take the form of equation (2.37). Instead, the diagonal elements of

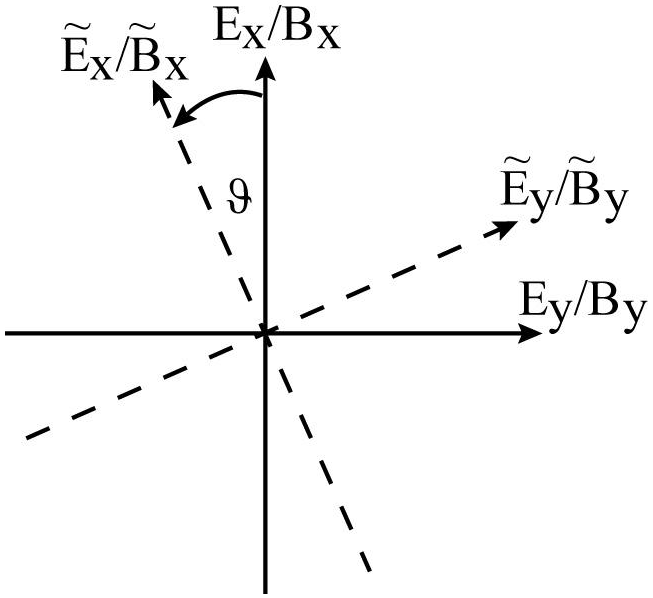

Figure 2.7: Change in direction of the reference coordinate system by mathematically rotating the electric and magnetic field components $\boldsymbol{E}$ and $\boldsymbol{B}$. $\widetilde{\boldsymbol{E}}$ and $\widetilde{\boldsymbol{B}}$ are the electric and magnetic field components in the rotated coordinate system for a counter clockwise rotation through an angle ϑ.

the tensor are also non-zero. By mathematically rotating the electric and magnetic field components, the direction of the reference coordinate system can be changed:

$$\widetilde{\boldsymbol{E}}(\omega) = \underline{\beta_\vartheta}\boldsymbol{E}(\omega) = \underline{\beta_\vartheta}\underline{\boldsymbol{Z}}(\omega) \cdot \boldsymbol{B}(\omega) = \underline{\beta_\vartheta}\underline{\boldsymbol{Z}}(\omega)\underline{\beta_\vartheta^T} \cdot \widetilde{\boldsymbol{B}}(\omega) \tag{2.38}$$

where $\widetilde{\boldsymbol{E}}(\omega)$ and $\widetilde{\boldsymbol{B}}(\omega)$ are the electric and magnetic field components in the rotated coordinate system, and $\underline{\beta_\vartheta}$ is the rotation matrix for a counter clockwise rotation through an angle ϑ (Figure 2.7):

$$\underline{\beta_\vartheta} = \begin{pmatrix} \cos\vartheta & \sin\vartheta \\ -\sin\vartheta & \cos\vartheta \end{pmatrix} \tag{2.39}$$

Therefore, the impedance tensor as a function of rotation angle takes the following form:

$$\underline{\boldsymbol{Z}}(\vartheta) = \begin{pmatrix} S_1 + S_2 \sin 2\vartheta + D_1 \cos 2\vartheta & D_2 - D_1 \sin 2\vartheta + S_2 \cos 2\vartheta \\ -D_2 - D_1 \sin 2\vartheta + S_2 \cos 2\vartheta & S_1 - S_2 \sin 2\vartheta - D_1 \cos 2\vartheta \end{pmatrix} \quad (2.40)$$

with the so-called modified impedances

$$S_1 = Z_{xx} + Z_{yy} \quad (2.41)$$

$$S_2 = Z_{xy} + Z_{yx} \quad (2.42)$$

$$D_1 = Z_{xx} - Z_{yy} \quad (2.43)$$

$$D_2 = Z_{xy} - Z_{yx} \quad (2.44)$$

To find the coordinate system of strike, one needs to determine the coordinate system in which the diagonal elements of the impedance tensor are zero. However, for real MT data the diagonal elements will never be completely equal to zero for two reasons: (i) measured MT data contain noise and (ii) a two-dimensional structure as described above is an idealized scenario which is unlikely to be found in the Earth. Therefore, one needs to determine the coordinate system in which the diagonal elements of the impedance tensor are minimized. Mathematically this problem can be described by several conditions, which all yield the same result in the absence of noise. One of these conditions requires that the term $|Z_{xx}(\vartheta)|^2 + \left|Z_{yy}(\vartheta)\right|^2$ is minimized. This condition results in the strike angle after Swift (1967):

$$\tan 4\alpha = \frac{2\mathrm{Re}(S_2 D_1)}{|D_1|^2 - |S_2|^2} \tag{2.45}$$

A measure for the validity of the assumption of a two-dimensional structure is given by the Swift skew

$$\kappa = \frac{|S_1|}{|D_2|} \tag{2.46}$$

which describes the discrepancy of the impedance tensor $\underline{\boldsymbol{Z}}$ from the off-diagonal form described in equation (2.37). For one-dimensional and idealized two-dimensional structures the Swift skew κ is close to zero, while values of $\kappa > 0.1$ indicate three-dimensional conductivity anomalies and structures.

2.2.4 Induction vectors

For two-dimensional conductivity structures, the electric currents flowing parallel to the strike direction induce not only a horizontal magnetic field perpendicular to strike (equation (2.32)) but also a magnetic field in the vertical direction (equation (2.31)). Similar to the impedance tensor $\underline{\boldsymbol{Z}}(\omega)$, which relates the horizontal electric and magnetic field components (equation (2.23)), it is also possible to relate the vertical magnetic field component $B_z(\omega)$ to the horizontal magnetic field components $B_x(\omega)$ and $B_y(\omega)$ through a complex transfer function $\boldsymbol{T}(\omega)$ (Parkinson, 1962; Wiese, 1964):

$$B_z(\omega) = \boldsymbol{T}(\omega)\begin{pmatrix} B_x(\omega) \\ B_y(\omega) \end{pmatrix} = \begin{pmatrix} T_x(\omega) & T_y(\omega) \end{pmatrix}\begin{pmatrix} B_x(\omega) \\ B_y(\omega) \end{pmatrix} \quad (2.47)$$

The transfer function $\boldsymbol{T}(\omega)$ is called tipper, as it tips the horizontal magnetic fields into the vertical direction, and can be illustrated by induction vectors. In the Parkinson convention, the real part of the induction vectors points towards conductive regions (Parkinson, 1962). The magnitude of the induction vectors is determined by the conductivity gradient (Parkinson, 1962), resulting in a good lateral but limited vertical resolution. In the alternative Wiese convention, the real part of the induction vectors points away from conductive regions (Wiese, 1964). Therefore, in both the Parkinson and Wiese convections the induction vectors are expected to be perpendicular to the strike direction of a two-dimensional structure.

2.2.5 Galvanic and magnetic distortion

As mentioned in section 2.2.2, even for two-dimensional resistivity structures in the coordinate system of strike the diagonal elements of the impedance tensor $\underline{\boldsymbol{Z}}$ can be non-zero. In addition to noise in the measured MT data, this might be caused by shallow conductivity anomalies. If the extent and depth of these anomalies is small compared to the corresponding skin depth p, the variations of the electric field are sufficiently slow to allow for the accumulation of free charges at the boundary of the anomalies. These free charges result in an

anomalous electric field within the conductivity anomaly, causing a galvanic distortion of the measured electric fields (e.g. Jones, 1988).

Mathematically the effect of the distortion can be described by splitting the impedance tensor into an inductive and galvanic part. The galvanic part can be described by a distortion matrix $\underline{\boldsymbol{C}}$, whose components are real and frequency independent. The inductive part is given by the impedance tensor $\underline{\boldsymbol{Z}}(\omega)$ that would have been measured in the absence of distortion (Bahr, 1988):

$$\boldsymbol{E}(\omega) = \underline{\boldsymbol{C}} \cdot \underline{\boldsymbol{Z}}(\omega) \cdot \boldsymbol{B}(\omega) \tag{2.48}$$

By multiplying the impedance tensor elements with the elements of the real distortion matrix, the amplitudes of the impedances are changed, while the phases remain unaffected. As a consequence, the apparent resistivity values might be shifted to higher or lower resistivity values. This phenomenon is called static shift (Jones, 1988).

For two-dimensional structures, the distortion causes the diagonal elements of the impedance tensor to be non-zero even in the coordinate system of strike:

$$\begin{aligned} \underline{\boldsymbol{C}} \cdot \underline{\boldsymbol{Z}}_{\boldsymbol{2D}}(\omega) &= \begin{pmatrix} c_{11} & c_{12} \\ c_{21} & c_{22} \end{pmatrix} \begin{pmatrix} 0 & Z_{xy}(\omega) \\ -Z_{yx}(\omega) & 0 \end{pmatrix} \\ &= \begin{pmatrix} -c_{12}Z_{yx}(\omega) & -c_{11}Z_{xy}(\omega) \\ -c_{22}Z_{yx}(\omega) & -c_{21}Z_{xy}(\omega) \end{pmatrix} \end{aligned} \tag{2.49}$$

As can be seen, the impedance tensor elements in each column have the same phase. As this phase equality only occurs in the coordinate system of strike, it

provides another way to determine the strike angle. The so-called phase sensitive strike angle (Bahr, 1988) can be written as:

$$\alpha = \frac{1}{2}\arctan\frac{[S_1, S_2] - [D_1, D_2]}{[S_1, D_1] + [S_2, D_2]} \tag{2.50}$$

where the commutator $[x, y]$ with $x, y \in \mathbb{C}$ is defined as

$$[x, y] = \mathrm{Re}(x)\mathrm{Im}(y) - \mathrm{Re}(y)\mathrm{Im}(x) = \mathrm{Im}(yx^*) \tag{2.51}$$

As before, a measure defining the validity of this superposition model can be defined. It is called the phase-sensitive skew:

$$\eta = \frac{(|[D_1, S_2] - [S_1, D_2]|)^{\frac{1}{2}}}{|D_2|} \tag{2.52}$$

If a coordinate system exists in which the impedance tensor takes the form described in equation (2.49), the phase-sensitive skew becomes zero. In this case, the regional structure is two-dimensional with localized, small scale conductivity anomalies close to the surface that distort the measured electric fields. For $\eta > 0.3$ the assumption of a distorted two-dimensional structure is no longer valid. Instead, the structure is a regional three-dimensional structure (Bahr, 1991).

A similar analysis was proposed by Groom & Bailey (1989) who decomposed the real distortion matrix $\underline{\boldsymbol{C}}$ into three separate matrices describing the effect of twist, shear and local anisotropy on the electric fields:

$$\underline{\boldsymbol{C}} \cdot \underline{\boldsymbol{Z}}_{\boldsymbol{2D}}(\omega) = g \cdot \underline{\boldsymbol{T}} \cdot \underline{\boldsymbol{S}} \cdot \underline{\boldsymbol{A}} \cdot \underline{\boldsymbol{Z}}_{\boldsymbol{2D}}(\omega) \tag{2.53}$$

where g is a scaling factor known as site gain, and $\underline{\boldsymbol{T}}$, $\underline{\boldsymbol{S}}$ and $\underline{\boldsymbol{A}}$ are the twist, shear and splitting tensors respectively:

$$\underline{\boldsymbol{T}} = \frac{\mathbf{1}}{\sqrt{\mathbf{1}+\boldsymbol{t}^{\mathbf{2}}}}\begin{pmatrix}1 & -t\\ t & 1\end{pmatrix} \tag{2.54}$$

$$\underline{\boldsymbol{S}} = \frac{\mathbf{1}}{\sqrt{\mathbf{1}+\boldsymbol{e}^{\mathbf{2}}}}\begin{pmatrix}1 & e\\ e & 1\end{pmatrix} \tag{2.55}$$

$$\underline{\boldsymbol{A}} = \frac{\mathbf{1}}{\sqrt{\mathbf{1}+\boldsymbol{s}}}\begin{pmatrix}1+s & 0\\ 0 & 1-s\end{pmatrix} \tag{2.56}$$

The site gain g and splitting tensor $\underline{\boldsymbol{A}}$ can be absorbed into the undistorted impedance tensor $\underline{\boldsymbol{Z}}_{\boldsymbol{2D}}(\omega)$ to yield an impedance tensor $\underline{\boldsymbol{Z}}_{\boldsymbol{2D}}{}'(\omega)$ that only differs from $\underline{\boldsymbol{Z}}_{\boldsymbol{2D}}(\omega)$ by a scalar factor. In this case, Groom & Bailey (1989) showed that in theory a unique solution to the decomposition problem in equation (2.53) exits. However, in practice a least square approach needs to be applied to decompose MT data with noise. McNeice & Jones (2001) extended this decomposition to multiple frequencies and sites in order to obtain a more robust estimate of the regional strike direction.

In addition to galvanic distortion of the electric fields, the magnetic fields can be distorted as a result of anomalous magnetic fields caused by distorted currents, for example due to channelling of direct currents by localized conductors (Jones, 1983). As the distortion of the magnetic field takes the form

$$\boldsymbol{B}(\omega) = \boldsymbol{B}(\omega) + \underline{\boldsymbol{D}} \cdot \boldsymbol{E}(\omega) \tag{2.57}$$

the distorted impedance tensor is given by (Chave & Smith, 1994):

$$\underline{\boldsymbol{Z}}(\omega) = \underline{\boldsymbol{C}} \cdot \underline{\boldsymbol{Z}}(\omega) \left(\underline{\boldsymbol{I}} + \underline{\boldsymbol{D}} \cdot \underline{\boldsymbol{Z}}(\omega) \right)^{-1} \tag{2.58}$$

where $\underline{\boldsymbol{I}}$ is the identity matrix. Like the galvanic distortion matrix $\underline{\boldsymbol{C}}$, the magnetic distortion matrix $\underline{\boldsymbol{D}}$ is real and frequency independent. However, after multiplication with the undistorted impedance tensor, the term $\left(\underline{\boldsymbol{I}} + \underline{\boldsymbol{D}} \cdot \underline{\boldsymbol{Z}}(\omega) \right)^{-1}$ becomes complex and frequency dependent, so that the magnetic distortion does not only affect the amplitudes of the impedances but also their phases. In the presence of strong current channelling phases exceeding 90° have been observed (Lezaeta & Haak, 2003). This is in contrast to galvanic distortion, for which the phases remain unaffected and stay within the 0°-90° quadrant. However, in general magnetic distortion can be neglected, as its effect decays with $\sqrt{\omega}$ (Groom & Bailey, 1991).

2.3 Magnetotelluric field measurements

Magnetotelluric field measurements require the measurement of the time variations in the two horizontal electric field components E_x and E_y as well as in the two horizontal and one vertical magnetic field components B_x, B_y and B_z. The vertical electric field E_z at the Earth's surface is small due to the insulating atmosphere, and therefore is not routinely measured. The measurements of these field components are generally made in a geomagnetic coordinate system (Figure

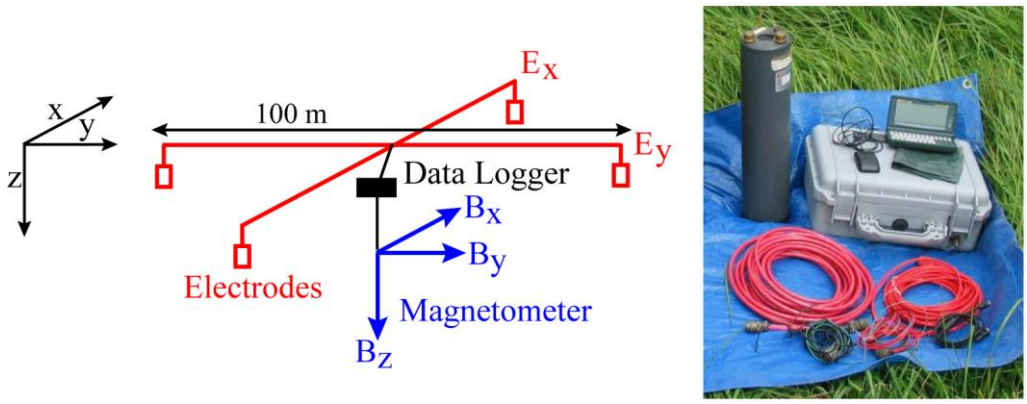

Figure 2.8: Typical MT setup using two 50-100m dipoles with non-polarizing electrodes to measure the two horizontal electric field components (E_x and E_y, with x and y corresponding to geomagnetic north and east respectively), and a set of induction coils or a fluxgate magnetometer to measure the two horizontal and one vertical magnetic field components (B_x, B_y and B_z). The photo shows a long-period NIMS data logger and fluxgate magnetometer. (Photo courtesy of Martyn Unsworth)

2.8). The electric field components are measured using two 50-100 m dipoles with non-polarizing lead-chloride electrodes at each end, which are buried in the ground. The use of metal stakes is to be avoided, as polarization voltages can be a significant source of noise. Measurements of the magnetic field components can be obtained from a set of induction coils for short period measurements (up to 100 s) or a three-component fluxgate magnetometer for long period measurements.

Figure 2.9 shows an example of magnetotelluric time series data collected using a long-period NIMS instrument. The time series can be converted into frequency dependent impedance estimates relating the perpendicular electric and magnetic field components (equation (2.24)) using a least-square method based on the auto-power and cross-power density spectra of the data (e.g. Sims et al., 1971). An alternative robust, multivariate analysis has been developed by Egbert (1997),

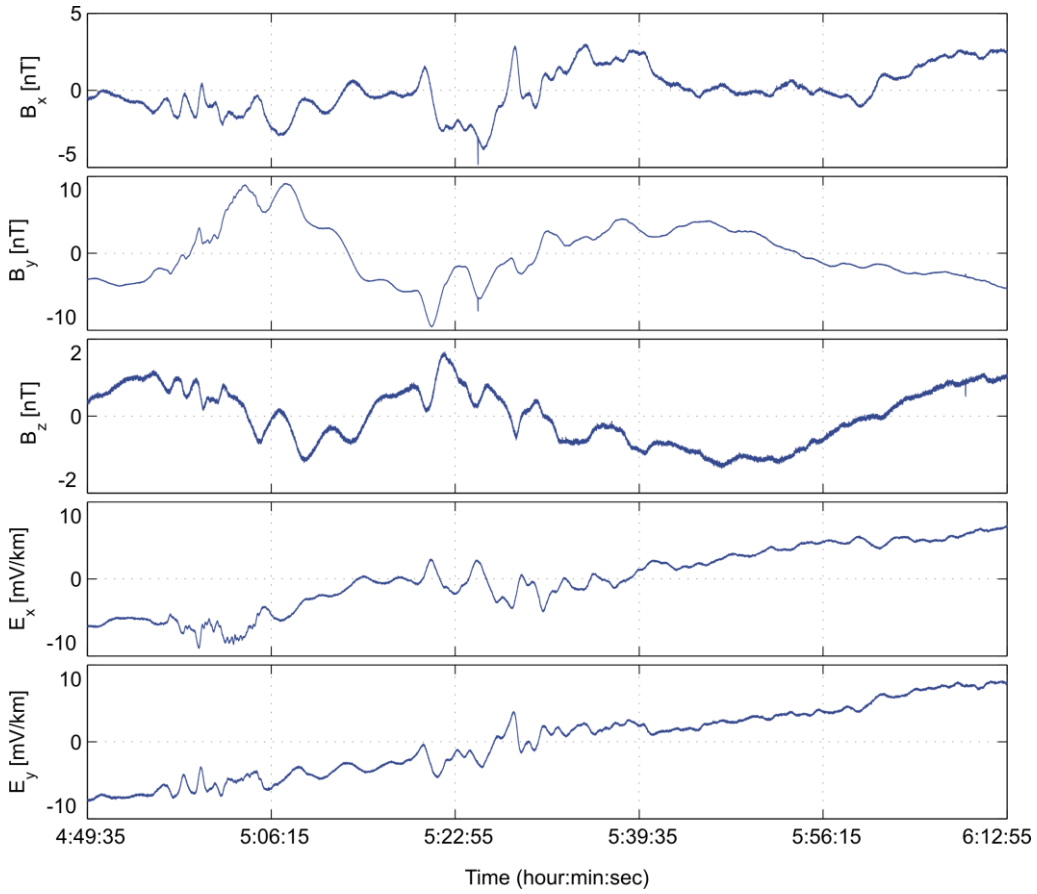

Figure 2.9: Example of magnetotelluric time series data collected with a long-period NIMS instrument, showing the time variations in two horizontal electric field components as well as two horizontal and one vertical magnetic field components. The time series data were collected in southern Alberta on October 8, 2010 between around 5 and 6 am. (courtesy of Greg Nieuwenhuis)

which provides better impedance estimates for non-Gaussian data errors. Impedance estimates can be further improved by removing coherent noise in the field components using remote reference (Gamble et al., 1979), in which a time series recorded simultaneously at a remote site is correlated with the time series of the local site.

2.4 Modelling of magnetotelluric data

Interpretation of magnetotelluric data in terms of the subsurface resistivity structure requires a conversion of the period dependence to depth, which can be obtained by (i) forward modelling and (ii) inversion of the magnetotelluric data. Forward modelling is a trial and error approach, in which the electrical resistivity structure of the subsurface is varied manually, until a model is found which can explain the measured magnetotelluric data. For a one-dimensional resistivity structure (i.e. a layered Earth) this can be achieved by using Wait's recursion formula (Wait, 1954) (section 2.2.1). The electrical conductivity σ_n and layer thickness d_n are varied manually and used to calculate the theoretical transfer function $C_1(\omega)$ for a range of periods. The theoretical transfer functions are then compared to the measured data and the model is updated until a layered Earth model is found that can reproduce the observed magnetotelluric measurements. While this forward modeling approach works well for a simple subsurface resistivity structure and small data sets, it can get very time-consuming for more complex Earth structures.

An alternative approach is the inversion of the magnetotelluric data, in which the measured magnetotelluric data are used to calculate a subsurface structure that explains the data. Mathematically, this can be expressed as a minimization problem, in which a subsurface resistivity model is sought that gives a minimum least-squares misfit χ^2 between the measured data $\boldsymbol{d}$ and the predicted data $\underline{\boldsymbol{F}}(\boldsymbol{m})$ with:

$$\chi^2 = \left\| \underline{\boldsymbol{W}} \left(\boldsymbol{d} - \underline{\boldsymbol{F}}(\boldsymbol{m}) \right) \right\|^2 \tag{2.59}$$

where $\underline{\boldsymbol{W}}$ is a weighting matrix, which weighs the data according to their data error. To overcome the non-uniqueness in solving this equation, an additional constraint is used, in which for example the model roughness $\underline{\delta}^2 \boldsymbol{m}$ is minimized:

$$J = \left\| \underline{\boldsymbol{W}} \left(\boldsymbol{d} - \underline{\boldsymbol{F}}(\boldsymbol{m}) \right) \right\|^2 + \tau \left\| \underline{\delta}^2 \boldsymbol{m} \right\|^2 \tag{2.60}$$

where τ is a trade-off parameter between the data misfit and the model roughness. A plot of model roughness versus data misfit for a range of trade-off parameters generally results in an L shaped curve. By choosing the trade-off parameter corresponding to the corner of this curve, equal emphasis is placed on minimizing the data misfit and the model roughness.

For a one-dimensional subsurface structure, equation (2.60) forms the foundation of the 1D Occam inversion, which tries to find the smoothest one-dimensional resistivity structure from magnetotelluric data (Constable, 1987). This regularized inversion has been extended to solve for two- and three-dimensional resistivity structures. Rodi & Mackie (2001) developed a non-linear conjugate gradient algorithm for the 2D inversion of magnetotelluric data. 3D inversion of magnetotelluric data has only recently become feasible with the improvements of computer hardware. A 3D inversion algorithm was developed by Siripunvaraporn et al. (2005).

In this thesis, magnetotelluric data collected along linear profiles will be interpreted. Dimensionality analysis of the data indicates, that the data are predominantly two-dimensional, so that the period of the magnetotelluric data will be converted to depth using the 2D inversion algorithm by Rodi & Mackie (2001). While the 2D inversion assumes that the obtained subsurface resistivity structure extends indefinitely in the horizontal direction perpendicular to the profile, possible off-profile variations can be investigated using the 3D inversion algorithm by Siripunvaraporn et al. (2005). However, such an analysis would be time-consuming and is beyond the scope of this thesis.

3 The Cascadia subduction zone and the Canadian Cordillera

3.1 Introduction

Subduction zones are convergent plate boundaries where a number of important tectonic processes occur. They play a major role in the growth of the continents by (a) providing a mechanism to generate rocks with intermediate to felsic composition from mafic mantle rocks through arc volcanism, (b) initiation of continent-continent collisions and (c) growth through terrane accretion. In addition, subduction zones play an important role in transporting fluids from the surface into the mantle where they affect both physical and chemical properties of the rocks (e.g. Rüpke et al., 2004). At shallow depths (< 15 km) these fluids are released due to compaction of the pore space of the subducting oceanic crust, while at larger depths fluids are released by metamorphic dehydration reactions of hydrous minerals (Hacker, 2008). One of the best studied examples of this type of convergent boundary is the Cascadia subduction zone, which is located on the west coast of North America. Here the oceanic Juan de Fuca plate is being subducted beneath the continental part of the North American plate (Figure 3.1). Due to its young age, the Juan de Fuca plate is hotter and therefore more buoyant than the subducting plates in other subduction zones, resulting in a shallow dip angle of 8-16˚ (Riddihough, 1979; Spence et al., 1985). The Cascadia subduction zone is the western boundary of the southern Canadian Cordillera, an area of extensive mountain ranges and plateaus extending as far east as the Canadian Rocky Mountains (Monger & Price, 2002).

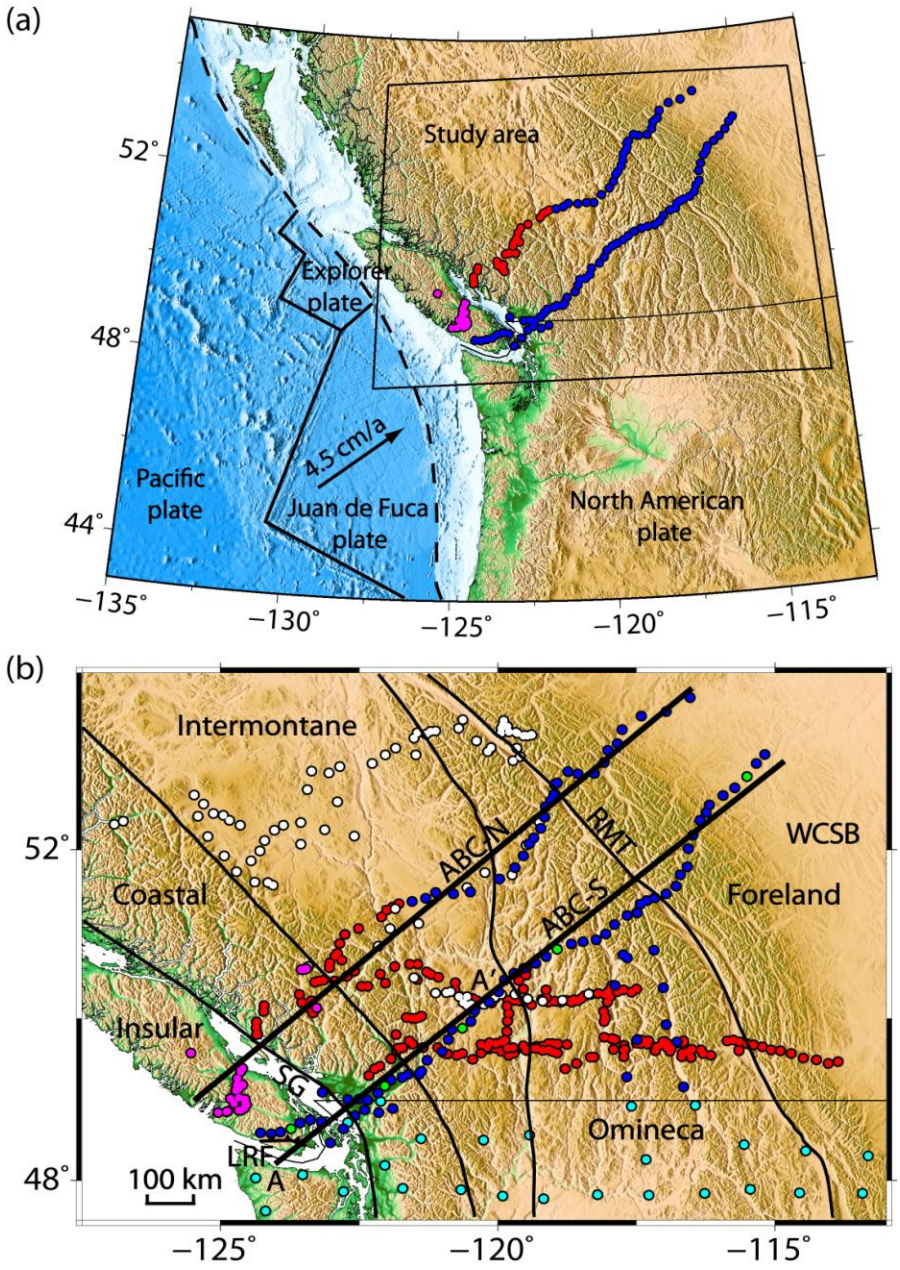

Figure 3.1: (a) Topography map of the Canadian Cordillera, including locations of two long period MT profiles. (b) Detailed map of the study area, showing morphological belts and available MT data. Blue: long-period MT data (University of Alberta); white: broadband MT data (Gough, 1986); red: broadband MT data (Lithoprobe); pink: broadband MT data (Kurtz, 1990); turquoise: long-period MT data (US-Array). Green dots indicate the locations of the MT stations shown in Figure 3.11. SG: Strait of Georgia; LRF: Leech River Fault; RMT: Rocky Mountain Trench; WCSB: Western Canadian Sedimentary Basin.

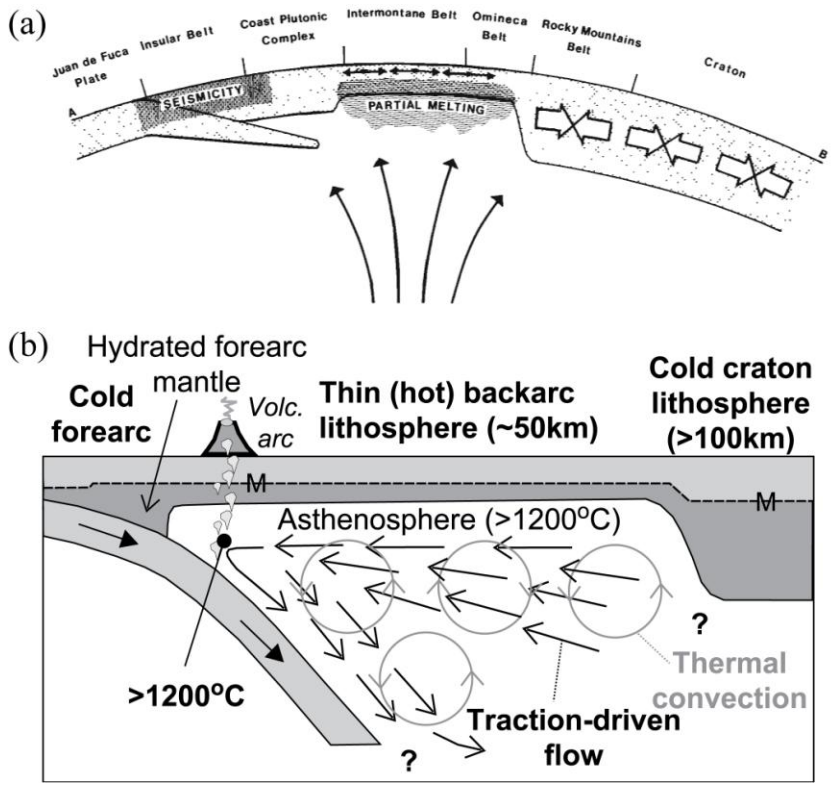

Figure 3.2: Possible explanations for the hot temperatures in the backarc of the Canadian Cordillera: (a) Schematic diagram of the Canadian Cordillera with upflow in the mantle, slow convergence at the continental edge, a short and thin subducted plate, extensional stress in the Intermontane and Omineca Belts and compression in the craton. (reprinted from Gough, 1986)[1] (b) Schematic diagram of the of the Canadian Cordillera with key temperature constraints. Two wedge flow geometries are shown: traction-driven mantle flow and vigorous, small scale thermal convection of a weak, low-viscosity asthenosphere. (reprinted from Currie et al., 2004a)[2]

The forearc region of the Cascadia subduction zone extends from the trench of the subducting Juan de Fuca plate to the Garibaldi volcanic arc in the Coastal Belt. East of the volcanic arc is the backarc region, which extends to the Rocky Mountain Trench (Figure 3.1).

Previous geophysical research has shown that the backarc mantle of the Cascadia subduction zone is unusually hot, despite the cooling effect of the subducting Juan

de Fuca plate (Currie & Hyndman, 2006). Hot mantle temperatures extending several hundred kilometres into the backarc cannot be explained by simple traction-driven mantle flow (Currie et al., 2004a). In this kind of flow, material from the mantle wedge, which is entrained and carried downwards with the subducting plate, gets replaced by hot mantle from the backarc. Instead, heat transport from the deep mantle through, for example, ambient mantle upwelling (Gough, 1986) or vigorous, small scale convection of a weak, low-viscosity asthenosphere (Currie et al., 2004a) is required to explain the hot temperatures in the backarc (Figure 3.1).

To understand what kind of mantle flow can occur in the Cascadia subduction zone, it is necessary to constrain the rheology of the upper mantle. The rheology is determined by the composition, temperature and presence of fluid phases (Bürgmann & Dresen, 2008 and references therein). In particular, aqueous fluids can have a profound effect on deformation processes by lowering the solidus temperature of the mantle (Appendix B.4). For temperatures above the solidus, partial melting occurs, which lowers the viscosity of the rocks and enhances ductile deformation of the upper mantle (Kohlstedt & Zimmerman, 1996 and references therein).

Electrical resistivities determined from magnetotelluric (MT) studies are inherently sensitive to the presence of fluid phases (Unsworth & Rondenay, 2013), providing an effective tool to study the rheology of the upper mantle. Previous broadband MT studies of the Cascadia subduction zone and the

Canadian Cordillera have determined the electrical resistivity structure of the crust to a depth of ~ 35 km (Gough, 1986; Ledo & Jones, 2001), but the lack of long-period MT data has prevented imaging of the upper mantle. The first long-period MT study of the Canadian Cordillera was described by Soyer & Unsworth (2006). In this chapter, an extension of this data set is presented, with data extending all the way to the Western Canadian Sedimentary Basin (ABC-S line). In addition, long-period MT data collected along an additional profile crossing the Canadian Cordillera to the north are presented (ABC-N line). These data have been used to generate 2D electrical resistivity models, which are used to determine the rheology of the backarc mantle of the Cascadia subduction zone.

It will be investigated to see if the non-uniqueness in the interpretation of the electrical resistivity models can be reduced by correlating the MT derived resistivity models with independent measurements of subsurface temperature. The subsurface temperatures will be calculated from seismic velocities derived from the body-wave tomography model by Mercier et al. (2009). This analysis will allow the composition and hydration state of the backarc mantle to be better constrained.

3.2 Geological and geophysical background

3.2.1 Geological history of the southern Canadian Cordillera

The geological history of the southern Canadian Cordillera has been characterized by terrane accretion, which has led to the growth of the North American continent

(Monger & Price, 2002 and references therein). Before the onset of subduction around 390 Ma, the Rocky Mountain Trench between the Omineca and the Foreland Belts represented a passive continental margin between the North American continent and the ocean at that time. With the beginning breakup of the Paleozoic supercontinent Pangaea around 185 Ma, the North American plate started moving northwestward over the Pacific Ocean basin, causing subduction of oceanic crust, thickening of the western continental margin as well as accretion of the first terranes. Further terrane accretion between 185 Ma and 100 Ma caused compression and thrust faulting, leading to uplift and erosion of previously accreted terranes. Around 85 Ma, the direction of movement of the North American plate changed northwards causing strike slip faulting in the Canadian Cordillera due to coupling between the continental and oceanic plates. Furthermore, a short lived period of extension in the southern Omineca Belt between 55 Ma and 45 Ma caused deep rocks to be exposed at the surface, while erosion caused further deposits of sedimentary rocks in the basins. Following this period of extension, the geological setting of the Canadian Cordillera remained relatively unchanged since 40 Ma ago.

Today, the Canadian Cordillera comprises five morphological belts (see Figure 3.1b). From east to west these belts are the Foreland Belt, Omineca Belt, Intermontane Belt, Coastal Belt and Insular Belt (see Monger & Price, 2002 for a detailed review).

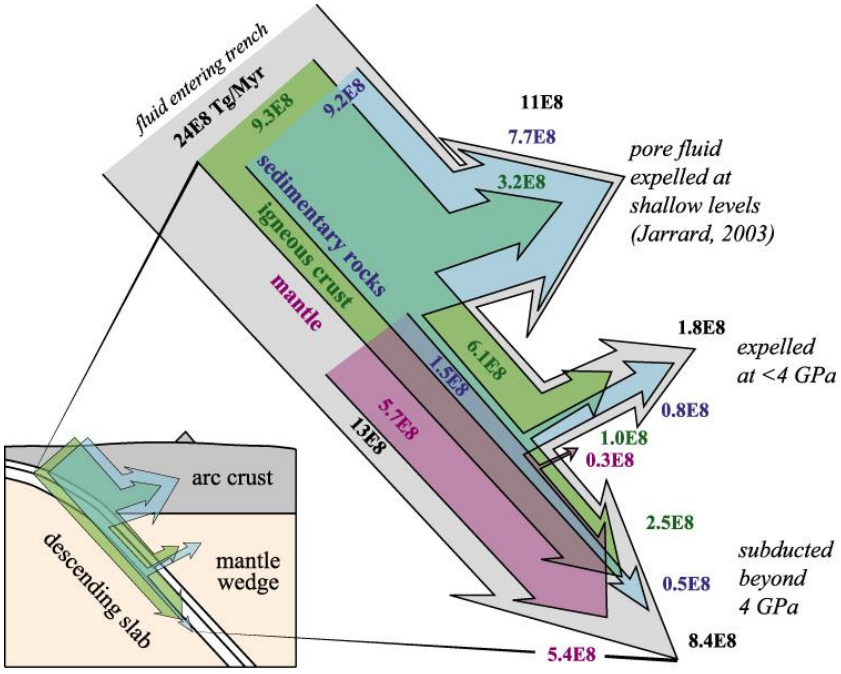

Figure 3.3: Simplified global H_2O flux from trench to postarc depths for oceanic lithosphere (subduction erosion and continental subduction not shown). Widths of arrows are scaled to flux magnitudes, which are given in Tg/Ma. Of the H_2O subducted at trenches in oceanic lithosphere ($24 \cdot 10^8$ Tg/Ma), 46% is driven off by the closure of pores ($11 \cdot 10^8$ Tg/Ma; Jarrard, 2003), another 19% ($4.6 \cdot 10^8$ Tg/Ma) is driven off by devolatilization at pressures <4 GPa, and 35% ($8.4 \cdot 10^8$ Tg/Ma) reaches postarc depths. (reprinted from Hacker, 2008)[3]

3.2.2 Composition of the forearc mantle

An important control on the rheology of the forearc mantle is the amount of water released from the subducting slab. Understanding the rheology of the forearc mantle of the Cascadia subduction zone therefore requires an understanding of the composition of the forearc mantle, as this is indicative of the metamorphic reactions occurring and the amount of water released in this region. Subduction places cold oceanic crust and mantle lithosphere beneath the forearc mantle wedge, where increased temperature and pressure conditions trigger metamorphic reactions within the subducting slab and the overlying mantle rocks (e.g.

Hyndman & Peacock, 2003). At shallow depths (less than 15 km), free water in the pore space of the subducting oceanic crust and subducted sediments is released into the overlying continental crust and mantle due to compaction. At greater depths (> 40 km, corresponding to ~1 GPa) fluids are released by metamorphic dehydration reactions of hydrous minerals, progressing through the blueschist - eclogite and greenschist - amphibolite - granulite - eclogite facies (Peacock, 1990). The released water causes metamorphic reactions of the overlying crust and mantle and, at greater depths, additional weakening and partial melting of the mantle rocks. The volume of water released is greatest in the forearc and decreases with depth (Hacker, 2008; Figure 3.3).

The forearc mantle consists of depleted ultramafic rocks, composed mainly of olivine and orthopyroxene with lesser amounts of clinopyroxine and spinel. It has temperature-pressure conditions in which a number of hydrous minerals, such as serpentine (chrysotile, lizardite and antigorite), talc, and brucite, are formed by metamorphism from hydrated ultramafic rocks. (Hyndman & Peacock, 2003 and references therein). At temperatures below 500°C, serpentine is the most abundant mineral as its Mg:Si ratio lies between that of the predominant mantle minerals olivine and orthopyroxene. Chrysotile and lizardite form at temperatures < 350°C. Under moderate temperatures of blueschist and greenschist facies conditions antigorite is formed which is stable up to 620°C at 1 GPa pressure. For olivine-rich compositions, brucite can coexist with serpentine up to temperatures of 500°C, while talc can coexist with serpentine for pyroxene-rich conditions up to 700°C.

Serpentine in the forearc mantle can be detected geophysically through decreased seismic velocities, increased Poisson's ratio, increased seismic reflectivity, increased magnetization and reduction in density (Hyndman & Peacock, 2003 and references therein). With 30% serpentinization, laboratory measurements show a decrease in seismic P-wave velocities of the continental mantle from 8.2 km/s to 7.2 km/s, an increase in Poisson's ratio from 0.26-0.28 to 0.30 and a reduction in density from 3000 kg/m^3 to 2500 kg/m^3 for an ultramafic composition (Hyndman & Peacock, 2003 and references therein). For the Cascadia subduction zone, teleseismic studies in Oregon observe the continental Moho at a depth of 36 km beneath the forearc (Bostock et al., 2002). The seismic velocities at that depth are 7.2-7.7 km/s, suggesting a serpentinization of up to 30% (Brocher et al., 2003). The associated decrease in mantle density has been used to explain the uplift of the Coastal Belt.

Serpentine was initially believed to be characterized by low electrical resistivities due to large amounts of interconnected magnetite (Stesky & Brace, 1973). However, more recent studies indicate high electrical resistivities for dry serpentine at mantle temperatures (Guo et al., 2011; Reynard et al., 2011), suggesting that other conductivity mechanisms such as aqueous fluids are required to explain low electrical resistivities observed in the forearc mantle (e.g. Soyer & Unsworth, 2006).

3.2.3 Previous geophysical studies of the Cascadia subduction zone and the Canadian Cordillera

3.2.3.1 Surface heat flow

The Canadian Cordillera is characterized by an elevated surface heat flow compared to the adjacent North American craton east of the Rocky Mountain Trench (RMT) (Currie et al., 2004; Currie & Hyndman, 2006, see Figure 3.4). The forearc region shows a low heat flow (30-40 mW/m^2), associated with the cooling effect of the subducting Juan de Fuca plate (Lewis et al., 1988). Temperatures are expected to be < 700°C at a depth of 40-60 km (Hyndman & Peacock, 2003), consistent with the stability field of serpentine in the forearc mantle wedge. The volcanic arc is characterized by a regional surface heat flow of ~80 mW/m^2, but the local surface heat flow can be significantly higher near volcanic centres. Further east, surface heat flow in the backarc increases from ~70 mW/m^2 in the Intermontane Belt to >100 mW/m^2 in the eastern Omineca Belt (Lewis et al., 1992; Hyndman & Lewis, 1999), associated with an increase in radiogenic heat production and in part crustal extension.

In contrast, the reduced mantle heat flow for the backarc region, i.e. after removing the effect of radiogenic heat production in the crust, is a relatively constant 75±15 mW/m^2 (Currie et al., 2004; Currie & Hyndman, 2006, see Figure 3.4), which is significantly higher than the average heat flow of 42±10 mW/m^2 above the North American craton (Rudnick et al., 1998). This suggests relatively

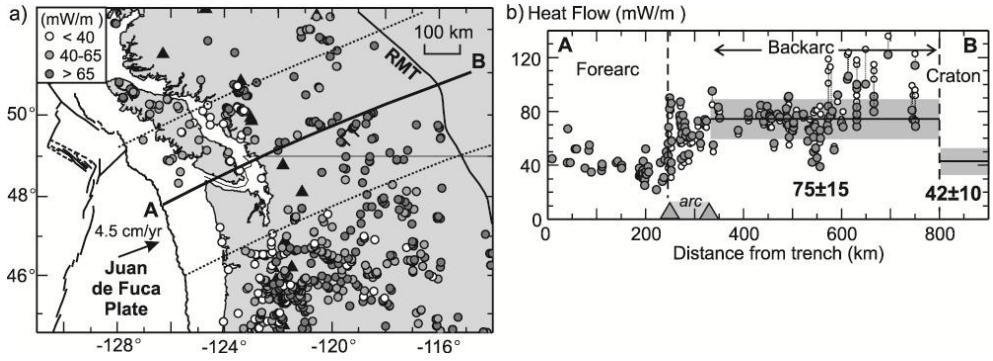

Figure 3.4: (a) Heat flow data for the northern Cascadia subduction zone. Solid triangles are active arc volcanoes. The eastern limit of the back arc is the Rocky Mountain Trench (RMT). The solid line is the heat flow profile location; dotted lines show the profile data width. (b) Heat flow profile along line A-B. The measured heat flow values (open circles) have been corrected for variations in near-surface heat generation (solid circles). (reprinted from Currie & Hyndman, 2006)[4]

uniform, but unusually high mantle temperatures in the backarc mantle compared to the North American Craton.

3.2.3.2 Mantle xenolith thermobarometry

Thermobarometry studies of mantle xenoliths provides another way of constraining the mantle temperatures in the source region of the xenoliths. By analyzing the mineral assemblages and textures of the xenoliths, it is possible to determine the pressure and temperature conditions at which the xenolith reached chemical equilibrium. Peridotite xenoliths from the southern Canadian Cordillera suggest mantle temperatures between 1000°C at 40 km depth and 1300°C at 60 to 70 km depth (Ross, 1983). These results are in good agreement with more recent studies of mantle xenolith from this region, which suggest mantle temperatures of 900-1040°C for depths of 38-50 km (Saruwatari et al., 2001).

3.2.3.3 Effective elastic thickness and density

The effective elastic thickness (T_e) of the lithosphere is mainly controlled by temperature and can be estimated by inferring the surface flexure from gravity and topography data. For the North American craton, the elastic thickness is generally greater than 80 km, indicating low upper mantle temperatures (~600°C at 80 km depth). In contrast, for the Canadian Cordillera, the effective elastic thickness is generally less than 20 km, suggesting higher crustal temperatures between 400°C to 600°C at 20 km depth (Hyndman et al., 2009).

In addition, crustal thickness and topography data can be used to estimate uppermost mantle temperatures as mantle density decreases with increasing temperature. The North American craton is characterized by a thick crust (~40 km) in combination with low elevation (< 500m), consistent with cold upper mantle temperatures. In contrast, most of the Canadian Cordillera has a thin crust (32-35 km) in combination with high elevations (1500-2000 m), suggesting high mantle temperatures in this region (Hyndman & Currie, 2011).

3.2.3.4 Seismic studies

Seismic velocities of the mantle can be measured using seismic refraction and seismic tomography and are primarily determined by temperature, and to a lesser extent composition (e.g. Cammarano et al., 2003). Elevated temperatures, the presence of fluids as well as partial melts generally decrease seismic velocities.

Seismic refraction studies observe the continental Moho beneath the backarc at a depth of 35 km (Clowes et al., 1995). The lithospheric thickness beneath the backarc is estimated to be 50 to 60 km based on wide angle reflection data (Clowes et al., 1995), consistent with temperature estimates of 1300°C at the base of the lithosphere predicted by conductive geotherms (Chapman, 1986).

Based on a comparison of seismic refraction data and the thermal lithospheric structure in North America, Black & Braile (1982) derived a relationship between the uppermost mantle velocity P_n in km/s and Moho temperature T_m in °C:

$$P_n = 8.456 - 0.000729\, T_m \qquad (3.1)$$

For the Canadian Cordillera, seismic refraction studies report P_n velocities of 7.7-7.9 km/s in the Intermontane and Omineca Belts, corresponding to Moho temperatures of 750°C to 1050°C. Beneath the volcanic arc, P_n velocities are as low as 7.6 km/s, corresponding to Moho temperatures of 1175°C. In contrast, P_n velocities of 8.1-8.2 km/s are reported for the Archean North American craton (Christensen & Mooney, 1995), corresponding to Moho temperatures of 350-490°C. The overall uncertainty in Moho temperature derived from P_n velocity is expected to be of the order ±150°C due to uncertainties in the temperature coefficients as well as anisotropy and compositional variations (Currie & Hyndman, 2006 and references therein).

Unusually high mantle temperatures compared to the North American craton are also suggested by seismic tomography, which indicates slower seismic velocities for the backarc mantle (1-3% for P waves, 3-8% for S waves; e.g. Frederiksen et

al., 2001; van der Lee & Frederiksen, 2005; Mercier et al., 2009) compared to global average mantle velocities. Beneath the Archean craton the mantle shows higher than average velocities (2-3% for P-waves, 3-4% for S-waves; e.g. Frederiksen et al., 2001; van der Lee & Frederiksen, 2005; Mercier et al., 2009).

While both seismic refraction and seismic tomography studies indicate elevated mantle temperatures in the backarc, the reduced seismic velocities might also be attributed to the presence of fluids, as laboratory measurements indicate that these can reduce seismic velocities primarily by enhancing the anelasticity of the rock (Karato, 2006).

3.2.3.5 Geodynamic models

The previously discussed geophysical observations indicate unusually high temperatures in the backarc mantle compared to the North American Craton despite the cooling effect of the subducting Juan de Fuca plate. Geodynamic modelling indicates that frictional heating along the surface of the subducting slab and latent heat associated with metamorphism in the forearc produce only a fraction of the heat required to explain these temperatures, so that additional heat transport through mantle flow is necessary to explain the observations (Currie et al., 2004a).

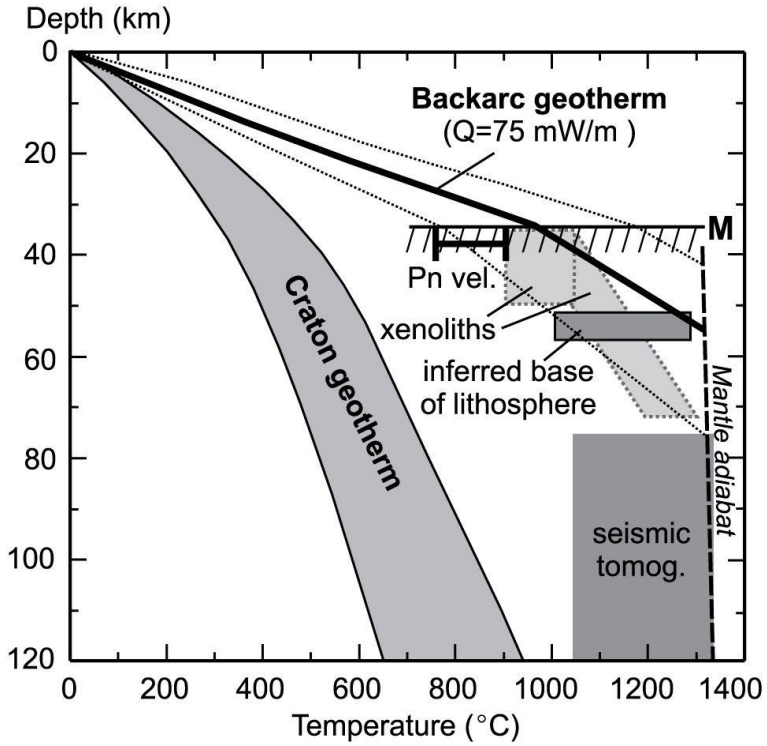

Figure 3.5: Geotherms for the backarc of the Canadian Cordillera (dotted lines represent 20% uncertainty) and the North American craton derived from surface heatflow data. Additional temperature constraints derived from seismic refraction, seismic tomography, mantle xenolith thermobarometry data. (reprinted from Currie & Hyndman, 2006)[5]

In addition, high mantle temperatures extend several hundred kilometres eastward into the backarc region. In previous studies of backarc basins, elevated temperatures have often been interpreted as the result of crustal extension (e.g. Watanabe et al., 1977). However, the last episode of extension in the Canadian Cordillera occurred during the Eocene, and was relatively short-lived (< 10 Ma) and spatially limited to a small region in the eastern Omineca Belt with no evidence for a regional episode of extension after this. A comparison with other subduction zone backarcs suggests that unusually high temperatures in the backarc mantle are common for most subduction zones (Currie & Hyndman,

2006). Geodynamic modelling indicates that these high temperatures are not consistent with simple slab-driven corner flow, in which material from the mantle wedge is entrained and carried downwards with the subducting plate, and then gets replaced by hot mantle from the backarc. Instead, heat needs to be carried up through vigorous mantle convection of a low viscosity mantle into the backarc region (Currie et al., 2004a).

To understand whether a low velocity mantle is consistent with the geophysical observations, it is necessary to further constrain the rheology of the backarc region. While previous geophysical observations have determined the thermal regime of the mantle (see Figure 3.5 for a summary), further observations are required to constrain the hydration state of the backarc mantle and to determine the effect on mantle viscosity.

3.2.4 Previous magnetotelluric studies

Magnetotelluric (MT) observations image the subsurface electrical resistivity structure (e.g. Simpson & Bahr, 2005). Broadband MT data are collected in the period range 0.001-1000 s, corresponding to imaging depths from the surface to the lower crust (~40 km depth). Long-period MT data extend this period range to 10,000 s, equivalent to imaging depths of up to several hundred kilometres, depending on the subsurface resistivity structure. The resistivity of crustal and upper mantle rocks is very sensitive to the presence of fluids, and therefore MT data can be used to infer the distribution of fluids and assess the rheological

structure of the crust and upper mantle. Information derived from MT is thus complementary to that obtained from seismic studies, which are also sensitive to the presence of fluids due to their effect on the anelasticity of the rock (Karato, 2006).

Over the last four decades, a number of electromagnetic studies have been used to investigate the crustal resistivity structure of the Canadian Cordillera and the Northern Cascadia subduction zone. Early broadband MT studies by Gough (1986) detected an extensive low-resistivity crustal structure beneath the Intermontane and Omineca Belts, which was explained by mantle derived water associated with extensive partial melting of the uppermost mantle. Gough (1986) proposed that the partial melting of the uppermost mantle was the result of ambient mantle upwelling.

A detailed MT study of the forearc region of the Cascadia subduction zone was conducted using broadband MT data on Vancouver Island (Kurtz et al., 1986; Kurtz et al., 1990, see Figure 3.6). Beneath Vancouver Island, the subducting Juan de Fuca plate dips towards the northeast at an angle of 8-16˚ (Riddihough, 1979; Spence et al., 1985). The MT study detected a 6 km thick northeast-dipping, conductive layer with a conductance of 200 S at depths greater than 20 km in the North American crust above the top of the subducting plate. The possibility of a thinner conductive layer was not investigated due to computational limitations on the size of the model mesh used for the two-dimensional modeling. The conductive layer is coincident with the so-called E-horizon, a 5-8 km thick set of

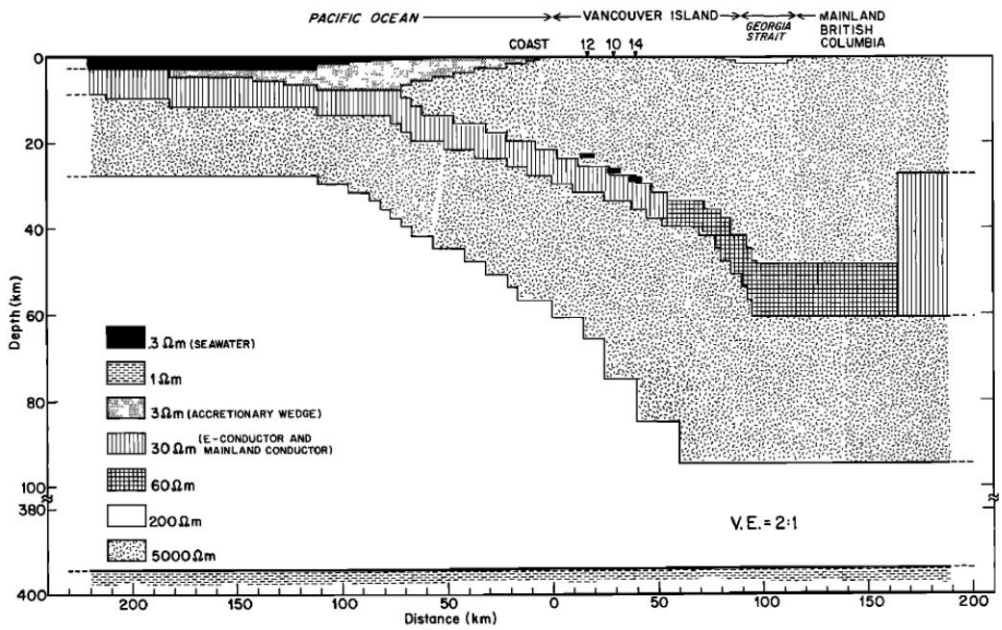

Figure 3.6: The two-dimensional resistivity model of the Cascadia subduction zone beneath Vancouver Island. The E-conductor (30 and 60 Ωm) is located above the top of the plate. The global decrease in resistivity is represented by a 1 Ωm half space below 390 km. The bold horizontal bars beneath sites 10, 12 and 14 on Vancouver Island indicate the depths to the seismic E-reflector. (reprinted from Kurtz et al., 1990)[6]

seismic reflectors associated with the top of the subducting Juan de Fuca plate (Green et al., 1986). Kurtz et al. (1986) interpret the conductive layer to be caused by 1.6-3.6 % saline fluids in the pore space of the North American crust above the subducting Juan de Fuca plate, provided by the subducting Juan de Fuca plate and through metamorphic dehydration reactions.

Similarly, based on a detailed analysis of the same set of MT data and seismic data, Hyndman (1988) suggests that the east-dipping, conductive layer and the coincident set of seismic reflectors are caused by 1-4% of pore water in the North American crust above the subducting plate. The Juan de Fuca plate is observed 10 km deeper than the conductive layer as a thin reflector dipping at 15˚. The

observed water is the result of metamorphic dehydration reactions in the subducting oceanic plate and gets trapped by an impermeable layer associated with silicate precipitation caused by hydration reactions in the colder, overlying continental crust (Hyndman, 1988).

Further broadband MT measurements were made as part of the multidisciplinary Lithoprobe program to study the southern Canadian Cordillera (Figure 3.1). Inversion models derived from these broadband MT data show a resistive upper crust overlying a conductive lower crust (Ledo & Jones, 2001) consistent with the results of Gough (1986). Electrical resistivities in the lower crust of the Intermontane Belt are between 100 and 300 Ωm and are relatively uniform along strike. In the Omineca Belt, lower crustal resistivities are between 10 and 50 Ωm in the south, increasing by up to two orders of magnitude towards the north. Ledo & Jones (2001) interpreted the lower crustal resistivities in the southern Omineca Belt to be caused by saline fluids, which were introduced into the crust as a result of magmatic flow from the mantle associated with the short-lived extension in this region during the Eocene (Monger & Price, 2002). They suggested that variations in the lower crustal resistivities are mainly due to variations in the amount of fluids as well as their geometrical distribution and interconnection in the crust.

Whereas the previous broadband MT studies have successfully mapped the resistivity of the crust of the Canadian Cordillera, the lack of long period MT data has hindered the extension of this analysis to mantle depths.

A newer study by Soyer & Unsworth (2006) has extended the previous analyses to mantle depths by collecting long-period MT data along a 350 km long SW-NE profile extending from the Insular Belt across the Coastal Belt into the Intermontane Belt. Beneath Vancouver Island, inversion models derived from these data show a conductive layer at ~20 km depth, consistent with the observations by Kurtz et al. (1986), and interpreted to be caused by interconnected saline fluids released from the subducting Juan de Fuca plate. Further east, the data detected a conductive forearc mantle wedge at 50-60 km depth, coincident with a zone of low seismic velocities. Soyer & Unsworth (2006) suggested that the low electrical resistivities and seismic velocities cannot be explained by serpentinization of the forearc mantle as lizardite, the low velocity form of serpentinite, is not stable under upper mantle temperature and pressure conditions (see section 3.2.2). Instead, serpentinite in the forearc mantle wedge is more likely present in the form of antigorite, which is characterized by high electrical resistivities and seismic velocities when dry (Guo et al., 2011; Reynard et al., 2011). Therefore, a fluid phase with a fluid content of 1-5% is required to explain the magnetotelluric and seismic observations.

3.3 New long-period magnetotelluric observations

The long-period MT study by Soyer & Unsworth (2006) has provided some information on the electrical resistivity structure of the upper mantle beneath the Canadian Cordillera. However, the profile did not extend across the entire backarc

and was limited to the Insular, Coastal and western Intermontane Belts (A-A' in Figure 3.1b). In addition, the single profile of MT data does not allow along strike variations in the electrical resistivity of the crust and upper mantle to be investigated.

To address this shortcoming, additional long-period magnetotelluric data were collected in 2003 and 2004 as part of a previous study at 63 stations with a spacing of ~15 km along the ABC-S profile crossing the entire backarc (Figure 3.1). The data were collected using a combination of LIMS (Long period Intelligent Magnetotelluric System) and NIMS (Narod Intelligent Magnetotelluric System) instruments and cover the period range 1-10,000 s.

Long-period MT data were then collected in 2006 and, as part of this study, in 2009 at 29 stations with a spacing of ~15 km on the ABC-N line. These stations extended a profile of broadband magnetotelluric data that had previously been collected as part of the Lithoprobe experiment in 1989 and 1990. The long period MT data were collected using a combination of LIMS and NIMS instruments and cover the period range 1-10,000 s, whereas the broadband MT data were collected using the Phoenix V5 system and cover the period range 0.01-1000 s.

On both profiles, the measured electrical and magnetic field time-series were converted into impedance estimates relating perpendicular electric and magnetic field components using the robust, multivariate processing algorithm by Egbert (1997). Coherent noise in the field components was removed using remote reference processing (Gamble et al., 1979).

3.4 Dimensionality of the long-period ABC MT data

3.4.1 Tensor decomposition analysis

Interpretation of MT data requires an understanding of the dimensionality of the data. Several methods have been developed to estimate the electromagnetic strike direction (Simpson & Bahr, 2005). One widely used and accepted method is the decomposition of the impedance tensor that was originally proposed by Groom & Bailey (1989), and extended to multiple frequencies and sites by McNeice & Jones (2001). By using multiple frequencies and sites, a more robust estimate of the regional strike direction is obtained (section 2.2.5).

For the MT data available for the Canadian Cordillera a single-site, multi-frequency analysis of the electrical strike direction was performed for each station, with stations grouped into the five morphological belts. Stations were grouped in accordance with their location, and strike analysis was conducted for the period bands 10-100 s, 100-1000 s and 1000-10,000 s. Rose diagrams of the strike directions obtained for each belt were then plotted in map form (Figure 3.7). As the calculated strike directions contain an inherent 90° ambiguity, both solutions are plotted (black and white wedges respectively). The ambiguity was solved by considering the regional geological structure, with the interpreted strike direction plotted as black wedges.

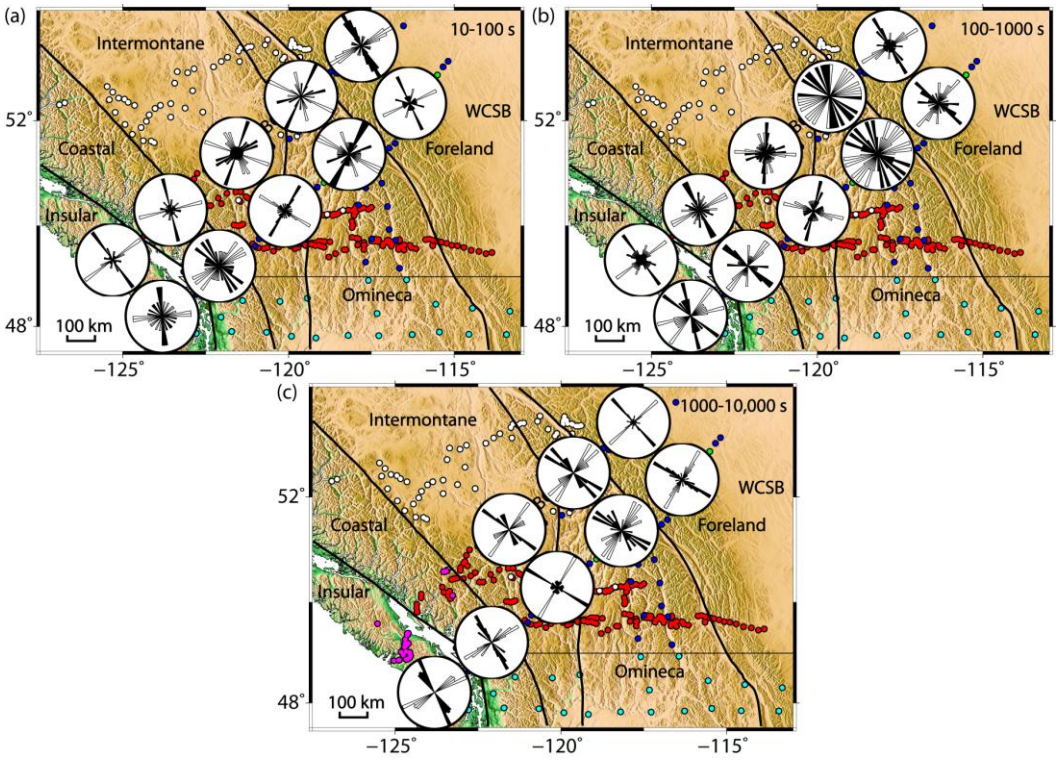

Figure 3.7: Results of a single site, multi-frequency strike analysis for period bands (a) 10-100 s, (b) 100-1000 s and (c) 1000-10,000 s. Black and white wedges correspond to the two solutions of the strike analysis, as the strike direction contains an inherent 90° ambiguity. The ambiguity was solved by considering the regional geological structure, with the interpreted strike direction plotted as black wedges.

3.4.1.1 Strike direction for the ABC-N profile

For the ABC-N line, data in the period bands 10-100 s and 100-1000 s show a strike direction of N30°W for the Insular and Coastal Belts. Further east, in the Intermontane and Omineca Belts the strike direction rotates to N15°E to N30°E for the short period band 10-100 s and N-S for the period band 100-1000 s, consistent with previous observations by Ledo & Jones (2001), who attributed the change in strike direction in this region to local clockwise rotation of crustal structures between the mid-Cretaceous and Eocene. In the Foreland Belt the strike

direction is N30°W, consistent with the strike direction of the Canadian Rocky Mountains and western margin of the Western Canadian Sedimentary Basin (WCSB). For the long period band 1000-10,000 s the strike direction for the Intermontane, Omineca and Foreland Belts is N60°W to N45°W. This can be explained by the strike of the coast line, which is of importance at these periods due to the low resistivity of the sea water (0.3 Ωm) (Parkinson & Jones, 1979). No long period data are available for the Insular and Coastal Belts on the ABC-N profile.

3.4.1.2 Strike direction for the ABC-S profile

For the ABC-S line, the general strike direction for the period bands 10-100 s and 100-1000 s in the Insular and Coastal Belts ranges between N45°W and N30°W. The only exception is for the short period band 10-100 s in the Insular Belt, which exhibits E-W strike, associated with the local strike direction of the Leech River fault (Figure 3.1b). As for the ABC-N line, strike in the Intermontane and Omineca Belts ranges between N15°E and N30°E, again consistent with previous results by Ledo & Jones (2001). The strike direction in the Foreland Belt is N30°W and N45°W for period bands 10-100 s and 100-1000 s respectively, which is in agreement with the strike direction of the Canadian Rocky Mountains and margin of the WCSB. For the long period band 1000-10,000 s, strike direction is N30°W for the Insular and Coastal Belts and N60°W for the Intermontane, Omineca and Foreland Belts. These long-period strike directions

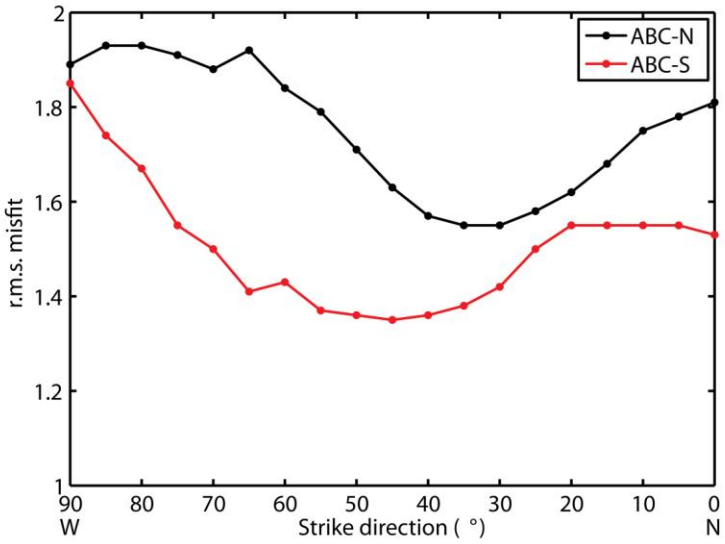

Figure 3.8: r.m.s. misfit of the tensor decomposition model for a constrained single site, multi-frequency strike for a fixed strike direction for every 5° between North and West.

are in good agreement with the strike direction of the coast line. On both profiles, data in the Omineca Belt are highly distorted, most likely due to current channelling (e.g. Jones, 1983), and as a result the strike direction for the period band 100-1000 s is not well defined.

3.4.1.3 Consistency of the MT data with a strike direction of N45°W

With the exception of the period bands 10-100 s and 100-1000 s in the Intermontane and Omineca Belts, the strike direction along both profiles is generally between N60°W and N30°W, suggesting an average strike of N45°W. To check for consistency with the measured MT data, the strike analysis was repeated with the strike directions fixed for every 5° between North and West for all periods. At the same time, a single shear and a single twist angle were

calculated for each station over the entire period range. For all strike directions the r.m.s. misfit of the tensor decomposition model at each station was calculated (Figure 3.8). For the ABC-N line, the strike analysis yields a misfits below 1.6 for strike directions between N40°W and N25°W, while for the ABC-S line misfits below 1.4 occur for a strike direction between N55°W and N35°W.

To see the effect of varying strike direction on the different period bands and stations, the r.m.s. misfit of the tensor decomposition model is plotted in pseudosection form for strike directions fixed at N60°W, N45°W and N30°W, and compared to the results from the unconstrained single site, multi-frequency analysis discussed above (Figure 3.9). For both profiles, the r.m.s. misfit for the unconstrained strike analysis is generally small (< 1), except for some stations in the short period band 10-100 s as well as stations in the Omineca Belt near the Rocky Mountain Trench, consistent with the poorly defined strike direction in this region. The overall misfit increases when strike is fixed at a specific angle for all stations and period bands, but remains generally below 1.5. For the ABC-N profile, a strike direction of N30°W provides a good misfit for the period bands 10-100 s and 100-1000 s, while N45°W provides a better misfit for the long-period band 1000-10,000 s. For a strike direction of N60°W, misfit in the Foreland Belt significantly increases, making it inconsistent with the MT data. For the ABC-S profile, a strike direction of N45°W provides an acceptable r.m.s. misfit for all morphological belts for the long-period band 1000-10,000 s.

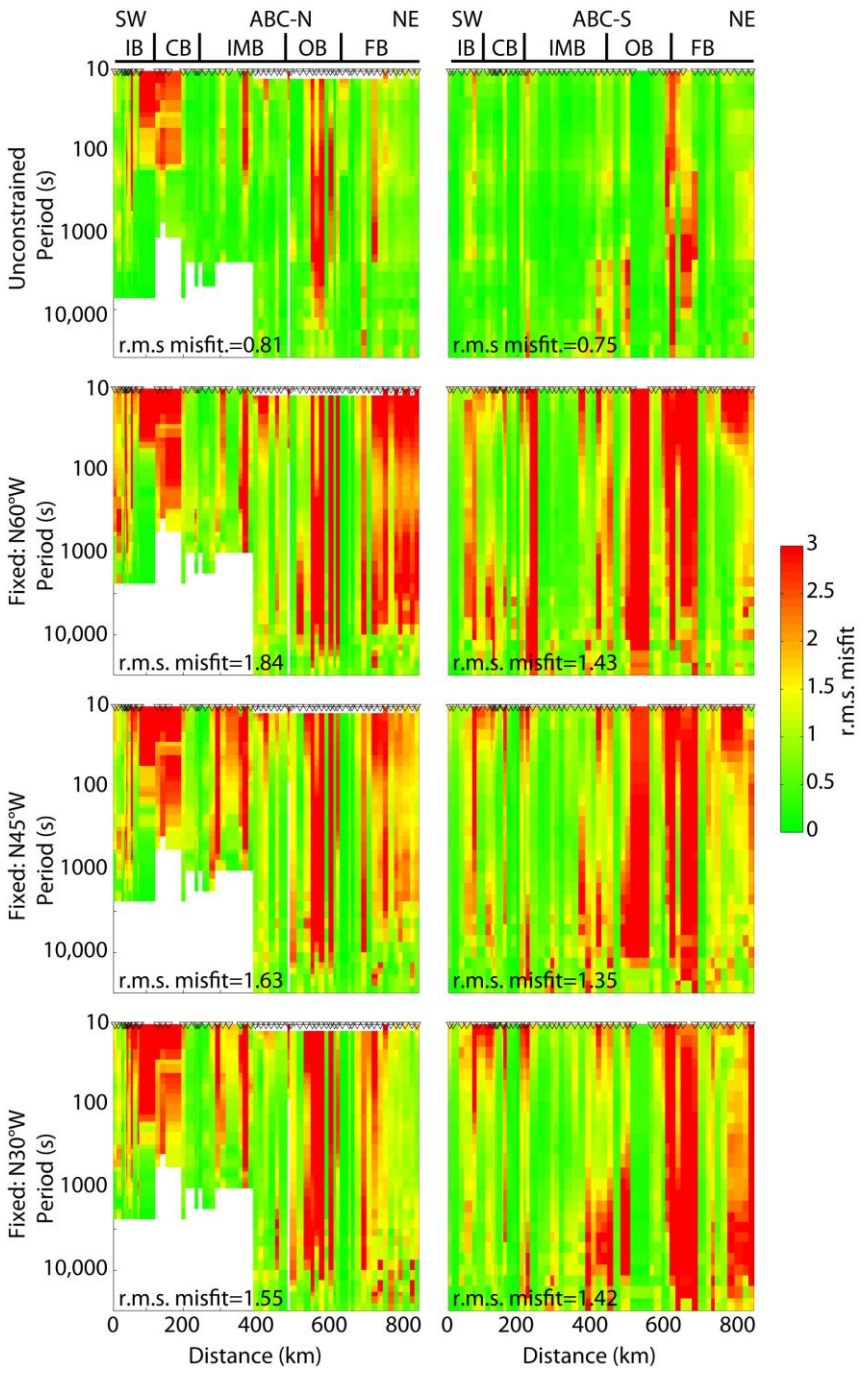

Figure 3.9: r.m.s. misfit of the tensor decomposition model for an unconstrained (top row) and constrained single site, multi-frequency strike analysis for the ABC-N (left) and ABC-S (right) line. For the constrained strike analysis the strike direction was fixed at N60°W (second row), N45°W (third row) and N30°W (bottom row). IB: Insular Belt; CB: Coastal Belt; IMB: Intermontane Belt; OB; Omineca Belt; FB: Foreland Belt.

In contrast, a strike direction of N30°W only provides an acceptable misfit for the Insular and Coastal Belts, while a strike direction of N60°W only provides an acceptable misfit for the Foreland Belt. Therefore, a strike direction of N45°W provides the most consistent estimate for both profiles at long periods. The 90° ambiguity in strike direction was solved by considering the regional geological structure. The complete decomposition results for a strike direction of N45°W can be found in Appendix A.1.

3.4.2 Induction vectors

Whereas the previous section investigated the dimensionality of the data based on the electromagnetic impedance tensor, an additional understanding of dimensionality can be obtained from induction vectors derived from magnetic field data (section 2.2.4). Induction vectors represent the complex ratio of the vertical and horizontal magnetic fields and are associated with lateral conductivity variations. In the Parkinson convention, the real part of the induction vectors points towards conductive regions, with the magnitude of the induction vector determined by the conductivity gradient (Parkinson, 1962). Therefore, for a two dimensional structure the induction vectors are expected to be perpendicular to the strike direction.

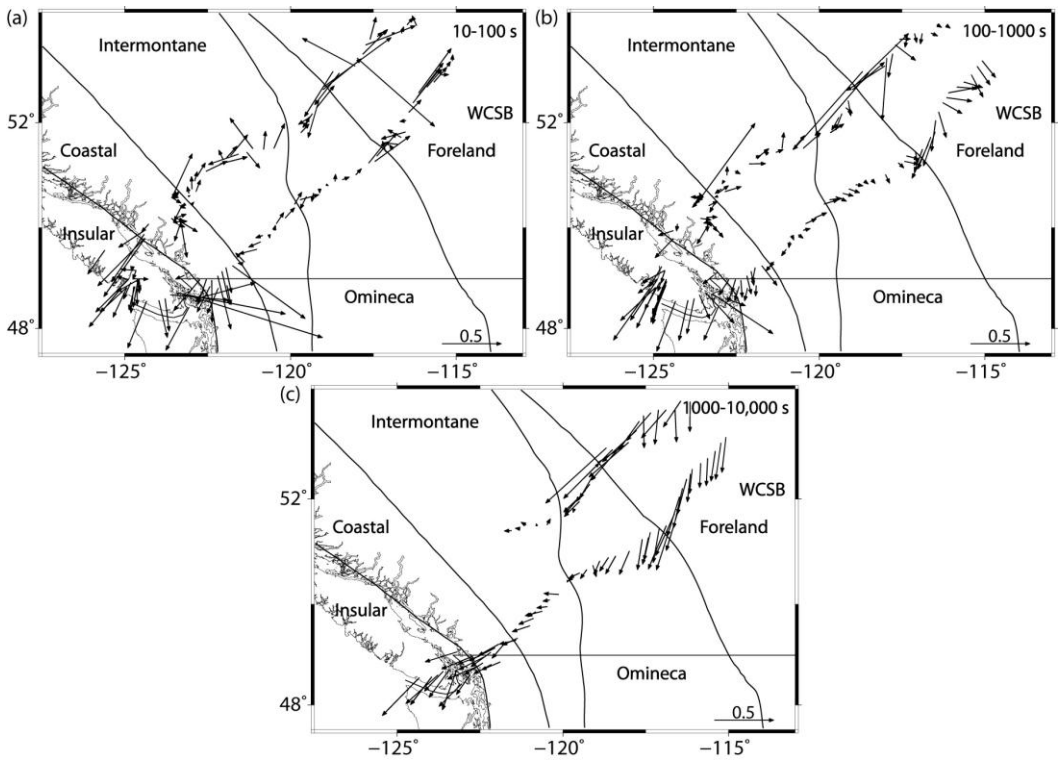

Figure 3.10: Real parts of the induction vectors using the Parkinson convention (Parkinson, 1962) for period bands (a) 10-100 s, (b) 100-1000 s and (c) 1000-10,000 s.

Figure 3.10 shows the real part of the induction vectors using the Parkinson convention for the period bands 10-100 s, 100-1000 s and 1000-10,000 s. For the short period band 10-100 s, the induction vectors show variability both in direction and magnitude due to local conductivity anomalies in the upper crust. For periods of 100-1000 s, induction vectors in the Insular and Coastal Belts point towards the coast and the low resistivity ocean. Induction vectors in the Intermontane and Foreland Belts point in opposite directions towards the centre of the Omineca Belt, but are slightly disturbed towards the area south of the ABC-S profile. This observation suggests a low resistivity zone beneath the Omineca Belt, which based on the period range considered, is possibly located in the lower

crust or upper mantle. For the long period band 1000-10,000 s, the induction vectors for all stations point towards the low resistivity ocean, generally decreasing in magnitude with increasing distance from the coast. One exception is the induction vectors in the Foreland Belt, which are similar in magnitude to the induction vectors in the Insular Belt. The increased magnitudes are most likely caused by the combined effect of the low resistivity ocean (Parkinson & Jones, 1979) and a low resistivity zone extending westward of the Omineca Belt. This idea is supported by the strong suppression of the induction vector magnitudes in the Intermontane Belt.

As the induction vectors for the period bands 100-1000 s and 1000-10,000 s are generally parallel to the profile and perpendicular to the N45°W strike direction determined in the previous section, the magnetic field data also support a two-dimensional analysis of the MT data.

3.5 Characteristics of the ABC MT data

3.5.1 Typical MT curves

Based on the previous strike analysis, the MT data for the ABC-N and ABC-S profiles were rotated to a strike direction of N45°W. To illustrate along-profile variations and quality of the data, representative apparent resistivity and phase curves have been plotted (Figure 3.11) with the station locations highlighted on the topography map in Figure 3.1. Assuming a two-dimensional subsurface structure, the data can be separated into two independent modes: (a) transverse

electric (TE) mode with the electric field parallel to the geological strike and (b) transverse magnetic (TM) mode with the magnetic field parallel to the geological strike (section 2.2). Apparent resistivity and phase are related through a Hilbert transform, where an increase in apparent resistivity is associated with a phase less than 45°, while a decrease in apparent resistivity is associated with a phase greater than 45°. Amplitudes of the apparent resistivities can be affected by galvanic distortion (section 2.2) and therefore only changes in apparent resistivity will be discussed.

For the Insular Belt (station ABC-106), the MT data are characterized by a decrease in apparent resistivity with period in both modes at periods less than 100 s. This decrease in apparent resistivity is associated with increasing sensitivity to the low resistivity of the ocean. At periods greater than 100 s, the data show an increase in apparent resistivity. The increase in apparent resistivity is more prominent in the TM mode, causing lower phases in the TM mode than in the TE mode.

In the Coastal Belt (station ABC-120), the TE mode is characterized by a decrease in apparent resistivity with period, while the TM mode shows a general increase in apparent resistivity with period.

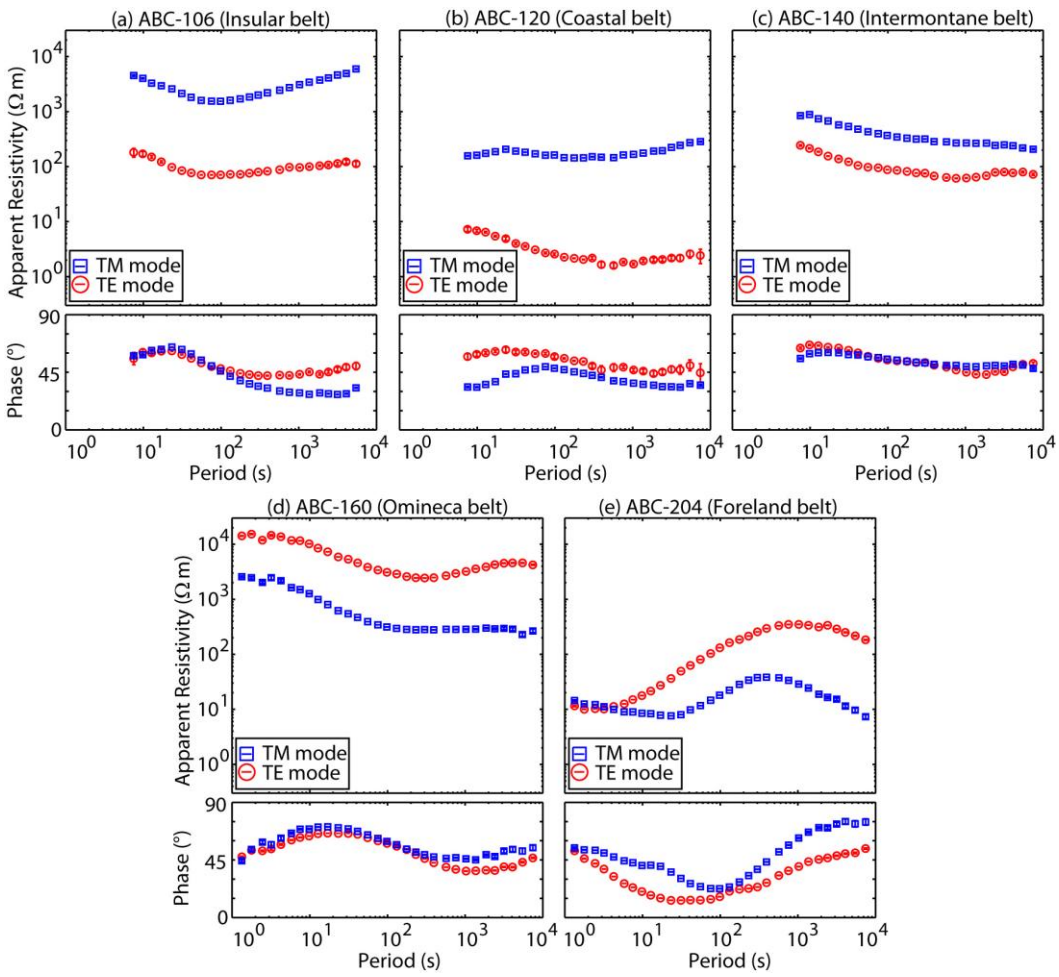

Figure 3.11: Examples of typical apparent resistivity and phase curves for five MT stations: (a) ABC-106, (b) ABC-120, (c) ABC-140, (d) ABC-160 and (e) ABC-204. MT data were rotated to a strike direction of N45°W. Locations of the MT stations are indicated by green dots in Figure 3.1.

In the Intermontane (station ABC-140) and Omineca Belts (station ABC-160), both modes generally show a decrease in apparent resistivity with increasing period, consistent with a decrease in resistivity as the MT data begin to sample the low-resistivity lower crust, as observed by Ledo & Jones (2001), and upper mantle. At periods greater than 1000 s in the Omineca Belt, the TE mode indicates an increase in apparent resistivity.

In the Foreland Belt (station ABC-204), the data show low apparent resistivities at periods less than 10 s in both modes, associated with the low resistivities of sedimentary rocks in the WCSB. At periods in the range 10-1000 s, the data show an increase in apparent resistivity. This is likely associated with crystalline basement rocks. At periods greater than 1000 s, the data are characterized by a decrease in apparent resistivity, associated with the low resistivities of the upper asthenosphere. The increase in apparent resistivity is more prominent in the TE mode, causing lower phases in the TE mode than in the TM mode.

For all stations, the phases are consistent with the apparent resistivity data, with phases less than 45° for an increase and greater than 45° for a decrease in apparent resistivity with period.

3.5.2 Pseudosections of the ABC magnetotelluric data

Pseudosections provide a convenient way of displaying a large MT data set comprising many MT sounding curves by plotting the MT data as a function of position along profile and depth. Figure 3.12 and Figure 3.14 show pseudosections for both TE and TM apparent resistivities and phases as well as for the vertical magnetic field data, for the ABC-N and ABC-S profiles respectively. White areas indicate stations and periods at which no data were collected or at which data were excluded due to poor data quality.

For the ABC-N line, the TE and TM pseudosections indicate high electrical resistivities at periods less than 100 s in the Insular, Coastal and western

Intermontane Belts. The broad-band MT data collected in this region is limited to a maximum period of a few hundred seconds, so no information is available at longer periods. In contrast, for the ABC-S line, the TE and TM pseudosections indicate lower electrical resistivities at periods < 100 s in this region than along the ABC-N line. In addition, a region of low electrical resistivities in the Coastal Belt is observed in the TE mode for periods less than 100 s. Resistivities in this region increase with increasing period.

For the eastern Intermontane and Omineca Belts, the TE and TM data indicate a general decrease in resistivity with increasing period, consistent with the decrease in resistivity with depth reported by Ledo & Jones (2001).

In the Foreland Belt, the TE data shows low resistivities at periods less than 100 s, associated with the low resistivity sedimentary rocks of the WCSB. Electrical resistivities increase for periods greater than 100 s. The TM data also show the low resistivity sedimentary rocks of the WCSB as low resistivities at periods less than 100 s. Unlike the TE data, the TM data show another low resistivity zone for periods greater than 1000 s, extending west underneath the Omineca Belt.

As before, the phases are consistent with the apparent resistivity data, with phases less than 45° for an increase and greater than 45° for a decrease in apparent resistivity with period.

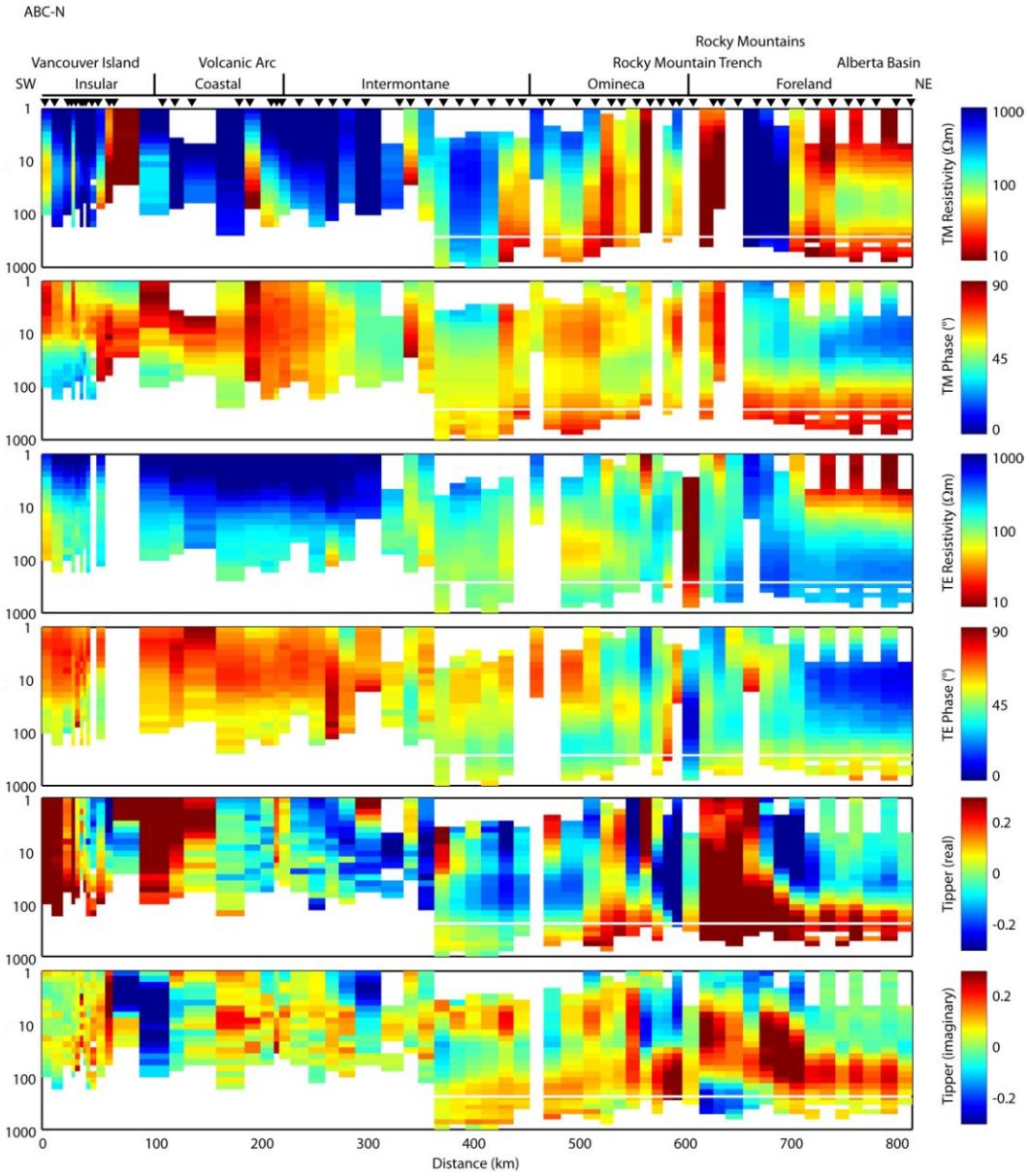

Figure 3.12: Pseudosections for the ABC-N profile showing the magnetotelluric data for a N45°W coordinate system. The top two panels show the apparent resistivity and phase for the TM mode, the middle two panels show the apparent resistivity and phase for the TE mode and the bottom two panels show the vertical magnetic field data. White areas correspond to stations and periods with no data.

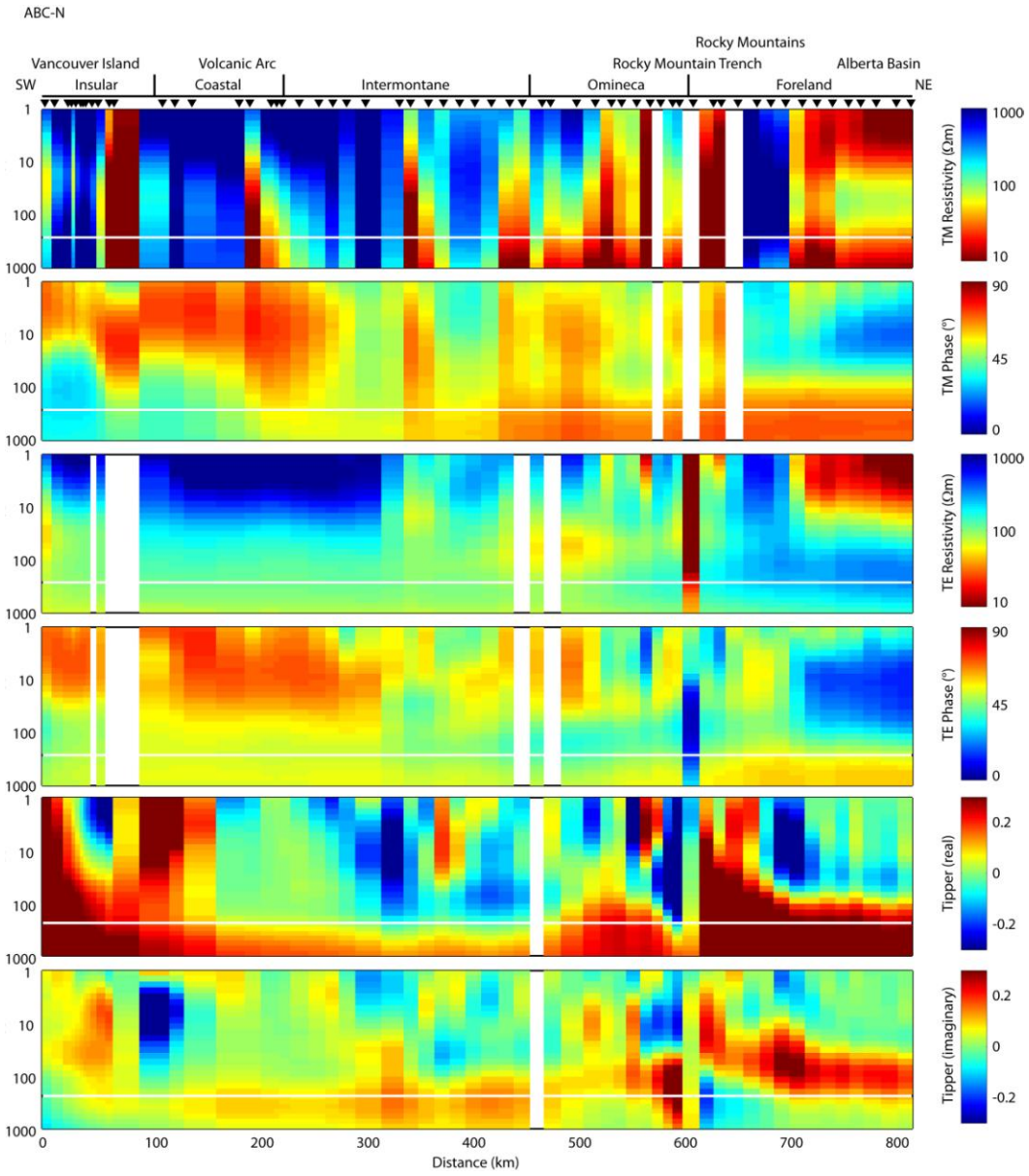

Figure 3.13: Pseudosections for the ABC-N profile showing the model response of the electrical resistivity model shown in Figure 3.17. The top two panels show the apparent resistivity and phase for the TM mode, the middle two panels show the apparent resistivity and phase for the TE mode and the bottom two panels show the vertical magnetic field data. White areas correspond to stations and periods with no data.

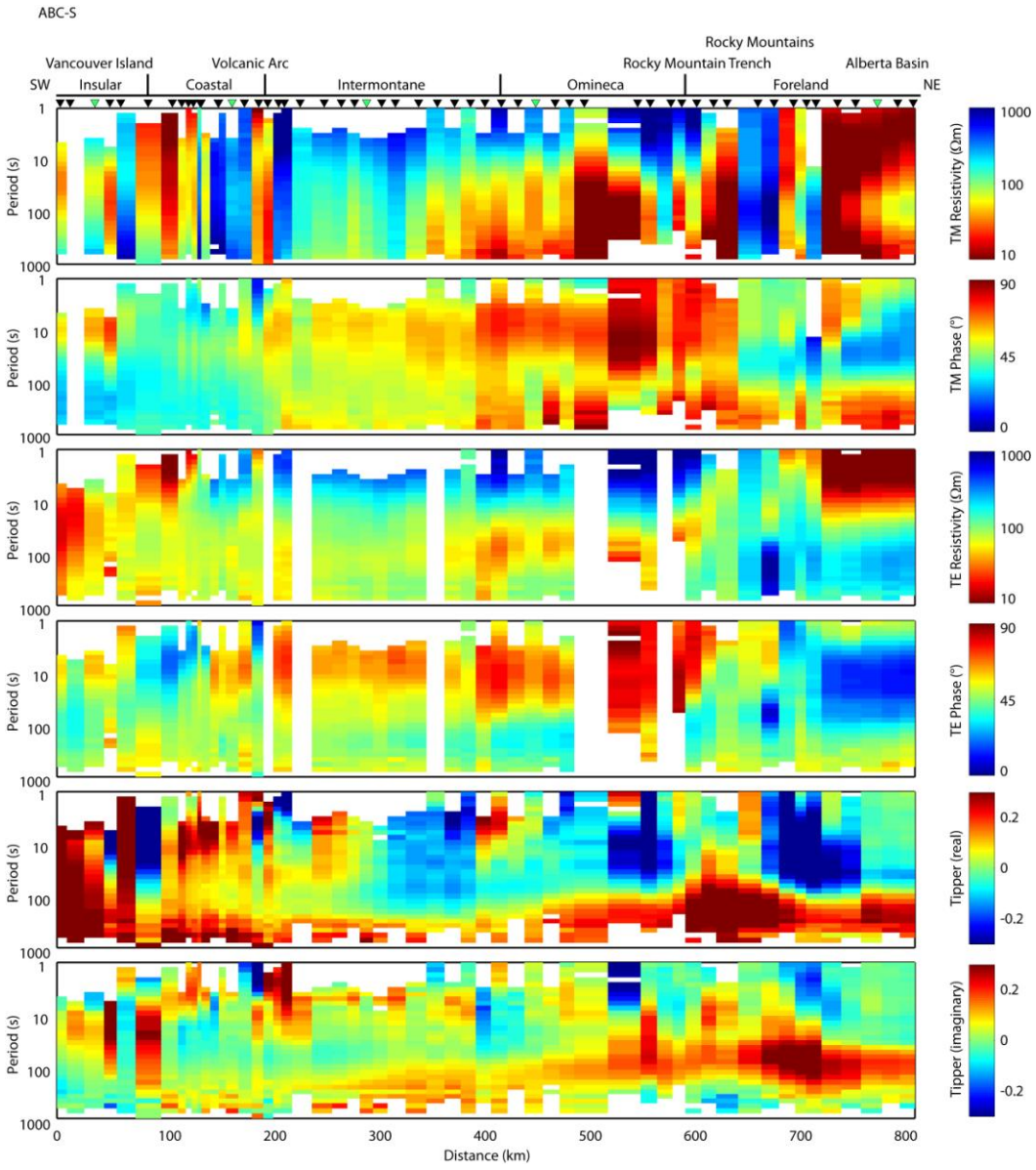

Figure 3.14: Pseudosections for the ABC-S profile showing the magnetotelluric data for a N45°W coordinate system. The top two panels show the apparent resistivity and phase for the TM mode, the middle two panels show the apparent resistivity and phase for the TE mode and the bottom two panels show the vertical magnetic field data. White areas correspond to stations and periods with no data.

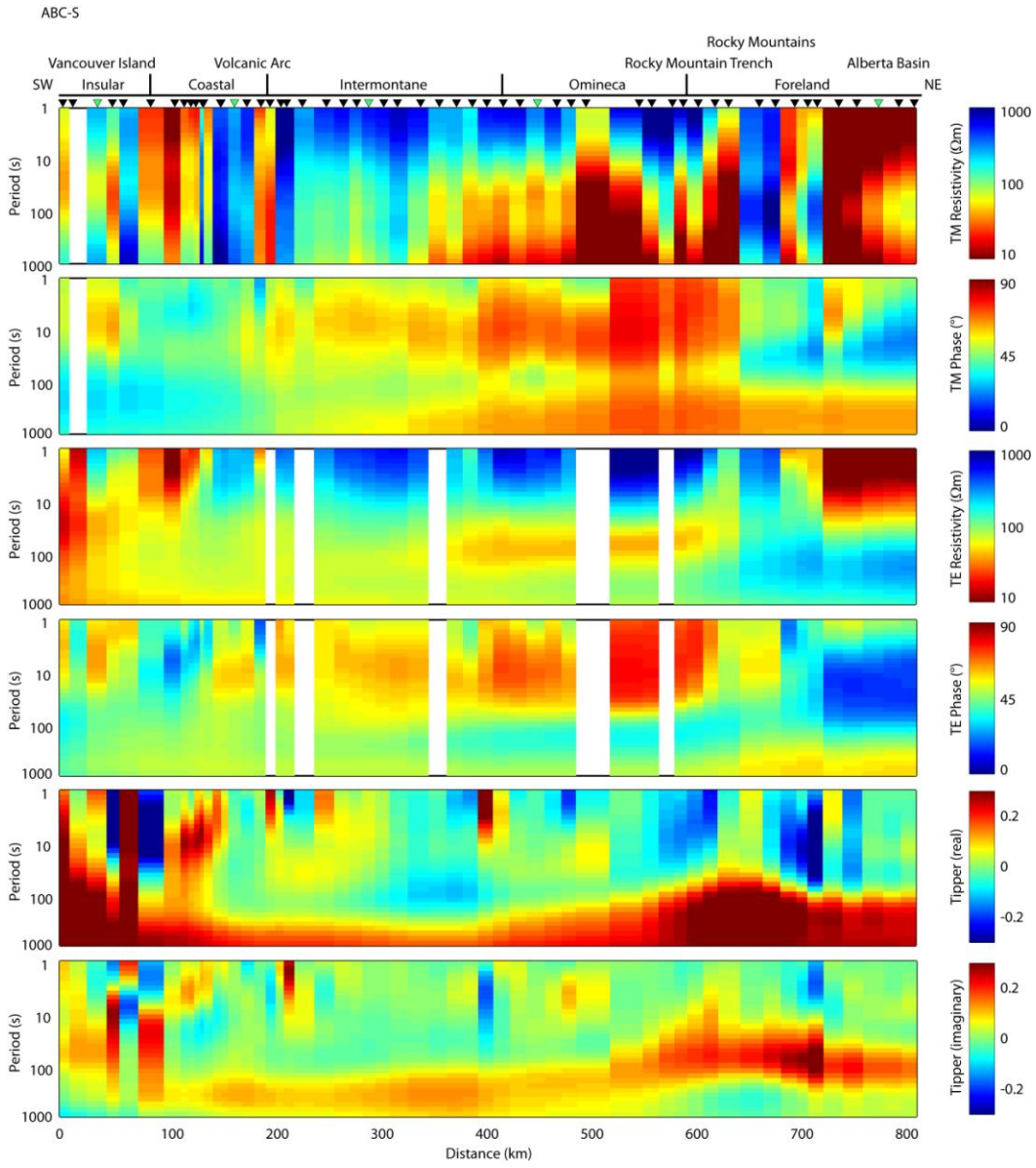

Figure 3.15: Pseudosections for the ABC-S profile showing the model response of the electrical resistivity model shown in Figure 3.17. The top two panels show the apparent resistivity and phase for the TM mode, the middle two panels show the apparent resistivity and phase for the TE mode and the bottom two panels show the vertical magnetic field data. White areas correspond to stations and periods with no data.

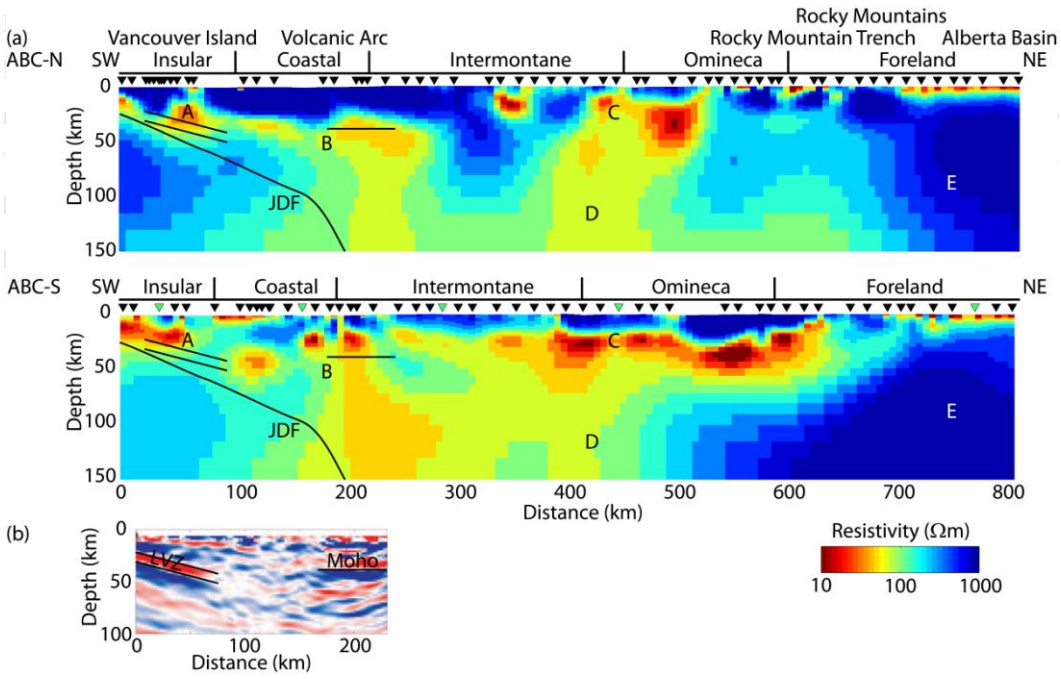

Figure 3.17: (a) Electrical resistivity models for the ABC-N (top) and ABC-S (middle) profiles generated using the 2D nonlinear conjugate gradient inversion algorithm of Rodi & Mackie (2001). A regularization parameter of $\tau = 3$ and a smoothing factor of $\alpha = 3$ were used in the inversions. The electrical resistivity models fit the MT data with an overall r.m.s. misfit of 2.50 (ABC-N) and 2.34 (ABC-S). Black triangles indicate location of MT stations; green triangles indicate the locations of the MT stations shown in Figure 3.11. Black line (JDF) represents top of the subducting Juan de Fuca plate, inferred from seismic refraction data (Clowes et al., 1995). Letters 'A' to 'E' correspond to model features discussed in section 3.7. (b) Relative seismic S wave velocities from receiver function analysis of Nicholson et al. (2005)[7]. A low velocity zone (LVZ) and the continental Moho interface are shown. These features are also superimposed on the electrical resistivity models in (a).

3.6 Inversion of the ABC MT data

The rotated MT data were used to generate 2D electrical resistivity models using the 2D nonlinear conjugate gradient inversion algorithm of Rodi & Mackie (2001). Figure 3.17 shows resistivity models for the ABC-N and ABC-S profiles, derived from a joint inversion of TM and TE impedance and vertical magnetic field data. Some stations show TM phases exceeding 90°, most likely caused by

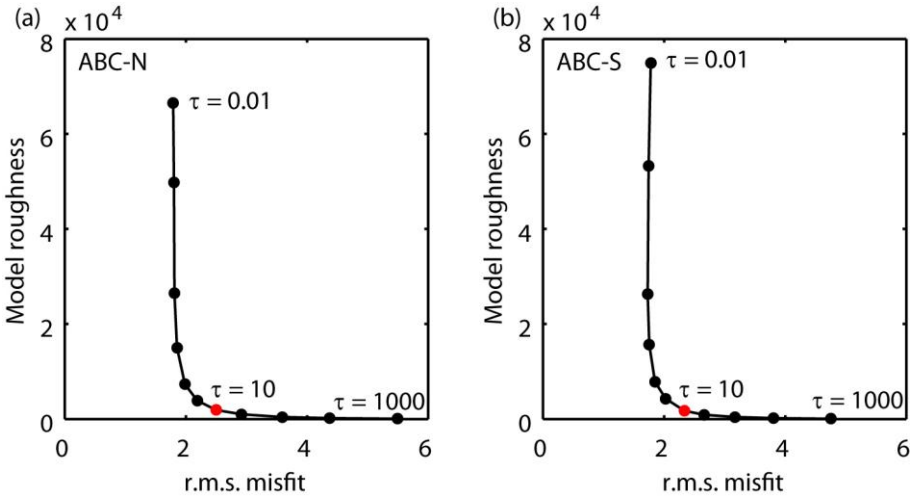

Figure 3.18: Trade-off curves between model roughness and r.m.s. misfit for (a) the ABC-N line and (b) the ABC-S line. The trade of parameter $\tau = 10$ used in the inversion of the MT data is highlighted in red.

channelling of direct currents by localized conductors (e.g. Jones, 1983). At these stations the TM data were excluded from the inversion, as these out of quadrant phases cannot be fit by the 2D inversion. For all other MT data an error floor of 20% in apparent resistivity and 5% in phase (expressed in equivalent apparent resistivity percent, with 5% corresponding to 1.45°) was applied, i.e. data errors that were below these error floor values were set to the error floor. By choosing a larger error floor for the apparent resistivity, less emphasis is put on fitting the apparent resistivity data, as these might be affected by galvanic distortion (section 2.2.5). The error floor for the vertical magnetic fields was set to an absolute magnitude of 0.04. The Pacific Ocean was modelled as a 2.5 km thick layer with a resistivity of 0.3 Ωm.

A smoothing factor $\alpha = 3$ was applied to the horizontal derivatives in the inversion, leading to an increased smoothness in the horizontal direction. The

regularization parameter τ provides a trade-off between overall model roughness and data misfit. Figure 3.18 shows a plot of model roughness versus r.m.s. data misfit for a range of trade-off parameters for both the ABC-N and ABC-S profiles. It can be seen that small τ values produce models with small r.m.s. misfit, but large model roughness. Large τ values on the other hand lead to smooth models at the cost of an increased r.m.s. misfit. For the profiles in this study, a regularization parameter τ = 3-10 corresponds to the corner of the L shaped curve, and therefore places equal emphasis on minimizing the data misfit and the model roughness. The obtained electrical resistivity models for τ = 10 fit the data with an overall r.m.s. data misfit of 2.50 (ABC-N) and 2.34 (ABC-S). The data fit is generally good for both the TM and TE impedance as well as the vertical magnetic field data, as illustrated by the pseudosections in Figure 3.13 and Figure 3.15.

3.7 Interpretation of the ABC resistivity models

The general subsurface structure of the electrical resistivity models for the ABC-N and ABC-S profiles shown in Figure 3.17 is quite similar. In the following section, the common model features as well as differences will be described.

3.7.1 Subduction zone conductor ('A')

Beneath the Insular and Coast Belt in the west, the electrical resistivity models show an east dipping, resistive feature associated with the subducting Juan de

Fuca plate and the underlying oceanic mantle. Above the resistor, the profiles show a conductor at a depth of ~ 20 km in the crust of the North American plate ('A'), dipping east at an angle of ~15° and extending as far east as the Strait of Georgia. This conductor with a conductance of 250-300 S is similar to the conductor observed beneath Vancouver Island by Kurtz et al. (1990). Beneath Vancouver Island, the conductor is coincident with a teleseismic low S-wave velocity zone associated with the top of the subducting Juan de Fuca plate (Bostock et al., 2002; Nicholson et al., 2005). These observations suggest that the conductor is most likely caused by interconnected aqueous fluids released from the slab (section 3.2.4).

3.7.2 Forearc mantle wedge and volcanic arc ('B')

Another zone of low resistivities is observed at ~30 km depth beneath the forearc in the Coastal Belt ('B'). Previous studies of the Cascadia subduction zone in Oregon have attributed these low resistivities to serpentinization of the mantle wedge (Bostock et al., 2002). However, as dry serpentine at mantle temperatures is characterized by high electrical resistivities (Guo et al., 2011; Reynard et al., 2011), an alternative conductivity mechanism, such as free aqueous fluids, is required to explain the observed low resistivities (Soyer & Unsworth, 2006). Low resistivities are also observed at 20-50 km beneath the volcanic arc, associated with fluids released from the subducting slab and possible upward migration of slab-induced melt. Cooling and solidification of this melt at the base of the crust

could provide significant amounts of water, which would explain the low crustal resistivities in this region (Soyer & Unsworth, 2006). Resistivities increase along strike towards the north, and whereas the ABC-S profile indicates reduced resistivities beneath the volcanic arc down to the top of the subducting plate, resistivities in the forearc of the ABC-N profile are 100 Ωm, similar to the resistivities observed in the backarc region.

3.7.3 Crustal conductor ('C')

A crustal conductor is found beneath the Intermontane and Omineca Belts ('C') with the top of the conductor located at ~20 km depth. Along the ABC-N profile, low resistivities can be found beneath the western part of the Intermontane and the eastern part of the Omineca Belt. Further south, along the ABC-S profile, the low resistivity crust extends beneath both the Intermontane and Omineca Belts, with the lowest resistivities found beneath the Omineca Belt. The resistivities beneath the Omineca Belt show a general north-south decrease along strike, in agreement with observations by Jones & Gough (1995) and Ledo & Jones (2001).

3.7.4 Upper mantle resistivity structure ('D' and 'E')

The uppermost mantle beneath the backarc also shows reduced electrical resistivities (~100 Ωm) extending as far east as the Rocky Mountain Trench at depth greater than 60 km ('D'), suggesting a shallow asthenosphere. The observed mantle resistivities cannot be explained by dry olivine, unless implausibly high

mantle temperatures in excess of 1500°C are assumed (see Appendix B.1.1 for electrical resitivity of dry olivine), but require an additional conductivity mechanism. One possible mechanism is through aqueous fluids released from the subducting slab and distributed in the backarc mantle, which can lower the electrical resistivities by hydrogen diffusion (Karato, 1990). In addition, aqueous fluids can also lower the melting temperature of the mantle, allowing for dehydration melting of mantle rocks (Hirschmann et al., 2009), which could lead to a further reduction in electrical resistivity.

The electrical properties of the shallow asthenosphere beneath the Canadian Cordillera are in contrast to the high mantle resistivities (~1000 Ωm) observed beneath the Foreland Belt ('E'). These high resistivities are associated with the lithosphere beneath the North American craton, which extends to depths of ~200 km (Türkoğlu et al., 2009). The ABC-N profile shows a well defined resistivity transition between the Omineca and Foreland Belts east of the Rocky Mountain Trench, while the ABC-S profile indicates high resistive mantle rocks extending underneath the Omineca Belt at depths greater than 100 km. The boundary between the Omineca and Foreland Belts is also characterized by a dramatic change in surface heat flow, elastic thickness and seismic velocities (section 3.2.3).

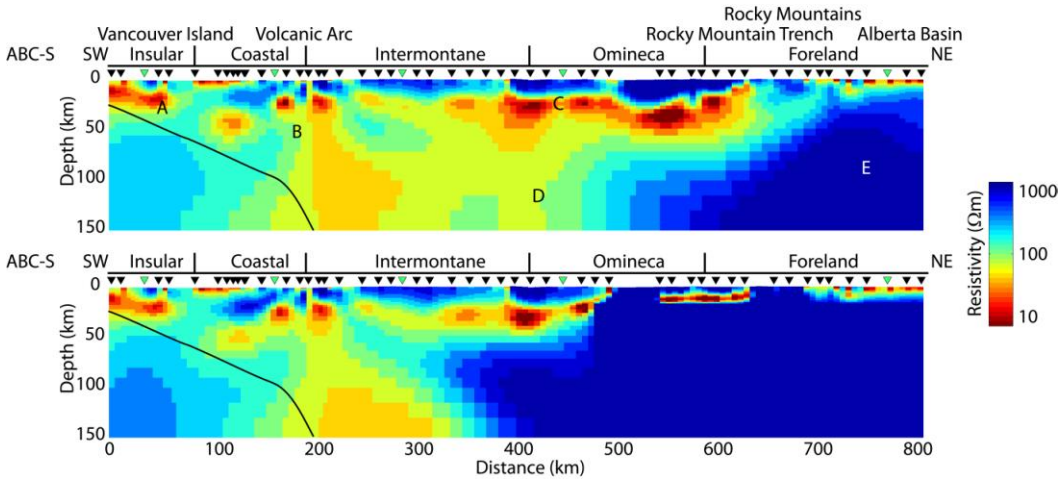

Figure 3.19: Electrical resistivity model for an unconstrained (top) and constrained inversion (bottom) of the ABC-S data. The electrical resistivity of the constrained model is fixed to 100 Ωm at depths greater than 50 km beneath the Omineca and Foreland Belts. The constrained electrical resistivity model fit the data with an overall r.m.s. misfit of 3.03 compared to an r.m.s. of 2.34 for the unconstrained inversion.

A constrained MT inversion was used to test how well the MT data could constrain the location of the transition between the low resistivity backarc mantle and the high resistivity lithosphere of the North American craton on the ABC-S line. In this inversion, the model resistivities were fixed at a value of 1000 Ωm at depths greater than 50 km beneath the Omineca and Foreland Belts. These resistivities are comparable to the high mantle resistivities observed further east beneath the Foreland Belt. The same data errors, smoothing factor α and regularization parameter τ as in section 3.6 were used in the constrained inversion. The obtained resistivity model fits the data with an r.m.s. misfit of 3.03 (Figure 3.19) compared to an r.m.s. of 2.34 for the unconstrained inversion. With the mantle resistivity fixed at 1000 Ωm, the inversion placed the low resistivities, originally observed in the uppermost mantle, into the crust.

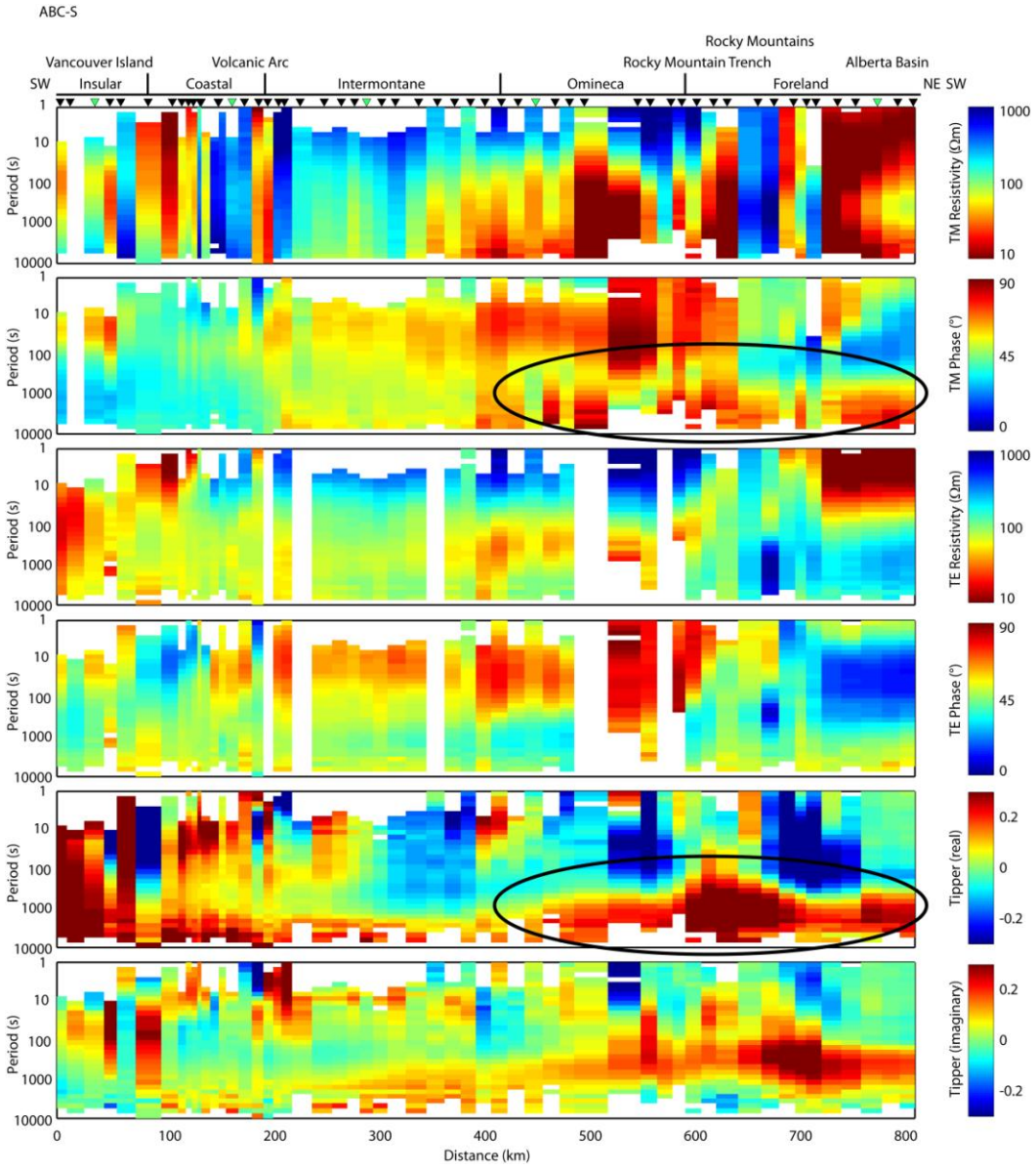

Figure 3.20: Pseudosections for the ABC-S profile showing the magnetotelluric data for a N45°W coordinate system. The top two panels show the apparent resistivity and phase for the TM mode, the middle two panels show the apparent resistivity and phase for the TE mode and the bottom two panels show the vertical magnetic field data. Black ellipses highlight regions of significantly reduced data fit of the constrained electrical resistivity model shown in Figure 3.19. White areas correspond to stations and periods with no data.

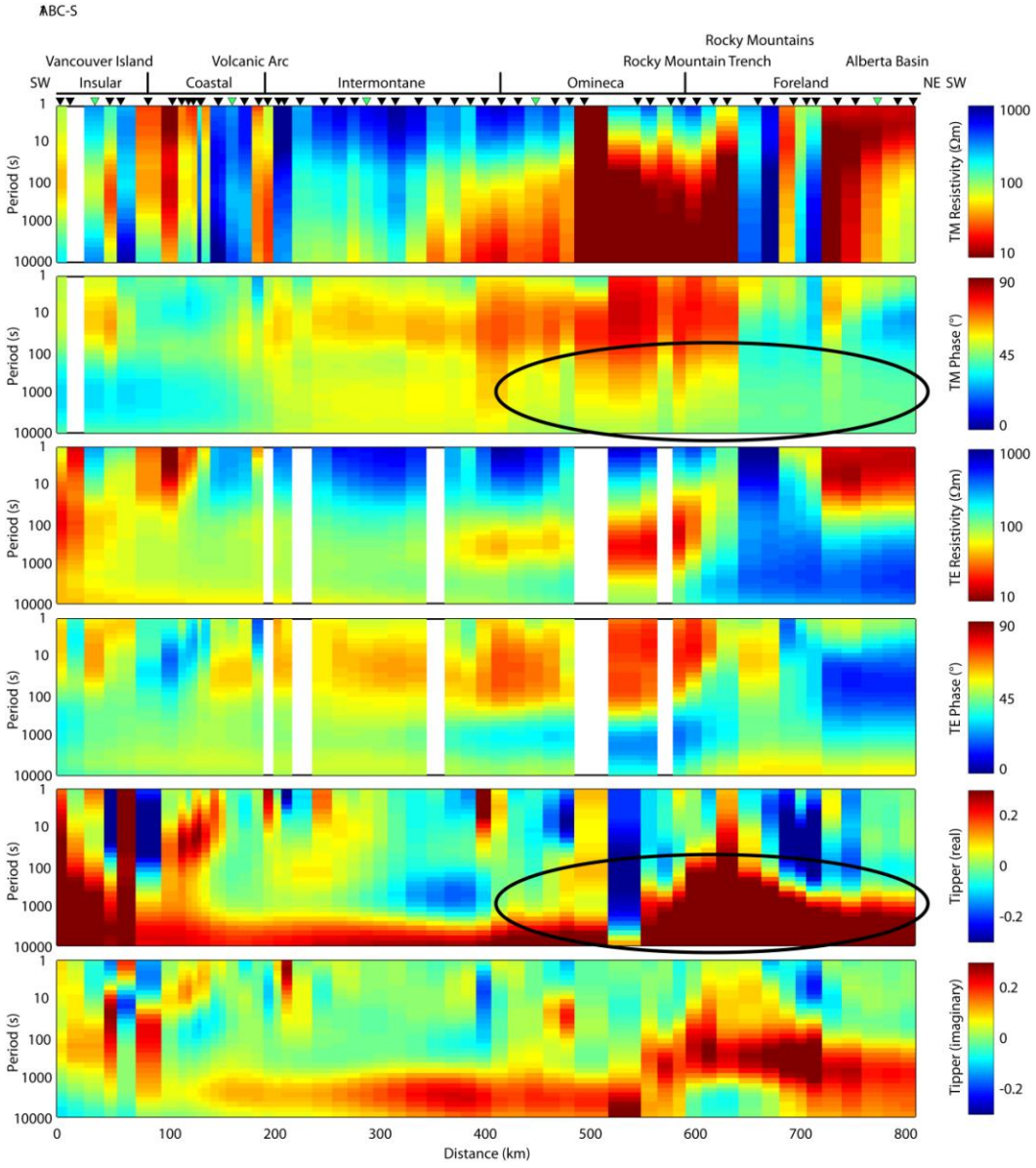

Figure 3.21: Pseudosections for the ABC-S profile showing the model response of the constrained electrical resistivity model shown in Figure 3.19. The top two panels show the apparent resistivity and phase for the TM mode, the middle two panels show the apparent resistivity and phase for the TE mode and the bottom two panels show the vertical magnetic field data. Black ellipses highlight regions of significantly reduced data fit of the constrained electrical resistivity model shown in Figure 3.19. White areas correspond to stations and periods with no data.

The corresponding model responses of the constrained inversion are shown in pseudosection form in Figure 3.20. Beneath the Insular, Coastal and Intermontane Belts the data fit remains relatively unchanged compared to the unconstrained inversion (see pseudosection in Figure 3.21). However, a significantly worse data fit is obtained beneath the Omineca and Foreland Belts. In particular, the constrained inversion is not able to fit the high phases in the TM mode for periods larger than 1000 s. In addition, at these periods the constrained inversion yields vertical magnetic field amplitudes, which are significantly higher than required by the data. These results suggest that low resistivities in the uppermost mantle beneath the Omineca Belt are required to explain the measured data.

3.8 Summary

Previous geophysical studies have shown that the mantle of the Canadian Cordillera is unusually hot, with high temperatures extending from the forearc several hundred kilometres eastward into the backarc region. Geodynamic studies indicate that these high temperatures require heat to be carried up into the backarc region through, for example, ambient mantle upwelling or vigorous mantle convection of a low viscosity mantle. Whereas previous geophysical observations have constrained the thermal regime of the mantle quite well, further observations are required to further constrain the rheology, and in particular the hydration state of the backarc mantle and to determine the effect of mantle hydration on mantle viscosity.

In this chapter, the first long-period MT data extending across the entire backarc region of the Southern Canadian Cordillera were presented. The electrical resistivity models obtained for two parallel 800 km profiles show the following features:

1. Beneath Vancouver Island, the electrical resistivity models show an east-dipping conductor at depths of ~20 km in the crust of the North American plate (‘A’), coincident with a low S-wave velocity zone associated with the top of the Juan de Fuca plate (Nicholson et al., 2005). This conductor is similar to that proposed by Kurtz et al. (1990), and most likely associated with the release of aqueous fluids from the underlying subducting plate.

2. In the forearc, a conductive mantle wedge is observed (‘B’), which is interpreted to be caused by free aqueous fluids. This result is in agreement with previous long-period MT studies of the forearc region by Soyer & Unsworth (2006). Another conductivity anomaly is found at 20-50 km depth beneath the volcanic arc, associated with fluids released from the subducting slab and possible upward migration of slab-induced melt in this region.

3.The electrical resistivity models show low resistivities in the lower crust of the Intermontane and Omineca Belts (‘C’), consistent with observations by Ledo & Jones (2001). These low resistivities are most likely caused by saline fluids with variations mainly due to fluid content and interconnection.

4.In the backarc mantle, reduced electrical resistivities are observed at depths greater 60 km (‘D’), suggesting a shallow asthenosphere compared to the

North American craton where magnetotelluric data image the lithosphere-asthenosphere boundary at ~200 km (Türkoğlu et al., 2009). Whereas the transition between the backarc and the adjacent North American craton is well defined between the Omineca and Foreland Belts along the ABC-N profile, the ABC-S profile indicates highly resistive mantle rocks extending underneath the Omineca Belt at depths greater than 100 km. The low resistivities in the backarc require either hydrogen diffusion, partial melting of the mantle or a combination thereof, as will be discussed in chapter 4

4 Estimation of water content and melt fraction in the upper mantle beneath the Canadian Cordillera

Electrical resistivity models derived from MT data can be interpreted in terms of the type and amount of fluids required to explain the observed resistivities of the mantle. Soyer & Unsworth (2006) showed that the low resistivities in the mantle beneath the ABC-S profile cannot be explained by dry olivine (Figure 4.1, SO2 model by Constable et al. (1992)). Instead, they can be explained by resistivities by either aqueous fluids dissociated into hydrogen ions with a hydrogen saturation of 50-100% or by less than 4% partial melt (Figure 4.1). As this analysis was limited to the southern part of the ABC-S profile, in section 4.1 it will be extended to include the entire backarc length of both the ABC-N and ABC-S profiles. However, considerable non-uniqueness is associated with this interpretation, as it difficult to distinguish whether the reduced electrical resistivities relative to the dry mantle are due to aqueous fluids, partial melts or a combination thereof.

The goal of this chapter is to attempt to reduce this non-uniqueness. Thermodynamic models can be used to estimate the effect of water on dehydration melting of the nominally anhydrous upper mantle (Hirschmann et al., 2009). This will allow reduction of the non-uniqueness associated with the interpretation of the electrical resistivity models by constraining the regions in which dehydration melting can occur (section 4.2.1). Regions in which dehydration melting cannot occur need to be explained solely by the presence of aqueous fluids, while regions of dehydration melting will require a combination

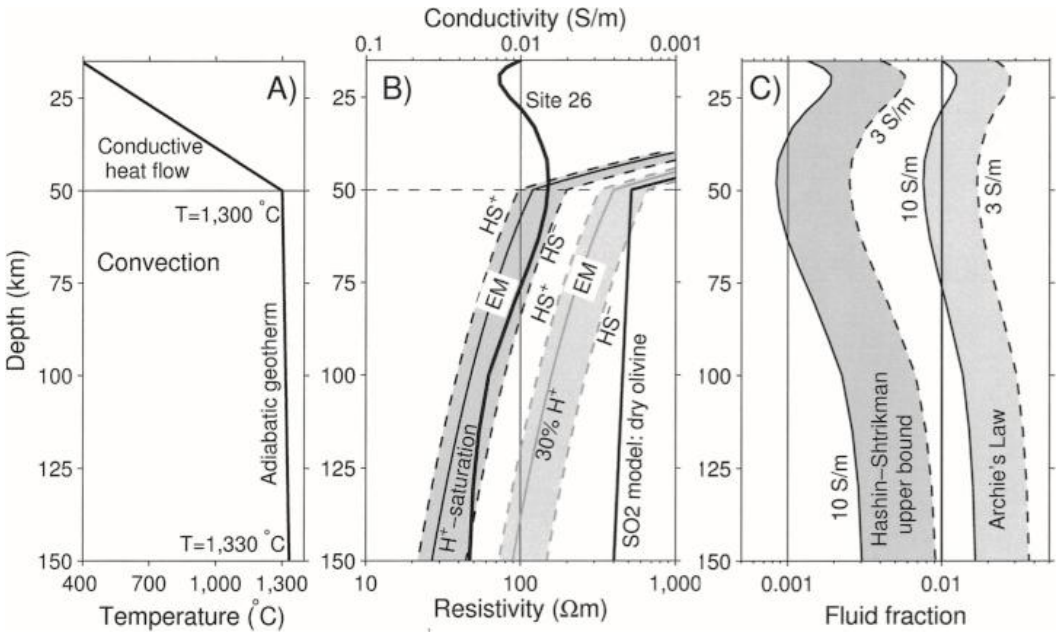

Figure 4.1: Possible explanations of elevated backarc mantle conductivities by either hydrogen diffusion through olivine minerals or by an interconnected conductive fluid phase. (a) Simplified geotherm used to calculate expected conductivities based on H+ diffusion for 100% and 30% hydrogen-saturated olivine, shown in (b), together with modeled conductivities. HS± mark upper and lower Hashin-Shtrikman bounds, used to convert highly anisotropic conductivities of wet olivine to isotropic values. EM—effective media theory (Shankland & Duba, 1990). Also shown is SO_2 model for dry olivine from Constable et al. (1992). (c) Fluid fractions reproducing modeled conductivities, assuming two-phase medium with resistive host (0.001 S/m) and fluid conductivity of 3 and 10 S/m, using upper Hashin-Shtrikman bound for ideal connectivity and Archie's Law with exponent 1.5 for conservative estimate. (reprinted from Soyer & Unsworth 2006)[8]

of aqueous fluids and partial melt (section 4.2.2). A key part in estimating the type and amount of fluids required to explain the observed resistivities is a knowledge of the mantle temperature. In section 4.3 seismic velocities obtained from seismic tomography by Mercier et al. (2009) will be used to estimate the mantle temperatures beneath the Canadian Cordillera.

4.1 Estimation of fluid content without additional constraints

4.1.1 Estimation of water content

The presence of water enhances the electrical conductivity of the mantle through several processes, including (a) diffusion of hydrogen ions (H^+) formed by the dissociation of water molecules (Karato, 1990), (b) by increasing the mobility of existing charge carriers, such as Mg^{2+} and Fe^{2+} (Karato et al., 1986) and (c) by lowering the mantle solidus, causing increased melt fractions (Hirschmann et al., 2009). To constrain the water content in the mantle, it is necessary to estimate the effects of hydrogen diffusion on electrical resistivity. Following the approach of Karato (1990), the results of laboratory measurements on hydrogen diffusivity (Mackwell & Kohlstedt, 1990) and solubility (Lizarralde et al., 1995) in olivine will be used to estimate the amount of hydrogen (and thus water) dissolved in the mantle. The results will be compared to more recent studies on the electrical conductivity of olivine in the presence of water by Wang et al. (2006). As both laboratory studies by Karato (1990) and Wang et al. (2006) were conducted on olivine, the forearc mantle will be excluded from the analysis, as it is expected to be metasomatized and contain significant amounts of serpentine (section 3.2.2). The following analyses will therefore focus on the backarc mantle east of the volcanic arc.

A key part in estimating the water content is a knowledge of temperature as a function of depth. In this section, a simplified geotherm will be used, where temperatures increase from 950°C to 1300°C in the uppermost mantle between 35

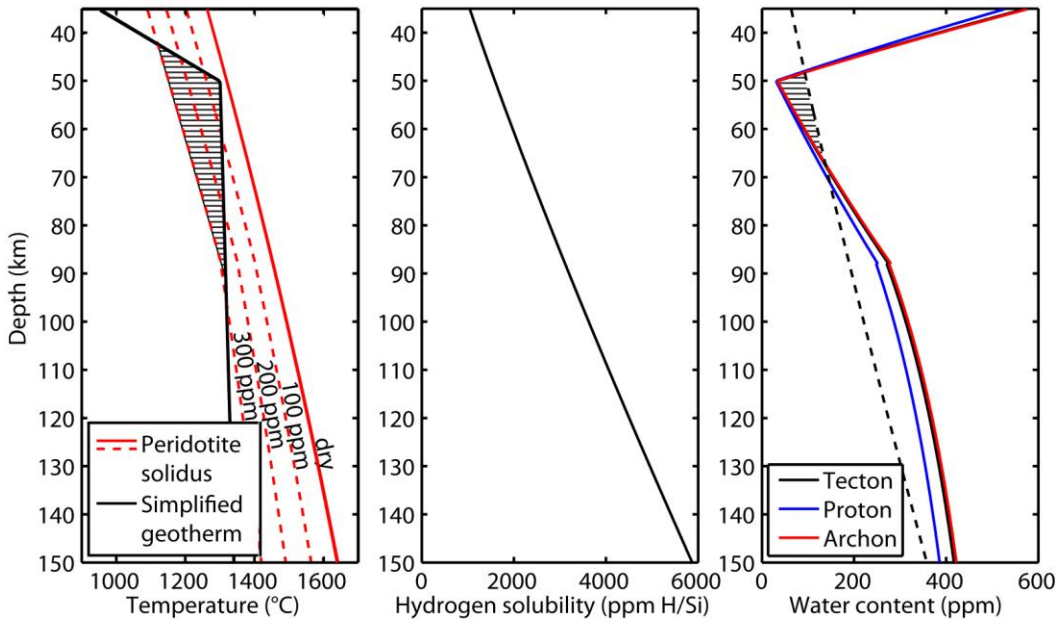

Figure 4.2: (a) Simplified geotherm (Currie & Hyndman, 2006), dry peridotite solidus (Hirschmann et al., 2009) and solidus in the presence of water (Hirschmann et al., 2009) as a function of depth. The shaded area corresponds to conditions under which dehydration melting can occur. (b) Hydrogen solubility as a function of depth. (Lizarralde et al., 1995) (c) Water content required to reduce the dry solidus in (a) to temperatures equal to the simplified geotherm for different mantle compositions. The dashed line corresponds to the water content corresponding to the hydrogen solubility shown in (b). The shaded area corresponds to conditions under which dehydration melting can occur.

km and 50 km, and with a constant adiabatic gradient of 0.4°C/km for depths greater than 50 km (Figure 4.2, Currie & Hyndman, 2006). The methods described in Appendix B.1 can be used to estimate the maximum hydrogen content and saturation required to explain the observed electrical resistivities. Whereas the temperatures in this section are assumed to be laterally uniform, a more realistic temperature model which includes lateral temperature variations will be discussed in section 4.3.

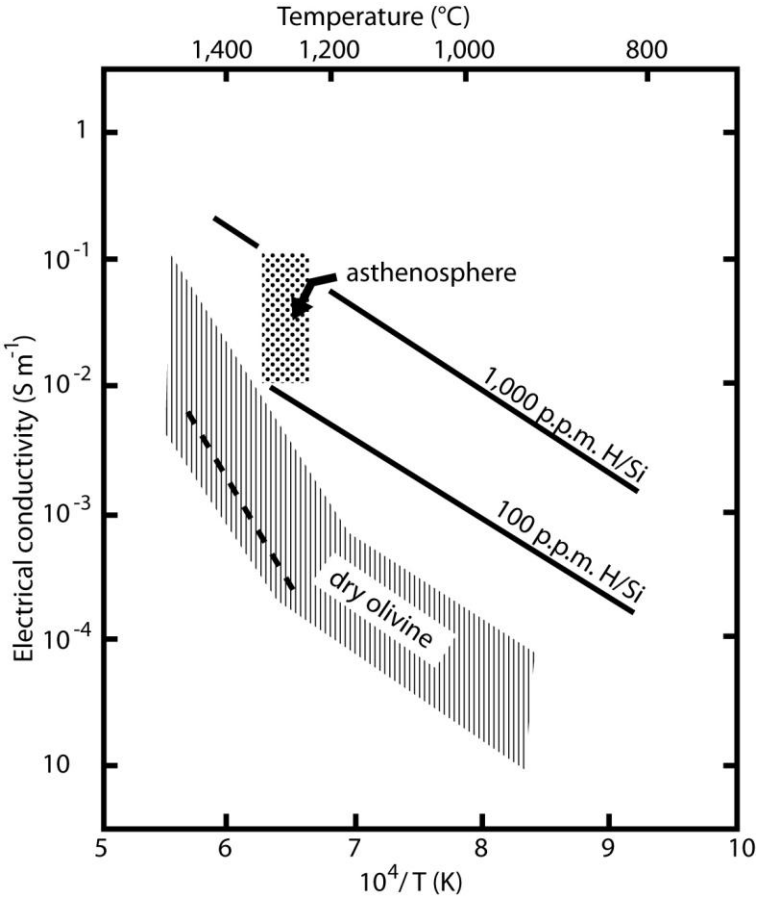

Figure 4.3: Electrical conductivity in olivine as a function of temperature and hydrogen content. Data for dry olivine correspond to hatched region. The dashed line shows the electrical conductivity calculated from the diffusion coefficients of Mg^{2+} (or Fe^{2+}) under dry conditions. Solid lines show the electrical conductivity values calculated from laboratory data on the diffusivity of hydrogen. The dotted region indicates the range of conductivity estimated from geomagnetic soundings and the estimated temperature of the asthenosphere. This region coincides with the estimated conductivity for a hydrogen content of ~200-2000 ppm H/Si. (adapted from Karato, 1990)[9]

4.1.1.1 Water content based on Karato (1990)

Karato (1990) proposed that the electrical conductivity of olivine in the presence of aqueous fluids can be described by the Nernst-Einstein relationship in equation (B.9) (see Appendix B.1.2). Figure 4.3 shows the electrical conductivity along the

most conductive axis of a single olivine crystal for a range of temperatures and hydrogen contents, using laboratory measurements on hydrogen diffusivity by (Mackwell & Kohlstedt, 1990). The electrical conductivities show a strong temperature-dependence due to the temperature effect on hydrogen diffusivity (see the Arrhenius relationship in equations (B.11) to (B.13)), and are several orders of magnitude higher than for dry olivine.

Lizarralde et al. (1995) described how these results can be used to calculate the water content required to explain measurements of electrical resistivity, if an isotropic mantle composition is assumed (see Appendix B.1.2). Following their approach, Figure 4.4 and Figure 4.5 (second panels) show the hydrogen content required to explain the electrical resistivity models of the ABC-N and ABC-S profiles respectively. It can be seen that hydrogen content generally decreases with depth. This can be attributed to an increase in temperature and therefore hydrogen diffusivity, so that less hydrogen is required to explain the observed electrical resistivities.

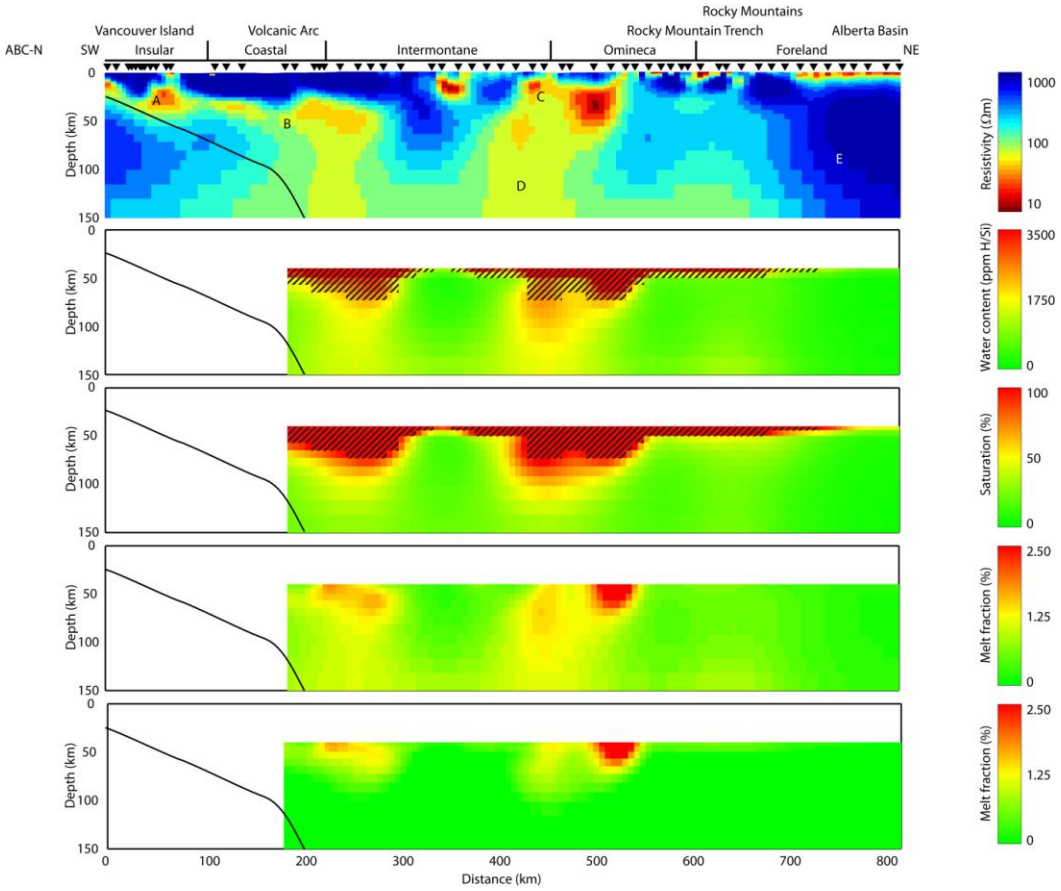

Figure 4.4: Electrical resistivity model (top panel), the inferred hydrogen content (second panel) and hydrogen saturation (third panel) based on Karato (1990), melt fraction in the absence of water (fourth panel) and melt fraction for 100 % water saturation (bottom panel) for the ABC-N profile. The shaded areas correspond to regions where the inferred hydrogen content exceeds the hydrogen solubility limit in olivine.

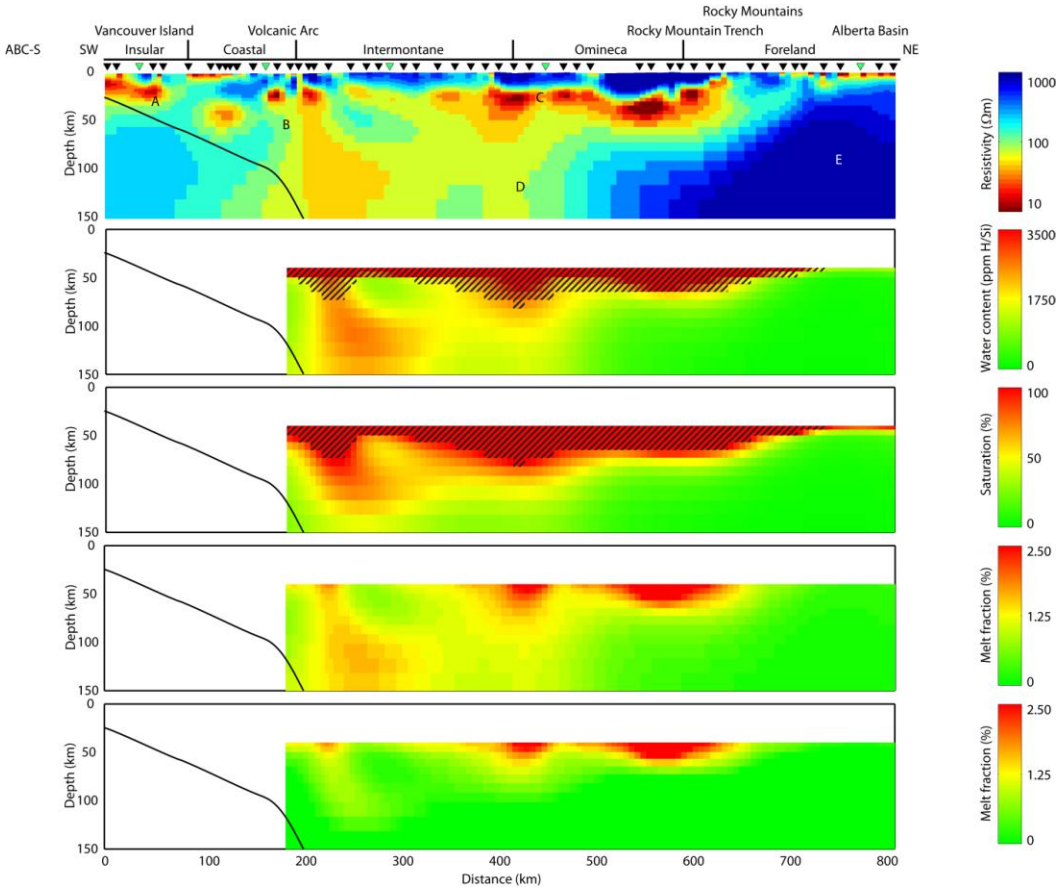

Figure 4.5: Electrical resistivity model (top panel), the inferred hydrogen content (second panel) and hydrogen saturation (third panel) based on Karato (1990), melt fraction in the absence of water (fourth panel) and melt fraction for 100 % water saturation (bottom panel) for the ABC-S profile. The shaded areas correspond to regions where the inferred hydrogen content exceeds the hydrogen solubility limit in olivine.

The highest hydrogen concentrations are required beneath the volcanic arc, as well as beneath the Intermontane and Omineca Belts, where the observed electrical resistivities are the lowest. In these regions, the required hydrogen content exceeds 1750 ppm H/Si (equivalent to a water content of ~0.01 wt-% H_2O, see Appendix B.5 for conversion) for depths less than 75 km. This hydrogen content mostly exceeds the hydrogen solubility limit, which ranges between ~1000-2500 ppm H/Si (~0.005-0.015 wt-% H_2O) for depths between 35 and 75 km (equation (B.10), Figure 4.2). As a result, for regions in which the required hydrogen content exceeds the solubility limit (corresponding to a hydrogen saturation exceeding 100%), an additional conductivity mechanism such as partial melting is required.

For depths greater than 75 km, the required hydrogen content beneath the volcanic arc is ~1500 ppm H/Si (~0.009 wt-% H_2O) for the ABC N profile and ~2000 ppm (~0.012 wt-% H_2O) for the ABC-S profile. Beneath the Intermontane and Omineca Belts the hydrogen content is generally less than 1750 ppm H/Si (~0.01 wt-% H_2O). This hydrogen content is well below the hydrogen solubility limit, which ranges between ~2500-6000 ppm H/Si (~0.015-0.035 wt-% H_2O) for depths between 75 and 150 km (equation (B.10), see Figure 4.2). Therefore, the observed electrical resistivities at these depths can be explained by aqueous fluids only, but additional conductivity mechanisms are not ruled out.

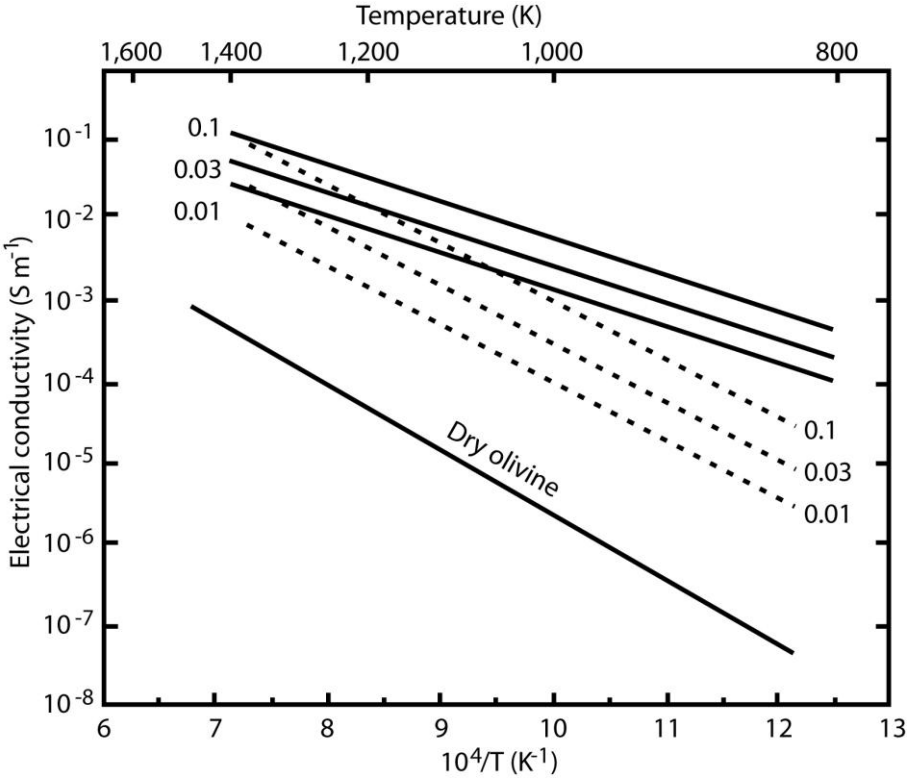

Figure 4.6: A plot of electrical conductivity versus inverse temperature. The numbers next to each line indicate the water content (in wt%). Solid lines with numbers are the results of multilinear regression of laboratory measurements on the electrical conductivity of olivine in the presence of water (Wang et al., 2006). The broken lines show the conductivity values calculated from water diffusion coefficients determined by Kohlstedt & Mackwell (1998) using the model by Karato (1990), and the conductivity for 'dry' olivine. (adapted from Wang et al., 2006)[10]

4.1.1.2 Water content based on Wang et al. (2006)

More recent laboratory measurements by Wang et al. (2006) on San Carlos olivine reported significantly higher conductivities than predicted by Karato (1990) (Figure 4.6). In addition, the measurements indicate a smaller activation enthalpy than for hydrogen diffusion, leading Wang et al. (2006) to the conclusion that a different conductivity mechanism (diffusion of free protons) may contribute to the higher conductivities.

The previous analysis was repeated using the parameters of Wang et al. (2006) (see Appendix B.1.3), and the calculated hydrogen content is shown in Figure 4.7 (middle panel). As before, shallow regions with low temperatures require larger amounts of water than deeper regions with high temperatures. However, the amount of water required to explain the observed electrical resistivities is significantly less than compared to the analysis in the previous section. The hydrogen content required in the upper mantle at depths less than 75 km is of the order of 175 ppm H/Si ($\sim 10^{-3}$ wt-% H_2O), while the amount of water in the backarc mantle below 75 km is generally less than 125 ppm H/Si ($\sim 0.75 \cdot 10^{-3}$ wt-% H_2O). These hydrogen contents are significantly less than the hydrogen solubility limit, so this analysis does not require any additional conductivity mechanisms, such as partial melting.

The large discrepancy between the two analyses can be attributed to the fact that the laboratory measurements of Wang et al. (2006) indicate a different conductivity mechanism than originally proposed by Karato (1990). In addition, the measurements by Wang et al. (2006) were conducted on a single crystal along the axis of highest conductivity. As the hydrogen diffusivity is anisotropic (Mackwell & Kohlstedt, 1990), the required hydrogen content is expected to be higher if an isotropic mantle is assumed. This effect will be further discussed in section 4.5.

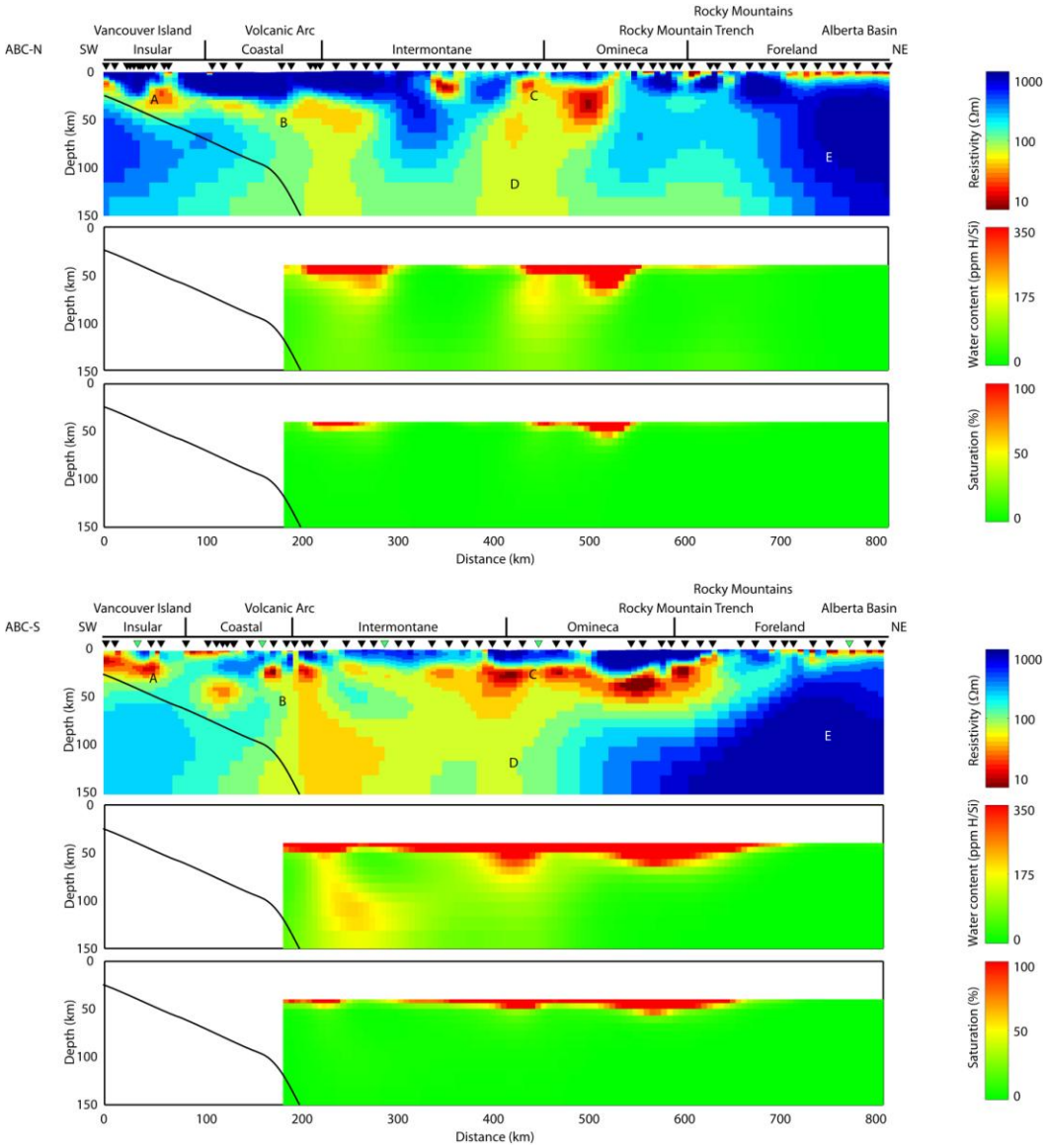

Figure 4.7: Electrical resistivity model (top panel), the inferred hydrogen content (middle panel) and hydrogen saturation (bottom panel) based on Wang et al. (2006), for the (a) ABC-N and (b) ABC-S profiles. No partial melting is required, as the inferred hydrogen content is below the hydrogen solubility limit.

4.1.2 Estimation of melt fraction

An alternative explanation for the observed low resistivities is the presence of melt (Soyer & Unsworth, 2006). Although the assumed simplified geotherm is below the dry mantle solidus (Figure 4.2), the presence of aqueous fluids will decrease the mantle solidus, allowing for dehydration melting of the mantle rocks (Hirschmann et al., 2009). To estimate the melt fraction required to explain the electrical resistivity models, a modification of Archie's Law (Glover et al., 2000) is used, which accounts for the presence of two conducting phases, i.e. in this case the mantle rock matrix and partial melt (see Appendix B.2). The conventional form of Archie's Law (Archie, 1942) cannot be used, as it only accounts for one conducting phase distributed within a non-conductive phase. For the mantle, the assumption of a non-conductive rock matrix is not valid as thermally-activated conduction through the rock matrix is significant.

To estimate the minimum and maximum melt fractions required to explain the MT data, two end-members will be considered: (i) The MT data are explained by a combination of aqueous fluids and partial melt. This case will give the minimum melt fraction required by the data. (ii) The MT data are explained solely by partial melt. This case will give the maximum melt fraction required by the data. The first end-member estimates the minimum melt fraction in the presence of aqueous fluids, assuming a hydrogen saturation of 100% throughout the mantle. In this case, the electrical conductivity of the hydrogen saturated rock matrix (σ_1) can be calculated using the model by Karato (1990) described in Appendix B.1.2. The model by Wang et al. (2006) will not be considered in this analysis, as no

additional conductivity mechanism was required to explain the electrical resistivity models as discussed in section 4.1.1.2. Typical electrical conductivities for melts (σ_2) range from 1 S/m to 10 S/m for temperatures between 1200°C and 1400°C (Tyburczy & Waff, 1983). The degree of interconnection of the melt phase is described by the cementation factor m, with larger values corresponding to a higher degree of interconnection. For this analysis, an electrical conductivity $\sigma_2 = 5$ S/m and a cementation factor $m = 1.3$ for the melt phase are assumed. The value for the cementation factor is based on laboratory studies of the *in situ* melt distribution in olivine rocks at different melt fractions by ten Grotenhuis et al. (2005). The effect of varying electrical conductivity and connectivity of the melt phase will be discussed in section 4.4.

The minimum melt fractions required to explain the electrical resistivity models are shown in Figure 4.4 and Figure 4.5 (bottom panels). As expected, partial melting occurs only in the regions where a hydrogen saturation larger than 100% is required (Figure 4.4 and Figure 4.5, third panels), and is generally limited to depths less than 75 km. Melt fractions are ~1.75%, but locally melt fractions of up to 4% are required to explain the observed resistivities in the Omineca Belt.

The alternate end-member estimates the maximum melt fraction in the absence of aqueous fluids, assuming a dry mantle composition. While this scenario is not realistic as the assumed mantle temperatures are below the dry solidus (Figure 4.2), it provides an upper limit on the required melt fraction. In the absence of aqueous fluids, the electrical conductivity of the mantle rock matrix (σ_1) can be

described by the SEO3 model for dry olivine (Constable, 2006). Using the same values for the electrical conductivity and the cementation factor of the melt phase, the minimum melt fractions required to explain the electrical resistivity models are shown in Figure 4.4 and Figure 4.5 (fourth panels). For depths less than 75 km, the required melt fractions are similar to the hydrated case. At depths larger than 75 km, melt fractions of ~1.25% are required to explain the low resistivities in the backarc mantle.

4.2 Effect of water on the mantle solidus temperature

Thermodynamic models can be used to estimate the effect of water on dehydration melting of the nominally anhydrous upper mantle (Hirschmann et al., 2009) and to constrain the regions in which dehydration melting can occur. For this, the water content required to reduce the mantle solidus temperature below the assumed mantle temperature is calculated (section 4.2.1). By comparing it to the water content required to explain the electrical resistivity models (section 4.1), it is possible to define regions in which the required water content is sufficient to reduce the mantle solidus temperature below the assumed mantle temperature. In this case, dehydration melting of the mantle rocks will occur, and the observed electrical resistivities need to be explained by a combination of water and partial melt (section 4.2.2). The maximum amount of either fluid phase is dependent on the assumed temperature model and can be calculated using a modification of Archie's law for two conducting phases (Glover et al., 2000).

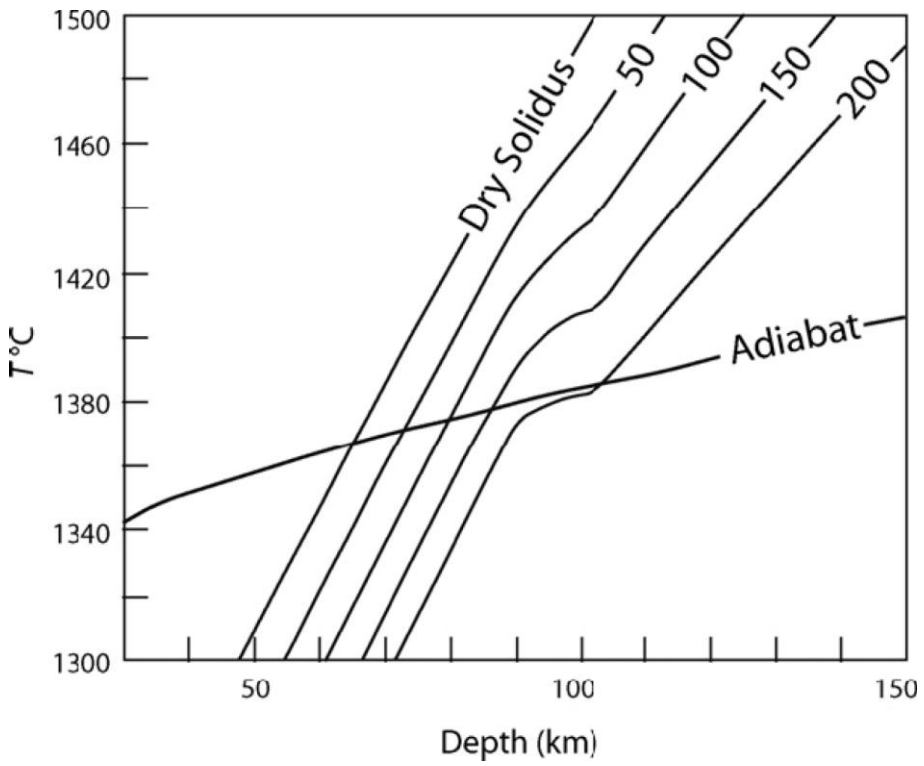

Figure 4.8: Calculated influence of small concentrations of H_2O on the solidus of peridotite at conditions applicable to partial melting beneath oceanic ridges. The mantle adiabat of Stixrude & Lithgow-Bertelloni (2007) intersects the dry solidus of peridotite (Hirschmann, 2000) at 66 km and the solidus of mantle with 50, 100, 150,and 200ppm H_2O at depths of 73, 80, 86, and 104 km, respectively. (reprinted from Hirschmann et al., 2009)[11]

4.2.1 Reduced mantle solidus in the presence of water

Water plays an important role for the rheology of a rock, as it will significantly reduce the melting temperature of the rock. For a given water content, it is possible to calculate the reduced solidus temperature at a given depth (pressure) using cryoscopic calculations (Figure 4.8; Appendix B.4). Similarly, if the temperature at a certain depth is known, the amount of water that is required to reduce the solidus temperature sufficiently to initiate dehydration melting can be

calculated, i.e. the amount of water required to reduce the solidus temperature so that it becomes equal to the actual temperature obtained from geophysical observations, such as surface heat flow or seismic constraints. In this section, the same simplified geotherm derived from surface heat flow and other constraints as in section 4 will be used. As this geotherm is based on an average surface heat flow value, it does not allow delineation of lateral variations in mantle temperature.

To determine the effect of water on dehydration melting of the nominally anhydrous upper mantle, a Tecton (mean spinel peridotite) composition was assumed (Griffin et al., 2003). This composition corresponds to a moderately depleted mantle characteristic for regions for which the last tectonothermal event in the overlying crust occurred since 1.0 Ga (based on the classification of Griffin et al. (2003)). The partition coefficients for the mantle minerals were taken from a compilation by Hirschmann et al. (2009). Figure 4.2 shows the minimum amount of water required to allow for dehydration melting at the temperatures determined from surface heat flow. It can be seen that in the uppermost mantle (35-50 km) the amount of water required for dehydration melting decreases from 550 ppm to 50 ppm, as the temperature at these depths increases from 950°C to 1300°C and approaches the dry peridotite solidus. At 50 km depth, the difference between the geotherm and the dry peridotite solidus is ~60°C. For depths larger than 50 km, the temperature difference between the geotherm and the dry solidus starts to increase, requiring larger amounts of water to allow for dehydration melting (~300 ppm and 400 ppm at 100 km and 150 km depth respectively).

4.2.2 Water content and degree of melting at the reduced mantle solidus

The water contents calculated in section 4.1 that are required to explain the electrical resistivity models in the absence of dehydration melting may not necessarily reflect the actual hydration state of the mantle. If the water content is high enough, it will cause a sufficient reduction of the mantle solidus to allow dehydration melting of the mantle rocks. By comparing the water content required to explain the electrical resistivity models (section 4.1) with the minimum water content required to allow dehydration melting at the temperatures determined from surface heatflow (section 4.2.1), it is possible to define the regions where dehydration melting occurs.

If the water content required to explain the electrical resistivity models is not sufficient to lower the mantle solidus to the temperatures given by the simplified geotherm, no dehydration melting occurs. In this case, electrical resistivities can be solely explained by hydrogen diffusion, and the water content is given by the calculations in section 4.1. If the water content exceeds the amount of water required to lower the reduced mantle solidus to the inferred temperatures, dehydration melting of the mantle rocks will occur. In this case, explaining the observed electrical resistivities requires a combination of hydrogen diffusion and partial melt.

Using a modification of Archie's law for two conducting phases (see Appendix B.2), it is possible to calculate the maximum degree of partial melting required by

the electrical resistivity data. For partial melting of a peridotite mantle in the presence of water, the two conducting phases correspond to the wet peridotite mantle, whose electrical conductivity σ_1 can be approximated by hydrogen diffusion in olivine (Appendix B.1), and melt with an electrical conductivity σ_2 and a melt fraction χ_2. The same values for the electrical conductivity and the cementation factor as in section 4.1.2 will be used (i.e. $\sigma_2 = 5$ S/m and $m = 1.3$).

As the degree of melting as a function of excess water content is unknown, the hydration state and degree of melting range between two end-members: (i) The electrical resistivity is explained solely by water and no partial melt. This case gives the maximum amount of water required by the electrical resistivity model, as discussed in section 4.1. (ii) The electrical resistivity is explained by a combination of water and partial melt, where the amount of water is equal to the minimum amount of water required to allow dehydration melting, as discussed in section 4.2.1. In this case, the degree of melting required to explain the data is the maximum amount of melt which is still in agreement with the electrical resistivity model. The actual water content and melt fraction are expected to be somewhere between the two end-member models discussed above.

4.2.2.1 Water content and melt fraction based on Karato (1990)

Figure 4.9 shows the minimum water content (middle panel) as well as the maximum melt fraction (bottom panel) for the regions where a sufficient amount of water is present to allow dehydration melting of the mantle rocks, based on the

model by Karato (1990) (Appendix B.1.2) and the simplified geotherm. For both the ABC-N and ABC-S profiles, the electrical resistivity models require ~250 ppm water in the uppermost mantle (35-50 km), where temperatures are the coldest. Additional water is required beneath the volcanic arc above the subducting Juan de Fuca plate. Between 50 km and 75 km depth, minimum water contents of up to 100 ppm are required in combination with partial melting of 1-2.5% in this region. Below 75 km depth, water contents of 100-150 ppm are required, which is not sufficient to allow dehydration melting in this region. Therefore, the presence of partial melt at these depths can be excluded.

4.2.2.2 Water content and melt fraction based on Wang et al. (2006)

In contrast to the model by Karato (1990), the minimum water content required to explain the electrical resistivity models based on the model by Wang et al. (2006) (Appendix B.1.3) is below the amount of water required to allow dehydration melting. As a result, the electrical resistivity models can be solely explained by hydrogen diffusion and generally do not require partial melt (Figure 4.10). Localized dehydration melting might occur at ~50 km depth beneath the Omineca Belt, but cannot be properly resolved by the electrical resistivity models. The reason for this is that the thickness of a low resistivity layer is not well constrained, so that the low resistivities below the Omineca Belt might be limited to the lower crust and not extend into the upper mantle.

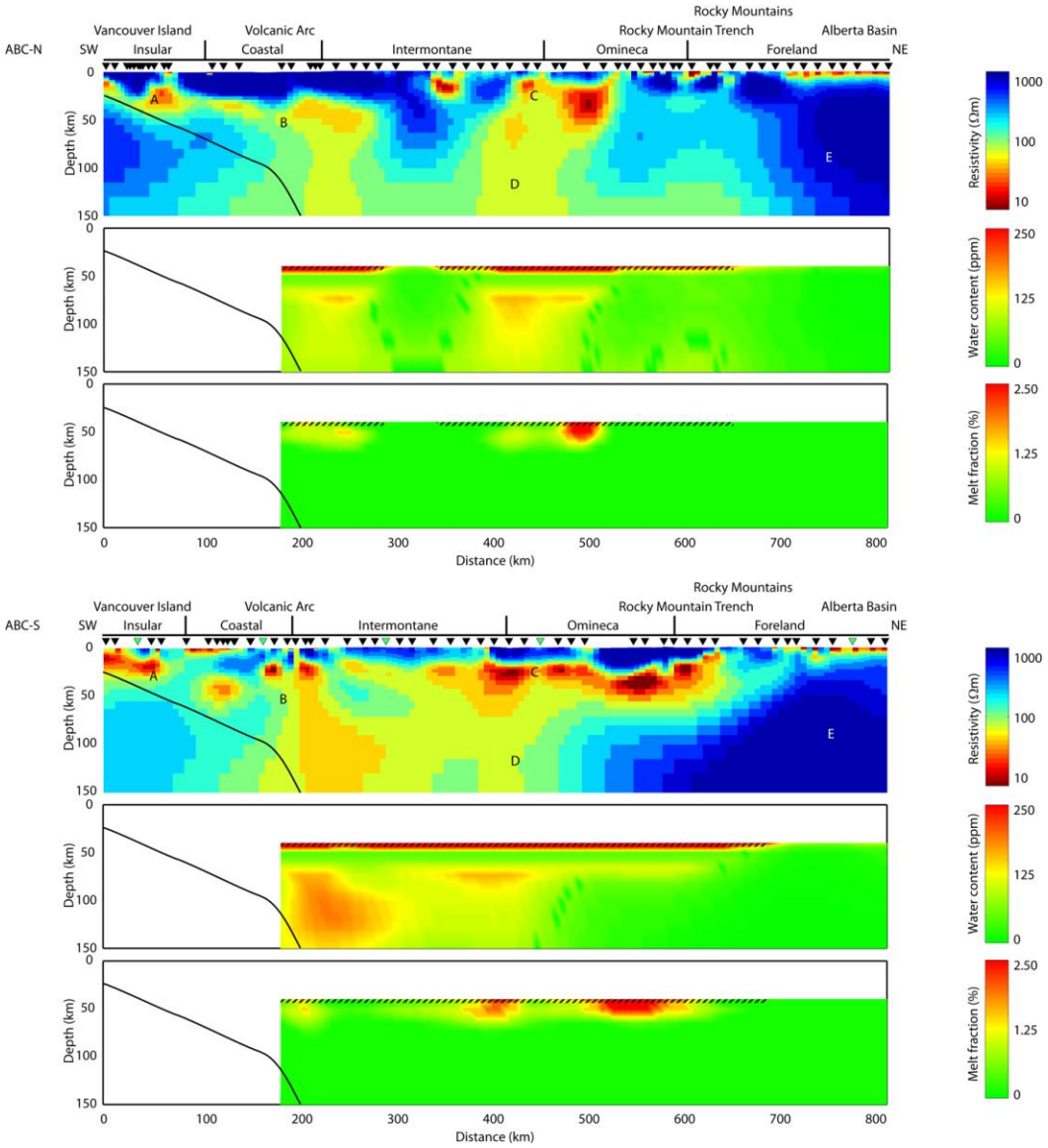

Figure 4.9: Electrical resistivity model (top panel), the inferred water content (middle panel) and melt fraction (bottom panel) required by the MT data based on Karato (1990) using a simplified geotherm for the (a) ABC-N and (b) ABC-S profiles.

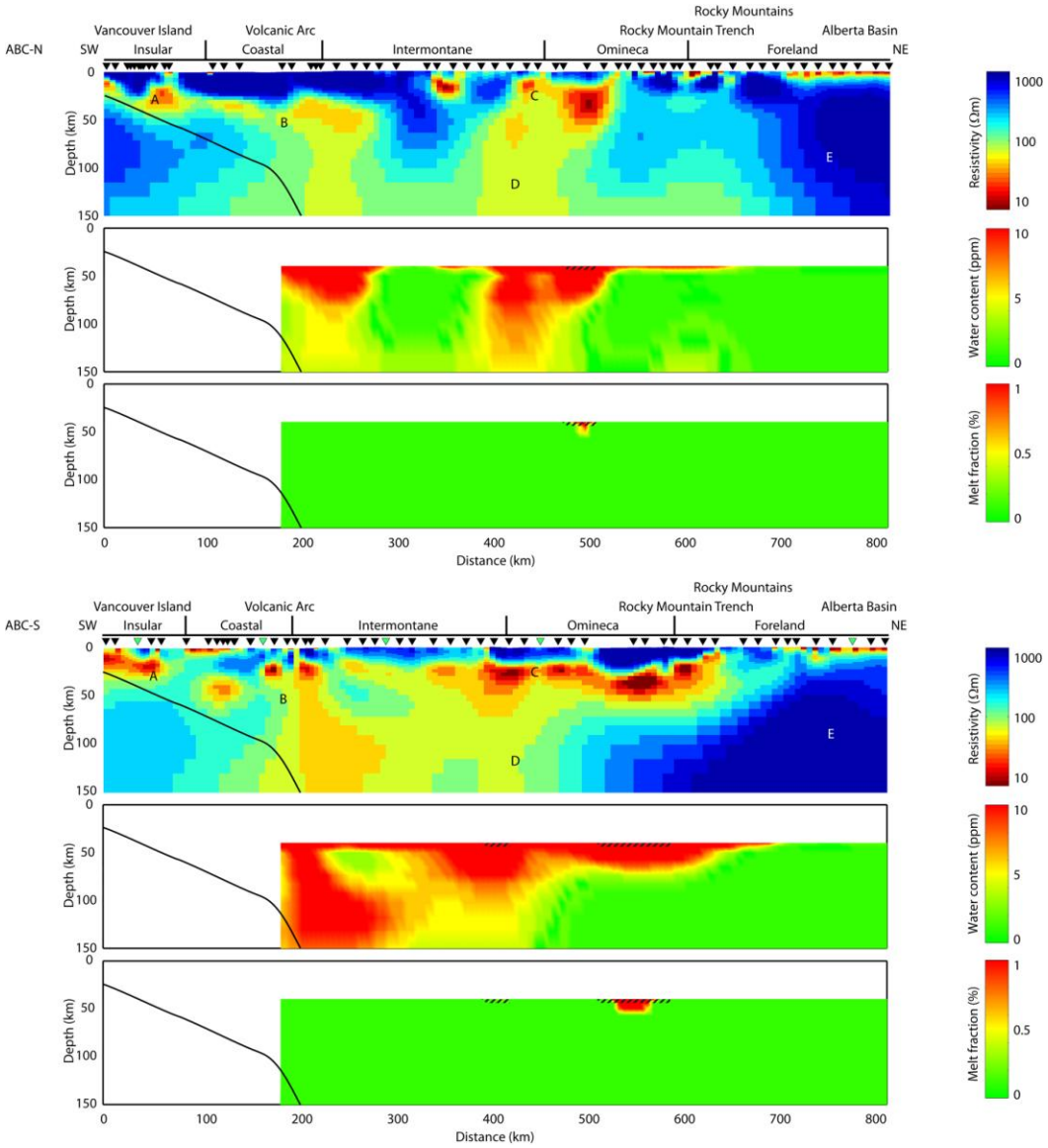

Figure 4.10: Electrical resistivity model (top panel), the inferred water content (middle panel) and melt fraction (bottom panel) required by the MT data based on Wang et al. (2006) using a simplified geotherm for the (a) ABC-N and (b) ABC-S profiles.

For both analyses in section 4.2.2.1 and 4.2.2.2, the required minimum water content is below the solubility limit of water in olivine (equation (B.10)), so that no additional free aqueous fluid phase is required.

4.3 Joint analysis of magnetotelluric and seismic data

In the previous section it was shown how reduction of mantle solidus temperature by the presence of aqueous fluids can be used to delineate possible regions of mantle melting. For this analysis, the temperature regime in the study area needs to be known. As a first approximation, a simplified geotherm based on surface heat flow data was used in the previous section. However, the simplified geotherm did not provide information on lateral temperature variations as it was calculated from the average surface heat flow and other constraints in the study area.

Seismic velocity is also sensitive to the fluid content as well as the temperature of the crust and upper mantle. In this section, it will be shown how seismic velocity data can be used to constrain lateral temperature variations beneath the Canadian Cordillera (section 4.3.1). Based on the obtained temperature model, the electrical resistivity model will then be used to estimate the water content required to explain the observed resistivities (section 4.3.2). In addition, the water content required to reduce the mantle solidus temperature below the assumed mantle temperature is calculated (section 4.3.3). By comparing it to the water content required to explain the electrical resistivity models, it is possible to define regions

in which dehydration melting of the mantle rocks will occur. In these regions, the observed electrical resistivities need to be explained by a combination of water and partial melt (section 4.3.4). The maximum amount of either fluid phase is dependent on the thermal regime calculated from the seismic velocity models (section 4.3.1).

4.3.1 Temperature constraints derived from seismic velocity models

Temperature is one of the key parameters in understanding the rheology of the backarc mantle in the Canadian Cordillera. Although direct temperature measurements are not available, there are several geophysical and geological techniques that can be used to infer the thermal regime of the backarc mantle. These include extrapolation of surface heat flow measurements to depth and mantle xenolith thermobarometry (section 3.2.3). However, both of these techniques have disadvantages. Significant uncertainties are associated with the extrapolation of surface heat flow measurements to depth due to poorly constrained thermal properties, while mantle xenolith thermobarometry is not very effective delineating lateral temperature variations. In addition, both methods do not measure the in-situ temperature but temperatures representative for a time in the past. An alternative approach to constrain the in-situ present-day temperature of the mantle is to use seismic velocities obtained, for example, from seismic tomography (e.g. Goes et al. 2000).

In the last decade, laboratory measurements have provided a way to constrain the parameters that determine seismic velocities at mantle depths. Of particular importance are the bulk and shear moduli, as well as the density of the rock as a function of temperature, pressure and composition. Based on these laboratory results, Goes et al. (2000) derived temperatures of the shallow mantle under Europe from seismic tomography, taking into account anharmonic effects (i.e. elastic effects, that are associated with no energy loss) and anelastic effects (i.e. dissipative effects, that associated with energy loss) on seismic velocity (Appendix B.3). Hyndman et al. (2009) applied the same method to S wave tomography data of Western North America by van der Lee & Frederiksen (2005).

Figure 4.11 and Figure 4.12 (second panels) show the P-wave velocity perturbation with reference to the global traveltime table IASP 91 (Kennett & Engdahl, 1991), which were derived from absolute P-wave velocities obtained from body-wave tomography (Mercier et al., 2009). The tomography model indicates a zone of high P-wave velocity beneath the Insular and Coastal Belt (1-2% for the ABC-N profile, 2-3% for the ABC-S profile), most likely associated with the cold, subducting Juan de Fuca plate. Beneath the Intermontane and Omineca Belts, the data show a low velocity zone (1-2% for the ABC-N profile, 0-1% for the ABC-S profile), suggesting elevated mantle temperatures in this region. To the west, the tomography model shows high P-wave velocity beneath the Foreland Belt (0-1% for the ABC-N profile, 1-3% for the ABC-S profile), associated with the cold lithosphere of the North American Craton.

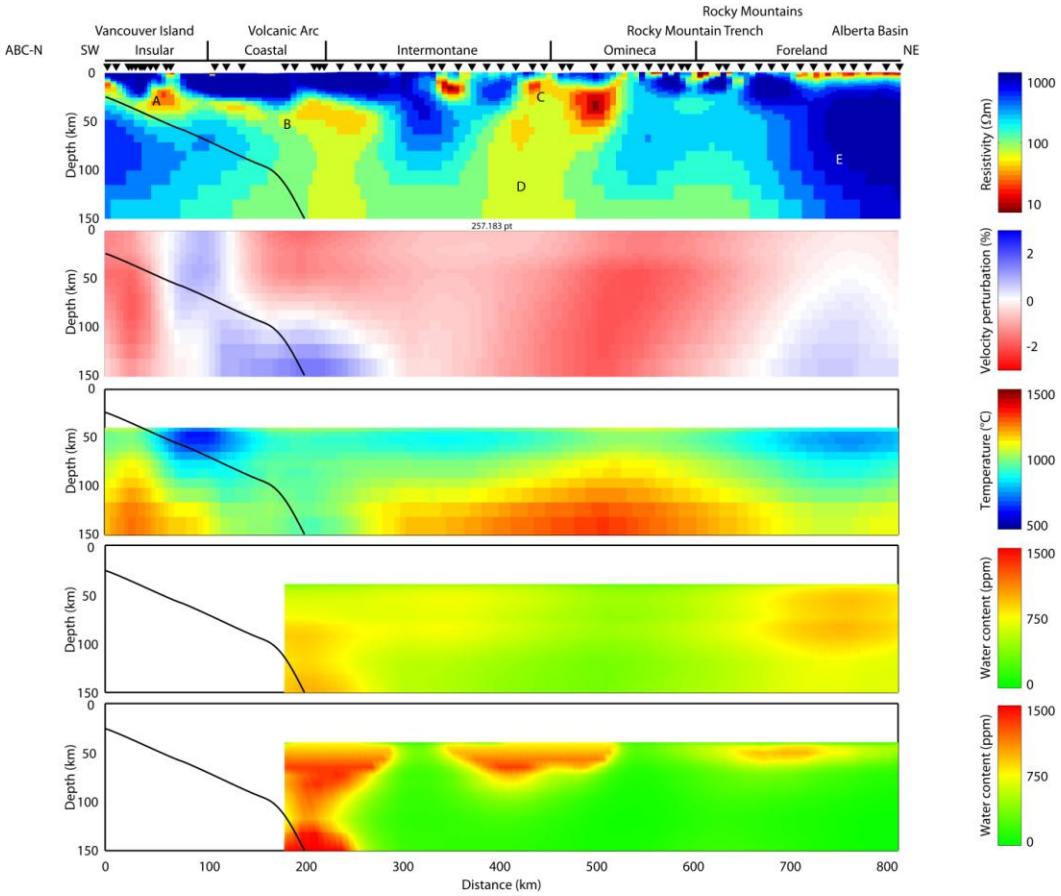

Figure 4.11: Electrical resistivity model (top panel), seismic P-wave velocity (second panel), temperature inferred from the seismic P-wave velocity (third panel), the water content at the mantle solidus calculated from the temperature model (fourth panel) and the water content required by the MT data based on Karato (1990) (bottom panel) for the ABC-N profile assuming no melt is present.

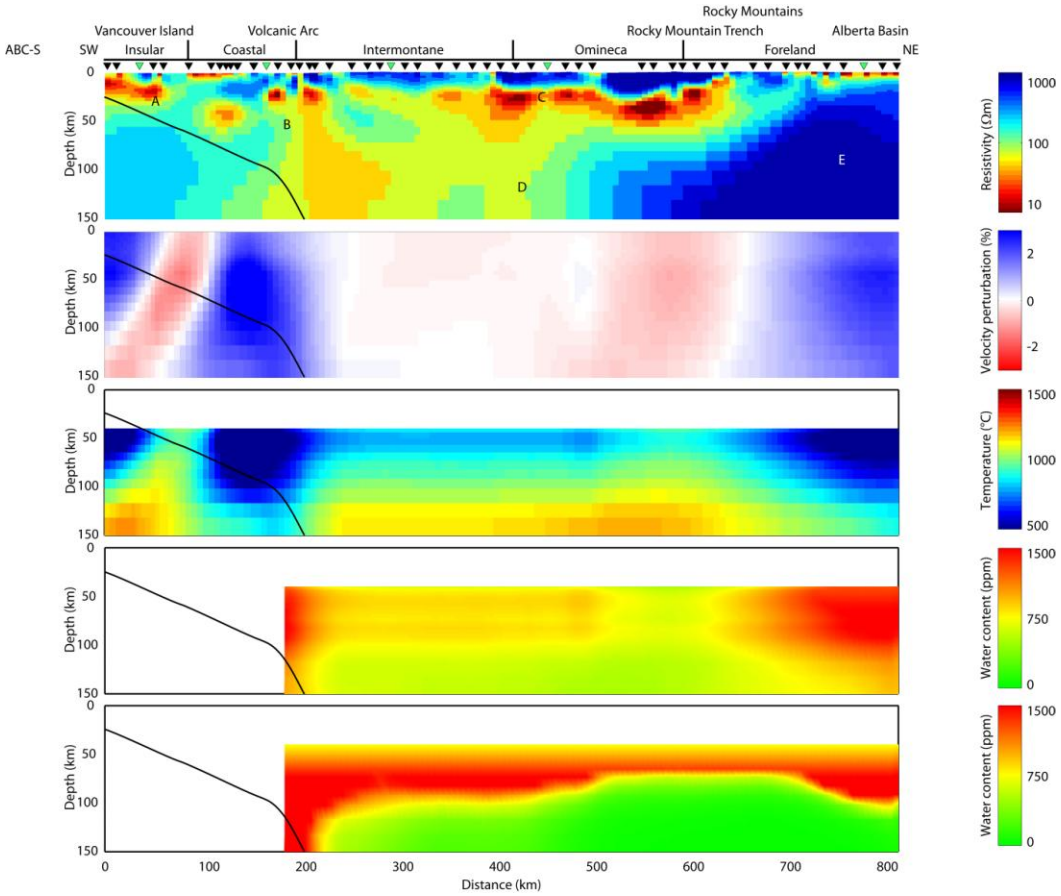

Figure 4.12: Electrical resistivity model (top panel), seismic P-wave velocity (second panel), temperature inferred from the seismic P-wave velocity (third panel), the water content at the mantle solidus calculated from the temperature model (fourth panel) and the water content required by the MT data based on Karato (1990) (bottom panel) for ABC-S profile assuming no melt is present.

The seismic tomography data were used to derive the mantle temperature of the Canadian Cordillera (see Appendix B.3), assuming a Tecton (mean spinel peridotite) composition (Griffin et al., 2003). Based on a similar analysis of S-wave tomography data of the Canadian Cordillera (van der Lee & Frederiksen, 2005), Hyndman et al. (2009) concluded that this composition yielded temperature estimates for the volcanic arc and backarc that are most consistent with independent temperature constraints for these regions. For the stable North American continent (east of the Rocky Mountain Trench), a Proterozoic mantle composition (after Griffin et al., 2003) resulted in slightly higher temperature estimates and provided the best agreement with independent temperature constraints. Therefore, by using a mean spinel peridotite composition for the entire model region, we underestimate the mantle temperature beneath the North American craton by 20°C-30°C. The anelasticity parameters were taken from Shapiro & Ritzwoller (2004), who modified the anelasticity model by Sobolev et al. (1996) by re-calibrating it against a global seismic velocity model. The anelasticity model was calculated for a frequency of 0.5 Hz, which is the lower bound of the frequency band used for the seismic tomography (Mercier et al., 2009).

Figure 4.11 and Figure 4.12 (third panels) show the obtained temperature model for the mantle of the Canadian Cordillera. The model for the ABC-N profile shows reduced temperatures beneath the Insular and Coastal Belts compared to the backarc mantle, associated with the cold, subducting Juan de Fuca plate. Temperatures in this region increase from ~700°C at 50 km depth to 900°C at 150

km depth. Beneath the Intermontane and Omineca Belts, the model indicates unusually high mantle temperatures ranging from 800°C-1000°C beneath the Moho at ~35 km depth to 1200°C-1300°C at 100-150 km depth. These temperatures are in good agreement with the backarc geotherm derived from surface heat flow data (Figure 4.2a; Currie & Hyndman, 2006). Further east beneath the Foreland Belt, the model shows lower temperatures compared to the backarc mantle, associated with the cold lithosphere of the North American Craton. Temperatures in this region vary from 800°C at 50 km depth to 1100°C at 150 km depth.

The temperature model for the ABC-S profile generally shows the same characteristics. However, temperatures are ~200°C lower compared to the ABC-N profile and therefore lower than temperature estimates from other geophysical observations.

Both the estimates on the anharmonic and anelastic effects are based on a dry composition in the absence of fluids and/or melt. Therefore, the temperature estimates derived from the seismic velocity models are expected to be too high, as the mantle in the Canadian Cordillera is inferred to contain water, based on the observed low electrical resistivities and the prograde metamorphism in the subducting slab associated with dehydration. In addition, there is significant uncertainty in the anelasticity model, which particularly affects regions of low seismic velocities. The anelasticity model used in this chapter is one of the more conservative models, and as a result might underestimate the mantle temperature.

If the effect of anelasticity was smaller (i.e. the temperature was higher), smaller amounts of water would be required to trigger dehydrous melting and to explain the observed electrical resistivities. The effect of alternative anelasticity models (Sobolev et al., 1996; Berckhemer et al., 1982) will be further discussed in section 4.4.

4.3.2 Water content in the absence of dehydration melting derived from electrical resistivity models

Using the temperatures derived from the seismic velocity models (section 4.3.1), the same analyses as presented in section 4.1.1 will be used to estimate the water content required to explain the observed electrical resistivities in the absence of dehydration melting. As before, the obtained water content might not necessarily reflect the actual hydration state of the mantle. Instead, if the water content is high enough, it will cause a sufficient reduction of the mantle solidus to allow for dehydration melting. In this case, the observed electrical resistivities need to be explained by a combination of hydrogen diffusion and partial melt, as will be discussed in section 4.3.4.

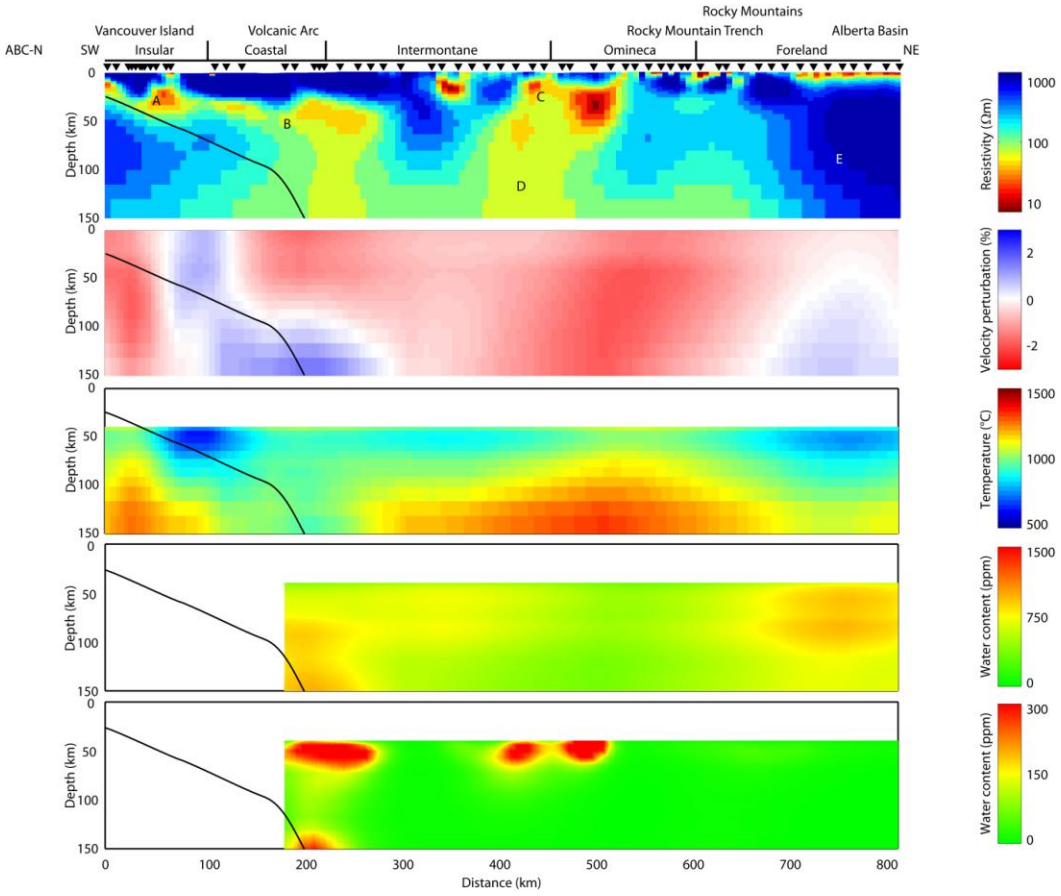

Figure 4.13: Electrical resistivity model (top panel), seismic P-wave velocity (second panel), temperature inferred from the seismic P-wave velocity (third panel), the water content at the mantle solidus calculated from the temperature model (fourth panel) and the water content required by the MT data based on Wang et al. (2006) (bottom panel) for the ABC-N profile assuming no melt is present.

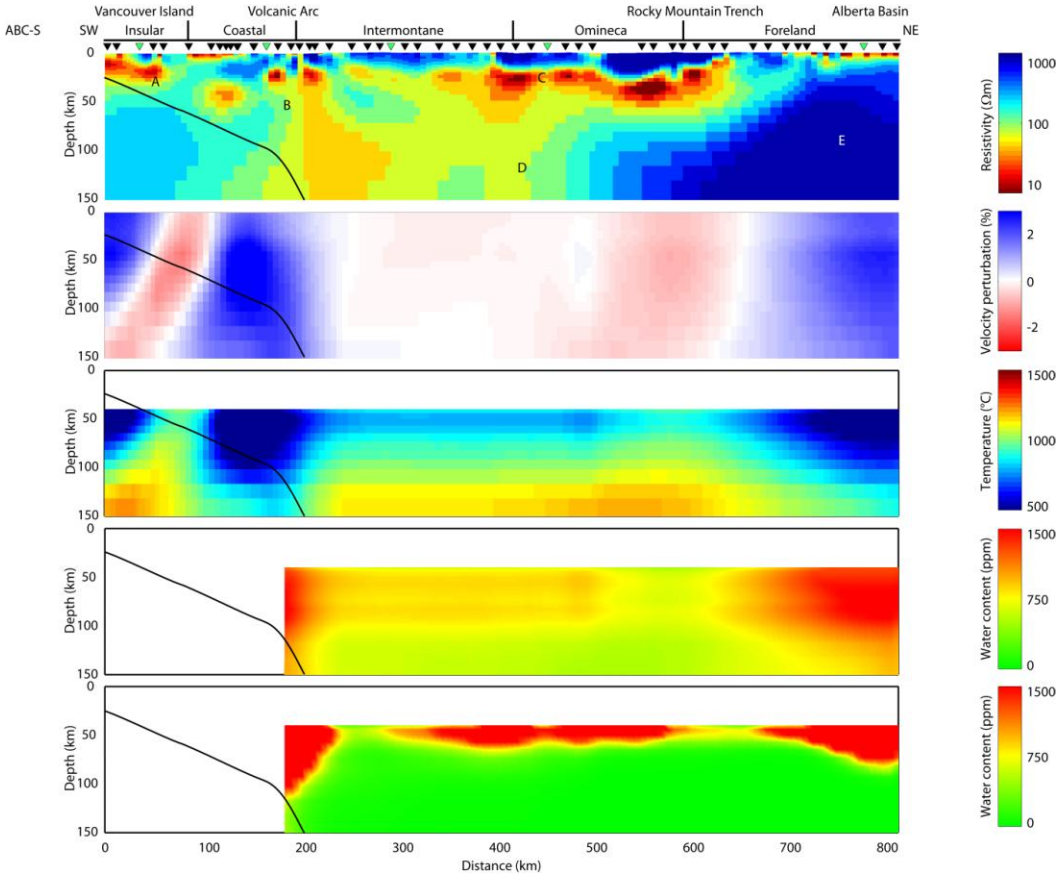

Figure 4.14: Electrical resistivity model (top panel), seismic P-wave velocity (second panel), temperature inferred from the seismic P-wave velocity (third panel), the water content at the mantle solidus calculated from the temperature model (fourth panel) and the water content required by the MT data based on Wang et al. (2006) (bottom panel) for the ABC-S profile assuming no melt is present.

4.3.2.1 Water content based on Karato (1990)

Figure 4.11 and Figure 4.12 (bottom panels) show the amount of water required to explain the electrical resistivity models in the absence of melt based on Karato (1990). As the electrical resistivity mainly depends on temperature and the amount of conductive fluid phases, regions with low temperatures require greater amounts of water than regions with high temperatures to explain low electrical resistivities. Therefore, the largest amounts of fluids are required beneath the volcanic arc as well as in the upper mantle of the backarc at depths less than 100 km. For the ABC-N profile, the required water content in these regions is generally between 750-1250 ppm. Below 100 km, the amount of water required to explain the low resistivities of the backarc mantle is generally less than 250 ppm due to the high temperatures at these depths. For the ABC-S profile, significantly higher amounts of water are required due to the colder temperature model. The water content exceeds 750 ppm for depths less than 100 km, and even below 100 km a water content of ~500 ppm is required.

4.3.2.2 Water content based on Wang et al. (2006)

The previous analysis was repeated using the results by Wang et al. (2006), with the required water content in the absence of melt being shown in Figure 4.13 and Figure 4.14 (bottom panels). As in section 4.1 the required water content based on Wang et al. (2006) is significantly lower than the water content based on Karato

(1990). The largest amounts of fluids are again required beneath the volcanic arc as well as at shallow mantle depths (less than 75 km) of the backarc. For the ABC-N profile, the water content beneath the volcanic arc is ~300 ppm for depths less than 75 km, decreasing to less than 150 ppm with depth. Less than 100 ppm of water is required in the backarc mantle, except for a small region beneath the western Omineca Belt, where the required water content is ~250 ppm for depths less than 75 km. As before, significantly larger water contents are required for the ABC-S profile, for which the required water content exceeds 1500 ppm beneath the volcanic arc and in the shallow backarc mantle. At depths larger than 75 km, less than 500 ppm of water is required in the backarc.

4.3.3 Reduced mantle solidus in the presence of water

Following the same approach as in section 4.2.1, the water content required to reduce the mantle solidus temperature below the temperatures derived from the seismic velocity models (section 4.3.1) is calculated. For this, the same Tecton (mean spinel peridotite) composition as well as the same partition coefficients for the mantle minerals as in section 4.2.1 were used.

Figure 4.11 and Figure 4.12 (fourth panels) show the minimum amount of water required to allow for dehydration melting. It can be seen that regions with reduced temperatures, i.e. beneath the Foreland Belt, require a higher water content to allow for dehydration melting (~1000 ppm for the ABC-N profile, up to 1500 ppm for the ABC-S profile). Beneath the Intermontane and Omineca Belts, the

required water content decreases with depth. At 50 km depth the required amount of water required ranges between 500 ppm and 750 ppm for the ABC-N and ABC-S profiles respectively. Generally only small amounts of water are required below 100 km due to the high temperatures. At these depths the required water content is less than 250 ppm for the ABC-N profile and less than 500 ppm for the ABC-S profile.

4.3.4 Water content and degree of melting at the reduced mantle solidus

Beneath the volcanic arc as well as the shallow mantle of the backarc, the water content required to explain the observed electrical resistivities exceeds the amount of water required for dehydration melting. Therefore, an additional melt phase is required to explain the electrical resistivities in these regions. As in section 4.2.2, a modification of Archie's Law for two conducting phases (see Appendix B.2) will be used to calculate the maximum degree of dehydration melting.

4.3.4.1 Water content and melt fraction based on Karato (1990)

Figure 4.15 shows the minimum water content (middle panel) as well as the maximum melt fraction (bottom panel) for the regions where a sufficient amount of water is present to allow for dehydration melting of the mantle rocks, based on the model by Karato (1990). For both the ABC-N and ABC-S profiles, the electrical resistivity models require water beneath the volcanic arc, with the minimum water content ranging from 750-1250 ppm for the ABC-N profile and

1000-1500 ppm for the ABC-S profile. Additional water is required at shallow mantle depths less than 100 km beneath the Intermontane and Omineca Belts, with water content ranging from 500-750 ppm for the ABC-N profile and 750-1000 ppm for the ABC-S profile. For depths larger than 100 km, the required water content is generally less than 500 ppm.

Beneath the volcanic arc and in the shallow mantle of the backarc, the electrical resistivity models require partial melt as an additional conductivity mechanism. Beneath the volcanic arc, melt fractions of 0.5-1.5% for the ABC-N profile and 1-2% for the ABC-S profile are required in addition to the amount of water discussed above. Partial melts are also required at depths less than 100 km beneath the Intermontane Belts, typically ranging between 0.5 and 1.5% for the ABC-N profile and between 1.5 and 2.5% for the ABC-S profile, but locally exceeding 2.5% beneath the Omineca Belt.

For both the ABC-N and ABC-S profiles, the required water content exceeds the solubility limit of water in olivine (equation (B.10)) beneath the volcanic arc as well as for depths less than 75-100 km in the backarc. Therefore, an additional free aqueous fluid phase might be present in these regions. To include this fluid phase in future analyses, a generalization of Archie's law for multiple conducting phases (Glover, 2010) instead of the modification for two conducting phases (Glover et al., 2000) could be used.

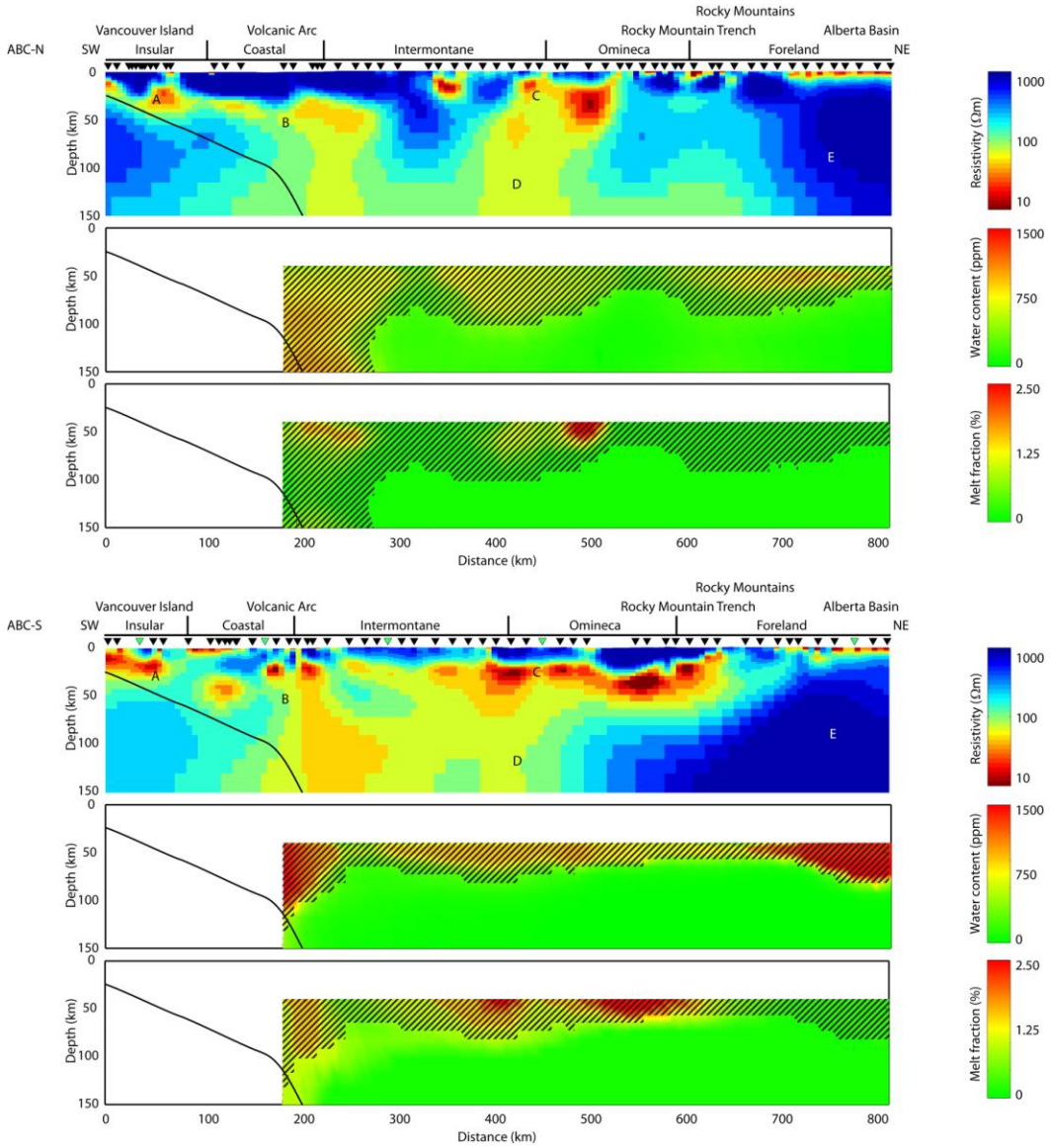

Figure 4.15: Electrical resistivity model (top panel), the inferred water content (middle panel) and melt fraction (bottom panel) required by the MT data based on Karato (1990) using temperatures inferred from seismic P-wave velocities for the (a) ABC-N and (b) ABC-S profiles. The shaded areas correspond to regions where the inferred hydrogen content exceeds the hydrogen solubility limit in olivine.

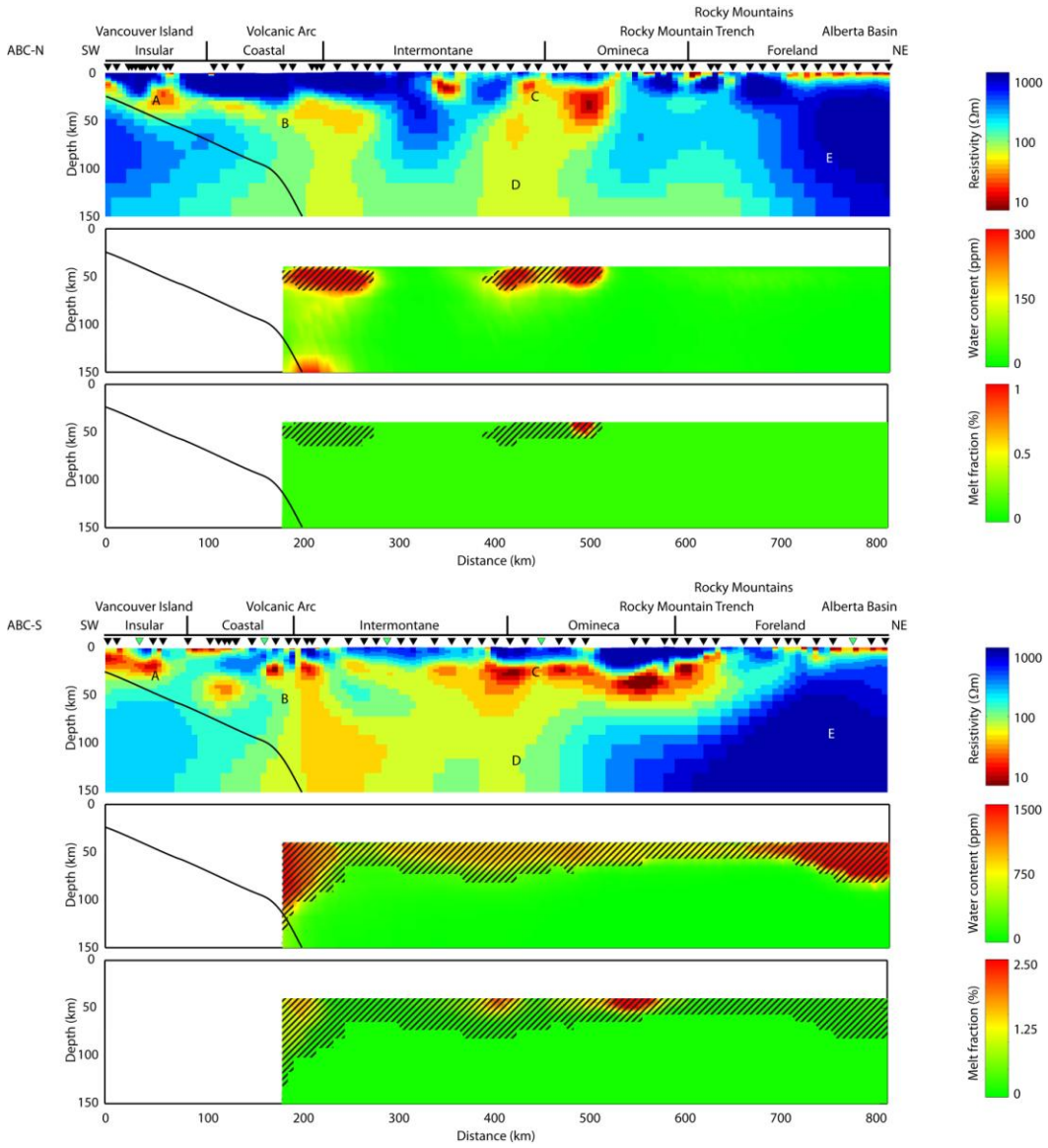

Figure 4.16: Electrical resistivity model (top panel), the inferred water content (middle panel) and melt fraction (bottom panel) required by the MT data based on Wang et al. (2006) using temperatures inferred from seismic P-wave velocities for the (a) ABC-N and (b) ABC-S profiles. The shaded areas correspond to regions where the inferred hydrogen content exceeds the hydrogen solubility limit in olivine.

4.3.4.2 Water content and melt fraction based on Wang et al. (2006)

Figure 4.16 shows the minimum water content (middle panel) as well as the maximum melt fraction (bottom panel) based on the model by Wang et al. (2006). For the ABC-N profile the minimum water content required to explain the electrical resistivity models is generally below the amount of water required to allow dehydration melting. As a result, the electrical resistivity models can generally be explained by hydrogen diffusion and do not require partial melt. An exception is beneath the Omineca Belt, where dehydration melting might occur at ~50 km depth. However, this localized zone of melting cannot be properly resolved by the electrical resistivity model.

For the ABC-S profile, the electrical resistivity model requires ~1500 ppm water in combination with 1-1.5% melt beneath the volcanic arc at depths less than 100 km. Beneath the Intermontane and Omineca Belts, ~1000 ppm of water in combination with 1-2% melt are required at depths less than 75 km. Below 75 km depth, less than 500 ppm of water are required, which is not sufficient to allow for dehydration melting in this region. Therefore, the presence of partial melt at these depths can be excluded on the basis of the analysis presented here.

For the ABC-N profile, the required water content exceeds the solubility limit of water in olivine (equation (B.10)) for depths less than 60 km beneath the volcanic arc, as well as locally beneath the Intermontane and Omineca Belts at depths less than 75 km. In contrast, for the ABC-S profile the required water content exceeds the solubility limit for depths less than 100 km beneath the volcanic arc as well as

for depths less than 75-100 km in the backarc. As before, an additional free aqueous fluid phase might be present in these regions. This fluid phase could be included in future analyses using a generalization of Archie's law for multiple conducting phases (Glover, 2010) instead of the modification for two conducting phases.

4.4 Discussion

The results presented in the previous chapters show how magnetotelluric and seismic data in combination with thermodynamic calculations on the reduction of the mantle solidus temperature in the presence of water can be used to constrain the thermal regime as well as the fluid content of the mantle in the Canadian Cordillera. It is important to note the assumptions that have been made during these calculations. These include:

1. In this analysis a Tecton (mean spinel peridotite) composition (Griffin et al., 2003) was used, which corresponds to a moderately depleted mantle composition for regions for which the last tectonothermal event in the overlying crust occurred since 1.0 Ga (based on the classification of Griffin et al. (2003)). In the following, the effect of more depleted compositions will be discussed, using a Proton and Archon composition (Griffin et al., 2003). These compositions are highly depleted in basaltic components (i.e. Ca, Al, Fe, etc.) compared to a primitive mantle composition, and are characteristic for regions with their last tectonothermal event 1 to 2.5 Ma (Proton) and >2.5 Ga (Archon) ago.

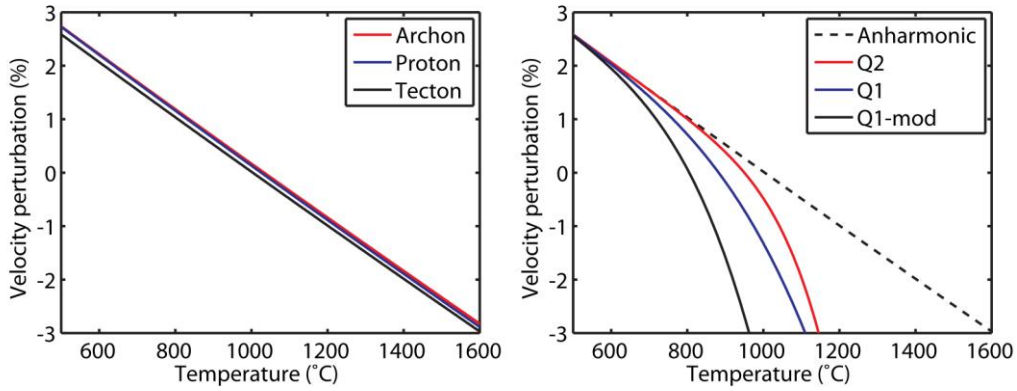

Figure 4.17: (a) Effect of composition on the perturbation of the anharmonic P-wave velocities with reference to the global traveltime table IASP 91 (Kennett & Engdahl, 1991) as a function of temperature at a depth of 75 km. An Archon, Proton and Tecton (mean spinel peridotite) composition were assumed (Griffin et al., 2003). (b) Effect of the attenuation model on the perturbation of the anelastic P-wave velocities with with reference to the global traveltime table IASP 91 (Kennett & Engdahl, 1991) as a function of temperature at a depth of 75 km. Attenuation models from Berckhemer et al. (1982) (Q2), Sobolev et al. (1996) (Q1) and Shapiro & Ritzwoller (2004) (modified from Sobolev et al. 1996, Q1-mod) were used. The dashed line corresponds to the perturbation of the anharmonic P-wave velocities for a Tecton composition.

Mantle composition will affect (a) the estimates of the water content required for dehydration melting as well as (b) the temperature constraints from seismic velocity data:

(a) Mantle composition affects the melt partition coefficient (equation (B.37)) and therefore the amount of water required to stabilize a hydrous melt phase. Figure 4.2 shows the water content required to allow dehydration melting for the three mantle compositions assuming a simplified geotherm derived from surface heat flow data (see section 4.1). It can be seen that the water content for the Tecton and Archon composition are very similar (~1% difference), while the Proton composition results in a water content ~7% less compared to the Tecton

composition. This difference is relatively small compared to the uncertainty in the temperature constraints, as discussed below.

(b) Figure 4.17a shows the perturbation of the anharmonic P-wave velocities with with reference to the global traveltime table IASP 91 (Kennett & Engdahl, 1991) as a function of temperature at a depth of 75 km (see Appendix B.3). It can be seen that the more depleted Proton and Archon compositions yield ~30°C higher temperature estimates than the moderately depleted Tecton composition for a given velocity. While this difference is relatively small, it should be noted that it gets further amplified by the choice of anelasticity model.

2. Seismic wave attenuation can have a significant effect on the observed seismic velocities (Karato, 1993). Figure 4.17b shows the perturbation of the anelastic P-wave velocities with with reference to the global traveltime table IASP 91 (Kennett & Engdahl, 1991) as a function of temperature at a depth of 75 km, using three different attenuation models for a frequency of 0.5 Hz (see Appendix B.3). For comparison, the perturbation of the anharmonic P-wave velocities for a Tecton composition has been plotted. It can be seen that, at low temperatures, all three attenuation models yield velocity perturbations similar to the anharmonic velocity perturbation. However, for higher temperatures the results differ significantly. For a given velocity perturbation, the temperatures inferred from the attenuation models are significantly lower (up to 650°C) compared to the anharmonic velocity perturbation. The uncertainty in these temperatures is expected to be ±100°C (Cammarano et al., 2003). The attenuation model used in

the analysis (Shapiro & Ritzwoller (2004), modified from Sobolev et al. (1996)) yields the lowest temperature estimates, which are 100°C to 200°C lower than for the attenuation models by Sobolev et al. (1996) and Berckhemer et al. (1982). Therefore, the analysis might underestimate the mantle temperature in regions with low seismic velocities compared to the other two attenuation models. As a result, it might overestimate the water content and melt fractions required to explain the electrical resistivity models in these regions.

3. The temperature calculations from seismic velocity data (see Appendix B.3) are based on a dry mantle composition. However, as discussed in section 4.1, a significant amount of aqueous fluids and/or partial melt are required to explain the electrical resistivities observed in the backarc mantle of the Canadian Cordillera. Laboratory measurements indicate that the presence of fluids reduces seismic velocities primarily by enhancing the anelasticity of the rock (Karato, 2006). Therefore, by assuming a dry mantle composition the analysis might overestimate the temperature in hot regions where anelasticity is important. Hyndman et al. (2009) estimate that for a substantially hydrated mantle the attenuation model by Shapiro & Ritzwoller (2004) (modified from Sobolev et al. (1996)) could yield temperatures that are ~50°C too high. However, this effect is balanced by the fact that this attenuation model might underestimate mantle temperatures compared to alternative attenuation models (see assumption 2).

4. The linear regression of hydrogen solubility $[H^+]_{\text{ppm Si}}$ in olivine as a function of pressure P up to 12 GPa derived by Lizarralde et al. (1995) (equation

(B.10)) is based on laboratory data collected at temperatures between 1100°C and 1300°C (Bai & Kohlstedt, 1992; Kohlstedt et al., 1996) using Fourier transform infrared (FTIR) spectroscopy and the uncalibrated spectroscopic method of Paterson (1982). The measurements indicate a strong dependence of hydrogen solubility on pressure, due to the pressure dependence of hydrogen and oxygen fugacity (Bai & Kohlstedt, 1992). However, they do not take into account temperature effects. As the temperature range used in the laboratory measurements is similar to the temperatures expected in the backarc mantle of the Canadian Cordillera, equation (B.10) provides a good approximation of the hydrogen solubility in olivine.

More recent laboratory studies using the spectroscopic method of Bell et al. (2003) determined a calibration of the FTIR spectroscopy, which suggests that the uncalibrated spectroscopic method of Paterson (1982) underestimates the hydrogen content by a factor of ~3.5 (Koga et al., 2003). As a result, the analyses will overestimate the regions in which an additional free aqueous fluid phase is required.

5. When estimating the melt fractions, a melt phase with intermediate electrical conductivity ($\sigma_2 = 5$ S/m) and electrical connectivity ($m = 1.3$) was assumed. For a higher electrical conductivity ($\sigma_2 > 5$ S/m) and/or electrical connectivity ($m < 1.3$), smaller melt fractions are required to explain the observed electrical resistivities, while for a lower electrical conductivity ($\sigma_2 < 5$ S/m) and/or electrical connectivity ($m > 1.3$) larger melt fractions are required.

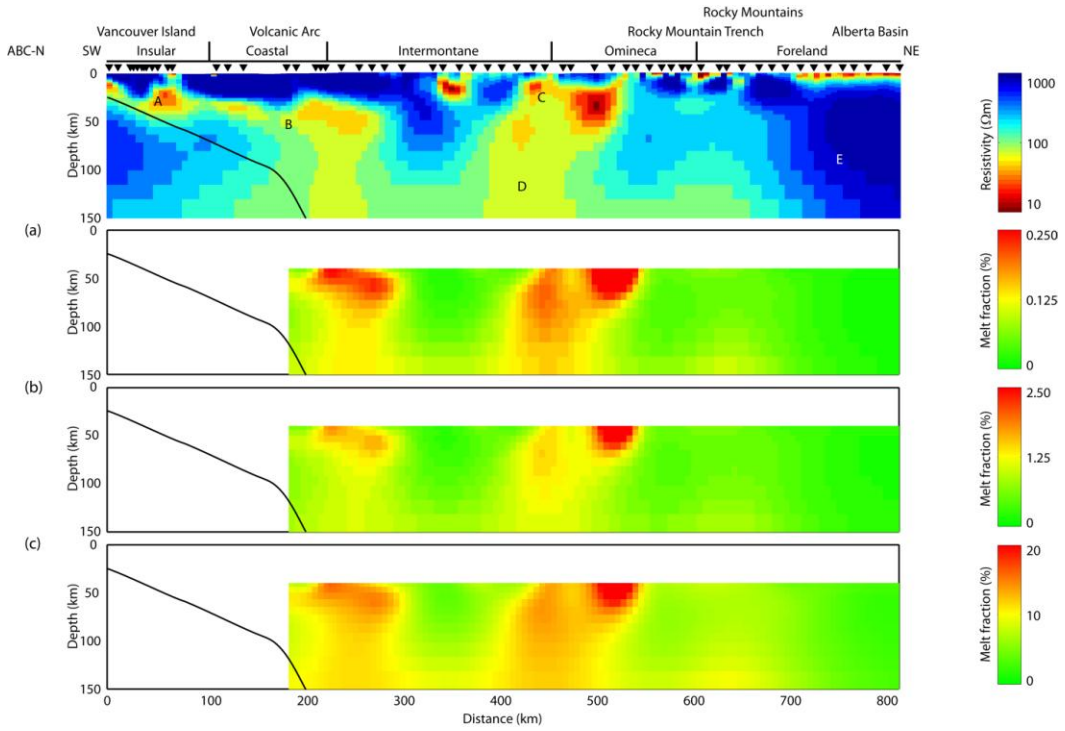

Figure 4.18: Electrical resistivity model (top panel) and the inferred melt fractions for the ABC-N profile for (a) high interconnection ($m = 1$) of a high conductivity melt phase ($\sigma_2 = 10$ S/m), (b) intermediate interconnection ($m = 1.3$) of an intermediate conductivity melt phase ($\sigma_2 = 5$ S/m) and (c) low interconnection ($m = 2$) of a low conductivity melt phase ($\sigma_2 = 1$ S/m).

Figure 4.18 shows the required melt fractions in the absence of water for the simplified geotherm used in section 4.1. For an electrical conductivity $\sigma_2 = 10$ S/m and a cementation factor $m = 1$, the required melt fractions reduce to less than 0.25% at shallow mantle depths. In contrast, for an electrical conductivity $\sigma_2 = 1$ S/m and a cementation factor $m = 2$ the required melt fractions range between 15 and 20%. For future analyses it would be desirable to include the effect of water on the electrical conductivity of the melt phase (Ni et al., 2011). For this, the amount of water in the melt phase can be calculated using equation (B.38).

6. The hydrogen diffusion coefficients in olivine are highly anisotropic, with hydrogen diffusivity along the [100] axis being 40 times higher than along the [001] axis (Mackwell & Kohlstedt, 1990). Therefore, strain induced lattice preferred orientation of the mantle minerals can significantly increase the electrical conductivity of the mantle in the presence of water (Simpson & Tommasi, 2005).

Mantle flow in the asthenosphere of the Cascadia subduction zone could be a possible source of lattice preferred orientation of the mantle minerals (Currie et al., 2004b; Tommasi et al., 2006). Therefore, as the analysis based on Karato (1990) uses an isotropic average of the electrical conductivity, it might overestimate the amount of water required to explain the electrical resistivity models. In contrast, the laboratory measurements by Wang et al. (2006) were conducted along the most conductive axis of the olivine crystal, without correction for an isotropic composition. Therefore, the analysis based on Wang et al. (2006) is likely to underestimate the water content. As a result, both analyses represent end members and provide a possible range of water contents in agreement with the observed electrical resistivities.

7. The calculation of the amount of water required for dehydration melting (Appendix B.4) assumed batch melting, for which the melt phase stays in contact with the residual rock crystal and the overall bulk composition of the system remains unchanged. The melt partition coefficient was assumed to be constant, but might vary with an increasing degree of melting, as the different mineral

components get progressively consumed. If fractional melting was assumed, in which the melt phase is removed from the system, equation (B.38) would have to be replaced by:

$$C_{H_2O}^{melt} = \frac{C_{H_2O}^0}{D_H^{perid/liq}} (1 - F)^{\frac{1}{D_H^{perid/liq} - 1}} \tag{4.1}$$

where $C_{H_2O}^0$ is the bulk water concentration, $D_H^{perid/liq}$ is the melt partition coefficient and F is the degree of melting. In addition, the continuously changing bulk composition needs to be taken into account, which is beyond the scope of this analysis.

In summary, composition plays a minor role in constraining the thermal regime as well as the fluid content of the mantle in the Canadian Cordillera. The attenuation model used in the conversion of seismic velocity to temperature is likely to underestimate the actual temperature of the backarc mantle. As a result, the analysis might overestimate the amount of water required to explain the electrical resistivity models. The analysis based on Karato (1990) is expected to provide a constraint on the maximum water content, as it requires significantly higher amounts of water than the analysis based on Wang et al. (2006). In addition, it assumes an isotropic mantle composition and therefore does not require lattice preferred orientation of the mantle minerals to explain the observed electrical resistivities.

4.5 Summary

The low resistivities in the backarc require either hydrogen diffusion, partial melting of mantle rocks or a combination thereof. Analysis of the magnetotelluric data provides constraints on either the water content or the melt fraction required to explain the observed electrical resistivities, if the temperature is known from independent geophysical measurements. However, this analysis does not take into account the effect of water on the mantle solidus temperature and cannot resolve the combined effect of hydrogen diffusion and partial melting on the electrical resistivities. Therefore, considerable non-uniqueness is associated with this interpretation in terms of the type and quantity of fluids needed to explain the low resistivities observed in the upper mantle.

The non-uniqueness in the interpretation can be reduced if a joint interpretation of electrical resistivity and seismic velocity data is implemented. As seismic velocity models are sensitive to the temperature of the crust and upper mantle, they can be used to constrain the mantle temperatures of the Canadian Cordillera. In combination with thermodynamic calculations, it is then possible to determine the effect of water on the mantle solidus temperature and to define regions where the water content is high enough to allow for partial melting.

Based on the more conservative model by Karato (1990), the joint analysis of the electrical resistivity and seismic velocity data suggests a well hydrated mantle with a water content of 750-1500 ppm beneath the volcanic arc, associated with

metamorphic dehydration reactions of hydrous minerals in this region. This amount of water is sufficient to lower the mantle solidus temperature and allow partial melting of mantle rocks with melt fractions between 0.5 and 2%. Additional water is required at shallow mantle depths (35-100 km) beneath the Intermontane and Omineca Belts, with water content increasing from 500-750 ppm in the north to 750-1000 ppm in the south. The shallow mantle in this region is also subject to partial melting, with melt fractions ranging between 0.5 to 1.5% in the north and 1.5 to 2.5% in the south. As the model by Wang et al. (2006) requires significantly less water than the model by Karato (1990), these numbers correspond to the maximum amount of water and melt required to explain the magnetotelluric data of the Canadian Cordillera.

The presence of water and partial melt has a significant effect on the rheology of the mantle by lowering its viscosity (Dixon et al., 2004). For the observed water contents of 500-1000 ppm beneath the Intermontane and Omineca Belts, viscosities between $3.1 \cdot 10^{19}$ and $3.9 \cdot 10^{19}$ Pa s at a depth of 75 km are calculated, if a strain rate of 10^{-15} s^{-1} is assumed. These viscosities are significantly lower than the global average for continental shield areas (~10^{20}-10^{21} Pa s) (Dixon et al., 2004), and could therefore allow vigorous mantle convection (e.g. Honda et al., 2002). This form of convection of a low viscosity mantle could provide a possible explanation for the hot temperatures in the backarc of the Canadian Cordillera (Currie et al., 2004a).

Further constraints on the presence of fluids in the backarc mantle can also be obtained from the analysis of S-wave velocities V_s as well as the ratio V_p/V_s. However, similar to the analysis presented here, this analysis would be significantly limited by the overall uncertainty of ±100°C in the conversion from seismic velocity to mantle temperature. Another major limitation in the presented analysis is the disagreement between the laboratory measurements of the electrical petrologists. To overcome these limitations, increasingly refined laboratory measurements on the electrical and seismic properties of mantle rocks are required to better constrain the mantle rheology using the joint analysis of electrical resistivity and seismic velocity data in the future.

5 Crustal flow in the India-Asia continent-continent collision*

5.1 Introduction

After study of the Cascadia subduction zone as an example of active subduction of oceanic crust beneath a continental plate, this chapter describes another major class of plate boundaries. Continent-continent collisions are convergent plate boundaries that have led to the assembly of the modern continents. They begin with the subduction of an oceanic plate beneath a continental plate, as discussed in the previous chapters, leading to the closure of an ocean basin to give a suture zone. Subduction continues until the continental plate collides with the continental part of the subducting plate, at which point subduction stops due to the low density of the continental crust compared to the underlying mantle (e.g. Unsworth, 2009). During the transition from oceanic subduction to continental collision, continental crust can be temporarily subducted to depths in excess of 100 km. At these depths, ultra-high-pressure metamorphism occurs, before the metamorphosed rocks may get rapidly exhumed and returned to the surface (e.g. Warren et al., 2008).

A number of examples of continent-continent collisions are interpreted in the geological record. These include (a) the collision of East and West Gondwana during the Neoproterozoic, which has formed the East African Orogen (e.g. Kröner & Stern, 2005) and (b) the collision of Gondwana and Laurasia in the late

* A version of this chapter has been published: Rippe, D. & Unsworth, M. (2010). Quantifying crustal flow in Tibet with magnetotelluric data. *Physics of the Earth and Planetary Interiors*, *179*(3-4), 107-121, doi: 10.1016/j.pepi.2010.01.009.

Paleozoic, which formed the supercontinent Pangaea (e.g. Matte, 2001). In order to better understand these ancient collisions, it is necessary to study modern examples of active continent-continent collisions. The best studied modern example is the collision of India and Eurasia that has formed the Himalaya and Tibetan Plateau over the last 70-40 million years (Yin & Harrison, 2000; Aitchison et al., 2007). After the closure of the Tethyan Ocean, the crust has thickened in southern Tibet to up to 85 km and formed a plateau with an average elevation of 5000 m (Fielding et al., 1994; Figure 5.1). The Tibetan Plateau has been extensively studied to determine which deformation processes are active in these regions. A wide range of tectonic processes have been proposed and numerous geodynamic models have been developed. These cover the spectrum between two end-member models. One end member proposes that lithospheric deformation is localized on a number of major strike-slip faults that define a series of rigid blocks (e.g. Tapponnier et al., 2001). The opposite end-member suggests continuous deformation of the crust and upper mantle over large parts of the plateau (England & Houseman, 1986; Shen et al., 2001).

Global positioning system (GPS) data from Tibet indicate a continuously varying strain field across the surface of the plateau (Zhang et al., 2004; Gan et al., 2007; Figure 5.2) favouring continuous crustal deformation over localized shear. However, the characteristics of this deformation at depth cannot be directly constrained and geophysical methods for determining the strength of the crust and mantle are required. A number of geophysical and geological observations suggest that the Tibetan crust is weak, as reviewed below.

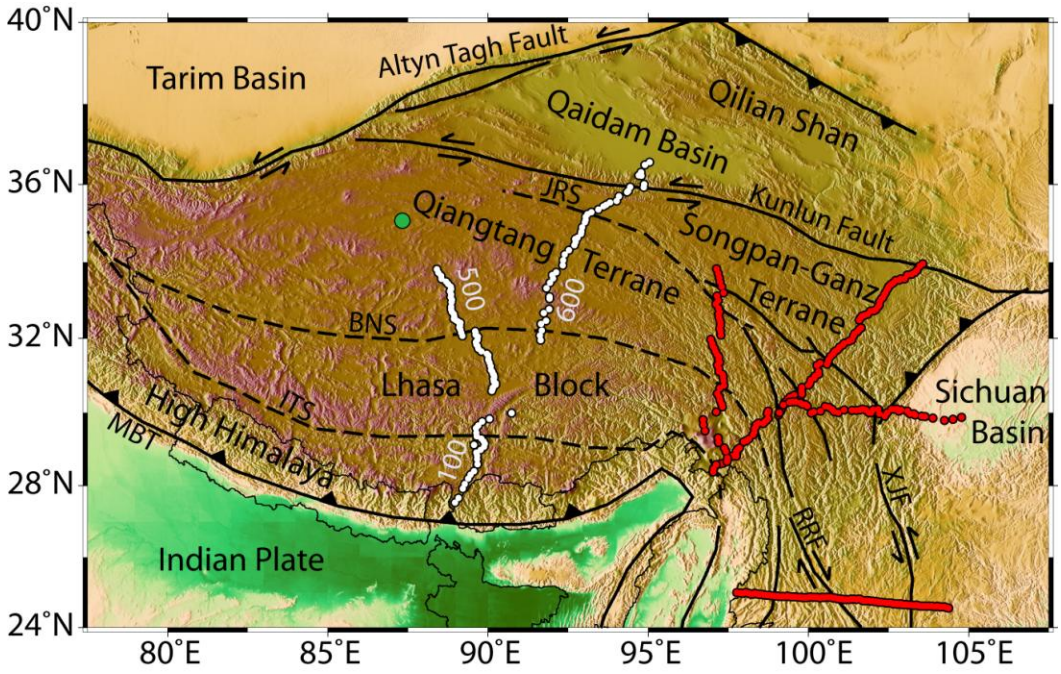

Figure 5.1: Topographic map of Tibet showing the major tectonic features and boundaries of the collision between India and Asia (MBT: Main Boundary Thrust, ITS: Indus Tsangpo Suture, BNS: Banggong-Nuijang Suture, JRS: Jinsha River Suture, RRF: Red River Fault, XJF: Xiaojiang Fault, KF: Kunlun Fault). Locations of INDEPTH magnetotelluric measurements are shown as white dots. Magnetotelluric profiles of Bai et al. (2010) are shown as red dots. Green dot shows the epicenter of the 1997 M_w 7.6 Manyi earthquake.

These observations have been used as the basis for geodynamic models of localized crustal channel flow in Tibet and the surrounding regions. Models invoking channel flow are based on the assumption that the strength of the middle to lower crust is less than that of the upper crust and underlying upper mantle (e.g. Turcotte & Schubert, 2002), such that deformation in this weakened layer may occur as a response to either plate motions, topography-induced pressure gradients or a combination thereof. Two types of crustal flow have been suggested. In the first, the observation of igneous rocks exposed in the High Himalaya, combined with geophysical interpretations of a fluidized, partially molten crust beneath

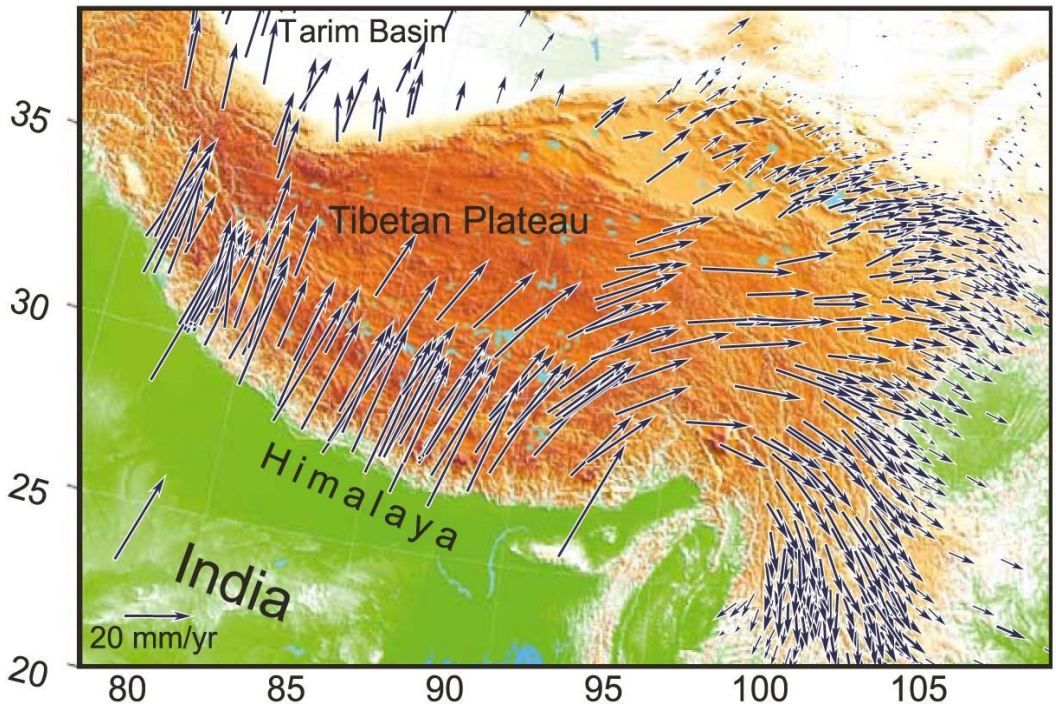

Figure 5.2: GPS velocity field of crustal motion of the Tibetan Plateau relative to the stable Eurasia. (adapted from Gan et al., 2007)[12]

southern Tibet (Nelson et al., 1996) led to the suggestion of a southward directed flow driven by topography-induced pressure gradients and surface erosion (Beaumont et al., 2001). A second type of crustal flow was proposed to be active in Eastern Tibet, based on the uplift of large areas of the Tibetan Plateau with little surface deformation (Royden et al., 1997). This was inferred to have been due to hydraulic uplift caused by a topography-induced outward flow of crustal material from the regions of the Tibetan Plateau with the thickest crust (Clark & Royden, 2000).

For channel flow to occur, the crust must be relatively weak, so that it is susceptible to deformation under topography-induced pressure gradients. The

strength of the crust is controlled by its composition, temperature and the presence of fluid phases such as partial melt. Laboratory measurements on partially molten rocks suggest that melt fractions in the range 5-10 % reduce the crustal strength by one order of magnitude (Rosenberg & Handy, 2005). In this chapter, the geophysical constraints on crustal strength are briefly reviewed, with a focus on the magnetotelluric observations that give information about subsurface electrical resistivity, a parameter that is particularly sensitive to the presence of fluid phases. A limitation of the previous MT analyses is that they have considered the bulk resistivity of the crustal flow channel (Unsworth et al., 2005), rather than the conductance which is the quantity most robustly determined by magnetotelluric data (Jones, 1992; section 2.2.1). A relationship is developed between the conductance of the layer and the velocity of channel flow within the layer. This is then applied to the magnetotelluric data collected on the Tibetan Plateau. It is shown that a conductance value of 7000-27,000 S can be considered a threshold for crustal flow at a geologically significant rate of 1 cm/a.

5.2 Geophysical and geological constraints on crustal rheology in Tibet

5.2.1 General constraints

One of the most prominent features of the Tibetan Plateau is the large extent of high elevations exhibiting a surprisingly low relief that may be due to isostatic compensation and some kind of flow in the lower crust (Fielding et al., 1994).

This idea is supported by maps of the spatial variation of the effective elastic thickness of the lithosphere (Jordan & Watts, 2005). Whereas the elastic thickness in the Himalayan foreland exceeds 100 km, it is typically less than 20 km in the interior of the Tibetan Plateau (Braitenberg et al., 2003). This small elastic thickness indicates that the middle to lower crust is not strong enough to provide the forces required to support the high elevation of the plateau.

The southern part of the Tibetan Plateau is characterized by a crustal thickness up to 85 km (Zhao et al., 1993) and high heat flow (> 82 mW/m^2; Wang, 2001). For comparison, the mean global heat flow for continental areas is 65 mW/m^2 (Pollack et al., 1993). In contrast, the regional heat flow in northern Tibet is 45 mW/m^2 which is lower than the global average (Wang, 2001). The thickened crust contributes to the elevated heat flow and crustal temperatures in southern Tibet. The conductive geotherms computed for continental lithosphere by Pollack & Chapman (1977) predict Moho temperatures in excess of 700°C in southern and even northern Tibet due to the unusual crustal thickness (> 65 km). Geodynamic modelling confirms that radiogenic heat production can heat the crust to temperatures high enough to melt rocks with a wet granitic composition (Thompson & Connolly, 1995). These high crustal temperatures are supported by a number of indirect temperature estimates. For example, the observation of a pronounced satellite magnetic low in the Earth's magnetic field indicates that the Curie isotherm (~550°C) is located in the upper crust at a depth of ~15 km over most of the Tibetan Plateau (Alsdorf & Nelson, 1999), suggesting that the

minimum melting temperature of wet granitic rocks (600 to 650°C; Lebedev & Khitarov, 1964) is reached at a depth of 16 - 18 km within the upper crust.

5.2.2 Seismic constraints on crustal rheology

The nature of the middle to lower crust can also be inferred from seismic observations. The chemical composition (e.g. felsic or mafic) has a significant effect on velocity (e.g. Christensen & Mooney, 1995). Temperature and the presence of aqueous fluids or partial melt also have a significant effect on the seismic velocity (Hyndman & Shearer, 1989; Hammond & Humphreys, 2000). Regional waveform modeling indicates average crustal P-wave velocities of 6.2 km/s in northern Tibet for a crustal thickness of ~65 km (Rodgers & Schwartz, 1998) and 6.0 km/s in southern Tibet for a crustal thickness of ~70 km (Rodgers & Schwartz, 1997), which are low compared to a global average of 6.45 km/s (Christensen & Mooney, 1995). A widespread low velocity layer has been reported in the middle crust beneath the southern Lhasa block (Nelson et al., 1996) and, in combination with other data, has been interpreted as a layer of partial melt. Recent teleseismic studies suggest that this layer extends into southeastern Tibet with spatially varying depth and velocity (Xu et al., 2007; Yao et al., 2008; Xu & Song, 2010). In northern Tibet, seismic data indicate high seismic attenuation in the upper mantle (Ni & Barazangi, 1983; McNamara et al., 1995) and crust (Fan & Lay, 2003) compared to southern Tibet, which has also been interpreted in terms of widespread partial melt.

The distribution of earthquakes provides further insight into crustal rheology. In southern Tibet, very few earthquakes have been observed below a depth of 20 km, which is interpreted to mark the transition from brittle to ductile rheology (Chen & Molnar, 1983). The observation of additional earthquakes in western and southern Tibet at sub-Moho depths (Chen & Yang, 2004) may indicate brittle behaviour in the upper mantle, suggesting a minimum in lithospheric strength at mid- to lower crustal depths. This minimum in lithospheric strength corresponds to a viscous lower crust between a brittle upper crust and brittle mantle.

A more direct way to constrain the effective viscosity of the middle to lower crust is by monitoring postseismic deformation. Following the 1997 M_w 7.6 Manyi earthquake near the western end of the Kunlun fault in northern Tibet (see Figure 5.1 for epicenter location), the postseismic deformation was modelled by viscoelastic stress relaxation in a half-space beneath an elastic lid requiring an effective viscosity of the mid- to lower crust of $4 \cdot 10^{18}$ Pa s (Ryder et al., 2007). Over the 4 year observation period, this effective viscosity was observed to increase, which is consistent with the lower crust having a power law rheology.

5.2.3 Previous magnetotelluric measurements in Tibet

Magnetotelluric (MT) observations measure variations in the naturally occurring electromagnetic fields at the Earth's surface and can be used to determine the subsurface electrical resistivity structure. The resistivity of crustal and upper mantle rocks is very sensitive to the presence of partial melts, and can be used to

infer the rheology of the crust and upper mantle (e.g. Unsworth et al., 2005). Information derived from MT is complementary to that obtained from passive seismic studies. In 1995, magnetotelluric data were collected on a 300 km long profile in southern Tibet (100-line in Figure 5.1) as part of the International Deep Profiling of Tibet and Himalaya (INDEPTH) project (Chen et al., 1996). The transect extended from the High Himalayas to the centre of the Lhasa block crossing the Indus Tsangpo suture. In 1998 and 1999, the transect was extended by two additional profiles (500-line and 600-line in Figure 5.1). The 400 km long 500-line extended from the centre of the Lhasa block to the centre of the Qiangtang terrane crossing the Banggong-Nuijang suture (Solon et al., 2005). The 600-line extended over 600 km across the Qiangtang and Songpan-Ganz terranes into the Qaidam basin crossing the Jinsha River suture and the Kunlun fault.

Two-dimensional resistivity models have been published for the 100-line and 600-line (Unsworth et al., 2004; Unsworth et al., 2005) and used both magnetotelluric modes (i.e. TE and TM modes) and vertical magnetic field data. However, the 500-line model of Wei et al. (2001) only used a subset of these data and cannot be objectively compared to the 100-line and 600-line models. As part of the current study, the full set of magnetotelluric data from the 500-line was inverted using the 2D inversion algorithm of Rodi & Mackie (2001). For the inversion the same control parameters as for the 600-line inversion of Unsworth et al. (2004) were used (see Appendix C.1 for details). The resistivity models for the three profiles are shown in Figure 5.3, along with the conductance (integrated conductivity) calculated from the surface to a depth of 100 km. The data fit is

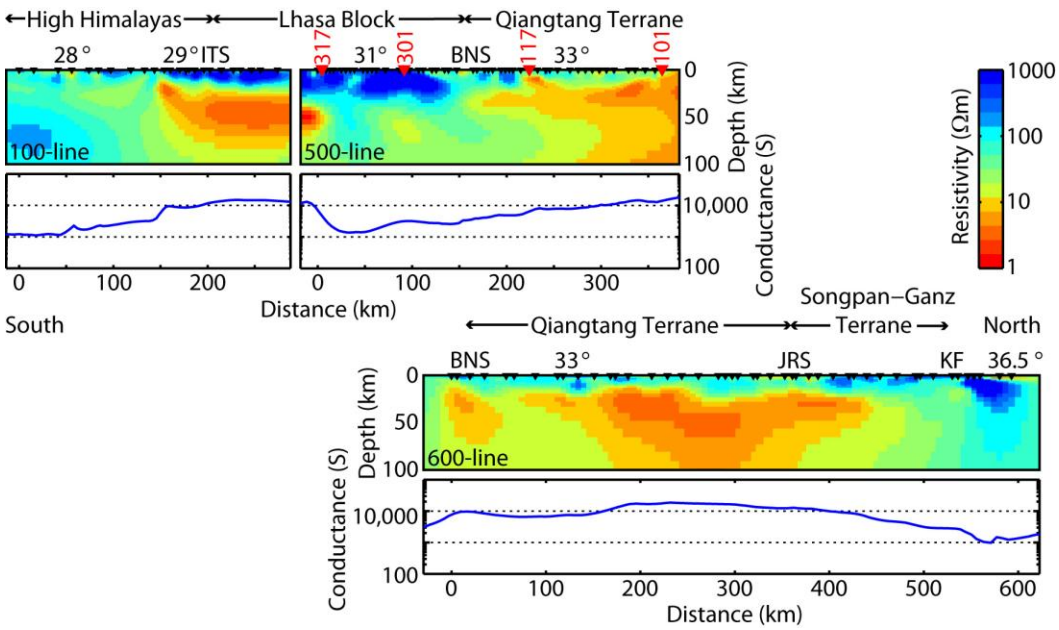

Figure 5.3: Resistivity models for 100-line (top left; Unsworth et al., 2005), 500-line (top right) and 600-line (bottom; Unsworth et al., 2004). The red triangles indicate the locations of the four stations shown in Figure 5.4. Below the resistivity models, the conductance integrated to a depth of 100 km is shown. See Figure 5.1 for abbreviations.

generally good as illustrated by the model response for four stations along the 500-line in Figure 5.4 and the pseudosection in Figure 5.5 and Figure 5.6.

The 100-line inversion model is characterized by a low resistivity layer beneath the Lhasa block with its top at midcrustal depths (20-25 km), which extends south of the Indus Tsangpo suture into the High Himalayas (28.75°). The corresponding conductances are in excess of 10,000 S and are 1-2 orders of magnitude greater than the average conductance of stable continental regions (Jones, 1992). A joint interpretation of the magnetotelluric data and seismic observations along the profile suggests that the high conductances in this region can be best explained by a thin layer of aqueous fluids overlying a thick layer of partial melt (Li et al.,

2003). Depending on its strength, this mid-crustal layer might be weak enough for channel flow to develop, as quantified below.

In contrast to the southern Lhasa block (100-line), the northern Lhasa block (500-line) is more resistive with an average conductance of 3000 S. North of the Banggong-Nuijang suture, the conductance increases gradually, with values up to 10,000 S occurring towards the centre of the Qiangtang terrane. A similar low-resistivity layer is also present beneath the southern part of the 600-line (Unsworth et al., 2004). Additional measurements by Bai et al. (2010) as part of the separate EHS3D (Eastern Himalayan Syntaxis 3D) project detected low resistivities extending from the Qiangtang terrane along the Jinsha River suture with conductances ranging from 15,000 to 30,000 S. It has been suggested that these low resistivities form a possible channel of plateau-wide crustal flow extending as far east as the Red River and Xiaojiang faults (Bai et al., 2010). Alternatively, these low resistivities could also be associated with enhanced interconnection of fluid-filled cracks in shear zones, as indicated by laboratory measurements on deformed mid- and lower crustal rocks (Tullis et al., 1996).

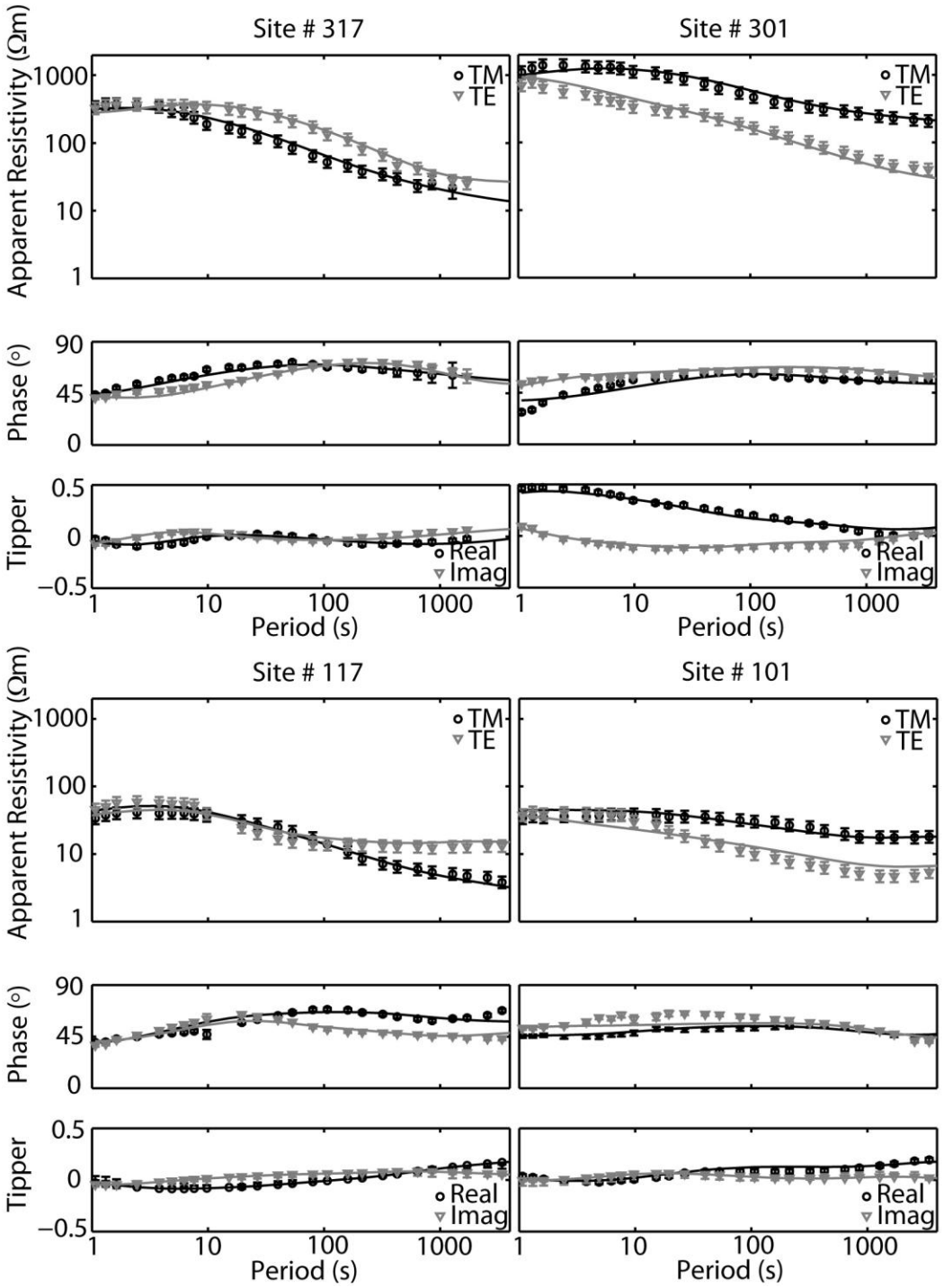

Figure 5.4: Apparent resistivity, phase and tipper curves for four stations on the 500-line. The data is rotated to strike direction N85°W. The continuous line represents the model response of the 2D resistivity model shown in Figure 5.3. See Figure 5.3 for locations along the 500-line.

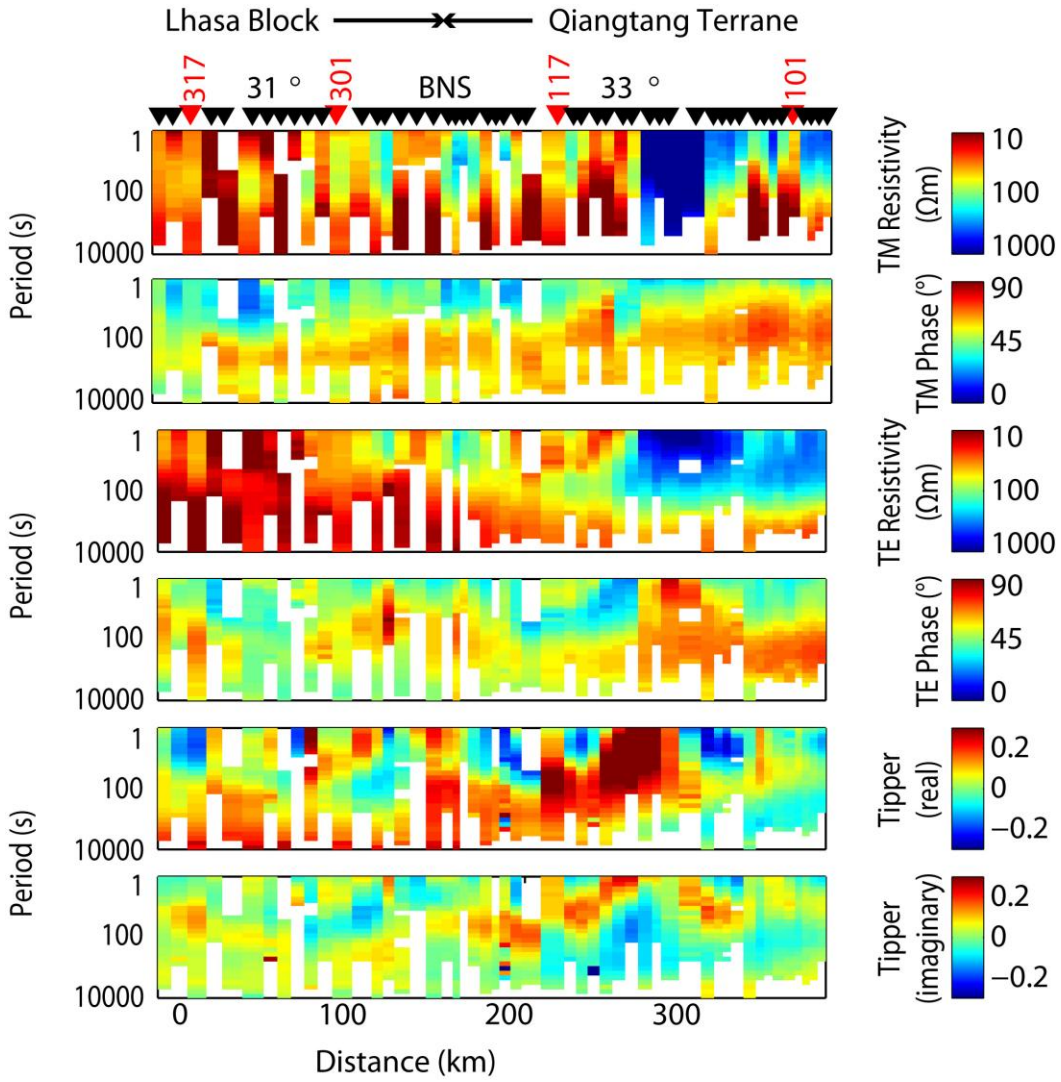

Figure 5.5: Pseudosections for the 500-line showing the magnetotelluric data for a N85°W coordinate system. The top two panels show the apparent resistivity and phase for the TM mode, the middle two panels show the apparent resistivity and phase for the TE mode and the bottom two panels show the vertical magnetic field data. White areas correspond to stations and periods with no data.

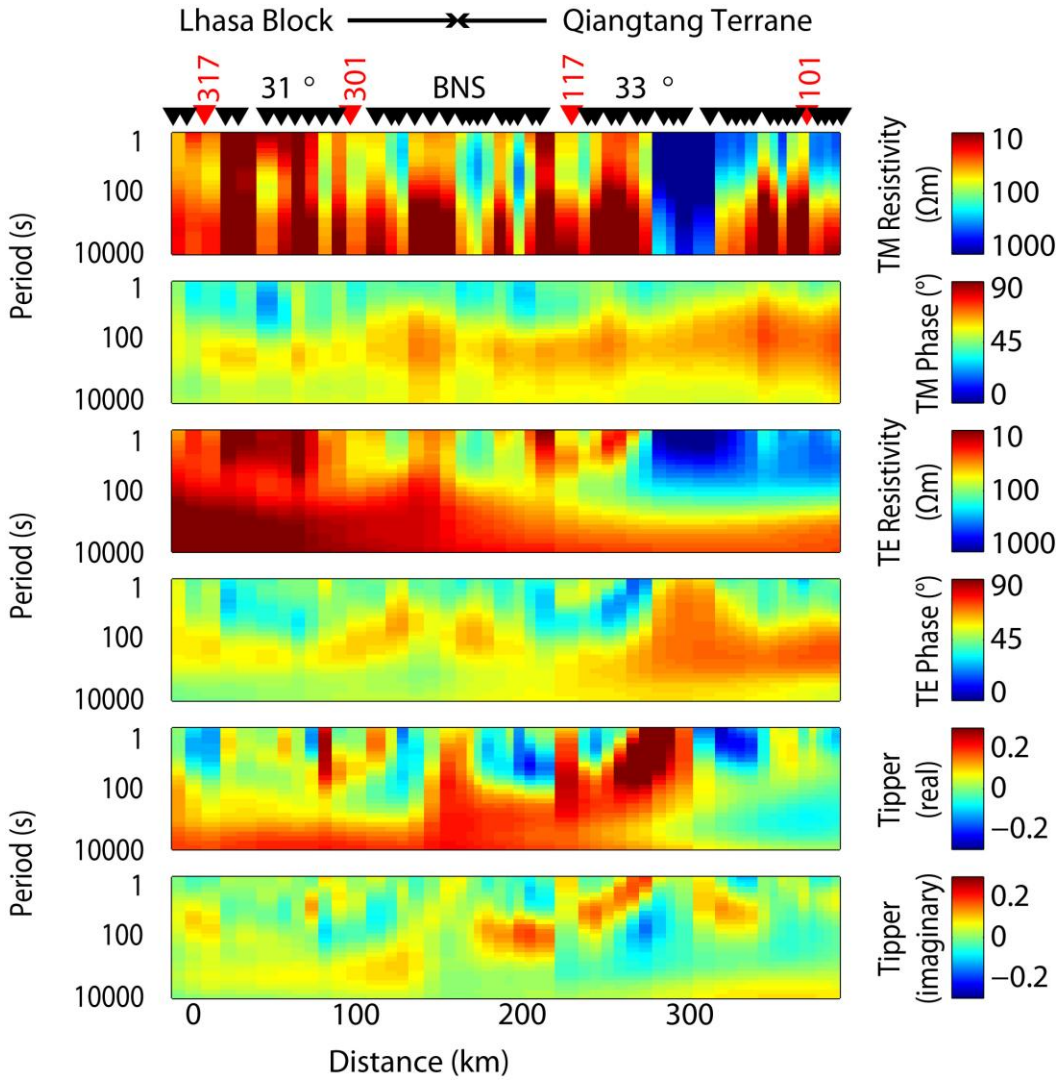

Figure 5.6: Pseudosections for the 500-line showing the model response of the electrical resistivity model shown in Figure 5.3. The top two panels show the apparent resistivity and phase for the TM mode, the middle two panels show the apparent resistivity and phase for the TE mode and the bottom two panels show the vertical magnetic field data. White areas correspond to stations and periods with no data.

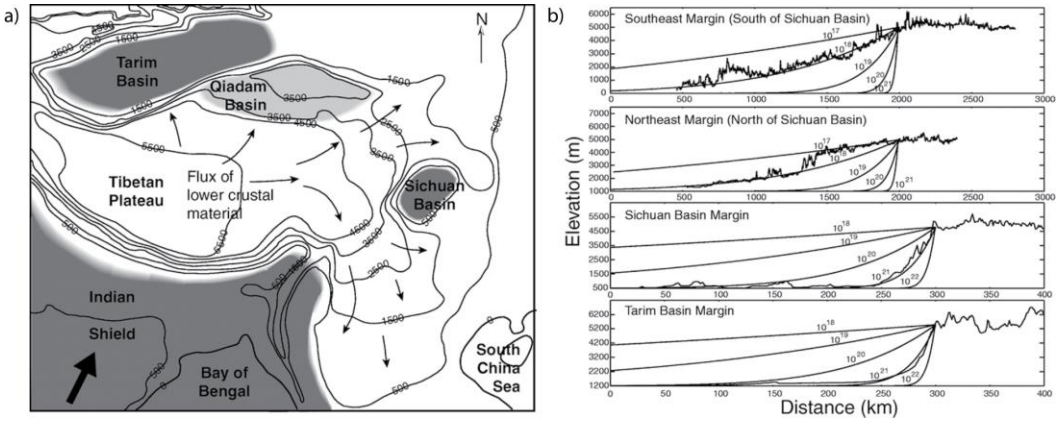

Figure 5.7: (a) Contour plot of smoothed elevations of Tibetan Plateau and surrounding regions. Contour interval is 1000 m. Areas shaded in dark gray represent regions of cold, strong, continental material; light gray area represents intermediate strength; and white areas represent weak crustal regions. Thus, lower crust escapes from beneath thickened, elevated central plateau through regions where crust is weak (b) Model results vs. maximum topographic profiles. Model profiles represent runs for uniform lower crustal channel of thickness h = 15 km and variable viscosity (labeled in Pa·s). (reprinted from Clark & Royden, 2000)[13]

5.2.4 Geodynamic models of channel flow

The observations listed above give information about the crustal properties, but cannot directly demonstrate that channel flow occurs. Geodynamic modelling is required to investigate what type of deformation will result from a given rheology structure for various boundary forces (plate motions, topography-induced pressure gradients or a combination thereof).

Clark & Royden (2000) modelled the eastward extension of the eastern margins of the Tibetan Plateau by flow driven by topography-induced pressure gradients, laterally confined by regions with strong lithosphere, such as the Sichuan and Tarim Basins (Figure 5.7a). This eastward flow was suggested by Royden et al.

(1997) on the basis of observed uplift that appears to have occurred with minimal upper-crustal shortening of the eastern margin (Burchfiel et al., 1995; Wang et al., 1998). To explain the one order of magnitude difference in the topographic gradient along the eastern margins of the plateau, high viscosities (10^{21} Pa s) are required in the lower crust beneath the steep western margin of the Sichuan basin, while lower viscosities (10^{18} Pa s) are required beneath the low gradient slopes northwest and southwest of the Sichuan Basin (Figure 5.7b). The viscosity of the lower crust beneath the central part of the plateau was calculated as 10^{16} Pa s (Clark & Royden, 2000). These results have been extended to explain the dynamic topography of the eastern plateau margin as a result of crustal flow past the rigid Sichuan Basin (Clark et al., 2005). Additional modeling by Copley & McKenzie (2007) indicates that the southeastward directed surface motion between the Sichuan basin and the Eastern Himalaya syntaxis can be explained by gravitationally driven flow with a stress-free lower boundary, laterally bounded by the rigid Indian lowlands and the Sichuan basin. The study suggests a power-law rheology for the crust with an effective viscosity of 10^{22} Pa s for this region.

For the eastward growth of the Tibetan Plateau to be explained by channel flow, a low-viscosity zone in the deep crust is required before the onset of crustal thickening in this area. Using two-dimensional thermomechanical studies Rey et al. (2010) showed that the uplift rates of the Tibetan Plateau require prethickening Moho temperatures of 500-600°C, which are inconsistent with channel flow over lateral distances in excess of 1000 km. Richardson et al. (2008) suggested that regional scale erosion of sedimentary rocks of the Sichuan basin as a result of

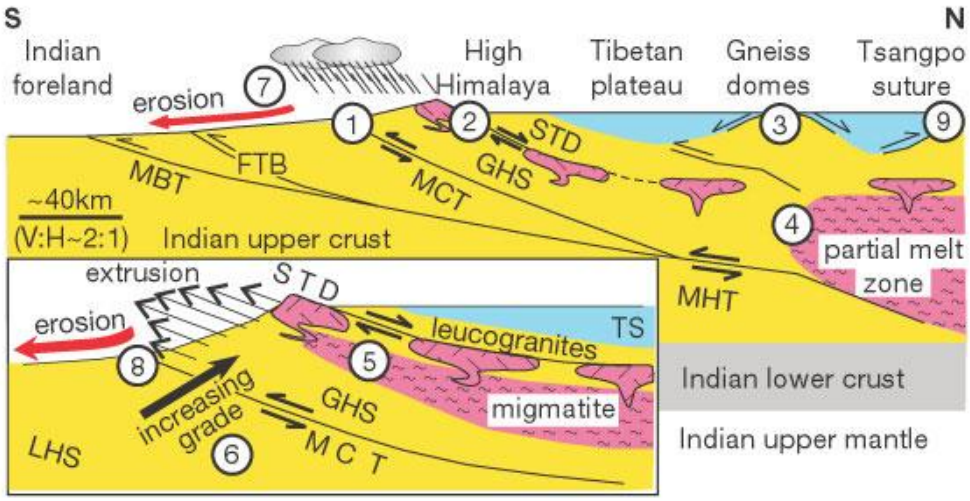

Figure 5.8: General tectonic features of the Himalaya and southern Tibet. Inset shows southern flank of Tibetan Plateau (not to scale). LHS, Lesser Himalayan sequence; GHS, Greater Himalayan sequence; TS, Tethyan sequence; MCT, Main Central thrust; STD, South Tibetan detachment; MHT, Main Himalayan thrust; MBT, Main Boundary thrust; FTB, fold-thrust belt. Colours: blue, weak upper crust; yellow, medium-strength middle crust; grey, strong lower crust; pink, melt-weakened middle crust (includes migmatite and plutons). Numbers correspond to tectonic features explained by the extrusion of a low-viscosity crustal channel. (reprinted from Beaumont et al. 2001)[14]

changes in the Yangtze River drainage system provide an alternative explanation for the high relief of the eastern margin of the Tibetan Plateau. In addition, basin filling due to inefficient drainage as a result of the evolution of the Tibetan river systems played an important role in smoothing out the topography relief generated by tectonic uplift (Liu-Zeng et al., 2008).

The same class of channel flow model can be applied to explain the southward directed surface motion in southern Tibet, with Indian lithosphere acting as a rigid, vertically deformable lower boundary of the flow channel (Copley & McKenzie, 2007). A more sophisticated model by Beaumont et al. (2001)

accounts for thermal-mechanical coupling and the effect of surface denudation along the southern margins of the plateau (Figure 5.8) to explain the exhumation of metamorphic rocks of the Greater Himalayan sequence in the High Himalayas (Wu et al., 1998). Assuming flow driven by a combination of plate motions and topography-induced pressure gradients, viscosities of the order 10^{19} Pa s are required to sustain channel flow in this region and to explain most of the geological features observed.

Geodynamic modelling also provides an effective way of investigating the processes active in the continent-continent collision and generally show a good fit to the geophysical and geological data. In contrast, the geophysical observations presented earlier in this chapter give an insight into the composition and rheological state of the crust beneath the Tibetan Plateau (see Klemperer, 2006 for a more detailed review), but do not uniquely determine which geodynamic processes control the crustal deformation. A complementary view of crustal rheology is provided by laboratory studies on rock mechanics. By establishing a relation between the geophysical observations and the geodynamic models that include these laboratory constraints a better understanding of the crustal deformation processes can be obtained (see Bürgmann & Dresen, 2008 for a review). In the remainder of this chapter, the principles of the channel flow model are introduced. Laboratory measurements on partially molten rocks are used to establish a relationship between the conductance and the flow parameters of the proposed crustal flow channel. The results are then applied to magnetotelluric measurements collected in Tibet.

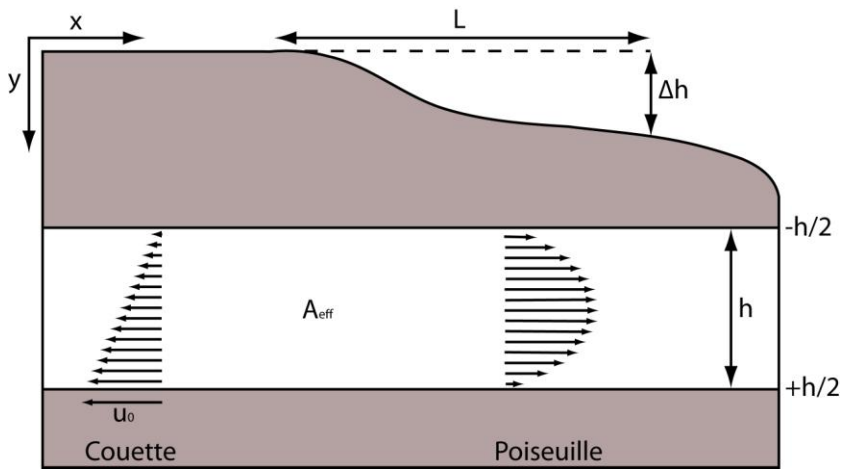

Figure 5.9: Schematic diagram of the channel flow model. The two possible end-members are displayed: Couette flow induced by relative movement of the upper and lower bounding layers and Poiseuille flow as a result of a horizontal pressure gradient due to topographic variations. Quantities labeled are defined in the text.

5.3 Principles of Channel flow

One of the first applications of channel flow in continental geodynamics was presented by Turcotte & Schubert (1982). As described above, it has been proposed as an explanation for a range of geological and geophysical observations in the Himalaya and Tibetan Plateau (Grujic, 2006; Godin et al., 2006 for a general overview), although there are still authors who question if it occurs (see Harris (2007) for a critical review). The simplest form shown in Figure 5.9 describes the deformation of a viscous fluid between two rigid, horizontal layers as a result of (1) a horizontal pressure gradient due to local lateral topography variations, (2) the motion of one of the bounding layers associated with large-scale tectonics, or a combination of (1) and (2). The shear stress τ leads to a

horizontal flow of the viscous fluid with a strain rate $\dot{\varepsilon}$, where τ and $\dot{\varepsilon}$ are related through the power law

$$\tau^n = A_{\text{eff}}\dot{\varepsilon} \tag{5.1}$$

with the power law exponent n and the material constant (or pre-exponential factor) A_{eff}. For Newtonian fluids, the power law exponent $n = 1$, and the material constant corresponds to the dynamic viscosity η. However, laboratory data indicates that most rocks deform as a non-Newtonian fluid with n in the range 2-4 (Carter & Tsenn, 1987) with the effective viscosity defined as:

$$\eta_{\text{eff}} = \frac{\tau}{2\dot{\varepsilon}} = \frac{1}{2}A_{\text{eff}}^{\frac{1}{n}}(\dot{\varepsilon})^{\frac{1}{n}-1} \tag{5.2}$$

The velocity profile of the fluid flow in a channel of height h depends on the horizontal pressure gradient $\frac{dp}{dx}$ and the relative velocity u_0 between the upper and lower bounding layers. For Newtonian fluids, Turcotte & Schubert (2002) showed that the flow is described as:

$$u(y) = \frac{1}{2\eta}\frac{dp}{dx}\left(y^2 - \frac{h^2}{4}\right) + u_0\left(\frac{1}{2} - \frac{y}{h}\right) \tag{5.3}$$

with a mean velocity

$$\bar{u} = \frac{h^2}{12\eta}\frac{dp}{dx} + \frac{u_0}{2} \tag{5.4}$$

where y is the channel thickness.

For non-Newtonian fluids, it is not possible to derive a linear superposition of the flow associated with horizontal pressure gradients and the flow caused by the motion of the bounding layers. Instead, the velocity profile is a hybrid between two end-members (a) Couette flow, for which the horizontal pressure gradient is zero, and (b) Poiseuille flow, in which the bounding layers are stationary. In case of Couette flow, the velocity varies linearly with y as

$$u(y) = u_0\left(\frac{1}{2} - \frac{y}{h}\right) \tag{5.5}$$

and the mean flow velocity in the channel is simply given by half the velocity of the upper bounding layer:

$$\bar{u} = \frac{u_0}{2} \tag{5.6}$$

For Poiseuille flow, the velocity profile takes the symmetric form

$$u(y) = \frac{1}{(n+1)A_{\text{eff}}}\left(\frac{dp}{dx}\right)^n\left(y^{n+1} - \frac{h^{n+1}}{2}\right) \tag{5.7}$$

with a mean velocity

$$\bar{u} = -\frac{1}{(n+2)A_{\text{eff}}}\left(\frac{dp}{dx}\right)^n\left(\frac{h}{2}\right)^{n+1} \tag{5.8}$$

If the fluid is non-Newtonian, the effective viscosity varies with strain rate. It will be lowest at the channel walls where the shear stress is highest and takes a maximum at the centre of the channel. Expressed in terms of the mean velocity $\bar{u}$, the minimum effective viscosity at the channel walls is given by

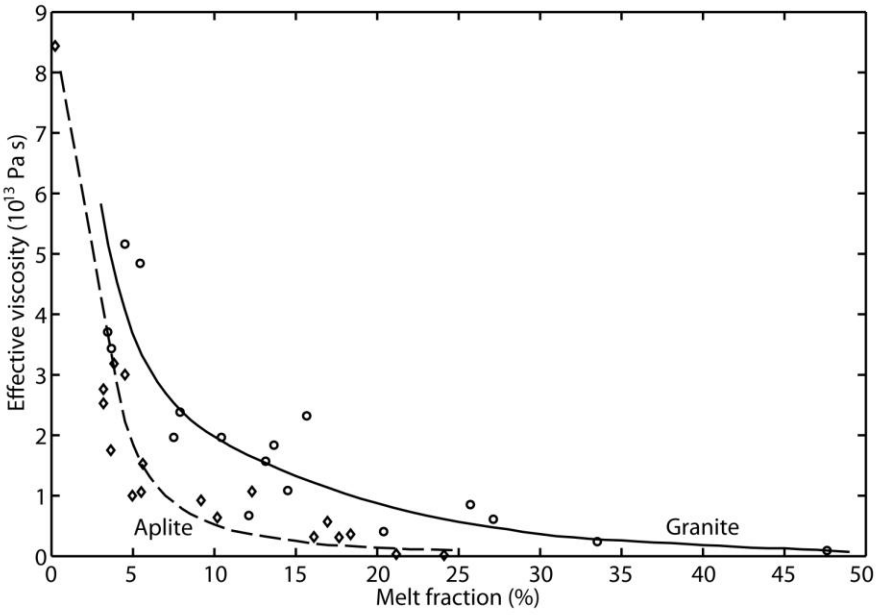

Figure 5.10: Effective viscosity as a function of melt fraction for granite (circles) and aplite (diamonds). Solid and dashed lines show best-fitting trends for granite and aplite respectively. (adapted from Rosenberg & Handy 2005)[15]

$$\eta_{\text{eff}} = -\frac{h^2}{8(n+2)\bar{u}}\frac{dp}{dx} \tag{5.9}$$

5.4 Relationship between flow velocity and observed conductance

Previous analyses of the magnetotelluric (MT) data from Tibet have interpreted the bulk electrical resistivity in terms of fluid fraction, which was then related to the effective viscosity (Unsworth et al., 2005). However, MT data is most sensitive to conductance (section 2.2) which is the product of the layer thickness and bulk conductivity (inverse of resistivity) (e.g. Jones, 1992). Conductance is a property of the entire layer, and MT data interpretation would be more robust if

the conductance could be related to a parameter describing the overall flow. As discussed below, the conductance of a layer can be used to estimate its fluid fraction, which is one of the key parameters that control the strength (effective viscosity) of the layer. Laboratory measurements on partially molten rocks indicate a reduction of their effective viscosity by one order of magnitude for melt fractions as low as 5-10% (Rosenberg & Handy, 2005; see Figure 5.10). The strength of the rocks determines whether channel flow at a geologically significant rate is possible under given boundary conditions and at what rate this deformation will occur. In the following section a relationship between the conductance and flow velocity is derived.

5.4.1 Relationship between mechanical and electrical properties

As described in the previous section, the effective viscosity of a non-Newtonian fluid depends on the strain rate. It is therefore more convenient to describe the rheology of a non-Newtonian fluid in terms of the material constant A_{eff} in the power law equation (5.1). For a given strain rate $\dot{\varepsilon}$ this constant can be calculated from the corresponding effective viscosity η_{eff} as

$$A_{\text{eff}} = \left(2 \frac{\eta_{\text{eff}}}{\varepsilon^{\frac{1}{n}-1}} \right)^{n} \tag{5.10}$$

Figure 5.11a shows A_{eff} as a function of melt fraction for dry granite and aplite at a pressure of 250 MPa and temperatures in the range 700-1100°C based on Rosenberg & Handy (2005). A power law exponent of $n = 3$ was used to

calculate A_{eff} from the effective viscosity in Figure 5.10 (Rutter & Neumann, 1995). Both granite and aplite are felsic igneous rocks commonly found in the continental crust. Granite is widely found in major intrusions and aplite is formed from residual granitic melt in the forms of veins. Figure 5.11a shows that the material constant for these rocks decreases as the melt fraction increases. Lower crustal rocks can have a more mafic composition, which would give a stronger rheology (e.g. Carter & Tsenn, 1987). This would result in a larger material constant for a given melt fraction compared to felsic rocks.

The bulk electrical resistivity of a rock also decreases as the fluid content (melt fraction) increases. A number of empirical relationships have been developed to characterize this effect and one of the most widely used is Archie's law (Archie, 1942) and its modifications. For a saturated, fluid bearing rock the bulk resistivity ρ is given as

$$\rho = a\rho_f \phi^{-m} \tag{5.11}$$

where ϕ is the porosity (which, for a saturated rock, equals the fluid fraction), ρ_f is the fluid resistivity, and m is the cementation factor which defines the geometry of the fluid filled pores. If the pores are spherical with little or no interconnection then $m = 2$ whereas a geometry with ellipsoidal pores or cracks corresponds to $m = 1$ and a higher degree of interconnection. a is an empirical factor typically in the range 0.5 to 2.5.

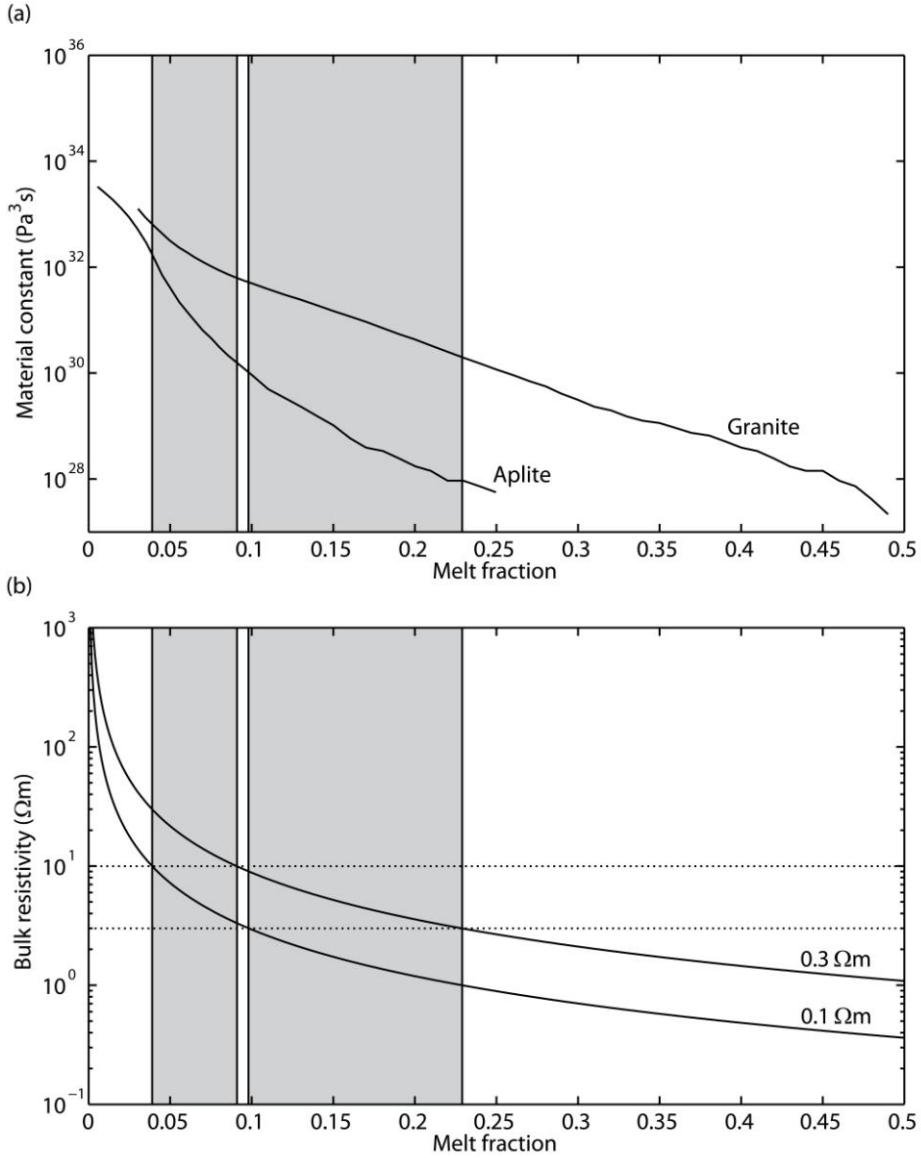

Figure 5.11: (a) Material constant as a function of melt fraction obtained from laboratory measurements on granite and aplite (Rosenberg & Handy, 2005). The shaded areas correspond to the range of melt fractions required to explain the magnetotelluric data in the northern Lhasa block (left) and the southern Lhasa block and Qiangtang terrane (right). (b) Bulk resistivity as a function of melt fraction obtained from Archie's Law for melt resistivities of 0.1 and 0.3 Ωm. The shaded areas indicate the range of melt fractions required to explain the magnetotelluric data in the northern Lhasa block (left) and the southern Lhasa block and Qiangtang terrane (right).

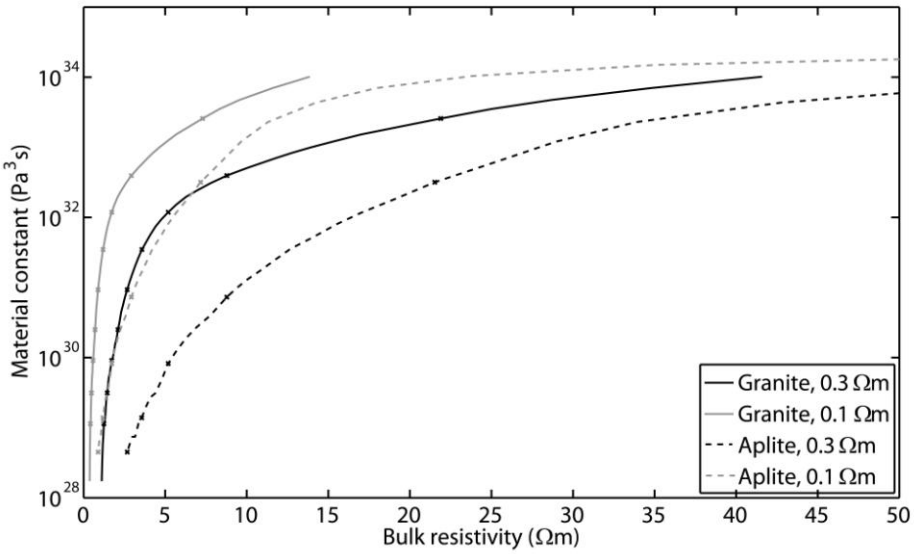

Figure 5.12: Material constant as a function of bulk resistivity obtained by relating the results from Archie's law to the laboratory measurements of Rosenberg & Handy (2005). The points on the curves mark melt fraction steps of 5 percent.

Roberts & Tyburczy (1999) measured the bulk resistivity of partially molten olivine-basalt rock as a function of temperature and estimated the parameters in Archie's law as $m = 0.98$ and $a = 0.73$. In their study, thermodynamical calculations were used to correct the results for variations in melt fraction and composition. A more recent study of the *in situ* melt distribution at different melt fractions by ten Grotenhuis et al. (2005) showed that Archie's Law is applicable with $m = 1.30$ and $a = 1.47$. The advantage of their study is that the measurements were conducted under isothermal conditions at a temperature of 1475°C, avoiding temperature effects on melt fraction and composition. It also covered a wider range of melt fractions, which makes their parameter estimate the preferred choice in the application of Archie's law for this study. Typical values

for the melt resistivity of dry rocks range between 0.1 and 1 Ωm (Tyburczy & Waff, 1983). For water saturated porous rocks, melt resistivities are slightly lower between 0.05 and 1 Ωm (Lebedev & Khitarov, 1964). For both dry and water saturated rocks, the melt resistivity decreases with temperature. In contrast, for water undersaturated melting, the melt resistivity increases with temperature due to dilution of the melt with water (Wannamaker, 1986). Melting at mid- to lower crustal depth is most likely water undersaturated with typical melt resistivities ranging between 0.1 and 0.3 Ωm (Wannamaker, 1986). Figure 5.11b shows the bulk resistivity as a function of melt fraction for these two melt resistivities. Assuming a 30 km thick low-resistivity layer beneath the northern Lhasa block, the observed conductance of 3000 S corresponds to a bulk resistivity of 10 Ωm. It can be seen that melt fractions of 4-9 % are required to explain this bulk resistivity. Similarly, the conductance of 10,000 S beneath the southern Lhasa block and the Qiangtang terrane corresponds to a bulk resistivity of 3 Ωm, requiring a melt fraction of 10-23 %.

Aqueous fluids, for comparison, have resistivities ranging from 0.01 to 10 Ωm with the lowest resistivities only occurring in high density fluids at temperatures of 300°C (Nesbitt, 1993). With a cementation factor m between 1.5 and 2, the degree of interconnection for aqueous fluids is usually lower than for partial melts (Hyndman & Shearer, 1989) requiring slightly larger fluid fractions compared to partial melts of equal resistivity to obtain the same bulk resistivity. In general, the degree of interconnection depends on the dihedral angle of the fluid and increases with decreasing dihedral angle. Holness (1992) reported that the dihedral angle

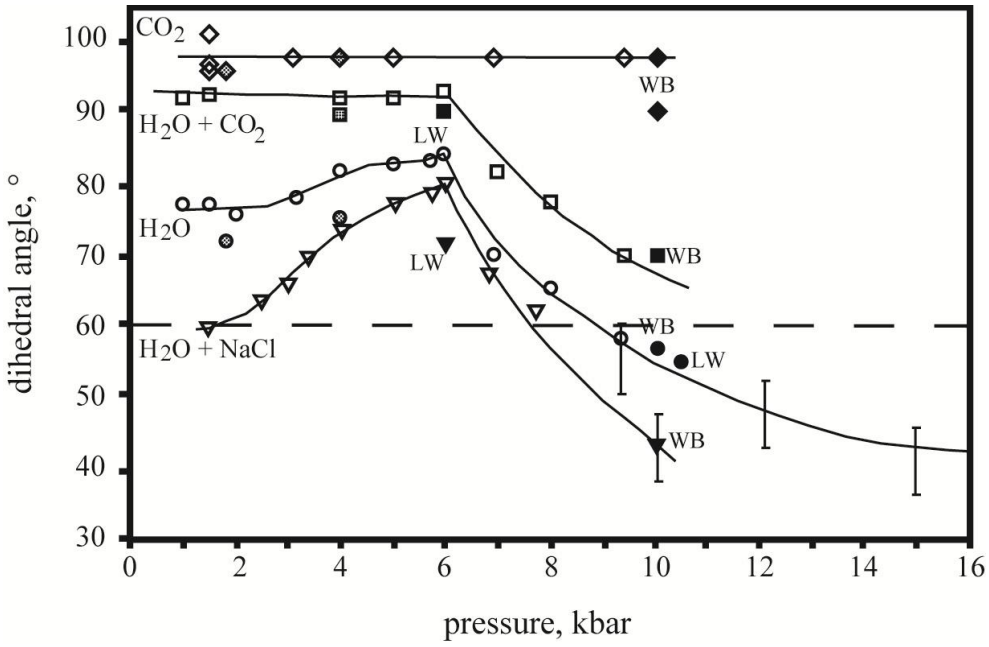

Figure 5.13: Fluid-solid dihedral angles as a function of pressure. Circles: quartz-H2O; squares: quartz-CO2-H2O; diamonds: quartz-CO2; triangles: quartz-NaCl. White symbols: Data reported in Holness (1992) at 800°C; black symbols: data reported in Watson & Brenan (1987) at 950-1150°C (WB) and in Laporte & Watson (1991) at 800°C (LW); shaded symbols: data reported at 1000°C. The error bars have been omitted for clarity; except for the quartz-H2O runs at high pressures. The Lines of best fit were sketched in by eye. (adapted from Holness, 1992)[16]

for pure water and saline fluids in quartz-rich rocks increases with pressure up to 600 MPa (~20 km depth) (Figure 5.13). Below this depth the dihedral angle decreases with pressure falling below a critical angle of 60° at 900 to 1000 MPa (~30 km depth) at which a stable interconnection of the aqueous fluid along the grain boundaries is obtained.

As both the rheological material constant (A_{eff}) and bulk electrical resistivity (ρ) decrease with increasing melt fraction, it is possible to determine a direct relationship between these two parameters. Figure 5.12 shows the material constant as a function of bulk resistivity for granite and aplite, assuming melt

resistivities of 0.1 and 0.3 Ωm. At low bulk resistivities, corresponding to high melt fractions, small variations in resistivity lead to changes of the material constant by several orders of magnitude. For increasing bulk resistivity, the material constant asymptotically approaches a constant value of the order 10^{34} Pa^3s. This can be explained by the decreasing melt fraction where the asymptotic value corresponds to the material constant of a completely crystallized rock.

5.4.2 Application to crustal channel flow in Tibet

Consider a channel with thickness h and bulk resistivity ρ which has a conductance *C* defined as

$$h = \rho C \tag{5.12}$$

The conductance of the channel, C, can be determined by a constrained inversion of the magnetotelluric data (Li et al., 2003), as shown in Figure 5.3 for the different regions of Tibet. The conductance of the channel will vary horizontally, and these changes can be due to changes in either ρ and/or h. Two end member scenarios can be considered (a) constant ρ and (b) constant h. In reality, variations in C will be caused by changes in both of these parameters. The flow parameters of the Couette flow can be directly determined from the relative velocity between the Indian and Asian plates. Based on GPS measurements, Bilham et al. (1997) estimated the slip rate of India beneath Tibet to be 2 cm/a. Using equation (5.6) the corresponding mean velocity of the Couette flow can be calculated as 1 cm/a. While the actual flow is likely a combination of both Couette and Poiseuille flow,

geodynamic studies consider topography variations to be the most important driving force for channel flow in Tibet (Clark & Royden, 2000; Beaumont et al., 2001). The following analysis will determine under which conditions Poiseuille flow as described in equations (5.7) to (5.9) is the dominant flow mode with flow velocities exceeding 1 cm/a.

From equations (5.8) and (5.12), the mean velocity of the Poiseuille flow can be expressed in terms of the bulk resistivity ρ and the measured conductance C of the channel:

$$\bar{u} = -\frac{1}{(n+2)A_{\text{eff}}}\left(\frac{dp}{dx}\right)^{n}\left(\frac{\rho C}{2}\right)^{n+1} \tag{5.13}$$

Similarly, the minimum effective viscosity at the channel walls (equation (2.9)) can be written as

$$\eta_{\text{eff}} = -\frac{(\rho C)^2}{8(n+2)\bar{u}}\frac{dp}{dx} \tag{5.14}$$

Application of the equations (5.13) and (5.14) requires an estimate of the horizontal pressure gradient. Assuming Airy-type isostatic compensation, Kruse et al. (1991) showed that the pressure gradient can be directly related to the surface topography:

$$\frac{dp}{dx} \approx \left(\frac{\rho_m - \rho_c}{\rho_m}\right)\frac{\rho_c g \Delta h}{\frac{L}{2}} \tag{5.15}$$

where Δh is the variation in topography, L is the corresponding length scale and ρ_m and ρ_c are the densities of the mantle and crust (Figure 5.9). For the regions in central Tibet, an elevation change by 5000 m over a distance of 500 km is assumed. With ρ_m = 3,300 kg/m^3 and ρ_c = 2,800 kg/m^3, the pressure gradient is of the order 80 Pa/m.

5.4.2.1 Constant bulk resistivity

The first situation to be considered is how the average flow velocity ($\overline{u}$) and effective viscosity (η_{eff}) will vary with conductance C, assuming that ρ is constant. In this case, changes in C are the result of a change in channel thickness, h. As the material constant in the power law rheology equation is related to the bulk resistivity (Figure 5.12), the flow velocity and effective viscosity are solely functions of conductance. Their relation is governed by a power law so that a logarithmic plot of the flow velocity as function of conductance will be a straight line:

$$\bar{u} = -\frac{\rho^{n+1}}{2^{n+1}(n+2)A_{\text{eff}}}\left(\frac{dp}{dx}\right)^n C^{n+1} \tag{5.16}$$

This flow velocity is then used to calculate the effective viscosity η_{eff} according to equation (5.14), which also plots as a straight line on a log-log plot as a function of conductance.

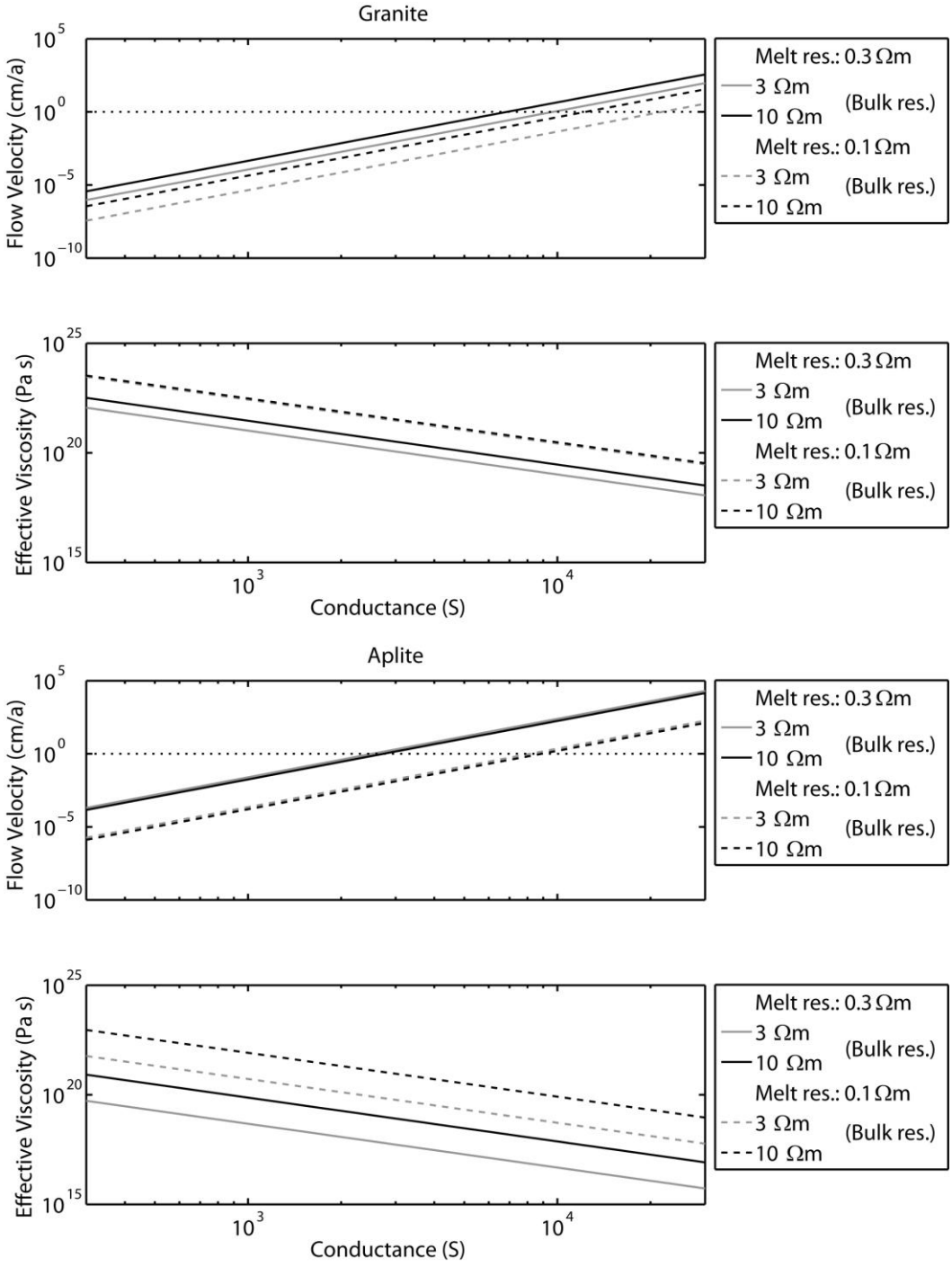

Figure 5.14: Flow velocity and effective viscosity as a function of conductance for granite (top) and aplite (bottom). Constant bulk resistivities of 3 and 10 Ωm were assumed.

Figure 5.14 shows the result for granite and aplite, assuming bulk resistivities of 3 and 10 Ωm and a power law exponent $n = 3$. It can be seen that conductances between 7000 and 22,000 S for granite and 2500 and 9000 S for aplite are required to obtain a flow velocity of the order 1 cm/a. For flow velocities exceeding this threshold, Poiseuille flow is the dominant flow mode and it provides an effective transport mechanism to account for considerable parts of the overall mass balance required in the continent-continent collision.

These results can be applied to conductances observed in MT data collected in different regions of Tibet (Figure 5.3). A comparison of the estimated average flow velocities and effective viscosities for these regions is shown in Figure 5.16 (top):

(a) Southern Lhasa block: Mid-crustal conductances of 10,000 S are observed along the 100-line beneath the southern Lhasa block. This conductance value predicts average flow velocities for granitic melts in the range 0.04 - 4.5 cm/a and effective viscosities in the range 10^{19} - $3 \cdot 10^{20}$ Pa s. For aplite melts, the flow velocities lie in the range 1.6 - 250 cm/a with effective viscosities between $4.5 \cdot 10^{16}$ and $8 \cdot 10^{19}$ Pa s. It should be emphasized that these calculations have assumed that the rocks are felsic in character. If the rock composition was more mafic, then the crust would be stronger leading to reduced flow velocities.

(b) Northern Lhasa block: For the northern Lhasa block on the 500-line, the resistivity model in Figure 5.3 has an average mid-crustal conductance of 3000 S.

The flow velocity predicted for this region is 0.0004 to 0.04 cm/a for granitic melt and 0.01 - 2 cm/a for aplite melt. The corresponding effective viscosities vary between $1 \cdot 10^{20}$ and $3.5 \cdot 10^{21}$ Pa s for granitic melt and $5 \cdot 10^{17}$ and $9 \cdot 10^{20}$ Pa s for aplite melt.

(c) Qiangtang terrane: Beneath the centre of the Qiangtang terrane the 500- and 600-line suggest again a low resistivity layer with its top at midcrustal depths (20-25 km) with conductances up to 10,000 S. The flow velocities and effective viscosities in this region are expected to be similar to the ones observed beneath the southern Lhasa block.

(d) Eastern Tibet: Additional magnetotelluric measurements from Eastern Tibet were reported by Bai et al. (2010) and required crustal conductances of 15,000 - 30,000 S in this region. These conductances correspond to predicted flow velocities of 0.2 - 365 cm/a and effective viscosities ranging between $1.2 \cdot 10^{18}$ and $1.3 \cdot 10^{20}$ Pa s for granitic melt. In case of aplite melt, the inferred flow velocities exceed 10 cm/a independent of the melt resistivity. The reason for these unreasonable large flow velocities is the assumption of a purely aplitic melt composition, as will be discussed in section 5.5.1.

These results suggest that there are two regions where channel flow at a geologically significant rate could occur. The first is the southern Lhasa block where the conductances are high enough to allow for southward directed flow towards the Indian foreland (Beaumont et al., 2001). The second is beneath the

Qiangtang terrane where flow is likely directed eastward extending along the Jinsha River suture (Clark & Royden, 2000). These two regions of channel flow are separated by the northern Lhasa block where the conductances appear to be too low to allow channel flow at a geologically significant rate.

5.4.2.2 Constant thickness

The other end member model is to account for variations in C through a variation in the bulk resistivity of the channel, assuming a constant channel thickness h. In this case, the bulk resistivity for a given conductance can be calculated from equation (5.12). The material constant will vary with C and ρ so plots of the average flow velocity will have a more complex variation:

$$\bar{u} = -\frac{1}{2^{n+1}(n+2)} \left(\frac{dp}{dx}\right)^n \frac{(\rho C)^{n+1}}{A_{\text{eff}}} \tag{5.17}$$

The same is true for the effective viscosity η_{eff} which can be calculated from the average flow velocity according to equation (5.14). These two quantities are plotted as a function of conductance in Figure 5.15 for channel thicknesses of 20 and 50 km. As the laboratory data of Rosenberg & Handy (2005) are limited to certain melt fractions (3-49 % for granite, 0-25 % for aplite), it was not possible to calculate the flow parameters for the entire range of conductances considered in the previous section.

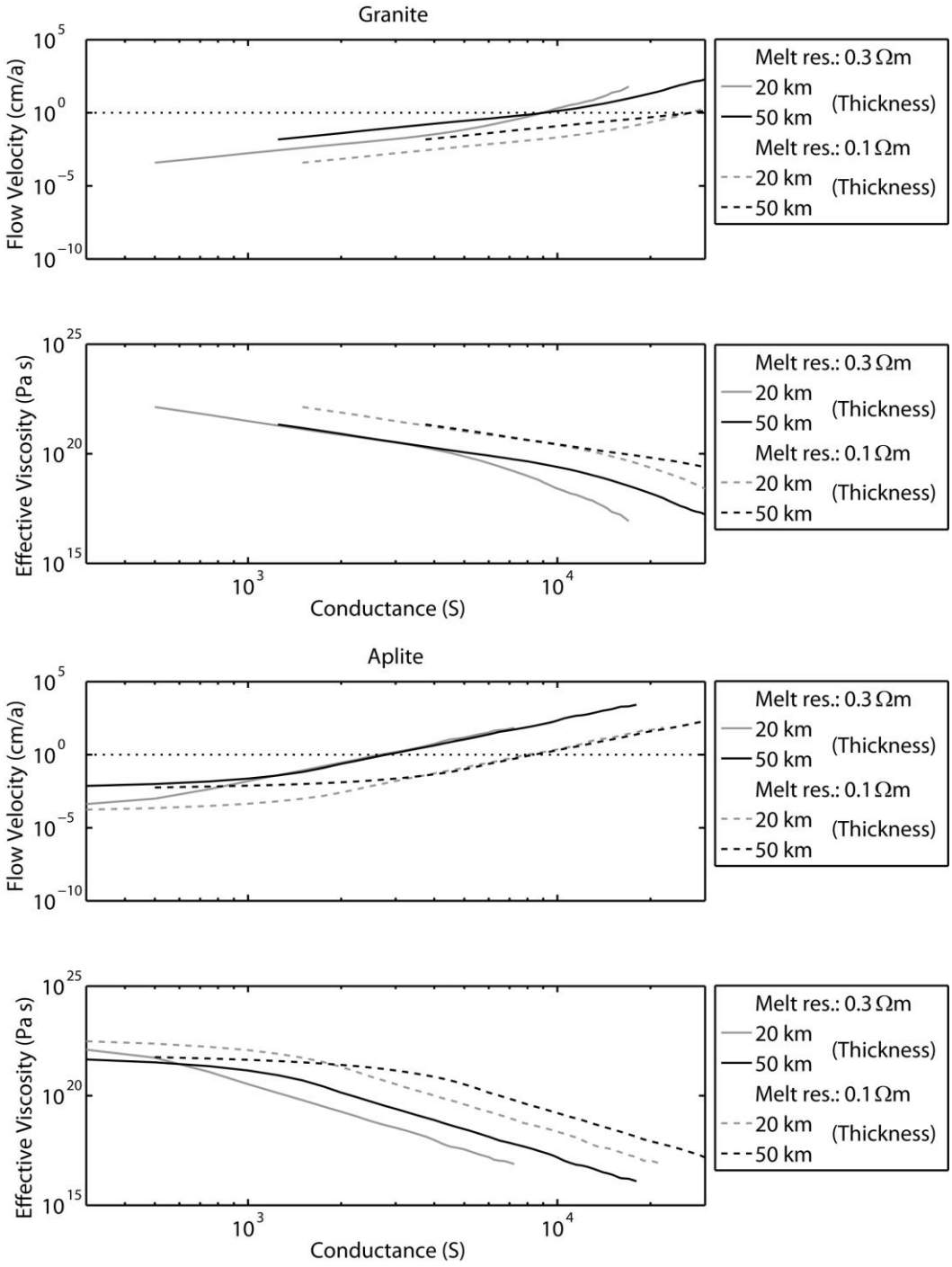

Figure 5.15: Flow velocity and effective viscosity as a function of conductance for granite (top) and aplite (bottom). Constant layer thicknesses of 20 and 50 km were assumed.

As for the constant bulk resistivity, higher conductances lead to a higher flow velocity and a lower effective viscosity due to the higher melt fractions required. In particular, conductances of 9000 - 27,000 S for granite and 2500 - 8500 S for aplite are required to obtain a flow velocity of the order 1 cm/a. These values are similar to the conductances estimated for constant bulk resistivities in the previous section, suggesting that Poiseuille flow is the dominant flow mode in regions with sufficiently high conductances.

The curves in Figure 5.15 can be used to interpret the conductances observed in the different regions of Tibet (Figure 5.3). A comparison of these values is shown in Figure 5.16 (bottom):

(a) Southern Lhasa block: For the southern Lhasa block on the 100-line the flow velocities for a conductance of 10,000 S lie between 0.02 and 2 cm/a for granitic melt and between 2 and 216 cm/a for aplite melt. The corresponding effective viscosities range from $2.5 \cdot 10^{18}$ and $3 \cdot 10^{20}$ Pa s in case of granitic melt and between $1.5 \cdot 10^{17}$ and $1.5 \cdot 10^{19}$ Pa s in case of aplite melt. Lower flow velocities would be possible if the rock composition in this region was more mafic.

(b) Northern Lhasa block: For the northern Lhasa block the flow velocities for a conductance of 3000 S on the 500-line range from 0.001 to 0.01 cm/a for granitic melts with corresponding effective viscosities between $3.5 \cdot 10^{20}$ and $3 \cdot 10^{21}$ Pa s. In case of aplite melt the flow velocities range between 0.01 to 1.5 cm/a with corresponding effective viscosities between $3.5 \cdot 10^{18}$ and $1.5 \cdot 10^{21}$ Pa s.

(c) Qiangtang terrane: Beneath the centre of the Qiangtang terrane the conductances on the 500- and 600-line are similar to the ones observed beneath the southern Lhasa block. Therefore, the flow velocities and effective viscosities in this region are expected to be the same as in (a).

(d) Eastern Tibet: The additional MT measurements from Eastern Tibet (Bai et al., 2010) observe conductances between 15,000 and 30,000 S, suggesting flow velocities of 0.07 – 192 cm/a and effective viscosities of $1.7 \cdot 10^{17}$ - $1.2 \cdot 10^{20}$ Pa s for granitic melt. For aplite melt, the estimated flow velocities exceed 10 cm/a independent of the melt resistivity. These unreasonable large flow velocities are again due to the assumption of a purely aplitic melt composition (see discussion in section 5.5.1).

As in the previous section the presented results suggest two possible zones of channel flow. Beneath both the southern Lhasa block and the Qiangtang terrane the minimum flow velocities are high enough to allow for southward directed flow towards the Indian foreland (Beaumont et al., 2001) and eastward directed flow along the Jinsha River suture (Clark & Royden, 2000). In contrast, for the northern Lhasa block the flow velocities for granitic melt are too low for flow at geologically significant rates. Instead, if channel flow in this region is observed it is most likely too slow to provide an effective mechanism for mass transport.

5.5 Discussion

5.5.1 Assumptions made in the calculations

The results presented above show that by considering the bulk electrical properties (i.e. the layer conductance), information can be derived about the bulk flow properties of a layer. It is important to note the assumptions that have been made during the calculation of the flow velocities and effective viscosities shown in Figure 5.14 and Figure 5.15. These include:

1. The calculations presented above assume a felsic composition, which is characteristic for the upper crust. Mafic rocks, which are characteristic for the lower crust, have a stronger rheology (e.g. Carter & Tsenn, 1987). A compilation of seismic velocity models by Mechie et al. (2011) shows that in Tibet the boundary between the felsic upper crust and the mafic lower crust is located at 30-40 km depth. For a channel located below this boundary, the strength and thus the effective viscosity of the flow channel would be higher due to the mafic composition. As a consequence, the expected flow velocities would be lower than the ones calculated. Additional laboratory measurements on more mafic rocks are required to determine to what degree the more mafic lower crust in Tibet is susceptible to crustal flow.

2. Assuming a felsic composition, mid-crustal rocks are probably best described by the laboratory results for granite. This is because during the crystallization of magmas under mid-crustal conditions, coarse-grained rocks of granitic composition are formed. The residual melt at the end of this process

crystallizes to aplite which is fine grained and intersects the granites in forms of veins. As a result, the melt might contain a significant fraction of aplite during the initial onset of melting which would lead to a larger strength reduction than for pure granite. However, for larger melt fractions the composition of the melt is predominantly granitic.

3. For the calculations of the flow velocity and effective viscosity, the thickness of the channel was assumed to be constant. This assumption is partly based on the fact that magnetotelluric measurements are not able to resolve the thickness of a conductive layer but only its conductance. Seismic observations could provide additional constraints on the thickness of the weakened mid-crustal layer. Using these observations, a more sophisticated model which accounts for lateral variations in the channel thickness could be developed.

4. The material constant (A_{eff}) in the power law rheological equation normally depends on temperature and pressure and consequently varies with depth, but it was chosen to be constant over the entire depth of the channel. As temperature and pressure variations in the middle crust are poorly known, it is only possible to define an average material constant for that depth range. However, the resulting error should be acceptable for this simplified model.

5. The power law exponent ($n = 3$) was chosen according to the laboratory measurements of Rutter & Neumann (1995). As the flow velocity in equation (2.32) can be either positive or negative depending on the pressure gradient, the power law exponent has to be odd. A power law exponent of $n = 1$

corresponding to Newtonian flow leads to unrealistic flow velocities exceeding 1 km/a, while an exponent of $n = 5$ corresponds to flow velocities less than 0.003 cm/a and prevents any kind of geologically significant crustal flow (equation (2.31)).

6. Due to the power law dependence of the flow velocity and the effective viscosity on the pressure gradient, the results presented above are particularly sensitive to variations in pressure gradient. The value of the pressure gradient used above was chosen for the central part of the Tibetan Plateau where variations in topography are only observed over large horizontal distances. However, near the edges of the plateau the topography variations occur on a much shorter horizontal scale. Therefore, the assumed pressure gradient represents a lower bound.

At the eastern margin of the Tibetan Plateau, for example, the elevation locally changes by 5000 m over a horizontal distance of 100 km (e.g. Clark & Royden, 2000). The resulting pressure gradient is 5 times larger than the one assumed in the above calculations. For a power law exponent of $n = 3$, this leads to an increase of the flow velocities by a factor of 125 (equation (2.23)) and to a reduction of the effective viscosities by a factor of 25 (equation (5.14)).

7. The model assumes laterally unconstrained channel flow and does not take lateral variations in crustal strength into account. Therefore, it cannot explain the dynamic topography of the eastern plateau margin which has been inferred to have produced steep gradients where flow is inhibited by the rigid Sichuan basin

and gentle slopes in regions of unobstructed flow (Clark et al., 2005). Instead, the highest flow velocities and lowest viscosities are found beneath the steep margins of the plateau contrary to the modeling studies by Clark & Royden (2000) which suggest high viscosities in this region. This suggests that the actual flow velocities are rate limited not by the viscosity of the unconstrained flow model, but by the resistance at the boundaries.

8. The temperature and pressure for partial melting in the middle crust was assumed to be the same as in the laboratory experiments that used a temperature of 700-1100°C and a pressure of 250 MPa. This pressure corresponds to a depth of 10 km and is therefore a factor of 2 to 3 too small. However, as the material constant in the power law is highly temperature dependant this pressure difference may not be significant. Instead, the estimate the effect of temperature T, equation (5.1) can be rewritten as

$$\tau^n = A'_{\text{eff}}\, e^{\frac{Q}{RT}}\dot{\varepsilon} \tag{5.18}$$

where A'_{eff} is the temperature independent material constant, Q is the activation energy and R the universal gas constant. If

$$A_{\text{eff}}^{T_0} = A'_{\text{eff}}\, e^{\frac{Q}{RT_0}} \tag{5.19}$$

is the material constant obtained from laboratory measurements at a temperature T_0, the material constant $A_{\text{eff}}^{\text{T}}$ at an arbitrary temperature T is given by

$$A_{\text{eff}}^{T} = A_{\text{eff}}^{T_0} e^{\frac{Q}{R}\left(\frac{1}{T}-\frac{1}{T_0}\right)} \tag{5.20}$$

Therefore, in order to take different temperatures into account the mean velocity in equation (5.8) needs to be multiplied by a factor $e^{-\frac{Q}{R}\left(\frac{1}{T}-\frac{1}{T_0}\right)}$.

In the calculation of the mean velocities in section 5.4, the temperatures in the middle crust were assumed to be the same as in the laboratory experiment (700-1100°C). Rutter & Neumann (1995) state the relationship between the melt fraction ϕ and the temperature T (given in °C) in their measurements as

$$\phi = \frac{1}{265.07} e^{0.00875T} \tag{5.21}$$

Therefore, the melt fractions of 4 to 23 percent required to explain the observed conductances in Tibet correspond to temperatures between approximately 810°C and 1020°C in the laboratory experiment. This range of temperatures is in agreement with the observed α-β-quartz transition in the southern Qiangtang terrane beneath the 500-line at a depth of 18 km corresponding to a temperature of 700°C (Mechie et al., 2004). The temperature gradient in this region was estimated as 39°C/km so that the above temperatures should be achieved 3 to 8 km below the transition.

However, even small uncertainties in the temperature estimate can significantly change the resulting flow parameters. Assuming an activation energy of 320 kJ/mol for granite melt (Rutter & Neumann, 1995) and an average temperature of 850°C for the laboratory measurements, a 150°C lower crustal temperature would

result in a reduction of the flow velocity and an increase in effective viscosity by a factor of 200. Similarly, for a 150°C higher crustal temperature the flow velocity and the effective viscosity would increase respectively decrease by a factor of 50.

Temperature has a strong effect not only on the degree of partial melting but also on the material constant and the bulk flow properties. Additional independent temperature estimates are therefore required to further constrain these parameters. This will help to better determine the extent of channel flow beneath the Tibetan Plateau and its role in the overall mass balance of the continent-continent collision.

5.5.2 Comparisons of the effective viscosities

A comparison of the estimated effective viscosities for granitic melt with the results obtained for gravitationally driven flow by other authors generally shows a good agreement for the different regions in Tibet (see Figure 5.16 and Figure 5.17):

(a) Southern Lhasa block: The conductance values of 10,000 S suggest effective viscosities between $1 \cdot 10^{19}$ and $3 \cdot 10^{20}$ Pa s beneath the southern Lhasa block assuming constant bulk resistivities of 3 and 10 Ωm. For constant thicknesses of 20 and 50 km the viscosities range between $2.5 \cdot 10^{18}$ and $3 \cdot 10^{20}$ Pa s. These results are in agreement with studies by Copley & McKenzie (2007) who model the

deformation in this region by southward directed crustal flow of a low viscosity layer (10^{20} Pa s) between rigid, but vertically deformable boundaries. Beaumont et al. (2001) suggest that slightly lower viscosities (10^{19} Pa s) are required to sustain channel flow. If the higher pressure gradients due to steeper topography gradients towards the plateau margin are taken into account, the effective viscosities estimated by the magnetotelluric observations will be reduced by approximately one order of magnitude, which is sufficiently low to sustain crustal flow beneath the High Himalayas.

(b) Northern Lhasa block: The average conductance of 3000 S beneath the northern Lhasa block corresponds to effective viscosities between $1 \cdot 10^{20}$ and $3.5 \cdot 10^{21}$ Pa s for constant bulk resistivities of 3 and 10 Ωm. Assuming constant thicknesses of 20 and 50 km the effective viscosities range between $3.5 \cdot 10^{20}$ and $3 \cdot 10^{21}$ Pa s. While no specific modelling studies for this region exist, the results by Beaumont et al. (2001) for the southern Lhasa block suggest that the effective viscosities determined here are at least one order of magnitude too high to allow channel flow. Lower effective viscosities could be possible if higher temperatures than suggested by seismic observations were assumed. A 150°C higher temperature would result in effective viscosities between $2 \cdot 10^{18}$ and $7 \cdot 10^{19}$ Pa s. While these viscosities are low enough to allow for channel flow, the flow might not be strongly pronounced with corresponding flow velocities between 0.02 and 2 cm/a.

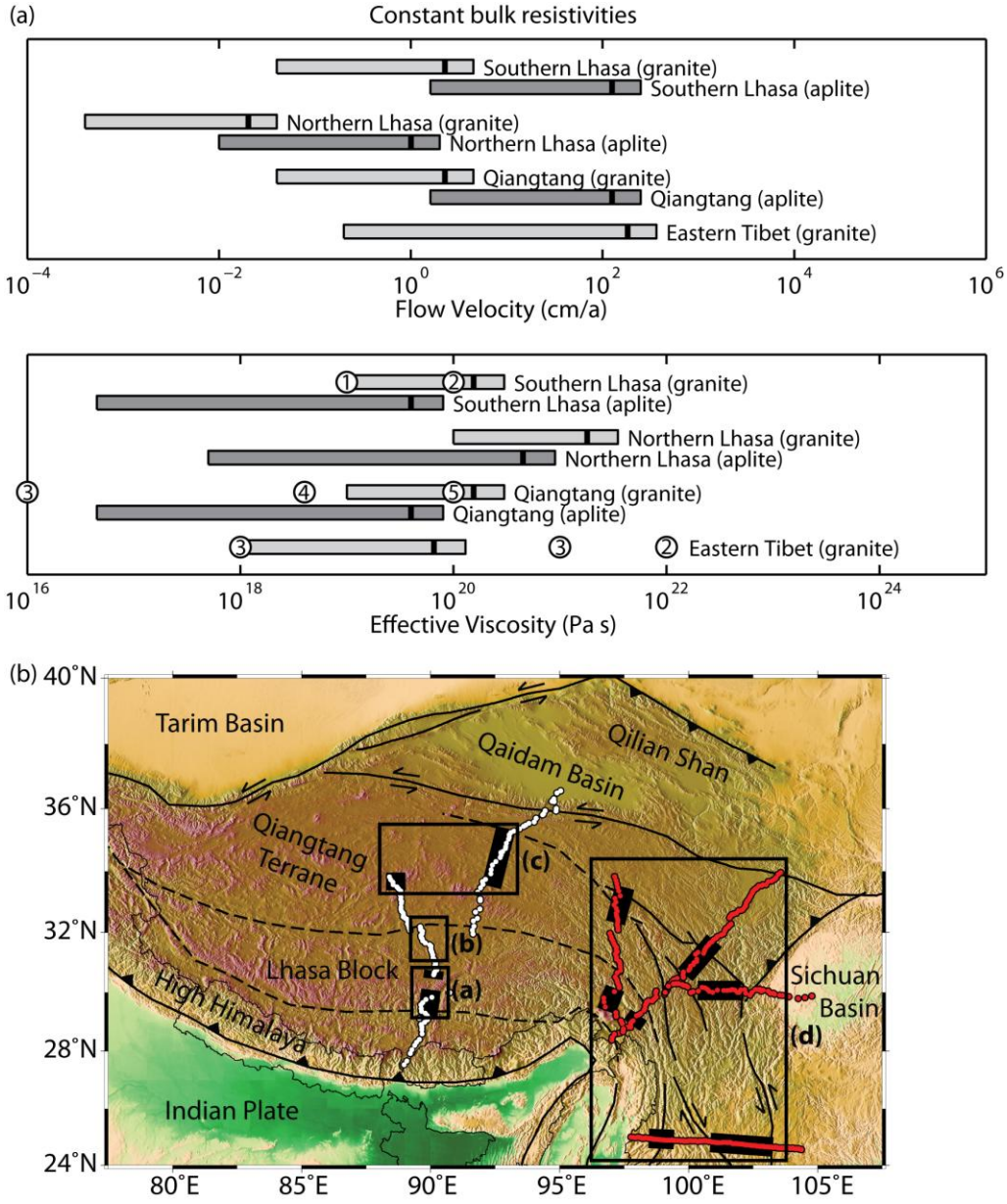

Figure 5.16: Comparison of the expected flow velocity and effective viscosities for the (a) southern Lhasa block, (b) northern Lhasa block, (c) Qiangtang terrane and eastern Tibet assuming constant bulk resistivities The different regions are highlighted on the map in (b). The black bars indicate the average values for the plotted range. The circles indicate viscosity estimates by (1) Beaumont et al. (2001), (2) Copley & McKenzie (2007), (3) Clark & Royden (2000), (4) Ryder et al. (2007) and (5) Bendick & Flesch (2007) for comparison. (b) Topographic map of Tibet. The regions discussed in this chapter are highlighted. The black bars correspond to regions with conductances exceeding 10,000S.

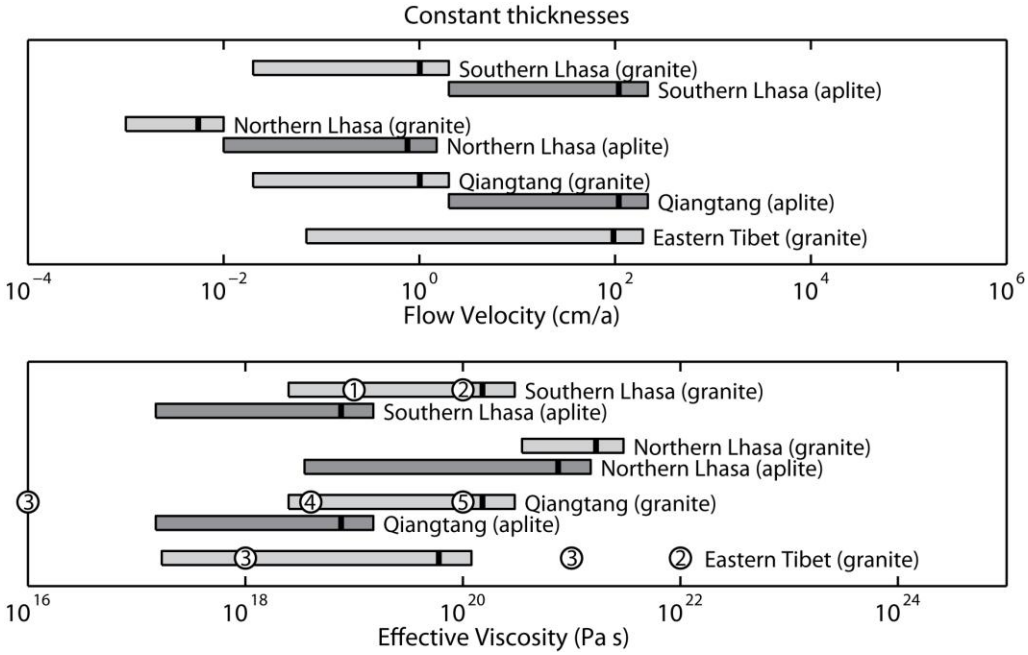

Figure 5.17: Comparison of the expected flow velocity and effective viscosities for the (a) southern Lhasa block, (b) northern Lhasa block, (c) Qiangtang terrane and eastern Tibet assuming constant thicknesses The different regions are highlighted on the map in Figure 5.16. The black bars indicate the average values for the plotted range. The circles indicate viscosity estimates by (1) Beaumont et al. (2001), (2) Copley & McKenzie (2007), (3) Clark & Royden (2000), (4) Ryder et al. (2007) and (5) Bendick & Flesch (2007) for comparison.

(c) Qiangtang terrane: The conductances beneath the Qiangtang terrane are similar to the ones in the southern Lhasa terrane and suggest effective viscosities between $1 \cdot 10^{19}$ and $3 \cdot 10^{20}$ Pa s for constant bulk resistivity and $2.5 \cdot 10^{18}$ and $3 \cdot 10^{20}$ Pa s for constant thickness in this region. The viscosities for constant bulk resistivity are about one order of magnitude larger than the best fitting viscosity of $4 \cdot 10^{18}$ Pa s suggested by Ryder et al. (2007) to explain the postseismic deformation after the 1997 Manyi earthquake, but the viscosity by Ryder et al. (2007) agrees with the viscosities for constant thickness. Geodynamic modelling studies by Clark & Royden (2000) indicate even lower viscosities (10^{16} Pa s)

beneath the central part of the plateau. In contrast, Bendick & Flesch (2007) suggest viscosities of the order 10^{20} Pa s for a low viscosity region with deformable boundaries. These viscosities agree well with the ones estimated in this chapter.

(d) Eastern Tibet: Beneath eastern Tibet the conductances exceed 30,000 S corresponding to effective viscosities between $1.2 \cdot 10^{18}$ and $1.3 \cdot 10^{20}$ Pa s assuming constant bulk resistivities of 3 and 10 Ωm. For constant thicknesses of 20 and 50 km, the effective viscosities are between $1.7 \cdot 10^{17}$ and $1.2 \cdot 10^{20}$ Pa s. These results are in agreement with studies by Clark & Royden (2000) who explain the topographic gradients along the eastern margins by eastward directed Poiseuille flow of a low viscosity layer (10^{18}-10^{21} Pa s) with rigid boundaries. In contrast, Copley & McKenzie (2007) use a model with a stress-free lower boundary, laterally bounded by the rigid Indian lowlands and the Sichuan basin. In this case, effective viscosities of 10^{22} Pa s are required to explain the southeastward directed surface motion between the Sichuan basin and the Eastern Himalaya syntaxis.

5.6 Summary

A number of geophysical observations in Tibet give evidence for the presence of a weak middle to lower crust. The most likely explanation for the reduced strength at these depths is a layer of partial melt. Laboratory measurements on partially molten granite indicate that melt fractions of 5-10 % can reduce the strength of

the rock by one order of magnitude. It is thus important to determine the amount of fluid present in the crust and to determine if flow would occur, and to estimate the velocity for the different flow modes (Couette and Poiseuille). In this chapter, it has been shown that magnetotelluric studies can give estimates of the partial melt fraction at mid- to lower crustal depths. In contrast to previous studies, a direct relationship between the parameters for Poiseuille flow and the electrical conductance of the channel has been established.

These relationships have been applied to different regions in Tibet to estimate possible Poiseuille flow velocities and to determine the extent of topography-driven channel flow:

(a) Southern Lhasa block: Magnetotelluric studies in the southern Lhasa block indicate a low resistivity layer at mid-crustal depths with conductances exceeding 10,000 S. Assuming constant bulk resistivities between 3 and 10 Ωm and a granitic composition, the flow velocities are predicted in the range 0.4 - 4.5 cm/a for a topographically induced pressure gradient of the order 80 Pa/m. Similarly, for constant thicknesses of 20 and 50 km the predicted flow velocities range between 0.02 and 2 cm/a. Given the higher pressure gradient towards the plateau margins these velocities support southward flow beneath the High Himalayas as suggested by thermal-mechanical modeling studies (Beaumont et al., 2001). The corresponding effective viscosities range between $1 \cdot 10^{19}$ and $3 \cdot 10^{20}$ Pa s in case of constant bulk resistivity and $2.5 \cdot 10^{18}$ and $3 \cdot 10^{20}$ Pa s in case of constant

thickness. They are in agreement with a viscosity of the order 10^{19} Pa s required to sustain crustal flow in the High Himalayas.

(b) Northern Lhasa block: For the northern Lhasa block, the average conductance was found to be 3000 S. This conductance corresponds to flow velocities between 0.0004 to 0.04 cm/a in case of constant bulk resistivity and 0.001 to 0.01 cm/a in case of constant thickness assuming a granitic composition. The corresponding effective viscosities range between $1 \cdot 10^{20}$ and $3.5 \cdot 10^{21}$ Pa s for constant bulk resistivity and $3.5 \cdot 10^{20}$ and $3 \cdot 10^{21}$ Pa s for constant thickness. Given the strong temperature dependence of the flow parameters, the minimum flow velocities might be larger if a higher temperature at mid-crustal depths than suggested by seismic observations (~850°C at 22 km depth) is assumed. For a 150°C higher temperature the flow velocities range between 0.02 to 2 cm/a. Therefore, if channel flow beneath the northern Lhasa block exists, the temperatures must be higher than suggested. However, even with higher temperatures the flow might not be strongly pronounced for regions with such a low conductance.

(c) Qiangtang terrane: Beneath the Qiangtang terrane, conductances similar to the ones beneath the southern Lhasa block were observed. The flow velocities and effective viscosities are expected to be of the same order as beneath the southern Lhasa block, strongly suggesting eastward directed Poiseuille flow.

(d) Eastern Tibet: Additional measurements by Bai et al. (2010) as part of the separate EHS3D project suggest that the zone of channel flow beneath the

Qiangtang terrane extends along the Jinsha River suture as far east as the Red River and Xiaojiang faults. The higher pressure gradient and conductances of up to 30,000 S towards the eastern plateau margin suggest a well developed channel beneath wide parts of the Qiangtang terrane as suggested by Clark & Royden (2000). The effective viscosities in this region range between $1.2 \cdot 10^{18}$ and $1.3 \cdot 10^{20}$ Pa s for constant bulk resistivity and $1.7 \cdot 10^{17}$ and $1.2 \cdot 10^{20}$ Pa s for constant thickness, which are in agreement with the viscosities required to explain the topographic gradients along the eastern margins.

In general, the channel flow in Tibet is likely a combination of both Couette and Poiseuille flow. Based on a slip rate estimate of 2 cm/a of India beneath Tibet (Bilham et al., 1997), the mean velocity of the Couette flow can be calculated as 1 cm/a. The power law relationship between the Poiseuille flow velocity and the conductance derived in this chapter suggests that topography-driven flow of comparable velocity will be observed as soon as the conductance exceeds a critical value. For a granitic composition, conductances between 7000 and 22,000 S in case of constant resistivity and between 9000 and 27,000 S in case of constant thickness are required to obtain Poiseuille flow velocities of the order 1 cm/a, assuming a temperature of 850°C and a lateral pressure gradient of 80 Pa/m. For flow velocities exceeding this threshold, Poiseuille flow is the dominant flow mode, contributing significantly to the overall mass balance required in the continent-continent collision. It should be emphasized that the calculations

presented in this chapter have assumed a felsic composition for the crustal material. If the rocks were more mafic in character, then the crust would be stronger leading to reduced flow velocities. Nevertheless, the highest flow velocities would still be expected in regions with the highest conductances, leaving the suggested possible flow patterns unchanged. Additional laboratory measurements on mafic rocks are required to determine to what degree topography variations in this case are still the most important driving force for channel flow in Tibet.

The range of conductances required for flow velocities of 1 cm/a is expected to shift to lower values for regions near the margins of the plateau where higher pressure gradients are expected. To further limit the range of conductances that are in agreement with channel flow, a more constrained temperature estimate in these regions is required. Furthermore, additional geophysical measurements would provide improved constraints on the composition, melt fraction and channel thickness, and thus on the flow parameters.

The relationships presented in this chapter allow the inclusion of magnetotelluric observations as a constraint in more sophisticated geodynamic modeling studies. Together with a well defined temperature model, these studies can allow insight into possible crustal flow patterns for Tibet, and thus a better understanding of the evolution of the collision between the Indian and Asian continents and other continental collision zones.

6 Conclusions

Convergent plate boundaries play a major role in the growth and assembly of the modern continents. To understand the deformation processes that have formed and shaped the continents, it is important to understand the rheology of the crust and mantle, which is controlled by their composition, temperature and the presence of fluid phases. Magnetotelluric observations provide a powerful tool to constrain the rheology of the crust and mantle, as they are particularly sensitive to temperature and the presence of small amounts of fluids, such as aqueous fluids or melt. In this thesis, two types of convergent boundary were discussed: (i) the Cascadia subduction zone located on the west coast of North America as an example of active subduction of oceanic crust beneath a continental plate and (ii) the Indian-Asian collision as an example of a modern continent-continent collision.

6.1 The Cascadia subduction zone and the Canadian Cordillera

Previous geophysical studies of the Canadian Cordillera have provided an understanding of the crustal structure in this region and show a change in geophysical parameters and structure across the western margin of the North American Craton. The Canadian Cordillera is characterized by high heat flow as well as low seismic velocities and low electrical resistivities in the uppermost mantle compared to the North American Craton, suggesting unusually high temperatures at these depths (Currie et al., 2004a).

In this thesis, an extension of the first long-period magnetotelluric study of the Canadian Cordillera by Soyer & Unsworth (2006) was presented. The combined magnetotelluric data set extends across the entire backarc region, and has been used to derive electrical resistivity models of the crust and mantle beneath the Canadian Cordillera. Previous analyses showed that the electrical resistivity models can be explained by either aqueous fluid or melt (Soyer & Unsworth, 2006) but weren't able to distinguish which of these fluids is present in different regions of the mantle. In this thesis, thermodynamic calculations on the reduction of the mantle solidus temperature in the presence of water (Hirschmann et al., 2009) were used to constrain regions of dehydration melting. A key aspect in this analysis is a knowledge of the mantle temperatures, which were calculated from seismic velocity data from Mercier et al. (2009). While there is significant uncertainty in the conversion from seismic velocity to mantle temperature, the presented analyses show how a joint interpretation of magnetotelluric and seismic data can help to reduce the non-uniqueness associated with the interpretation of magnetotelluric data.

In the forearc region, the electrical resistivity models indicate an east-dipping conductor and a conductive mantle wedge above the subducting Juan de Fuca plate, caused by the release of aqueous fluids from the subducting slab. Low resistivities are also found beneath the volcanic arc, which can be explained by a water content of 750-1500 ppm. This water content is sufficient to lower the mantle solidus temperature beneath the volcanic arc to allow dehydration melting with melt fractions between 0.5 and 2%.

Low resistivities in the backarc upper mantle at depths less than 60 km suggest a shallow asthenosphere compared to the adjacent North American craton where the lithosphere-asthenosphere boundary is at ~200 km (Türkoğlu et al., 2009). The boundary between the backarc and the adjacent North American craton is well defined between the Omineca and Foreland Belts for the northern part of the study area, while for the southern part, highly resistive mantle rocks extend underneath the Omineca Belt at depths greater than 100 km. The low resistivities in the backarc require aqueous fluids in the shallow upper mantle at depths less than 100 km. Based on the hydrogen diffusion model by Karato (1990), the water content in the backarc mantle increases from 500-750 ppm in the northern part to 750-1000 ppm in the southern part of the study area. In addition, partial melting with melt fractions ranging between 0.5 to 1.5% in the north and 1.5 to 2.5% in the south is required to explain the data. The alternate model by Wang et al. (2006) requires significantly less water than the model by Karato (1990). Therefore, these numbers correspond to the maximum amount of water and melt required to explain the magnetotelluric data of the Canadian Cordillera.

The presence of aqueous fluids and partial melt is expected to affect the rheology of the mantle by lowering its viscosity (Dixon et al., 2004). For a water content of of 500-1000 ppm in the backarc of the Canadian Cordillera, viscosities between $3.1 \cdot 10^{19}$ and $3.9 \cdot 10^{19}$ Pa s at a depth of 75 km were calculated, assuming a strain rate of 10^{-15} s^{-1}. As these viscosities are significantly lower than the global average for continental shield areas (~10^{20}-10^{21} Pa s), the backarc mantle might be susceptible to vigorous mantle convection (e.g. Honda et al., 2002). This result is

in agreement with geodynamic modeling studies, which require vigorous convection of a low viscosity mantle to explain the consistently high temperatures in the backarc region (Currie et al., 2004a).

6.2 The India-Asia continent-continent collision in Tibet

Several classes of geodynamic models have been proposed to explain the evolution of the Himalayan orogen and the Tibetan Plateau. Models invoking flow in a weak lower crustal layer (channel flow) have been successful in explaining a number of geological and geophysical observations (Clark & Royden, 2000; Beaumont et al., 2001). Geophysical observations indicate that the weak layer at mid- to lower crustal depths in Tibet may be the result of partial melting (Klemperer, 2006). Laboratory studies indicate one order of reduction in strength for melt fractions of 5‑10% (Rosenberg & Handy, 2005). In this thesis, the flow parameters associated with the channel flow model were estimated by relating these laboratory studies to magnetotelluric observations. The calculations show that in the Central Tibetan Plateau, if a crustal layer consists of partially molten felsic rocks, conductances in the range 7000‑27,000 S will produce crustal flow velocities of the order 1 cm/a. Beneath the southern part of the Lhasa block and the Qiangtang terrane magnetotelluric studies indicate conductances of up to 20,000 S. These conductances suggest effective viscosities of 2.5×10^{18} to 3×10^{20} Pa s, corresponding to flow velocities between 0.02 and 4.5 cm/a. Together with higher pressure gradients near the margins of the plateau these flow

parameters support the idea that channel flow could occur in these parts of Tibet. Additional MT measurements in eastern Tibet suggest that the zone of channel flow beneath the Qiangtang terrane extends along the Jinsha River suture as far east as the Red River and Xiaojiang faults (Bai et al., 2010). Lower crustal conductances (3000 S) are reported beneath the northern Lhasa block and crustal deformation by channel flow in this region is unlikely. Assuming a felsic rock composition, the minimum effective viscosity of the crust beneath the northern Lhasa block is estimated as 3×10^{20} Pa s. The corresponding flow velocities do not exceed 0.04 cm/a unless higher temperatures than suggested by seismic observations are assumed.

The two studies described in this thesis show how non-uniqueness in the interpretation of magnetotelluric data can be reduced by using constraints from additional geophysical or geochemical measurements. At the same time, the interpretation of the two convergent plate boundaries is limited by simplifications made during the analysis. Some of these simplifications are based on the lack of laboratory measurements and the limited understanding on how to extrapolate the results to crustal and mantle depths. Therefore, the presented analyses are expected to yield better constrained results as our understanding of laboratory measurements on the rheology of the crust and mantle improves.

Endnotes

[1] Reprinted from *Journal of Geophysical Research*, **91**(B2), Gough, D.I., Mantle Upflow Tectonics in the Canadian Cordillera, 1909-1919, Copyright 1986, with permission from American Geophysical Union

[2] Reprinted from *Earth and Planetary Science Letters*, **223**(1-2), Currie, C.A., Wang, K., Hyndman, R.D. & He, J., The thermal effects of steady-state slab-driven mantle flow above a subducting plate: the Cascadia subduction zone and backarc, 35-48, Copyright 2004, with permission from Elsevier

[3] Reprinted from *Geochemistry Geophysics Geosystems*, **9**(3), Hacker, B.R., H2O subduction beyond arcs, Copyright 2008, with permission from American Geophysical Union

[4] Reprinted from *Journal of Geophysical Research*, **111**(B8), Currie, C.A. & Hyndman, R.D., The thermal structure of subduction zone back arcs, 1-22, Copyright 2006, with permission from American Geophysical Union

[5] Reprinted from *Journal of Geophysical Research*, **111**(B8), Currie, C.A. & Hyndman, R.D., The thermal structure of subduction zone back arcs, 1-22, Copyright 2006, with permission from American Geophysical Union

[6] Reprinted from *Journal of Geophysical Research*, **95**(B7), Kurtz, R.D., DeLaurier, J.M. & Gupta, J.C., The Electrical Conductivity Distribution Beneath Vancouver Island: a Region of Active Plate Subduction, 10929-10946, Copyright 1990, with permission from American Geophysical Union

[7] Adapted from *Geophysical Journal International*, **161**(3), Nicholson, T., Bostock, M. & Cassidy, J.F., New constraints on subduction zone structure in northern Cascadia, 849-859, Copyright 2005, with permission from John Wiley and Sons

[8] Reprinted from *Geology*, **34**(1), Soyer, W. & Unsworth, M., Deep electrical structure of the northern Cascadia (British Columbia, Canada) subduction zone: Implications for the distribution of fluids, 53-56, Copyright 2006, with permission from Geological Society of America

[9] Adapted by permission from Macmillan Publishers Ltd: *Nature*, **347**(6290), Karato, S., The role of hydrogen in the electrical conductivity of the upper mantle, 272-273, Copyright 1990

[10] Adapted by permission from Macmillan Publishers Ltd: *Nature*, **443**(7114), Wang, D., Mookherjee, M., Xu, Y. & Karato, S., The effect of water on the electrical conductivity of olivine, 977-980, Copyright 2006

[11] Reprinted from *Physics of the Earth and Planetary Interiors*, **176**(1-2), Hirschmann M.M., Tenner T., Aubaud C. & Withers, A.C., Dehydration melting of nominally anhydrous mantle: The primacy of partitioning, 54-68, Copyright 2009, with permission from Elsevier

[12] Adapted from *Journal of Geophysical Research*, **112**(B8), Gan, W., Zhang, P., Shen, Z.-K., Niu, Z., Wang, M., Wan, Y., Zhou, D. & Cheng, J., Present-day crustal motion within the Tibetan Plateau inferred from GPS measurements, B08416, Copyright 2007, with permission from American Geophysical Union

[13] Reprinted from *Geology*, **28**(8), Clark, M.K. & Royden, L.H., Topographic ooze: Building the eastern margin of Tibet by lower crustal flow, 703, Copyright 2000, with permission from Geological Society of America

[14] Reprinted by permission from Macmillan Publishers Ltd: *Nature*, **414**(6865), Beaumont, C., Jamieson, R.A., Nguyen, M.H. & Lee, B., Himalayan tectonics explained by extrusion of a low-viscosity crustal channel coupled to focused surface denudation, 738-742, Copyright 2001

[15] Adapted from *Journal of Metamorphic Geology*, **23**(1), Rosenberg, C.L. & Handy, M.R., Experimental deformation of partially melted granite revisited: implications for the continental crust, 19-28, Copyright 2005, with permission from John Wiley and Sons

[16] Adapted from *Earth and Planetary Science Letters*, **114**(1), Holness, M.B., Equilibrium dihedral angles in the system quartz-CO2-H2-ONaCl at 800°C and 1–15 kbar: the effects of pressure and fluid composition on the permeability of quartzites, 171-184, Copyright 1992, with permission from Elsevier

[17] Reprinted from *Earth and Planetary Science Letters*, **180**(3-4), Glover, P.W.J., Hole, M.J. & Pous, J., A modified Archie's law for two conducting phases, 369-383, Copyright 2000, with permission from Elsevier

[18] Adapted from *Earth and Planetary Science Letters*, **277**(3-4), Hyndman, R.D., Currie, C.A., Mazzotti, S. & Frederiksen, A., Temperature control of continental lithosphere elastic thickness, Te vs Vs, 539-548, Copyright 2009, with permission from Elsevier

[19] Adapted from *Journal of Geophysical Research*, **105**(B5), Goes, S., Govers, R. & Vacher, P., Shallow mantle temperatures under Europe from P and S wave

tomography, 11153-11169, Copyright 2000, with permission from American Geophysical Union

[20] Adapted from *Earth and Planetary Science Letters*, **277**(3-4), Hyndman, R.D., Currie, C.A., Mazzotti, S. & Frederiksen, A., Temperature control of continental lithosphere elastic thickness, Te vs Vs, 539-548, Copyright 2009, with permission from Elsevier

Bibliography

Aitchison, J.C., Ali, J.R. & Davis, A.M., 2007. When and where did India and Asia collide? *Journal of Geophysical Research*, **112**(B5), 1-19.

Alsdorf, D. & Nelson, D., 1999. Tibetan satellite magnetic low: Evidence for widespread melt in the Tibetan crust? *Geology*, **27**(10), 943.

Archie, G.E., 1942. The electrical resistivity log as an aid in determining some reservoir characteristics. *Transactions of the American Institute of Mining, Metallurgical and Petroleum Engineers*, **146**, 54–62.

Aubaud, C., Hauri, E.H. & Hirschmann, M.M., 2004. Hydrogen partition coefficients between nominally anhydrous minerals and basaltic melts. *Geophysical Research Letters*, **31**(20), 2-5.

Bahr, K., 1991. Geological noise in magnetotelluric data: a classification of distortion types. *Physics of The Earth and Planetary Interiors*, **66**(1-2), 24-38.

Bahr, K., 1988. Interpretation of the magnetotelluric impedance tensor: regional induction and local telluric distortion. *Journal of Geophysics*, **62**, 119-127.

Bai, D. et al., 2010. Crustal deformation of the eastern Tibetan plateau revealed by magnetotelluric imaging. *Nature Geoscience*, **3**(5), 358-362.

Bai, Q. & Kohlstedt, D.L., 1992. Substantial hydrogen solubility in olivine and implications for water storage in the mantle. *Nature*, **357**(6380), 672-674.

Beaumont, C. et al., 2001. Himalayan tectonics explained by extrusion of a low-viscosity crustal channel coupled to focused surface denudation. *Nature*, **414**(6865), 738-42.

Bell, D.R. et al., 2003. Hydroxide in olivine: A quantitative determination of the absolute amount and calibration of the IR spectrum. *Journal of Geophysical Research*, **108**(B2), 1-9.

Bendick, R. & Flesch, L., 2007. Reconciling lithospheric deformation and lower crustal flow beneath central Tibet. *Geology*, **35**(10), 895.

Berckhemer, H. et al., 1982. Shear modulus and Q of forsterite and dunite near partial melting from forced-oscillation experiments. *Physics of the Earth and Planetary Interiors*, **29**(1), 30-41.

Bilham, R., Larson, K. & Freymueller, J., 1997. GPS measurements of present-day convergence across the Nepal Himalaya. *Nature*, **386**(6620), 61-64.

Black, P.R. & Braile, L.W., 1982. Pn velocity and cooling of the continental lithosphere. *Journal of Geophysical Research*, **87**(B13), 10557-10568.

Bostock, M.G. et al., 2002. An inverted continental Moho and serpentinization of the forearc mantle. *Nature*, **417**(6888), 536-8.

Braitenberg, C. et al., 2003. Spatial variations of flexure parameters over the Tibet–Quinghai plateau. *Earth and Planetary Science Letters*, **205**(3-4), 211-224.

Brocher, T.M. et al., 2003. Seismic evidence for widespread serpentinized forearc upper mantle along the Cascadia margin. *Geology*, **31**(3), 267.

Bruhn, R.L. et al., 2004. Deformation during terrane accretion in the Saint Elias orogen, Alaska. *Geological Society of America Bulletin*, **116**(7), 771.

Burchfiel, B.C. et al., 1995. Tectonics of the Longmen Shan and Adjacent Regions, Central China. *International Geology Review*, **37**(8), 661-735.

Bürgmann, R. & Dresen, G., 2008. Rheology of the Lower Crust and Upper Mantle: Evidence from Rock Mechanics, Geodesy, and Field Observations. *Annual Review of Earth and Planetary Sciences*, **36**(1), 531-567.

Cagniard, L., 1953. Basic Theory Of The Magneto-Telluric Method Of Geophysical Prospecting. *Geophysics*, **18**(3), 605.

Cammarano, F. et al., 2003. Inferring upper-mantle temperatures from seismic velocities. *Physics of The Earth and Planetary Interiors*, **138**(3-4), 197-222.

Carter, N.L. & Tsenn, M.C., 1987. Flow properties of continental lithosphere. *Tectonophysics*, **136**(1-2), 27-63.

Chapman, D.S., 1986. Thermal gradients in the continental crust. *Geological Society, London, Special Publications*, **24**(1), 63-70.

Chave, A.D. & Smith, J.T., 1994. On electric and magnetic galvanic distortion tensor decompositions. *Journal of Geophysical Research*, **99**(B3), 4669-4682.

Chen, L. et al., 1996. Electrically Conductive Crust in Southern Tibet from INDEPTH Magnetotelluric Surveying. *Science*, **274**(5293), 1694-1696.

Chen, W.-P. & Molnar, P., 1983. Focal depths of intracontinental and intraplate earthquakes and their implications for the thermal and mechanical properties of the lithosphere. *Journal of Geophysical Research*, **88**(B5), 4183-4214.

Chen, W.-ping & Yang, Z., 2004. Earthquakes beneath the Himalayas and Tibet: evidence for strong lithospheric mantle. *Science (New York, N.Y.)*, **304**(5679), 1949-52.

Christensen, N.I. & Mooney, W.D., 1995. Seismic velocity structure and composition of the continental crust: A global view. *Journal of Geophysical Research*, **100**(B6), 9761.

Clark, M.K., Bush, J.W.M. & Royden, L.H., 2005. Dynamic topography produced by lower crustal flow against rheological strength heterogeneities bordering the Tibetan Plateau. *Geophysical Journal International*, **162**(2), 575-590.

Clark, M.K. & Royden, L.H., 2000. Topographic ooze: Building the eastern margin of Tibet by lower crustal flow. *Geology*, **28**(8), 703.

Clowes, R.M. et al., 1995. Lithospheric structure in the southern Canadian Cordillera from a network of seismic refraction lines. *Canadian Journal of Earth Sciences*, **32**(10), 1485-1513.

Coney, P.J., Jones, D.L. & Monger, J.W.H., 1980. Cordilleran suspect terranes. *Nature*, **288**(5789), 329-333.

Constable, S., 2006. SEO3: A new model of olivine electrical conductivity. *Geophysical Journal International*, **166**(1), 435-437.

Constable, S., Shankland, T.J. & Duba, A., 1992. The Electrical Conductivity of an Isotropic Olivine Mantle. *Journal of Geophysical Research*, **97**(B3), 3397-3404.

Constable, S.C., 1987. Occam's inversion: A practical algorithm for generating smooth models from electromagnetic sounding data. *Geophysics*, **52**(3), 289.

Copley, A. & McKenzie, D., 2007. Models of crustal flow in the India-Asia collision zone. *Geophysical Journal International*, **169**(2), 683-698.

Coward, M. & Dietrich, D., 1989. Alpine tectonics — an overview. *Geological Society Special Publications*, **45**, 1-29.

Currie, C. et al., 2004a. The thermal effects of steady-state slab-driven mantle flow above a subducting plate: the Cascadia subduction zone and backarc. *Earth and Planetary Science Letters*, **223**(1-2), 35-48.

Currie, C.A. et al., 2004b. Shear wave anisotropy beneath the Cascadia subduction zone and western North American craton. *Geophysical Journal International*, **157**(1), 341-353.

Currie, C.A. & Hyndman, R.D., 2006. The thermal structure of subduction zone back arcs. *Journal of Geophysical Research*, **111**(B8), 1-22.

Dixon, J.E. et al., 2004. Lateral variation in upper mantle viscosity: role of water. *Earth and Planetary Science Letters*, **222**(2), 451-467.

Egbert, G.D., 1997. Robust multiple-station magnetotelluric data processing. *Geophysical Journal International*, **130**(2), 475-496.

England, P. & Houseman, G., 1986. Finite Strain Calculations of Continental Deformation 2. Comparison With the India-Asia Collision Zone. *Journal of Geophysical Research*, **91**(B3), 3664-3676.

Fan, G.-W. & Lay, T., 2003. Strong Lg Attenuation in the Tibetan Plateau. *Bulletin of the Seismological Society of America*, **93**(5), 2264-2272.

Fielding, E. et al., 1994. How flat is Tibet? *Geology*, **22**(2), 163.

Fowler, C.M.R., 2004. *The Solid Earth*, Cambridge University Press.

Frederiksen, A.W., Bostock, M.G. & Cassidy, J.F., 2001. S-wave velocity structure of the Canadian upper mantle. *Physics of The Earth and Planetary Interiors*, **124**(3-4), 175-191.

Gamble, T.D., Goubau, W.M. & Clarke, J., 1979. Magnetotellurics with a remote magnetic reference. *Geophysics*, **44**(1), 53.

Gan, W. et al., 2007. Present-day crustal motion within the Tibetan Plateau inferred from GPS measurements. *Journal of Geophysical Research*, **112**(B8), B08416.

Glover, P.W.J., 2010. A generalized Archie's law for n phases. *Geophysics*, **75**(6), E247.

Glover, P.W.J., Hole, M.J. & Pous, J., 2000. A modified Archie's law for two conducting phases. *Earth and Planetary Science Letters*, **180**(3-4), 369-383.

Godin, L. et al., 2006. Channel flow, ductile extrusion and exhumation in continental collision zones: an introduction. *Geological Society, London, Special Publications*, **268**, 1-23.

Goes, S., Govers, R. & Vacher, P., 2000. Shallow mantle temperatures under Europe from P and S wave tomography. *Journal of Geophysical Research*, **105**(B5), 11153-11169.

Gough, D.I., 1986. Mantle Upflow Tectonics in the Canadian Cordillera. *Journal of Geophysical Research*, **91**(B2), 1909-1919.

Green, A.G. et al., 1986. Seismic reflection imaging of the subducting Juan de Fuca plate. *Nature*, **319**(6050), 210-213.

Griffin, W.. et al., 2003. The origin and evolution of Archean lithospheric mantle. *Precambrian Research*, **127**(1-3), 19-41.

Groom, R.W. & Bailey, R.C., 1991. Analytic investigations of the effects of near-surface three-dimensional galvanic scatterers on MT tensor decompositions. *Geophysics*, **56**(4), 496.

Groom, R.W. & Bailey, R.C., 1989. Decomposition of Magnetotelluric Impedance Tensors in the Presence of Local Three-Dimensional Galvanic Distortion. *Journal of Geophysical Research*, **94**(B2), 1913-1925.

Grotenhuis, S.M. ten et al., 2005. Melt distribution in olivine rocks based on electrical conductivity measurements. *Journal of Geophysical Research*, **110**(B12), 1-11.

Grujic, D., 2006. Channel flow and continental collision tectonics: an overview. *Geological Society, London, Special Publications*, **268**(1), 25-37.

Guo, X., Yoshino, T. & Katayama, I., 2011. Electrical conductivity anisotropy of deformed talc rocks and serpentinites at 3GPa. *Physics of the Earth and Planetary Interiors*, **188**(1-2), 69-81.

Hacker, B.R., 2008. H_2O subduction beyond arcs. *Geochemistry Geophysics Geosystems*, **9**(3).

Hammond, W.C. & Humphreys, E.D., 2000. Upper mantle seismic wave velocity: Effects of realistic partial melt geometries. *Journal of Geophysical Research*, **105**(B5), 10975-10986.

Harris, N., 2007. Channel flow and the Himalayan-Tibetan orogen: a critical review. *Journal of the Geological Society*, **164**(3), 511-523.

Hess, H.H., 1962. History of Ocean Basins. In A. E. J. Engel, H. L. James, & B. F. Leonard, eds. *Petrologics studies: a volume in honor of A. F. Buddington*. Geological Society of America, pp. 599-620.

Hirschmann, M.M. et al., 2009. Dehydration melting of nominally anhydrous mantle: The primacy of partitioning. *Physics of the Earth and Planetary Interiors*, **176**(1-2), 54-68.

Hirschmann, M.M., 2000. Mantle solidus: Experimental constraints and the effects of peridotite composition. *Geochemistry Geophysics Geosystems*, **1**(10).

Holmes, A., 1931. Radioactivity and Earth Movements. *Transactions of the Geological Society of Glasgow*, **18**, 559-606.

Holness, M.B., 1992. Equilibrium dihedral angles in the system quartz-CO2-H2-ONaCl at 800°C and 1–15 kbar: the effects of pressure and fluid composition on the permeability of quartzites. *Earth and Planetary Science Letters*, **114**(1), 171-184.

Honda, S., Saito, M. & Nakakuki, T., 2002. Possible existence of small-scale convection under the back arc. *Geophysical Research Letters*, **29**(21).

Hyndman, R.D., 1988. Dipping Seismic Reflectors, Electrically Conductive Zones, and Trapped Water in the Crust Over a Subducting Plate. *Journal of Geophysical Research*, **93**(B11), 13391-13405.

Hyndman, R.D. et al., 2009. Temperature control of continental lithosphere elastic thickness, Te vs Vs. *Earth and Planetary Science Letters*, **277**(3-4), 539-548.

Hyndman, R.D. & Currie, C.A., 2011. Why is the North America Cordillera high? Hot backarcs, thermal isostasy, and mountain belts. *Geology*, **39**(8), 783-786.

Hyndman, R.D. & Lewis, T.J., 1999. Geophysical consequences of the Cordillera–Craton thermal transition in southwestern Canada. *Tectonophysics*, **306**(3-4), 397-422.

Hyndman, R.D. & Peacock, S.M., 2003. Serpentinization of the forearc mantle. *Earth and Planetary Science Letters*, **212**(3-4), 417-432.

Hyndman, R.D. & Shearer, P.M., 1989. Water in the lower continental crust: modelling magnetotelluric and seismic reflection results. *Geophysical Journal International*, **98**(2), 343-365.

Jarrard, R.D., 2003. Subduction fluxes of water, carbon dioxide, chlorine, and potassium. *Geochemistry Geophysics Geosystems*, **4**(5).

Jones, A.G., 1992. Electrical properties of the continental lower crust. In D. M. Fountain, R. J. Arculus, & R. W. Kay, eds. *Continental Lower Crust*. Amsterdam: Elsevier, pp. 81–143.

Jones, A.G., 1988. Static shift of magnetotelluric data and its removal in a sedimentary basin environment. *Geophysics*, **53**(7), 967.

Jones, A.G., 1983. The problem of current channelling: A critical review. *Geophysical Surveys*, **6**(1-2), 79-122.

Jones, A.G. & Gough, D.I., 1995. Electromagnetic images of crustal structures in southern and central Canadian Cordillera. *Canadian Journal of Earth Sciences*, **32**(10), 1541-1563.

Jordan, T. & Watts, A., 2005. Gravity anomalies, flexure and the elastic thickness structure of the India–Eurasia collisional system. *Earth and Planetary Science Letters*, **236**(3-4), 732-750.

Karato, S., 1990. The role of hydrogen in the electrical conductivity of the upper mantle. *Nature*, **347**(6290), 272-273.

Karato, S.-I., 2006. Remote Sensing of Hydrogen in Earth's Mantle. *Reviews in Mineralogy and Geochemistry*, **62**(1), 343-375.

Karato, S.-I., Paterson, M.S. & Fitzgerald, J.D., 1986. Rheology of Synthetic Olivine Aggregates: Influence of Grain Size and Water. *Journal of Geophysical Research*, **91**(B8), 8151-8176.

Karato, S.-ichiro, 1993. Importance of anelasticity in the interpretation of seismic tomography. *Geophysical Research Letters*, **20**(15), 1623.

Kennett, B.L.N. & Engdahl, E.R., 1991. Traveltimes for global earthquake location and phase identification. *Geophysical Journal International*, **105**(2), 429-465.

Klemperer, S.L., 2006. Crustal flow in Tibet: geophysical evidence for the physical state of Tibetan lithosphere, and inferred patterns of active flow. *Geological Society, London, Special Publications*, **268**(1), 39-70.

Koga, K. et al., 2003. Hydrogen concentration analyses using SIMS and FTIR: Comparison and calibration for nominally anhydrous minerals. *Geochemistry Geophysics Geosystems*, **4**(2), 1-20.

Kohlstedt, D.L., Keppler, H. & Rubie, D.C., 1996. Solubility of water in the α, β and γ phases of (Mg,Fe) 2 SiO 4. *Contributions to Mineralogy and Petrology*, **123**(4), 345-357.

Kohlstedt, D.L. & Mackwell, S.J., 1998. Diffusion of Hydrogen and Intrinsic Point Defects in Olivine. *Zeitschrift für Physikalische Chemie*, **207**, 147-162.

Kohlstedt, D.L. & Zimmerman, M.E., 1996. Rheology Of Partially Molten Mantle Rocks. *Annual Review of Earth and Planetary Sciences*, **24**(1), 41-62.

Kruse, S. et al., 1991. Lithospheric Extension Near Lake Mead, Nevada: A Model for Ductile Flow in the Lower Crust. *Journal of Geophysical Research*, **96**(B3), 4435-4456.

Kröner, A. & Stern, R.J., 2005. AFRICA | Pan-African Orogeny. In R. C. Selley, L. R. M. Cocks, & P. R., eds. *Encyclopedia of Geology*. Oxford: Elsevier, pp. 1-12.

Kurtz, R.D., DeLaurier, J.M. & Gupta, J.C., 1986. A magnetotelluric sounding across Vancouver Island detects the subducting Juan de Fuca plate. *Nature*, **321**(6070), 596-599.

Kurtz, R.D., DeLaurier, J.M. & Gupta, J.C., 1990. The Electrical Conductivity Distribution Beneath Vancouver Island: a Region of Active Plate Subduction. *Journal of Geophysical Research*, **95**(B7), 10929-10946.

Landauer, R., 1952. The Electrical Resistance of Binary Metallic Mixtures. *Journal of Applied Physics*, **23**(7), 779.

Laporte, D. & Watson, E.B., 1991. Direct Observation of Near-Equilibrium Pore Geometry in Synthetic Quartzites at 600°-800°C and 2-10.5 Kbar. *The Journal of Geology*, **99**(6), 873-878.

Lebedev, E.B. & Khitarov, N.I., 1964. Dependence on the beginning of melting of granite and the electrical conductivity of its melt on high water vapor pressure. *Geochemistry International*, **2**, 193-197.

Ledo, J. & Jones, A.G., 2001. Regional electrical resistivity structure of the southern Canadian Cordillera and its physical interpretation. *Journal of Geophysical Research*, **106**(B12), 30755-30769.

Lee, S. van der & Frederiksen, A., 2005. Surface wave tomography applied to the North American upper mantle. *Geophysical Monograph Series*, **157**, 67-80.

Lewis, T.J. et al., 1988. Subduction Of The Juan De Fuca Plate: Thermal Consequences. *Journal of Geophysical Research*, **93**(B12), 15207-15225.

Lewis, T.J., Bentkowski, W.H. & Hyndman, R.D., 1992. Crustal temperatures near the Lithoprobe Southern Canadian Cordillera Transect. *Canadian Journal of Earth Sciences*, **29**(6), 1197-1214.

Lezaeta, P. & Haak, V., 2003. Beyond magnetotelluric decomposition: Induction, current channeling, and magnetotelluric phases over 90°. *Journal of Geophysical Research*, **108**(B6), 1-20.

Li, S. et al., 2003. Partial melt or aqueous fluid in the mid-crust of Southern Tibet? Constraints from INDEPTH magnetotelluric data. *Geophysical Journal International*, **153**(2), 289-304.

Liu-Zeng, J. et al., 2008. Quantifying landscape differences across the Tibetan plateau: Implications for topographic relief evolution. *Journal of Geophysical Research*, **113**(F4), 1-26.

Lizarralde, D. et al., 1995. Northeastern Pacific mantle conductivity profile from long-period magnetotelluric sounding using Hawaii-to-California submarine cable data. *Journal of Geophysical Research*, **100**(B9), 17837.

Mackwell, S.J. & Kohlstedt, D.L., 1990. Diffusion of Hydrogen in Olivine: Implications for Water in the Mantle. *Journal of Geophysical Research*, **95**(B4), 5079-5088.

Matte, P., 2001. The Variscan collage and orogeny (480-290 Ma) and the tectonic definition of the Armorica microplate: a review. *Terra Nova*, **13**(2), 122-128.

McKenzie, D. & Jackson, J., 2002. Conditions for flow in the continental crust. *Tectonics*, **21**(6).

McKenzie, D.P. & Parker, R.L., 1967. The North Pacific: an Example of Tectonics on a Sphere. *Nature*, **216**(5122), 1276-1280.

McNamara, D.E., Owens, T.J. & Walter, W.R., 1995. Observations of regional phase propagation across the Tibetan Plateau. *Journal of Geophysical Research*, **100**(B11), 22215.

McNeice, G.W. & Jones, A.G., 2001. Multisite, multifrequency tensor decomposition of magnetotelluric data. *Geophysics*, **66**(1), 158.

Mechie, J. et al., 2004. Precise temperature estimation in the Tibetan crust from seismic detection of the α-β quartz transition. *Geology*, **32**(7), 601.

Mercier, J. et al., 2009. Body-wave tomography of western Canada. *Tectonophysics*, **475**(3-4), 480-492.

Monger, J. & Price, R., 2002. The Canadian Cordillera : Geology and Tectonic Evolution. *CSEG Recorder*, 17-36.

Morgan, W.J., 1968. Rises, Trenches, Great Faults, and Crustal Blocks. *Journal of Geophysical Research*, **73**(6), 1959-1982.

Mouthereau, F., Lacombe, O. & Vergés, J., 2012. Building the Zagros collisional orogen: Timing, strain distribution and the dynamics of Arabia/Eurasia plate convergence. *Tectonophysics*.

Myers, J. & Eugster, H.P., 1983. The system Fe-Si-O: Oxygen buffer calibrations to 1,500K. *Contributions to Mineralogy and Petrology*, **82**(1), 75-90.

Nelson, K.D. et al., 1996. Partially Molten Middle Crust Beneath Southern Tibet: Synthesis of Project INDEPTH Results. *Science*, **274**(5293), 1684-1688.

Nesbitt, B.E., 1993. Electrical Resistivities of Crustal Fluids. *Journal of Geophysical Research*, **98**(B3), 4301-4310.

Ni, H., Keppler, H. & Behrens, H., 2011. Electrical conductivity of hydrous basaltic melts: implications for partial melting in the upper mantle. *Contributions to Mineralogy and Petrology*, **162**(3), 637-650.

Ni, J. & Barazangi, M., 1983. High-frequency seismic wave propagation beneath the Indian Shield, Himalayan Arc, Tibetan Plateau and surrounding regions: high uppermost mantle velocities and efficient S n propagation beneath Tibet. *Geophysical Journal International*, **72**(3), 665-689.

Nicholson, T., Bostock, M. & Cassidy, J.F., 2005. New constraints on subduction zone structure in northern Cascadia. *Geophysical Journal International*, **161**(3), 849-859.

Parkinson, W.D., 1962. The Influence of Continents and Oceans on Geomagnetic Variations. *Geophysical Journal International*, **6**(4), 441-449.

Parkinson, W.D. & Jones, F.W., 1979. The geomagnetic coast effect. *Reviews of Geophysics*, **17**(8), 1999.

Paterson, M.S., 1982. The determination of hydroxyl by infrared absorption in quartz, silicate glasses and similar materials. *Bulletin de Minéralogie*, **105**, 20-29.

Peacock, S.A., 1990. Fluid Processes in Subduction Zones. *Science (New York, N.Y.)*, **248**(4953), 329-337.

Pichon, X. Le, 1968. Sea-Floor Spreading and Continental Drift. *Journal of Geophysical Research*, **73**(12), 3661-3697.

Pollack, H. & Chapman, D., 1977. On the regional variation of heat flow, geotherms, and lithospheric thickness☆. *Tectonophysics*, **38**(3-4), 279-296.

Pollack, H.N., Hurter, S.J. & Johnson, J.R., 1993. Heat Flow from the Earth's Interior: Analysis of the Global Data Set. *Reviews of Geophysics*, **31**(3), 267-280.

Rey, P.F., Teyssier, C. & Whitney, D.L., 2010. Limit of channel flow in orogenic plateaux. *Lithosphere*, **2**(5), 328-332.

Reynard, B., Mibe, K. & Moortèle, B.V. de, 2011. Electrical conductivity of the serpentinised mantle and fluid flow in subduction zones. *Earth and Planetary Science Letters*, **307**(3-4), 387-394.

Richardson, N.J. et al., 2008. Extraordinary denudation in the Sichuan Basin: Insights from low-temperature thermochronology adjacent to the eastern margin of the Tibetan Plateau. *Journal of Geophysical Research*, **113**(B4).

Riddihough, R.P., 1979. Gravity and structure of an active margin—British Columbia and Washington. *Canadian Journal of Earth Sciences*, **16**(2), 350-363.

Rippe, D. & Unsworth, M., 2010. Quantifying crustal flow in Tibet with magnetotelluric data. *Physics of the Earth and Planetary Interiors*, **179**(3-4), 107-121.

Roberts, J.J. & Tyburczy, J. a., 1999. Partial-melt electrical conductivity: Influence of melt composition. *Journal of Geophysical Research*, **104**(B4), 7055-7065.

Rodgers, A.J. & Schwartz, S.Y., 1998. Lithospheric structure of the Qiangtang Terrane, northern Tibetan Plateau, from complete regional waveform modeling: Evidence for partial melt. *Journal of Geophysical Research*, **103**(B4), 7137-7152.

Rodgers, A.J. & Schwartz, S.Y., 1997. Low crustal velocities and mantle lithospheric variations in southern Tibet from regional Pnl waveforms. *Geophysical Research Letters*, **24**(1), 9.

Rodi, W. & Mackie, R.L., 2001. Nonlinear conjugate gradients algorithm for 2-D magnetotelluric inversion. *Geophysics*, **66**(1), 174.

Rosenberg, C.L. & Handy, M.R., 2005. Experimental deformation of partially melted granite revisited: implications for the continental crust. *Journal of Metamorphic Geology*, **23**(1), 19-28.

Ross, J., 1983. The nature and rheology of the cordilleran upper mantle of british columbia: Inferences from peridotite xenoliths. *Tectonophysics*, **100**(1-3), 321-357.

Royden, L.H. et al., 1997. Surface Deformation and Lower Crustal Flow in Eastern Tibet. *Science*, **276**(5313), 788-790.

Royden, L.H., Burchfiel, B.C. & Hilst, R.D. van der, 2008. The geological evolution of the Tibetan Plateau. *Science (New York, N.Y.)*, **321**(5892), 1054-8.

Rudnick, R.L., McDonough, W.F. & O'Connell, R.J., 1998. Thermal structure, thickness and composition of continental lithosphere. *Chemical Geology*, **145**(3-4), 395-411.

Rutter, E.H. & Neumann, D.H.K., 1995. Experimental deformation of partially molten Westerly granite under fluid-absent conditions, with implications for the extraction of granitic magmas. *Journal of Geophysical Research*, **100**(B8), 15697.

Ryder, I. et al., 2007. Post-seismic motion following the 1997 Manyi (Tibet) earthquake: InSAR observations and modelling. *Geophysical Journal International*, **169**(3), 1009-1027.

Rüpke, L.H. et al., 2004. Serpentine and the subduction zone water cycle. *Earth and Planetary Science Letters*, **223**(1-2), 17-34.

Saruwatari, K. et al., 2001. Seismic anisotropy of mantle xenoliths and constraints on upper mantle structure beneath the southern Canadian Cordillera. *Tectonophysics*, **339**(3-4), 403-426.

Schmucker, U., 1973. Regional induction studies: A review of methods and results. *Physics of the Earth and Planetary Interiors*, **7**(3), 365-378.

Shankland, T.J. & Duba, A.G., 1990. Standard electrical conductivity of isotropic, homogeneous olivine in the temperature range 1200°-1500°C. *Geophysical Journal International*, **103**(1), 25-31.

Shapiro, N.M. & Ritzwoller, M.H., 2004. Thermodynamic constraints on seismic inversions. *Geophysical Journal International*, **157**(3), 1175-1188.

Shen, F., Royden, L.H. & Burchfiel, B.C., 2001. Large-scale crustal deformation of the Tibetan Plateau. *Journal of Geophysical Research*, **106**(B4), 6793-6816.

Simpson, F. & Bahr, K., 2005. *Practical Magnetotellurics*, Cambridge: Cambridge University Press.

Simpson, F. & Tommasi, A., 2005. Hydrogen diffusivity and electrical anisotropy of a peridotite mantle. *Geophysical Journal International*, **160**(3), 1092-1102.

Sims, W.E., Bostick, F.X. & Smith, H.W., 1971. The Estimation Of Magnetotelluric Impedance Tensor Elements From Measured Data. *Geophysics*, **36**(5), 938.

Siripunvaraporn, W., Egbert, G. & Uyeshima, M., 2005. Interpretation of two-dimensional magnetotelluric profile data with three-dimensional inversion: synthetic examples. *Geophysical Journal International*, **160**(3), 804-814.

Snider-Pellegrini, A., 1858. *La Création et ses Mystères dévoilés*, Paris: A. Franck et E. Dentu.

Sobolev, S.V. et al., 1996. Upper mantle temperatures from teleseismic tomography of French Massif Central including effects of composition, mineral reactions, anharmonicity, anelasticity and partial melt. *Earth and Planetary Science Letters*, **139**(1-2), 147-163.

Solon, K.D. et al., 2005. Structure of the crust in the vicinity of the Banggong-Nujiang suture in central Tibet from INDEPTH magnetotelluric data. *Journal of Geophysical Research*, **110**(B10), 1-20.

Soyer, W. & Unsworth, M., 2006. Deep electrical structure of the northern Cascadia (British Columbia, Canada) subduction zone: Implications for the distribution of fluids. *Geology*, **34**(1), 53-56.

Spence, G.D., Clowes, R.M. & Ellis, R.M., 1985. Seismic structure across the active subduction zone of western Canada. *Journal of Geophysical Research*, **90**(B8), 6754.

Stesky, R.M. & Brace, W.F., 1973. Electrical Conductivity of Serpentinized Rocks to 6 Kilobars. *Journal of Geophysical Research*, **78**(32), 7614-7621.

Stixrude, L. & Lithgowbertelloni, C., 2007. Influence of phase transformations on lateral heterogeneity and dynamics in Earth's mantle. *Earth and Planetary Science Letters*, **263**(1-2), 45-55.

Swift, C.M., 1967. *A magnetotelluric investigation of an electrical conductivity anomaly in the southwestern United States*. Massachusetts Institute of Technology.

Tapponnier, P. et al., 2001. Oblique stepwise rise and growth of the Tibet plateau. *Science (New York, N.Y.)*, **294**(5547), 1671-7.

Thompson, A.B. & Connolly, J.A.D., 1995. Melting of the continental crust: Some thermal and petrological constraints on anatexis in continental collision zones and other tectonic settings. *Journal of Geophysical Research*, **100**(B8), 15565.

Tikhonov, A.N., 1950. On determining electrical characteristics of the deep layers of the Earth's crust. *Doklady*, **73**(2), 295-297.

Tommasi, A. et al., 2006. Deformation and melt transport in a highly depleted peridotite massif from the Canadian Cordillera: Implications to seismic anisotropy above subduction zones. *Earth and Planetary Science Letters*, **252**(3-4), 245-259.

Tullis, J., Yund, R. & Farver, J., 1996. Deformation-enhanced fluid distribution in feldspar aggregates and implications for ductile shear zones. *Geology*, **24**(1), 63.

Turcotte, D.L. & Schubert, G., 2002. *Geodynamics*, Cambridge: Cambridge University Press.

Turcotte, D.L. & Schubert, G., 1982. *Geodynamics: Application of Continuum Physics to Geological Problems*, Wiley.

Tyburczy, J.A. & Waff, H.S., 1983. Electrical Conductivity Of Molten Basalt And Andesite To 25 Kilobars Pressure: Geophysical Significance And Implications For Charge Transport And Melt Structure. *Journal of Geophysical Research*, **88**(B3), 2413-2430.

Türkoğlu, E., Unsworth, M. & Pana, D., 2009. Deep electrical structure of northern Alberta (Canada): implications for diamond exploration. *Canadian Journal of Earth Sciences*, **46**(2), 139-154.

Unsworth, M. et al., 2004. Crustal and upper mantle structure of northern Tibet imaged with magnetotelluric data. *Journal of Geophysical Research*, **109**(B2), 101029/.

Unsworth, M., 2009. Magnetotelluric Studies of Active Continent–Continent Collisions. *Surveys in Geophysics*, **31**(2), 137-161.

Unsworth, M. & Rondenay, S., 2013. Mapping the Distribution of Fluids in the Crust and Lithospheric Mantle Utilizing Geophysical Methods. In D. Harlov & H. Austrheim, eds. *Metasomatism and the Chemical Transformation of Rock*. Berlin Heidelberg: Spinger, pp. 535-598.

Unsworth, M.J. et al., 2005. Crustal rheology of the Himalaya and Southern Tibet inferred from magnetotelluric data. *Nature*, **438**(7064), 78-81.

Vine, F.J. & Matthews, D.H., 1963. Magnetic Anomalies Over Oceanic Ridges. *Nature*, **199**(4897), 947-949.

Wait, J.R., 1954. On The Relation Between Telluric Currents And The Earth's Magnetic Field. *Geophysics*, **19**(2), 281.

Wang, D. et al., 2006. The effect of water on the electrical conductivity of olivine. *Nature*, **443**(7114), 977-80.

Wang, E. et al., 1998. Late Cenozoic Xianshuihe-Xiaojiang, Red River, and Dali fault systems of southwestern Sichuan and central Yunnan, China. *Special Paper-Geological Society of America*, **327**, 1-108.

Wang, Y., 2001. Heat flow pattern and lateral variations of lithosphere strength in China mainland: constraints on active deformation. *Physics of The Earth and Planetary Interiors*, **126**(3-4), 121-146.

Wannamaker, P.E., 1986. Electrical Conductivity of Water-Undersaturated Crustal Melting. *Journal of Geophysical Research*, **91**(B6), 6321-6327.

Wannamaker, P.E., Hohmann, G.W. & Ward, S.H., 1984. Magnetotelluric responses of three-dimensional bodies in layered earths. *Geophysics*, **49**(9), 1517.

Ward, S.H., 1983. Controlled source electrical methods for deep exploration. *Surveys in Geophysics*, **6**(1), 137–152.

Warren, C.J., Beaumont, C. & Jamieson, R.A., 2008. Modelling tectonic styles and ultra-high pressure (UHP) rock exhumation during the transition from oceanic subduction to continental collision. *Earth and Planetary Science Letters*, **267**(1-2), 129-145.

Watanabe, T., Langseth, M.G. & Anderson, R.N., 1977. Heat flow in back-arc basins of the Western Pacific. In M. Talwani & W. C. Pitman, eds. *Island Arcs, Deep Sea Trenches and Back-Arc Basins, Maurice Ewing Series*. Washington, D.C.: American Geophysical Union, pp. 137-161.

Watson, B.E. & Brenan, J.M., 1987. Fluids in the lithosphere, 1. Experimentally-determined wetting characteristics of CO2H2O fluids and their implications for fluid transport, host-rock physical properties, and fluid inclusion formation. *Earth and Planetary Science Letters*, **85**(4), 497-515.

Wegener, A., 1912. Die Entstehung der Kontinente. *Geologische Rundschau*, **3**(4), 276-292.

Wei, W. et al., 2001. Detection of widespread fluids in the Tibetan crust by magnetotelluric studies. *Science*, **292**(5517), 716-9.

Weidelt, P., 1972. The inverse problem of geomagnetic induction. *Zeitschrift für Geophysik*, **38**, 257-289.

Wiese, H. von, 1964. Geomagnetische Tiefentellurik. *Pure and Applied Geophysics PAGEOPH*, **57-57**(1), 31-46.

Wu, C. et al., 1998. Yadong cross structure and South Tibetan Detachment in the east central Himalaya (89°–90°E). *Tectonics*, **17**(1), 28.

Xu, L., Rondenay, S. & Der Hilst, R.D. van, 2007. Structure of the crust beneath the southeastern Tibetan Plateau from teleseismic receiver functions. *Physics of the Earth and Planetary Interiors*, **165**(3-4), 176-193.

Xu, Y., Shankland, T.. & Duba, A.., 2000. Pressure effect on electrical conductivity of mantle olivine. *Physics of the Earth and Planetary Interiors*, **118**(1-2), 149-161.

Xu, Z.J. & Song, X., 2010. Joint inversion for crustal and Pn velocities and Moho depth in Eastern Margin of the Tibetan Plateau. *Tectonophysics*, **491**(1-4), 185-193.

Yao, H., Beghein, C. & Der Hilst, R.D. van, 2008. Surface wave array tomography in SE Tibet from ambient seismic noise and two-station analysis - II. Crustal and upper-mantle structure. *Geophysical Journal International*, **173**(1), 205-219.

Yin, A. & Harrison, T.M., 2000. Geologic Evolution of the Himalayan-Tibetan Orogen. *Annual Review of Earth and Planetary Sciences*, **28**(1), 211-280.

Zhang, P.-Z. et al., 2004. Continuous deformation of the Tibetan Plateau from global positioning system data. *Geology*, **32**(9), 809.

Zhang, Y., 2008. *Geochemical Kinetics*, Princeton University Press.

Zhao, W. et al., 1993. Deep seismic reflection evidence for continental underthrusting beneath southern Tibet. *Nature*, **366**(6455), 557-559.

Appendix

A.1 Tensor decomposition of the ABC magnetotelluric data

The ABC magnetotelluric data were decomposed based on the tensor decomposition method proposed by Groom & Bailey (1989), which was extended to handle multiple frequencies and sites by McNeice & Jones (2001) (section 2.2.5). Based on the analysis presented in section 3.4.1 a strike direction of N45°W provides the most consistent strike direction estimate for both the ABC-N and ABC-S lines.

Figure A.1 shows the single site, multi-frequency analysis decomposition results for the ABC-N and ABC-S lines for a fixed strike direction of N45°W. As part of this decomposition, a single shear and a single twist angle were calculated for each station over the entire period range. The calculated twist angle is generally small and for most sites smaller than 20°. The calculated shear angles show a larger variation. The largest values are found in the Omineca Belt, where shear angles exceed 30°. No site gain and splitting angle were calculated, as they affect the magnetotelluric impedance data by only a scalar factor (section 2.2.5). In addition to the decomposition parameters proposed by Groom & Bailey (1989), a channelling angle was calculated, which describes the magnetic effect on the distortion of the magnetotelluric data (described by the magnetic distortion matrix $\underline{\boldsymbol{D}}$ in equation **(2.32)**). The channelling angle generally ranges between 45° and 60°. However, as the effect of magnetic distortion decays with $\sqrt{\omega}$, it can generally be neglected (Groom & Bailey, 1991).

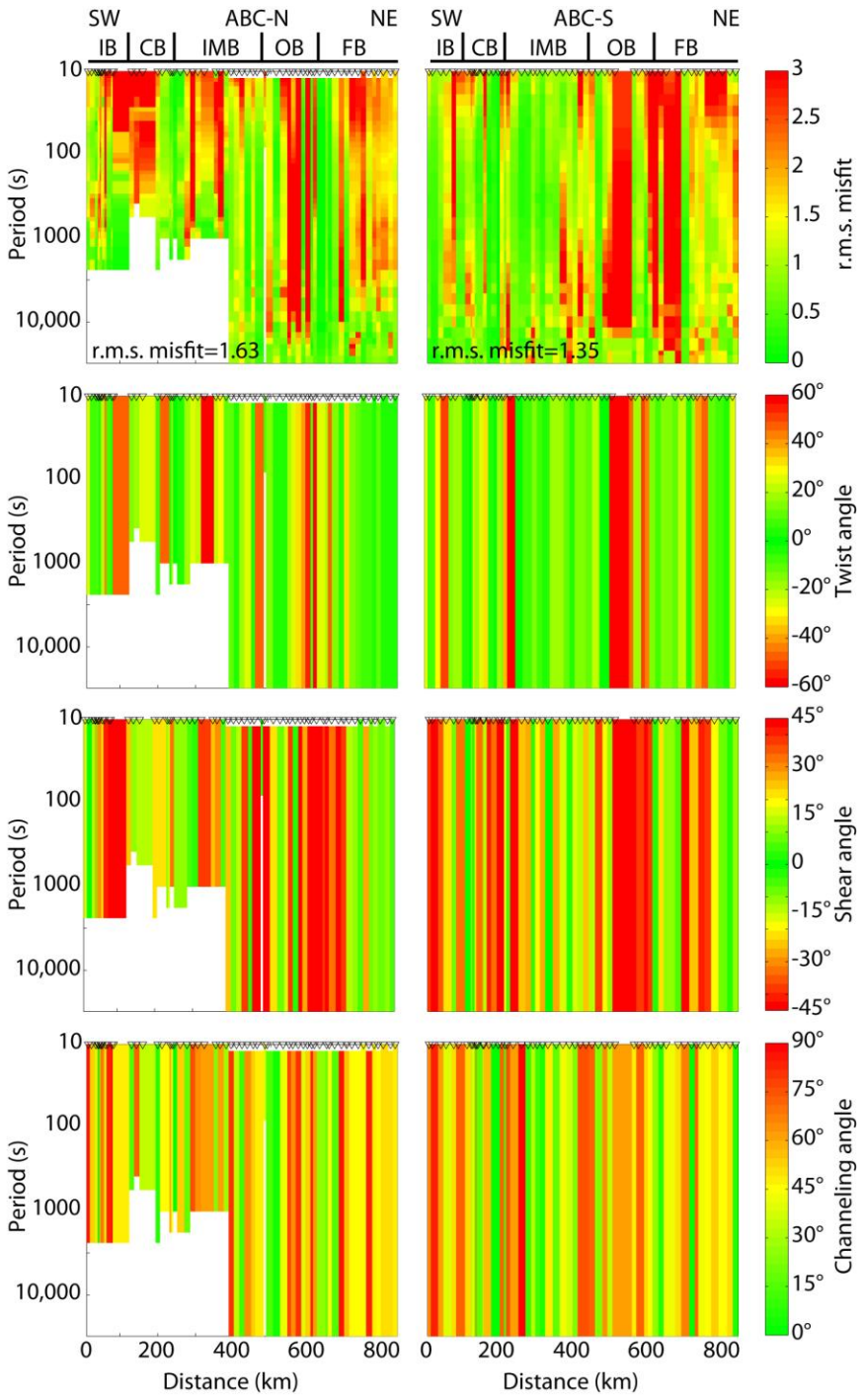

Figure A.1: Decomposition results for a single site, multi-frequency analysis for the ABC-N (left) and ABC-S (right) lines for a fixed strike direction of N45°W. The r.m.s. misfit (top row), twist angle (second row), shear angle (third row) and channeling angle (bottom row) are shown. IB: Insular belt; CB: Coastal belt; IMB: Intermontane belt; OB; Omineca belt; FB: Foreland belt.

B.1 Electrical resistivity of the peridotite mantle in the presence of water

B.1.1 Electrical conductivity of dry olivine according to Constable (2006)

In the absence of any fluid phases, laboratory measurements indicate that the electrical resistivity of a peridotite mantle is strongly temperature-dependent, whereas the effect of pressure is relatively small (Xu et al., 2000). The electrical resistivity is mainly determined by the most common mantle minerals (olivine and pyroxene). Given the dominance of olivine in terms of both volume fraction and electrical resistivity, Constable (2006) approximated the resistivity of a dry peridotite mantle to first order by the electrical resistivity of olivine only. Taking into account the concentration and mobility of polaron and magnesium vacancies and their dependence on oxygen fugacity, Constable (2006) derived a relationship describing the conductivity of olivine as a function of temperature (SEO3 model, Figure B.1):

$$\sigma_{SEO3} = \left[\mathrm{Fe}^{\bullet}_{\mathrm{Mg}}\right]\mu_{\mathrm{Fe}}e + 2\left[V''_{\mathrm{Mg}}\right]\mu_{\mathrm{Mg}}e \tag{B.1}$$

with mobilities

$$\mu_{\mathrm{Fe}} = 12.2 \cdot 10^{-6} e^{-1.05eV/kT} \tag{B.2}$$

$$\mu_{\mathrm{Mg}} = 2.72 \cdot 10^{-6} e^{-1.09eV/kT} \tag{B.3}$$

and concentrations

$$\left[\mathrm{Fe}_{\mathrm{Mg}}^{\bullet}\right] = b_{\mathrm{Fe}}(T) + 3.33 \cdot 10^{24} e^{-0.02eV/kT} f_{O_2}^{1/6} \quad \text{(B.4)}$$

$$\left[V_{\mathrm{Mg}}''\right] = b_{\mathrm{Mg}}(T) + 6.21 \cdot 10^{30} e^{-1.83eV/kT} f_{O_2}^{1/6} \quad \text{(B.5)}$$

of the polaron and magnesium vacancies, where e is the electronic charge, T is the temperature and k is the Boltzmann's constant. b_{Fe} and b_{Mg} are the defect concentrations extrapolated from measurements at temperatures of 1000°C, 1100°C and 1200°C (Constable, 2006):

$$b_{\mathrm{Fe}}(\mathrm{T}) = 5.06 \cdot 10^{24} e^{-0.357eV/kT} \quad \text{(B.6)}$$

$$b_{\mathrm{Mg}}(\mathrm{T}) = 4.58 \cdot 10^{26} e^{-0.752eV/kT} \quad \text{(B.7)}$$

For the oxygen fugacity f_{O_2} the widely used formulation of Myers & Eugster (1983) for a quartz–fayalite–magnetite (QFM) buffer was used:

$$\mathrm{f}_{\mathrm{O}_2} = 10^{-2.44419/\mathrm{T}+13.296} \quad \text{(B.8)}$$

B.1.2 Electrical conductivity in the presence of water according to Karato (1990)

Karato (1990) proposed that, in the presence of aqueous fluids, dissolved hydrogen causes a significant reduction in the electrical resistivity of olivine, caused by charge transport through protons and/or enhanced diffusion of Mg^{2+} and Fe^{2+} ions in the presence of hydrogen. In this case, the conductivity can be described by a Nernst-Einstein relationship:

$$\sigma = \frac{cDq^2}{kT} \tag{B.9}$$

where c is the hydrogen concentration, D is the hydrogen diffusivity, q is the hydrogen charge, k is the Boltzmann constant and T is the temperature. Following the approach of Lizarralde et al. (1995), the effects of hydrogen diffusion on electrical resistivity can be determined using laboratory measurements of the diffusivity and solubility in olivine, as outlined below.

The maximum hydrogen concentration can be estimated using laboratory measurements on hydrogen solubility $[H^+]_{\text{ppm Si}}$ in olivine for temperatures of 1100°C and 1300°C and pressures P up to 12 GPa (Bai & Kohlstedt, 1992; Kohlstedt et al., 1996), which can be fit by a linear regression of log $([H^+]_{\text{ppm Si}})$ vs log (P) (Lizarralde et al., 1995):

$$[H^+]_{\text{ppm Si}} = 10^{-0.61\pm0.04} P^{1.19\pm0.01} \text{ (MPa)} \tag{B.10}$$

Laboratory measurements of hydrogen diffusivity D in olivine at temperatures (T) between 800°C and 1100°C and a pressure of 0.30 GPa indicate an anisotropic behaviour, with the diffusivity along the three crystallographic axes being described by an Arrhenius relationship (Mackwell & Kohlstedt, 1990):

$$D_a = (6 \pm 3)10^{-5} e^{-\frac{130\pm30}{RT}} \tag{B.11}$$

$$D_b = (5 \pm 4)10^{-6} e^{-\frac{130\pm30}{RT}} \tag{B.12}$$

$$D_c \approx 0.01 D_a \tag{B.13}$$

Based on these laboratory measurements, the electrical conductivity for each of the three crystallographic directions can be calculated for varying temperatures and pressures. For comparison with the electrical resistivity models, it is necessary to calculate the isotropic average of the electrical conductivity. Several spatial averaging methods have been suggested to calculate this (see Shankland & Duba, 1990 for a comparison), and in our analysis we use the effective medium theory by Landauer (1952):

$$\sigma_{EM} = \frac{1}{4}\Bigg((3f_1 - 1)\sigma_1 + (3f_2 - 1)\sigma_2 + \Big(\big((3f_1 - 1)\sigma_1 + (3f_2 - 1)\sigma_2 \big)^2 + 8\sigma_1\sigma_2 \Big)^{\frac{1}{2}} \Bigg) \tag{B.14}$$

with $f_1 = f_2 = 0.5$. σ_1 and σ_2 are set to be the serial and parallel averages σ_s and σ_p respectively, which can be calculated as:

$$\sigma_s^{-1} = \frac{1}{3}(\sigma_a^{-1} + \sigma_b^{-1} + \sigma_c^{-1}) \tag{B.15}$$

$$\sigma_p = \frac{1}{3}(\sigma_a + \sigma_b + \sigma_c) \tag{B.16}$$

where σ_a, σ_b and σ_c correspond to the conductivities along the three crystallographic axes (Figure B.1).

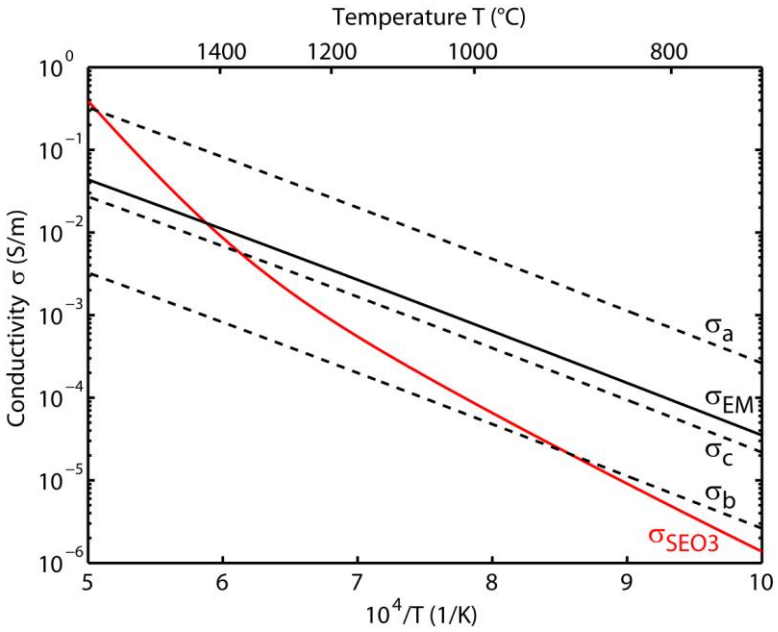

Figure B.1: Electrical conductivity as a function of temperature. The red line corresponds to the SEO3 model for dry olivine (Constable, 2006). The black dashed lines correspond to the electrical conductivities along the three crystallographic axes of olivine for hydrogen diffusion (Karato, 1990) with a hydrogen concentration of 1000 ppm H/Si, using the hydrogen diffusivity data from Mackwell & Kohlstedt (1990). The solid black line corresponds to the isotropic average of the electrical conductivities along the three crystallographic axes of olivine, calculated using the effective medium theory by Landauer (1952).

B.1.3 Electrical conductivity in the presence of water according to Wang et al. (2006)

Wang et al. (2006) investigated the Nernst-Einstein relationship (B.9) through laboratory measurements on San Carlos olivine, which revealed a strong dependence of conductivity on water content but only a modest dependence on temperature. Based on their measurements, they found that the electrical conductivity for wet olivine was given by:

$$\sigma_H = AC_w^r e^{-\frac{H^*}{RT}} \tag{B.17}$$

where C_w is the water content (in wt-%), A and r are constants, H^* is the activation enthalpy and T is temperature. For wet olivine, the constants were found to be $A = 10^{(3.0\pm0.4)}\frac{S}{m}$ and $r = 0.62 \pm 0.15$; the activation enthalpy was found to be $H^* = 87 \pm 5\frac{kJ}{mol}$. At low temperatures, the observed conductivities are significantly higher than the ones calculated by Karato (1990). In addition, the obtained activation enthalpy is smaller than the one for diffusion of hydrogen, leading Wang et al. (2006) to the conclusion that other conductivity mechanisms than the ones proposed by Karato (1990) are required.

B.2 A modification of Archie's law for two conducting phases

Several mixing models have been proposed to calculate the electrical conductivity of a multi-phase system. One commonly used model to explain the electrical conductivity in the presence of a fluid phase is Archie's law. However, Archie's Law assumes that the electrical conductivity of the fluid phase is several orders of magnitude higher than the electrical conductivity of the solid rock matrix, such that the rock matrix does not contribute. While this is true for crustal rocks, this assumption is no longer valid at mantle depths due to the relatively low resistivity of the predominant mantle mineral olivine.

Glover et al. (2000) presented a modification of Archie's law to account for two conducting phases. For two phases with conductivities σ_1 and σ_2 and volume fractions $1-\chi_2$ and χ_2, the effective electrical conductivity σ_{eff} is given by:

$$\sigma_{\text{eff}} = \sigma_1(1-\chi_2)^{\frac{\log(1-\chi_2^m)}{\log(1-\chi_2)}} + \sigma_2\chi_2^m \tag{B.18}$$

where m is the cementation factor of the second phase, associated with its connectivity. Large exponents (m > 2) correspond to a low electrical connectivity, while small exponents (m < 2) are indicative of a high electrical connectivity. The cementation factor p for the first phase is dependent on the cementation factor m, and therefore does not appear explicitly in the equation above.

The importance of using the modification of Archie's Law in case of a low resistivity rock matrix is illustrated in Figure B.2. Figure B.2a shows the predicted conductivities as a function of the cementation factor m for the conventional and modified Archie's Laws, assuming a conductivity σ_1=0.015 S/m for the rock matrix and σ_2=0.3 S/m for the fluid phase with a volume fraction χ_2=10%. While the two forms of Archie's Law converge for small values of the cementation factor, the conventional form of Archie's Law underestimates the predicted conductivities, and for m>1.5 predicts conductivities below the range of allowed conductivities (i.e. between 0.015 S/m and 0.3 S/m). Similarly, Figure B.2b shows the predicted volume fractions of the fluid phase as a function of the cementation factor m for the conventional and modified Archie's Law, assuming an effective conductivity σ_{eff}=0.0178 S/m of the rock and fluid phase. While the modified

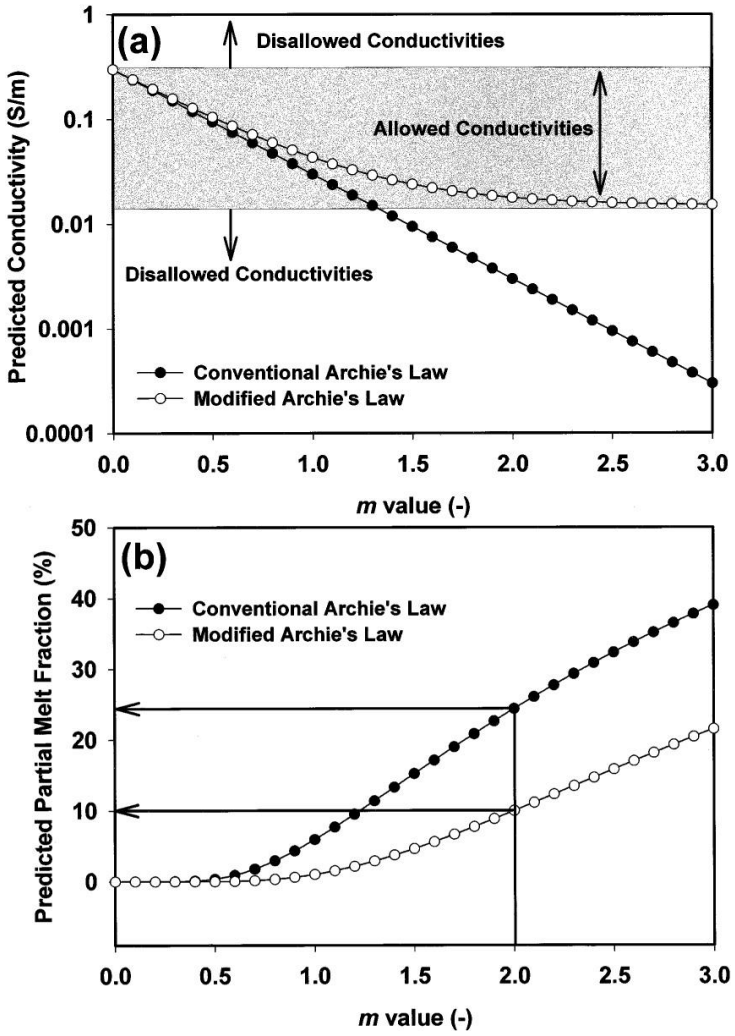

Figure B.2: (a) Predicted conductivity as a function of the cementation factor m for the conventional and modified Archie's Laws for σ_1=0.015 S/m, σ_2=0.3 S/m and χ_2=10%. (b) Predicted volume fraction as a function of the cementation factor m for the conventional and modified Archie's Laws for σ_1=0.015 S/m, σ_2=0.3 S/m and σ_{eff}=0.0178 S/m. (reprinted from Glover et al., 2000)[17]

form of Archie's Law predicts the correct fluid fraction (10% for a cementation factor m=2), the conventional form of Archie's Law significantly overestimates the volume fraction required to explain the effective conductivity.

B.3 Temperature constraints from seismic velocity models

Seismic velocities can be used to estimate mantle temperatures if the bulk and shear moduli as well as the density of the rock as a function of temperature, pressure and composition are known (Goes et al., 2000). The method is based on the forward calculation of seismic P and S wave velocities, taking into account anharmonic and anelastic effects on seismic velocity.

In a first step, the anharmonic effect on seismic velocity is calculated. Anharmonicity changes with varying composition of the mantle. In this thesis, a Tecton (mean spinel peridotite), Proton and Archon composition were used (Griffin et al., 2003; Table B.1) Based on laboratory results of the elastic parameters and density of the five upper mantle minerals olivine, orthopyroxene, clinopyroxine, garnet and spinel (Goes et al., 2000; Table B.2), the bulk and shear moduli K_i and μ_i of each mineral can be calculated as a function of temperature T and pressure P:

$$K_i(P,T) = K_i(P_0,T_0) + (T - T_0)\frac{\partial K_i}{\partial T} + (P - P_0)\frac{\partial K_i}{\partial P} \quad \text{(B.19)}$$

$$\mu_i(P,T) = \mu_i(P_0,T_0) + (T - T_0)\frac{\partial \mu_i}{\partial T} + (P - P_0)\frac{\partial \mu_i}{\partial P} \quad \text{(B.20)}$$

where T_0 and P_0 correspond to the reference temperature and pressure at the Earth's surface.

Composition	Olivine Mg_2SiO_4	Ortho-pyroxene $MgSiO_3$	Clino-pyroxene $CaMgSi_2O_6$	Spinel $MgAl_2O_4$	Garnet $Mg_3Al_2Si_3O_{12}$	Magnesium number
Tecton	0.66	0.17	0.09	0	0.08	89.9
Proton	0.69	0.25	0.02	0	0.04	92.7
Archon	0.7	0.17	0.06	0	0.07	90.6

Table B.1: Modal mineral proportions for a Tecton (mean spinel peridotite), Proton and Archon mantle composition (Griffin et al., 2003). (adapted from Hyndman et al., 2009)[18]

The density ρ_i of each mineral depends on the temperature T and pressure P as well as the magnesium number X and the thermal expansion coefficient α:

$$\rho_i(P,T) = \rho_i(P_0,T_0)\left(1 - \alpha(T - T_0) + \frac{P - P_0}{K_i}\right) + X\frac{\partial \rho_i}{\partial X} \tag{B.21}$$

with the thermal expansion coefficient α given by:

$$\alpha = \alpha_0 + \alpha_1 T + \alpha_2 T^{-1} + \alpha_3 T^{-2} \tag{B.22}$$

For a known composition, the bulk and shear moduli $\langle K \rangle$ and $\langle \mu \rangle$ and the density $\langle \rho \rangle$ of the mantle can be calculated as the weighted average:

$$\langle K \rangle = \frac{1}{2}\left(\sum_i \lambda_i K_i + \left(\sum_i \frac{\lambda_i}{K_i}\right)^{-1}\right) \tag{B.23}$$

$$\langle \mu \rangle = \frac{1}{2}\left(\sum_i \lambda_i \, \mu_i + \left(\sum_i \frac{\lambda_i}{\mu_i}\right)^{-1}\right) \tag{B.24}$$

$$\langle \rho \rangle = \sum_i \lambda_i \rho_i \tag{B.25}$$

with λ_i being the volumetric fraction of each mineral. Using these moduli and density, the anharmonic P wave and S wave velocities v_p and v_s at the specified temperature and pressure conditions can then be calculated as:

$$v_p = \sqrt{\frac{\langle K \rangle + \frac{4}{3}\langle \mu \rangle}{\langle \rho \rangle}} \tag{B.26}$$

$$v_s = \sqrt{\frac{\langle \mu \rangle}{\langle \rho \rangle}} \tag{B.27}$$

After the anharmonic seismic velocities are known, the anelastic effect on the seismic velocities needs to be calculated, which takes into account the frequency-dependent effects of attenuation. The main effect of anelasticity is associated with the shear modulus and can be expressed in terms of the Q factor Q_μ for S waves:

$$Q_\mu = A\omega^a \exp\left(\frac{aE^*}{RT}\right) = Q_s \tag{B.28}$$

where ω is the frequency of the seismic wave and A, a and E^* are constant. E^* can be expressed in terms of the activation energy H^* and activation volume V^*:

$$E^* = H^* + PV^* \tag{B.29}$$

Mineral	Units	Olivine Mg_2SiO_4	Ortho-pyroxene $MgSiO_3$	Clino-pyroxene $CaMgSi_2O_6$	Spinel $MgAl_2O_4$	Garnet $Mg_3Al_2Si_3O_{12}$
ρ	10^3 kg/m^3	3.222(2)	3.198(5)	3.280(5)	3.578(5)	3.565(5)
$\partial\rho/\partial X$		1.182(5)	0.804(5)	0.377(5)	0.702(5)	0.758(5)
K_s	Gpa	129(1)	111(2)	105(1)	198(5)	173(2)
$\partial K/\partial T$	Gpa/K	-16(2)	-12(3)	-13(3)	-28(5)	-21(2)
$\partial K/\partial P$		4.2(2)	6.0(5)	6.2(3)	5.7(8)	4.9(5)
μ	Gpa	82(2)	81(2)	67(2)	108(3)	92(1)
$\partial\mu/\partial T$	Gpa/K	-14(1)	-11(2)	-10(2)	-12(3)	-10(1)
$\partial\mu/\partial P$		1.4(1)	2.0(1)	1.7(2)	0.8(5)	1.4(1)
α_0	10^{-4} K^{-1}	0.2010	0.3871	0.3206	0.6969	0.0991
α_1	10^{-7} K^{-2}	0.1390	0.0446	0.0811	-0.0108	0.1165
α_2	10^{-2}	0.1627	0.0343	0.1347	-3.0799	1.0624
α_3	K	-0.3380	-1.7278	-1.8167	5.0395	-2.5000

Table B.2: Compilation of elastic parameters (Goes et al., 2000 and references therein). Error estimates in the last digit are given in parantheses. (adapted from Goes et al., 2000)[19]

The Q factor Q_p for P waves can be calculated as:

$$Q_p^{-1} = (1 - L)Q_k^{-1} + LQ_\mu^{-1} \tag{B.30}$$

where Q_k is usually considered a constant with $Q_k \to \infty$ and L can be calculated in terms of the anharmonic seismic velocities v_p and v_s:

Anelasticity model	A	b	E* (kJ/mol)	V* (cm^3/mol)
Q1	0.148	0.15	500	20
Q1-mod	0.049	0.15	500	20
Q2	$2*10^{-4}$	0.25	584	21

Table B.3: Anelasticity parameters for the attenuation models from Sobolev et al. (1996) (Q1), Shapiro & Ritzwoller (2004) (modified from Sobolev et al. 1996, Q1-mod) and Berckhemer et al. (1982) (Q2). (adapted from Hyndman et al., 2009)[20]

$$L = \frac{4}{3}\left(\frac{v_s}{v_p}\right)^2 \tag{B.31}$$

Based on these results, the anelastic P and S wave velocities $v_{p,anel}$ and $v_{s,anel}$ can then be calculated as:

$$v_{p,anel} = V_p\left(1 - \frac{2Q_p^{-1}}{\tan\left(\frac{\pi a}{2}\right)}\right) \tag{B.32}$$

$$v_{s,anel} = V_s\left(1 - \frac{2Q_s^{-1}}{\tan\left(\frac{\pi a}{2}\right)}\right) \tag{B.33}$$

A couple of commonly used anelasticity models exist in the literature, which differ in their temperature dependence on the seismic velocity (e.g. Shapiro & Ritzwoller, 2004; Sobolev et al., 1996; Berckhemer et al., 1982; Table B.3). Unfortunately no anelasticity data exist for the different minerals, therefore varying composition cannot be taken into account in this step of the analysis.

B.4 Reduced mantle solidus in the presence of water

The effect of water on the mantle solidus can be determined using cryoscopic calculations (Hirschmann et al., 2009). In a first step, it is necessary to determine the solidus temperature T of a dry peridotite mantle as a function of pressure P. Based on laboratory measurements it can be parameterized as (Hirschmann, 2000; Hirschmann et al., 2009):

$$T(°\mathrm{C}) = -5.104P^2 + 132.899P + 1120.661 \text{ for } P < 10 \text{ GPa} \tag{B.34}$$

$$T(°\mathrm{C}) = -1.092(P-10)^2 + 32.39(P-10) + 1935 \text{ for } 10 \text{ GPa} < P < 23.5 \text{ GPa} \tag{B.35}$$

$$T(°\mathrm{C}) = 26.53(P-23.5) + 2175 \text{ for } P > 23.5 \text{ GPa} \tag{B.36}$$

For temperatures greater than the solidus, the peridotite undergoes partial melting. If any water is present during this process, it will redistribute between the solid phase and the melt phase. This partition is described by the melt partition coefficient $D_H^{perid/liq}$:

$$D_H^{perid/liq} = X_{ol}D_H^{ol/liq} + X_{opx}D_H^{opx/liq} + X_{cpx}D_H^{cpx/liq} + X_{gt}D_H^{gt/liq} + X_{spn}D_H^{spn/liq} \tag{B.37}$$

and depends on the modal proportion X_i and the melt partition coefficient $D_H^{i/liq}$ of each of the mantle minerals olivine (ol), orthopyroxene (opx), clinopyroxine (cpx), garnet (gt) and spinel (spn).

Melting can either occur through batch melting or fractional melting. For batch melting, the melt phase stays in contact with the residual rock crystal. Therefore, the overall bulk composition of the system remains the same. In contrast, for fractional melting, the melt phase is removed from the system due to density differences, leading to a continuously changing bulk composition.

For the following calculations batch melting is assumed, in which case the concentration of the water in the melt phase $C_{H_2O}^{melt}$ is given by:

$$C_{H_2O}^{melt} = \frac{C_{H_2O}^{0}}{D_H^{perid/liq}(1-F)+F} \tag{B.38}$$

where $C_{H_2O}^{0}$ is the bulk water concentration and F is the degree of melting. The concentration of the water in the residual rock crystal $C_{H_2O}^{perid}$ is given by:

$$C_{H_2O}^{perid} = \frac{C_{H_2O}^{0} D_H^{perid/liq}}{D_H^{perid/liq} + F(1-D_H^{perid/liq})} \tag{B.39}$$

Aubaud et al., (2004) have used a cryoscopic approach (i.e. determination of the freezing or melting point) based on empirical and thermodynamic calculations to estimate the effect of water on the solidus temperature. The reduced solidus temperature T for a given amount of water, which is assumed to be completely dissociated to hydroxyl $X_{OH^-}^{melt}$, compared to the dry case T_{perid}^{fusion} is given by:

$$T = \frac{T_{perid}^{fusion}}{\left(1 - \frac{R}{\Delta \hat{S}_{perid}^{fusion}} \ln\left(1 - X_{OH^-}^{melt}\right)\right)} \tag{B.40}$$

where $\Delta \hat{S}_{perid}^{fusion}$ is the molar entropy of fusion. The molar entropy of fusion can be related to the entropy of fusion per unit mass $\Delta S_{perid}^{fusion}$ through:

$$\Delta \hat{S}_{perid}^{fusion} = M \Delta S_{perid}^{fusion} \tag{B.41}$$

where M is the number of grams in one mole of silicate.

Of particular importance in the above calculations is the conversion from the amount of water as mass fraction (i.e. in weight %) to hydroxyl mole fraction. As water partitions into the melt phase, part of the total amount of dissolved water H_2O_t reacts with oxygen atoms in the melt to form OH groups, leading to an equilibrium (Zhang, 2008):

$$H_2O\ (melt) + O\ (melt) \leftrightarrow 2OH\ (melt) \tag{B.42}$$

In terms of mole fractions, this reaction can be written as:

$$[H_2O_t] = [H_2O_m] + \frac{1}{2}[OH] \tag{B.43}$$

If we assume that all the water in the melt phase dissociates to OH, its mole fraction is related to the total amount of dissolved water through:

$$[OH] = 2\,[H_2O_t] \tag{B.44}$$

There are three possible definitions on how the mole fraction of the total amount of dissolved water can be calculated, based on whether the oxygen is treated as one, two/three or eight units (Zhang, 2008):

i) For a single oxygen basis, the mole fraction of the total amount of water is given as:

$$[H_2O_t] = \frac{\frac{C}{18.015}}{\frac{C}{18.015} + \frac{(1-C)}{W}} \tag{B.45}$$

where C is the mass fraction of the total amount of water and W is the mass of the dry rock per mole of oxygen.

ii) An alternative is to treat each oxide (e.g. SiO_2, Al_2O_3) as one unit. In this case the mole fraction of the total amount of water is given by:

$$[H_2O_t] = \frac{\frac{C}{18.015}}{\sum \frac{C_i}{W_i}} \tag{B.46}$$

where C_i and W_i are the mass fraction and molar mass of each oxide component respectively.

iii) In the eight oxygen basis, an eight oxygen molecule like $NaAlSi_3O_8$ is considered and treated as one unit. In this case the mole fraction of the total amount of water is given by:

$$[H_2O_t] = \frac{\frac{C}{18.015}}{\frac{C}{18.015} + \frac{(1-C)}{W}} \quad \text{(B.47)}$$

where W is the molar mass of the eight oxygen molecule (262.22 for $NaAlSi_3O_8$).

B.5 Measurement of water content

The water content C_{H_2O} in the upper mantle is commonly expressed as a mass fraction, i.e. the mass of water m_{H_2O} dissolved in a given mass of rock. As olivine is the main constituent of the upper mantle, it is common to express the water content in terms of the mass of olivine m_{ol}:

$$C_{H_2O} = \frac{m_{H_2O}}{m_{ol}} \quad \text{(B.48)}$$

The above equation assumes that the mass of water is significantly smaller than the mass of olivine, i.e. $m_{H_2O} \ll m_{ol}$. Otherwise the denominator of equation (B.48) would have to be replaced by the overall mass of both constituents.

For small amounts of water it is common to express the water content in weight percent:

$$C_{H_2O} = \frac{m_{H_2O}}{m_{ol}} \cdot 100 \text{ [wt-\%]} \quad \text{(B.49)}$$

or in parts per million:

$$C_{H_2O} = \frac{m_{H_2O}}{m_{ol}} \cdot 10^6 \text{ [ppm]} \quad \text{(B.50)}$$

An alternative notation commonly used when describing the effect of hydrogen diffusion on electrical conductivity is using the number or mole fraction, i.e. the amount of H atoms divided by the amount of Si atoms, typically expressed in parts per million H/Si:

$$C_{H/Si} = \frac{N_H}{N_{Si}} \cdot 10^6 \ = \frac{n_H}{n_{Si}} \cdot 10^6 [\text{ppm H/Si}] \tag{B.51}$$

To relate the number or mole fraction in equation (B.51) to the mass fraction in equation (B.49), it is necessary to first express it in terms of the amount of water molecules to the amount of olivine molecules:

$$C_{H/Si} = x^{-1} \frac{N_{H_2O}}{N_{Ol}} \cdot 10^6 \ = x^{-1} \frac{n_{H_2O}}{n_{Ol}} \cdot 10^6 [\text{ppm H/Si}] \tag{B.52}$$

where x is the amount of H atoms per Si atoms contributing to the hydrogen diffusion. The amount of a substance n can be expressed in terms of its mass m divided by its molar mass M

$$n = \frac{m}{M} \tag{B.53}$$

so that equation (B.52) can be written as:

$$C_{H/Si} = x^{-1} \frac{m_{H_2O}}{m_{Ol}} \frac{M_{Ol}}{M_{H_2O}} \cdot 10^6 \text{ [ppm H/Si]} \tag{B.54}$$

Substituting equation (B.49) into equation (B.54), the conversion between the water content C_{H_2O} and the hydrogen concentration $C_{H/Si}$ is given by:

$$C_{H/Si} \text{ [ppm H/Si]} = x^{-1} \frac{M_{Ol}}{M_{H_2O}} \cdot 10^4 \ \cdot C_{H_2O} \text{ [wt-\%]} \tag{B.55}$$

The molar mass of water is $M_{H_2O} = 18\frac{g}{mol}$ and the molar mass of olivine is $M_{Ol} = 147.5\frac{g}{mol}$ assuming a $(Mg,Fe)_2SiO_4$ composition. Therefore, equation (B.55) becomes:

$$C_{H/Si}\,[\text{ppm H/Si}] = x^{-1} \cdot 8.2 \cdot 10^4 \cdot C_{H_2O}\,[\text{wt-\%}] \qquad \text{(B.56)}$$

The most common mechanism of hydrogen dissolution in olivine is the one in which two protons from the water molecule go to the lattice site that is usually occupied by the Mg or Fe atom (Kohlstedt et al., 1996; Karato, 2006). The replaced Mg or Fe atom moves to the surface and reacts with the oxygen atom from the water to form MgO or FeO:

$$H_2O\,(fluid) + M_M^{\times} \leftrightarrow (2H)_M^{\times} + MO \qquad \text{(B.57)}$$

where M corresponds to either Mg or Fe.

C.1 Magnetotelluric measurements in Tibet

The magnetotelluric data for the three profiles presented in section 5.2.3 was inverted using the 2D inversion algorithm of Rodi & Mackie (2001). Initial inversions just used the transverse magnetic (TM) mode (Wei et al., 2001) because these data are generally less influenced by 3D induction effects than the transverse electric (TE) mode (Wannamaker et al., 1984). However, inclusion of the TE mode gives a more robust resistivity model, provided that 3D effects are not significant. Unsworth et al. (2005) published an inversion of the 100-line with both the TM-mode impedance and vertical magnetic field data included. The TE mode impedances were found to be significantly distorted at a number of stations.

Unsworth et al. (2004) published a full TM mode, TE mode, vertical magnetic field mode inversion of the 600-line data. An inversion of the entire 500-line with TE mode included has not been published, so this was undertaken as part of the current study, and used the same data (TM, TE and vertical magnetic fields) and control parameters as in the 600-line inversion of Unsworth et al. (2004). For the inversion an error floor of 20% in apparent resistivity and 5% in phase (expressed in equivalent apparent resistivity percent, with 5% corresponding to 1.45°) was applied, i.e. data errors that were below these error floor values were set to the error floor. The error floor for the vertical magnetic fields was set to an absolute magnitude of 0.02. The horizontal derivatives in the inversion were multiplied by a smoothing factor $\alpha = 3$, leading to an increased horizontal smoothness. The regularization parameter of the inversion was chosen as $\tau = 10$, resulting in a resistivity model with an overall r.m.s misfit of 1.96. The resistivity models for the three profiles are shown in Figure 5.3 along with the conductance (integrated conductivity) from the surface to a depth of 100 km. The model response for four stations along the 500-line is shown in Figure 5.4. The data fit is generally good, as illustrated by the pseudosections in Figure 5.5 and Figure 5.6.